# Cell Polarity Shapes the Epidermal Growth Factor Morphogen Gradient During *C. elegans* Vulval Induction and Reciprocal Epidermal Growth Factor Signaling Orients Cell Polarity to Promote Vulval Morphogenesis

---

**Dissertation**

**zur**

**Erlangung der naturwissenschaftlichen Doktorwürde**
**(Dr. sc. nat.)**

**vorgelegt der**

**Mathematisch-naturwissenschaftlichen Fakultät**

**der**

**Universität Zürich**

**von**

**Louisa Mereu**

**von**

**Walenstadt SG**

**Promotionskommission**

**Prof. Dr. Alex Hajnal (Vorsitz)**
**Prof. Dr. Esther Stoeckli**
**Prof. Dr. Markus Affolter**
**Prof. Dr. Stefan Luschnig**

**Zürich, 2017**

# Zusammenfassung

Epidermale Wachstumsfaktoren (EGF) sind Signalmoleküle, die durch Bindung an Rezeptoren der EGFR-ErbB-Familie wirken, indem die trans-autophosphorylierung durch die Tyrosin-Kinase-Aktivität des Rezeptors induziert wird. Der phosphorylierte Rezeptor kann hochkomplexe und vielseitige zelluläre Signalnetzewerke instruieren, wobei mehrere zelluläre Reaktionen wie Wachstum, Überleben, Zellteilung, Differenzierung, Migration und Apoptose reguliert werden. Krebszellen akkumulieren häufig Mutationen in Regulatoren oder Inhibitoren der ErbB-Signaltransduktionswege oder in ErbB Genen und ermöglichen ihnen so, den uneingeschränkten Zugang zu Zellproliferation, Überleben und Migration, um in die umliegenden Gewebe einzudringen. Die Forschung zu diesem Thema ist umfangreich. Je mehr wir darüber verstehen, desto mehr erkennen wir, wie viel es noch zu lernen gibt. Die regulatorischen Akteure des EGFR- Signaltransduktionswege sind konserviert in allen Lebewesen, weshalb Forschung in niederen Organismen, wie z. B. *Caenorhabditis elegans*, aufgrund ihrer reduzierten Zahl von ErbB-Liganden und Rezeptoren, von großem Nutzen sein kann. *C. elegans* hat nur je einen homologen EGF Ligand (LIN-3) und EGFR Rezeptor (LET-23). Die Entwicklung der *C. elegans* Vulva ist ein hervorragendes Modell, um Regulatoren der EGFR Signaltransduktion zu untersuchen. Während der Larvenentwicklung von *C. elegans*, sondert eine spezialisierte Uteruszelle, die Ankerzelle (AC), den LIN-3 Liganden in abgestufter Weise ab. LIN-3 fungiert als Morphogen. In hoher Dosis induziert es ein primäres Vulva-Zellschicksal und in niedriger Dosis ein sekundäres vulva Zelle Schicksal. In der ventralen Epidermis der Larven, gibt es sechs äquipotente epidermale Zellen (P3.p-P8.p), die als Vulva-Vorläuferzellen (VPCs) bezeichnet werden, und bei der Stimulation mit LIN-3 ein Vulva-Zell-Schicksal annehmen können. Um das induktive Signal zu erhalten, exprimieren sie den LET-23-Rezeptor überwiegend an ihrer basolateralen Membran. Aktiviertes LET-23 induziert den RAS / MAPK-Weg und fördert ein primäres Vulva-Zellschicksal und eine Hochregulierung von Notch-Liganden. Die Aktivierung von Notch in den benachbarten Zellen fördert ein sekundäres Vulva-Zelle-Schicksal und hemmt die MAPK-Signalisierung. Zusammen bilden diese Signale das typische 2 °-1 °-2 ° Vulva-Zelle-Schicksalmuster, in dem P6.p unweigerlich das Zentrum nimmt. Die Mislokalisierung von LET-23 zur apikalen Membran bewirkt eine erweiterte Ausbreitung des LIN-3-Liganden und bei einer leichten Hyperinduktion von RAS eine ektopische Vulva-Zelle-Schicksal-Adoption unter den VPCs. Dies zeigt, dass die Regulierung des LIN-3-Morphogen-Gradienten der übermässigen LET-23 Signalinduktion entgegenwirkt. Nach der Vulva-Zelle-Schicksal-Adoption teilen sich die Zellen dreimal und erzeugen insgesamt 22 Zellen, die in verschiedene untergeordneten Schicksale gegliedert sind, und auf jeder Seite der AC in gespiegelt Form gegliedert sind. Während der Vulva-Morphogenese verändern die Zellen ihre Form, bilden Prozesse und migrieren gezielt auf ihre jeweiligen Partner Zellen zu. Diese Umstrukturierung bildet schliesslich das komplette Vulva Organ. Die sich entwickelnde Vulva und der Uterus sind jeweils von einer Basalmembran umgeben. Um eine kontinuierliche Verbindung zwischen den beiden Organen herzustellen, muss die AC die Membranen durchdringen und zwischen die proximalen Vulva-Zellen, die VulF-Zellen, gezielt eindringen. Der direkte Kontakt der AC mit den vulF Zellen ist eine Voraussetzung für die dorsale Ausdehnung des Vulva-Lumens und eine Verbindung zum Uterus. In dieser Arbeit zeigen wir, dass die AC-Polarität eine Voraussetzung für eine gerichtete EGF-LIN-3-Ligand Diffusion ist, und somit die Morphogen-Gradienten-Ausbreitung begrenzt. Die LIN-3-Polarität wird durch einen unbestimmten Mechanismus, der zwei relativ unbekannte Proteine, das Neuropeptid NLP-26 und den G-gekoppelten Rezeptor SRA-9 umfasst, unabhängig von der allgemeinen AC-Polarität reguliert. Die beiden Proteine liefern der AC eine richtungsgebende Information, die LIN-3 speziell in Richtung der nächstgelegen VPC polarisiert. Diese gerichtete LIN-3 Sekretion erhöht die robuste Spezifizierung der Vulval-Zell-Schicksale. Wir finden weiter, dass die Vulva-Zellen zu Beginn der Vulval-Morphogenese LIN-3 in einer wechselseitigen Weise exprimieren. Vulva-spezifische Verringerung der *lin-3* Expression, sowie übermässige und unspezifische *lin-3*-Expression verursachen Fehler in der AC-Polarität, der AC Positionierung und in der Vulva-Morphogenese.

Unsere Daten zeigen eine neuartige Funktion von LIN-3 als induzierendes und leitendes Signal für das vermitteln der AC Polarisierung was eine normale Vulva-Morphogenese begünstigt.

# Summary

Epidermal growth factors (EGF) are signaling molecules, which act by binding to receptors of the EGFR ErbB family, thereby inducing trans-autophosphorylation by the receptor's tyrosine-kinase activity. The phosphorylated receptor can orchestrate highly complex, intricate and versatile cellular signaling networks, regulating multiple cellular responses, such as growth, survival, proliferation, differentiation, migration and apoptosis. Cancer cells frequently accumulate mutations in regulators or inhibitors of the ErbB pathways or in ErbB encoding genes, empowering them with unconstrained access to cell proliferation, survival and migration to invade adjacent tissues. The research on this topic therefore is extensive. However, the more we understand about the different induced canonical and non-canonical effectors and their integration and cross-talk with other signaling networks, the more we realize how much there still is to learn. The regulatory players of the EGFR pathway are highly conserved throughout all organisms, investigating the regulation of EGFR signaling in lower organisms, such as *Caenorhabditis elegans* can be of great use, due to its reduced number in ErbB ligands and receptors. *C. elegans* has only one EGF related ligand, LIN-3, and one EGFR related receptor, LET-23. Development of the *C. elegans* vulva is an excellent model to study regulators and modifiers EGFR signalin. During the *C. elegans* larval development, a specialized uterine cell, the anchor cell (AC), secrets EGF LIN-3 in a graded manner, which can act as a morphogen and at a high dose, induce a primary (1°) vulval cell fate and at a low dose a secondary (2°) vulval cell fate. In the ventral epidermis of the larva there are six equipotent epidermal cells (P3.p-P8.p), termed the vulva precursor cells (VPCs), which can adopt a vulval cell fate upon stimulation with LIN-3. To receive the inductive signal, they express the LET-23 receptor predominantly on their basolateral membrane. Activated LET-23 induces the RAS/MAPK pathway, promotes a 1° vulval cell fate and causes the upregulation of Notch ligands. Notch activation in the adjacent cells promotes a 2° vulval cell fate and inhibits MAPK signaling. Together, these pathways produce the typical 2°-1°-2° vulval cell fate pattern, in which P6.p invariably takes the center. Mislocalization of LET-23 to the apical membrane causes a wider spreading of the LIN-3 ligand, and upon mild hyper-induction of RAS, evokes ectopic vulval cell fate adoption amongst the VPCs. This shows that regulation of the LIN-3 morphogen gradient counteracts ectopic LET-23 signal induction. After vulval cell fate adoption, the cells divide three times generating a total of 22 cells, which are patterned into distinct subfates mirrored on each side of the AC. During vulval morphogenesis, the cells undergo cell shape changes and migration, which forms the vulval organ. The developing vulva and uterus are each surrounded by the basement membrane. To establish a continuous connection between the two organs, the AC has to breach the basement membranes and contact the most proximal vulval cells, the vulF cells. This AC vulF contact is a requisite for dorsal expansion of the vulval lumen, and a connection to the uterus. In this thesis, we show that AC polarity is a requisite for directed EGF LIN-3 ligand diffusion, and thus confines morphogen gradient spreading. LIN-3 polarity is regulated independently of general AC polarity by an unknown mechanism, involving two uncharracterized proteins, the neuropeptide NLP-26 and the G-coupled receptor SRA-9.

The two proteins supply directional information to the AC, which polarizes LIN-3 specifically towards the closest VPC. This directed LIN-3 secretion enhances robust vulval cell fate adoption. We further find that at the onset of vulval morphogenesis, the vulval cells express LIN-3 in a reciprocal fashion. Vulva-specific *lin-3* depletion as well as ectopic *lin-3* expression caused defects in AC polarity, AC mispositioning and vulval morphogenesis defects. Our data indicate a novel function of LIN-3 as an AC polarity and guidance cue during AC mediated vulval morphogenesis.

# Contents

# 1. Introduction

## 1.1 Epidermal Growth Factor signaling orchestrates an intricate and complex network of downstream signaling pathways

The ErbB family of Epidermal growth factor receptors (EGFR), are type I transmembrane receptors of the epidermal growth factor family (EGF-family), of extracellular protein ligands. Epidermal growth factors (EGF) are signaling molecules, which act by binding with great affinity to their receptor, thereby inducing its dimerization (Dawson et al., 2005). In case of constitutively dimeric receptors ligand binding induces minor structural rearrangements (Freed et al., 2015), leading to trans-autophosphorylation by the receptor's tyrosine-kinase activity. The activated receptor then recruits its downstream effectors, which can interact with the phosphorylated tyrosines in the ErbB receptor's kinase domain via their SH2 domain, promoting their phosphorylation and activation, instigating different downstream signal transduction cascades (Schlessinger, 2000). This stimulates a variety of possible cellular responses, such as growth, survival, proliferation, differentiation, migration and regulation of apoptosis. EGFR signaling can induce a variety of downstream signaling pathways, including RAS-ERK (Garrington and Johnson, 1999), PI3K-AKT (Bjorge et al., 1990) (Rodriguez-Viciana et al., 1994), PLC-γ1 (Anderson et al., 1990; Chattopadhyay et al., 1999), SRC (Tice et al., 1999) and STAT (David et al., 1996; Leaman et al., 1996) (Fig. 1.1.1). EGFR signaling thus evokes a multitude of cellular responses through all these downstream effectors, which likewise can interact and modify each other (Wee and Wang, 2017). However, how the EGFR receptor selectively or predominantly activates a specific downstream pathway from a whole network of possible effectors, and thereby brings about the appropriate cellular response, remains a highly complex and obscure matter and presents a topic of extensive investigation. Increased and aberrant EGFR signaling has long since been associated with cancer formation and progression (Cowley et al., 1986; Wong et al., 1987), and many cancer cells are characterized by their level or specific aberrations in receptor signaling , and are used to predict the state of the tumor progression and to make prognoses of a patients recovering probability (Slamon et al., 1987). It is therefore not surprising that many cancer therapies include drugs that specifically target and inhibit EGFR signal transduction. Sadly, the cancer cells evolve strategies to overcome the drug conveyed restrictions and thus frequently acquire drug resistance (Chen et al., 2012; Yun et al., 2008). Gaining a clearer understanding of how EGFR signaling is regulated and what condition leads to the induction of a specific signal transduction pathway is a key requisite for future approaches in the development of novel targeted cancer therapies. One factor that is necessary and additionally can fine-tune and regulate EGFR induced signal transduction specificity, is its ligand. Increased ligand availability, or ectopic ligand expression are linked to cancer progression and metastasis (Di Fiore et al., 1987; Gao et al., 2016; Mosadegh et al., 2008).

The manner, in which the EGF ligand is perceived by the EGFR receptor in terms of its spatial and temporal availability, as well as its structural nature and binding affinity can influence EGFR signaling, processing and trafficking (Roepstorff et al., 2009; Singh et al., 2007; Singhai et

al., 2014; Takemura et al., 1997; Zand et al., 2011).
EGFR ligands are synthesized as transmembrane precursor proteins (Massagué and Pandiella, 1993), which can signal in membrane bound form in a juxtacrine manner (Wong et al., 1989), or be cleavage by metalloprotease, and signal as a secreted, soluble molecules (Suzuki et al., 1997). The temporal, quantitative and qualitative nature, in which the ligand is presented plays a key role in the regulation of differential responses in EGFR signaling, this has been shown for cell fate specification(Katz et al., 1995), apoptosis (Iwamoto et al., 1999) and cell migration (Wyckoff et al., 2004). Their subcellular localization therefore comprises a capacity to regulate ligand availability and promote autocrine or paracrine signaling (Dempsey and Coffey, 1994).
Studies on EGFR signaling predominantly are focused on the receptor, however it is clear that regulation of the EGF ligand plays a vital role during development as well as in cancer formation, and understanding its role in instigating differential cellular responses during development of multicellular organisms, can help inspire new ideas and approaches in the search for effective cancer therapies.
The main research projects in this thesis are focused on how alterations in localized or subcellular EGF ligand expression can fine-tune cell-fate adoption and direct cell polarity. We investigated how tissue specific aberrations in EGF levels and subcellular localization pattern alterations promote defects during organogenesis of the vulva in the model organism *Caenorhabditis elegans*.

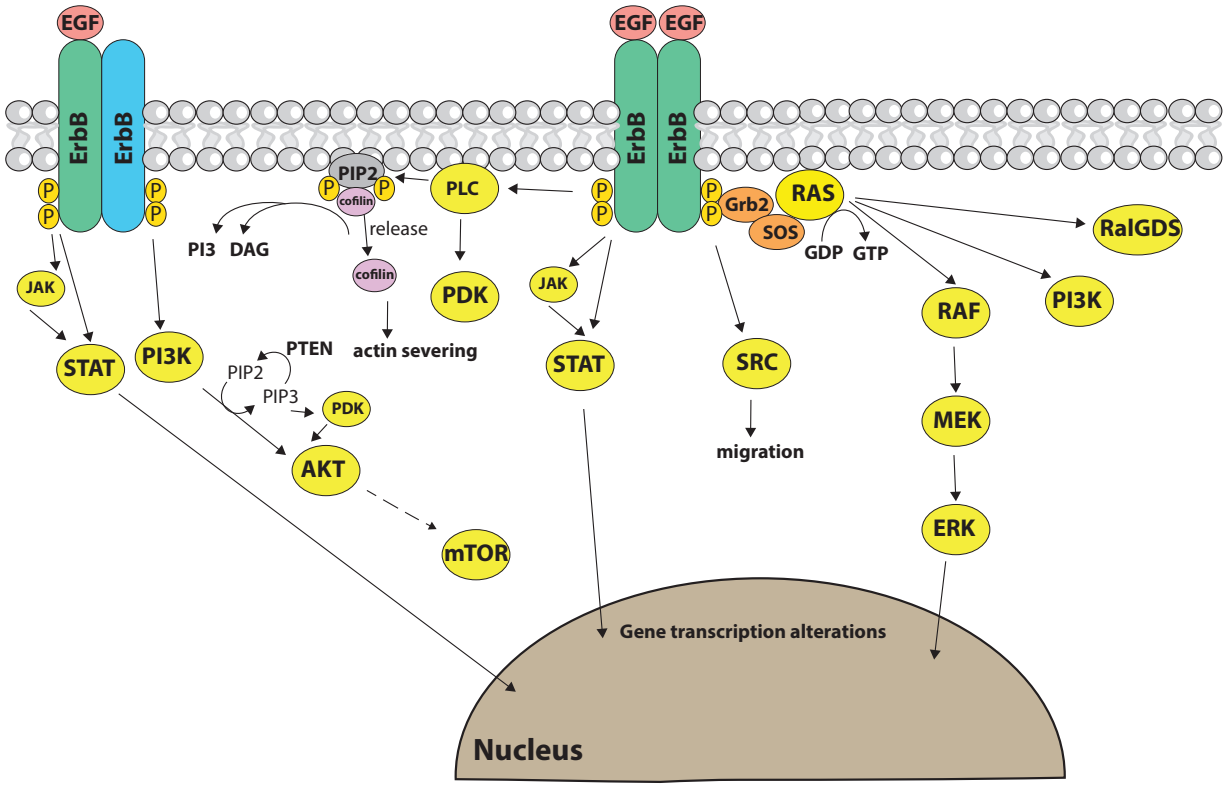


**Fig. 1.1.1 Cartoon illustrates the potentially induced downstream effectors by ErbB homo or heterodimers**

### 1.1.1 The Epidermal growth factor ligand and receptor families

The EGFR or ErbB family of genes and its ligands have multiple homologs and orthologs in all organisms. In humans, the ErbB family of receptors is made up of four classes of genes, ErbB1/ EGFR/ HER1, ErbB2/NEU/ HER2, ErbB3/HER3 and ErbB4/HER4. They encode for proteins, which upon ligand binding, can form different homo- or hetero-dimer combinations with each other (Schlessinger, 2000). The mature EGF receptor consists of three main domains, the extracellular, the transmembrane and the intracellular tyrosine kinase and tail domain. The extracellular domain is made up of two ligand binding and two cysteine rich, dimerization arm domains, which exist as two alternated repeating sections (Ward et al., 1995)(Fig. 1.1.2). There exist distinct differences between the ErbB groups, for instance, ErbB2 does not possess a ligand-binding domain, yet can promote signal transduction as a hetero-dimer (Graus-Porta et al., 1997). ErbB3 in contrast does not contain a kinase domain, but can still conduct signaling as a heterodimer (Holbro et al., 2003).
The seven epidermal growth factor (EGFR) ligands are EGF, heparin-binding EGF-like growth factor (HB-EGF), betacellulin (BTC), Transforming growth factor alpha (TGF-α), amphiregulin (AR), epiregulin (EPR) and epigen (EPG) (Fig.1.1, A)(Harris et al., 2003). An additional group of EGF-related genes exists, termed the neuregulins (Falls, 2003). The EGF and neuregulin ligands are grouped into three categories, depending on their preferred ErbB binding partners. EGF, AR, TGF-α and EPG specifically bind to ErbB1/EGFR. The second category binds to both EGFR and ErbB4, and includes EPR, BTC and HB-EGF. The third class is comprised of the neureguline family (NRG1-4), which do not bind EGFR. NRG1 and NRG2 bind to ErbB3 and ErbB4 and NRG3 and NRG4 only bind to ErbB4 (Chang et al., 1997; Falls, 2003) (Fig. 1.1.2).
Most members of the EGF family of ligands are type I transmembrane proteins, containing one functional EGF motive, which is a 40 amino acid long sequence with six spatially conserved cysteine (C) residues (CX7 CX4–5 CX10–13 CXCX8 C) that form three intramolecular disulfide bonds (C1-C3, C2-C4, C5-C6) (Van Zoelen et al., 2000). The EGF domain constitutes the ligands binding and signal transducing property. However, the overall protein sequence similarity between the different EGF ligands is low, and they show differences in glycosylation and herparin binding sites (Harris et al., 2003). They also show great variation in their extracellular cleavage site and in the length of their juxtamembrane domain, which serve to convey proteolytic cleavage efficiency (Hinkle et al., 2004). Mammalian EGF precursor ligands are usually cleaved at the ectodomain by members of the ADAM family of membrane-anchored metalloprotease (Sahin et al., 2004). Members of the Rhomboid family of seven-pass-transmembrane intramembrane serine proteases, have been shown to play a role in premature EGF precursor ligand proteolytic processing, in invertebrates as well as mammalian cells (Adrain et al., 2011 , Dutt et al., 2004; Wasserman et al., 2000).

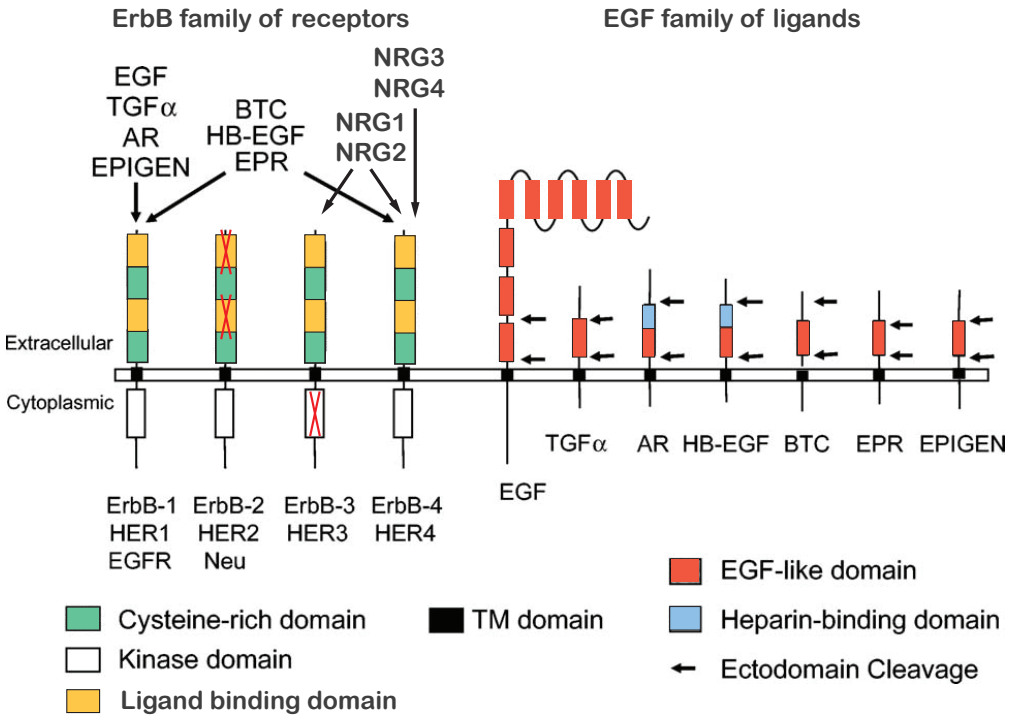


Adapted from: R.C. Harris et al. / Experimental Cell Research 284 (2003) 2–13

**Figure 1.1.2 Epidermal growth factor ligand and the ErbB receptor family signaling**

Cartoon shows the different ErbB family members; ERbB1-4, and the mammalian EGF family of ligands. The different domains are indicated, and the preferred ErbB binding partner for each EGF ligands as well as the family of Neuregulins is demonstrated. Red crosses mark defects in binding domain or kinase domain, present in ErbB2 and ErbB3 respectively. The figure was adapted from an illustration in the review by R.C. Harris et al. in 2003.

### 1.1.2 How epidermal growth factor ligands regulate EGFR signaling

It is clear that the ligands play a decisive role in regulating differential EGFR mediated cellular responses. Some mechanisms have been revealed by previous research, but there are still many open questions. In a nutshell, one of the most obvious variants in differential EGFR signaling is that each of the described ligands displays individual binding affinity and dissociation rates under specific environmental conditions. The ligands also have differential binding preferences to specific ErbB types (Jones et al., 1999) and can promote specific homo- or heterodimerization. For instance, EGF and TGF-α specifically bind EGFR ErbB1, and promote heterodimer formation with ErbB2, rather than EGFR homodimer formation. On the other hand, AR and BTC form both homo and heterodimer types at equal frequency (Macdonald-Obermann and Pike, 2014). Thus, the EGF ligands can influence ErbB receptor signaling by promoting different homo- or heterodimer combinations, which in turn can affect the period and the amplitude of EGFR signal transduction (Tzahar et al., 1998). Another feature in which EGF ligands have been shown to regulate signaling, is by influencing ErbB receptor trafficking by endocytic sorting upon receptor internalization (Roepstorff et al., 2009). It was shown that HB-EGF, AR or BTC induced receptor internalization always lead to lysosomal degradation of the receptor, whereas TGF-α and EPR-induced receptor internalization always lead to receptor recycling. EGF induction, mostly lead to receptor degradation, but also induced receptor recycling (Roepstorff et al., 2009). The cause of the differential sorting can be explained by conditional, differential ligand receptor affinities and dissociation rates, which induce and promote the degree and sustainment of receptor ubiquitination. Thus, ligand receptor binding affinity and dissociation rates are important factors, which modulate ErbB signaling.
EGFR signaling in healthy, "wild-type" organisms is dependent on EGF ligand induction or by receptor mediated trans-activation (Graus-Porta et al., 1997). Cancer cells, frequently accumulate EGFR specific mutations, enabling them to bypass ligand dependent signal propagation (Guo et al., 2015). During an organisms developmental, ligand availability constitutes a limiting condition for EGFR signaling, and specific subcellular ligand distribution and processing, localized ligand production and differential soluble ligand concentrations are instructive factors for differential cellular responses (Katz et al., 1995; Singh and Harris, 2005). Restricted ligand expression can also limit the range of secretion and thus restrict ectopic receptor induction. TGF-α predominantly signals in an autocrine or paracrine manner in Madin-Darby canine kidney (MDCK) cells, and even upon transgenic upregulation of the TGF-α precursor protein in these cell lines, soluble TGF-α could not be detected in the culture medium (Dempsey and Coffey, 1994). This suggests that restriction of secreted TGF-α might be an important requisite for normal tissue or organism development. Accordingly, it was found that ectopic TGF-α expression in transgenic mice leads to developmental defects and hyperplasia, indicating that TGF-α has an oncogenic potential (Sandgren et al., 1990). Loss in TGF-α function causes tissue specific defects, namely in eye and hair-follicle development (Luetteke et al., 1993). Together, this suggests that TGF-α expression is tightly regulated and confined to specific tissues during mammalian development.
Localized ligand expression and intracellular trafficking of membrane bound ligands present effective methods of regulating ligand availability during multicellular development. Pro-TGF-α, Pro-AR and pro-EPR have all been shown to localize specifically to the basolateral membrane of

polarized MDCK cells (Brown et al., 2001). However, for each of the ligands, a separate strategy mediates its localization. For basolateral localization of pro-TGF-α, the cargo targeting and recognition protein Naked2 is required to mediate fusion of pro-TGF-α containing vesicles to the cell membrane. Consequently, downregulation of Naked2 leads to accumulation of pro-TGF-α containing vesicles in the cytoplasm (Li et al., 2007). Pro-AR localization is not affected by loss in Naked2 function (Li et al., 2004). Pro-EGF is equally sorted both to the apical and the basolateral membranes in MDCK cells, but is predominantly proteolytically cleaved and released at the basolateral membrane, and the pro-EGF transmembrane protein thus accumulates at the apical side (Dempsey et al., 1997). Pro-EPR is sorted to the basolateral surface, dependent on a tyrosine-based motif in the its cytoplasmic domain, and Mistrafficking of pro-EPR to the apical surface of MDCK cells results in hyperproliferative and locally invasive tumors (Singh et al., 2013). These data suggest that the subcellular localization of multiple epidermal growth factor precursor ligands presents an important part in the regulation of EGFR signaling.
All these examples give insight into the complex manner, in which the EGF ligands regulate developmental processes, and that their influence is crucial for wild-type development. Loss of function mutations in mammalian EGFR ligands have no severe effect on development and viability, even when combined as double or triple mutants (Dahlhoff et al., 2013; Luetteke et al., 1999). This shows that the ligands can function redundantly, which adds a level of complexity to studies examining novel function of EGFR ligands.
Studies on the nematode, *Caenorhabditis elegans*' sole EGF ligand and receptor, therefore present an advantage in the quest of novel regulators and functions of EGF ligands and their homologs.

### 1.1.3 *lin-3*, the sole *Caenorhabditis elegans* EGF homolog

The only EGF family member of ligands in *C. elegans* is LIN-3 (Hill and Sternberg, 1992). This holds advantages and disadvantages for studies focused on the signaling molecule. Mutations conveying complete loss of function to the gene results in early larval viability, due to loss in proper excretory-duct formation (Abdus-Saboor et al., 2011; Ferguson and Horvitz, 1985). This shows that unlike in mammals, no other putative EGF family members can compensate for loss of LIN-3 function, and accordingly, LIN-3 is charged with multiple functions in *C. elegans* development and behavior. In addition to larval viability, LIN-3 signaling is required for vulval cell fate induction (Ferguson and Horvitz, 1985; Hill and Sternberg, 1992), male spicule development (Chamberlin and Sternberg, 1994), P12 neuroblast cell fate specification (Jiang and Sternberg, 1998), uterine uv1 cell fate specification (Chang et al., 1999), regulation of apoptosis (Jiang and Wu, 2014), for hermaphrodite ovulation (Clandinin et al., 1998) and to convey a sleep like state, normaly preceeding larval ecdysis or under situations of intense stress (Hill et al., 2014; Van Buskirk and Sternberg, 2007). Previous research has thus shown that LIN-3 is repeatedly required during *C. elegans* development. The challenging aspect in the investigation of putative novel functions of LIN-3 consist in the early larval lethality of null mutants. Another challenging feature lies in the spectrum of differential isoforms and transcriptional start-sites. The *lin-3* gene is located on chromosome IV and spans a sequence of approximately 10 kb including all known regulatory elements and has three putative transcriptional start-sites (Liu et al., 1999; Saffer et al., 2011). Like mammalian EGF ligands, LIN-3 is produced as a class I trans-

membrane precursor protein with, from N- to C-terminus, a signal peptide, one EGF like repeat, a transmembrane region and a cytoplasmic tail (Fig.1.1, D). There are four known isoforms, which differ in their exon composition at the translated juxtamembrane region, the region between the EGF-like repeat and the transmembrane domain of the protein (Dutt et al., 2004; Van Buskirk and Sternberg, 2007), which corresponds to the site at which proteolytic cleavage can occur. So far however, only one LIN-3 processing protease has been identified. ROM-1, a *C. elegans* seven-pass transmembrane serine proteases, Rhomboid family member, which is specifically required for cleavage of the "long" LIN-3 isoform (Dutt et al., 2004). The length of the translated LIN-3 precursor protein can vary between 421 and 477 AA (www.wormbase.org). In this study, we focused our research on putative novel roles of LIN-3 during vulval development, and how LIN-3 secretion is fine-tuned during vulval induction.

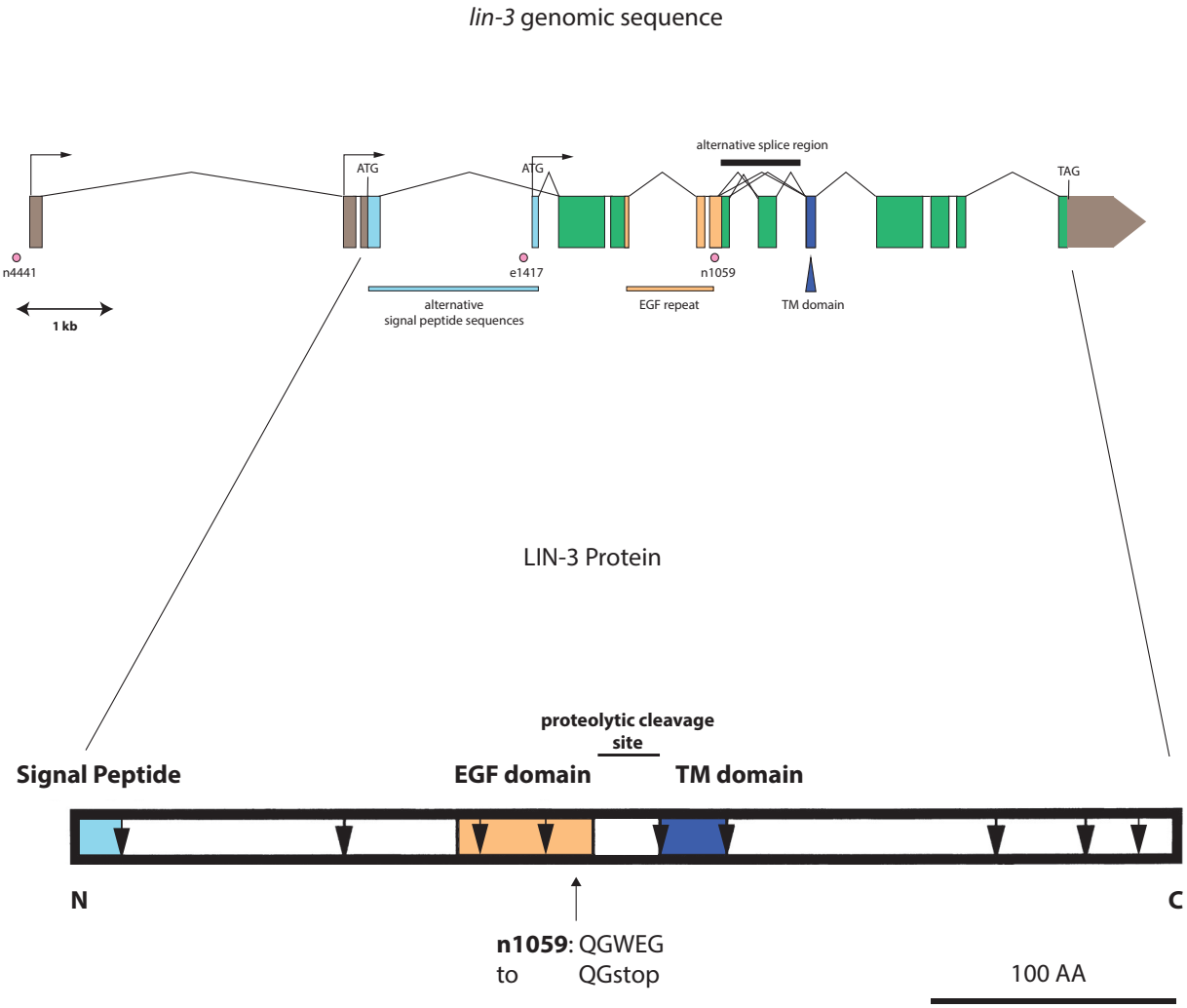


**Figure 1.1.3 Epidermal growth factor ligand**

The illustration shows the genomic structure of the sole *C. elegans* EGF family member, *lin-3*. Boxes represent exons and connecting lines represent introns. Green boxes represent protein-coding exons, and in addition, exons coding for specific protein domains are color coordinated and appropriately labeled in the figure. The three arrows, issuing from the exons, illustrate putative transcription start sites. The *lin-3* alleles n4441, e1417 and n1059 locations are indicated in gene as landmarks.
Illustration of translated LIN-3 protein domains. The protein domains are adapted from J. Liu et al. 1999.

## 1.2 *C. elegans*, a tool in the quest for novel gene functions and interactions

In its natural habitat, the nematode *Caenorhabditis elegans* resides in soil and feeds on *E. coli* bacteria and can be isolated from almost anywhere around the world. Evolutional comparison studies make use of this fact and investigate the genome variations of wild *C. elegans* isolates form all over the world (Dolgin et al., 2008; Thomas et al., 2015). The strain that was established as wild-type and is used for research in most *C. elegans* focused laboratories, was isolated in Bristol in 1965 and a line of this strain, N2, was then studied by Sydney Brenner, who first established protocols for the handling of the newly established model organism (Brenner, 1974). In the meantime, pioneer work performed in *C. elegans* has led to deeper insight into key-biological functions including micro RNA and RNA interference (Fire et al., 1998; Reinhart et al., 2000), apoptosis (Kimble and Hirsh, 1979; Metzstein et al., 1998), cell-fate specification (Greenwald et al., 1983; Sternberg, 2004; Sternberg and Horvitz, 1986), axon guidance (Chan et al., 1996) and cell polarity (Goldstein and Hird, 1996; Kemphues et al., 1988).
The properties that make *C. elegans* so desirable as a model are, just to name a few, its small size, transparency, easy and cheap maintenance, useful storing capacity, as well as its invariable cell lineage. *C. elegans* presents vast advantages in the search for novel gene interactions, in its practicability in whole genome, sensitized or targeted screens, tailored to the research question of interest (Wang and Sherwood, 2011). Although a worm seems to be far away from humans, measured on an evolutionary scale, approximately 40% of the protein sequences have human homologs (Shaye and Greenwald, 2011). These qualities taken together make it a desirable model in the investigation of biological processes. In our research group, we are interested in the main conserved signaling pathways, such as EGFR/RAS/MAPK, Wingless (WNT) and DELTA/NOTCH, and at what level they interact or are modulated. In *C. elegans* vulva development all these pathways act synergetic or opposing to produce a functional vulval organ. Such as in general *C. elegans* development, vulva development follows invariable events of cell fate and cell divisional processes.

### 1.2.1 A short overview to the *C. elegans* life cycle

The *C. elegans* life cycle begins with fertilization of the egg inside the hermaphrodite either by male insemination, or through self-fertilization, and ends during adulthood after approximately three and a half days, when the adult hermaphrodite worm acquires the stage, in which it is able to lay eggs. After hatching, the worm goes through four larval stages (L1-L4, Fig. 1.2.1) (www.wormbook.org). To transverse from one stage to the next, the worm enters into a molting process, which requires a sleep-like state (Raizen et al., 2008), and encompasses shedding of the worms cuticle, a process which is mediated by secreted metalloproteases, such as NAS-37 (Davis et al., 2004). If environmental conditions are unfavorable during development, for instance due to lack of food, *C. elegans* larvae can enter an alternative dauer larval stage after L1, increasing its survival probability. When food is available again, the worm reenters the normal life cycle and continues larval development from the L4 stage on. At standard conditions of 20°C, the second larval (L2) stage is entered approximately 15 hours, the third stage (L3) 24 hours and the fourth stage (L4) 34 hours after hatching. Vulval induction is initiated at the end of the second (L2) larval stage (Hill and Sternberg, 1992), and vulval morphogenesis is completed during the last molting stage that converts the L4 larva into an adult (Sharma-Kishore et al., 1999).

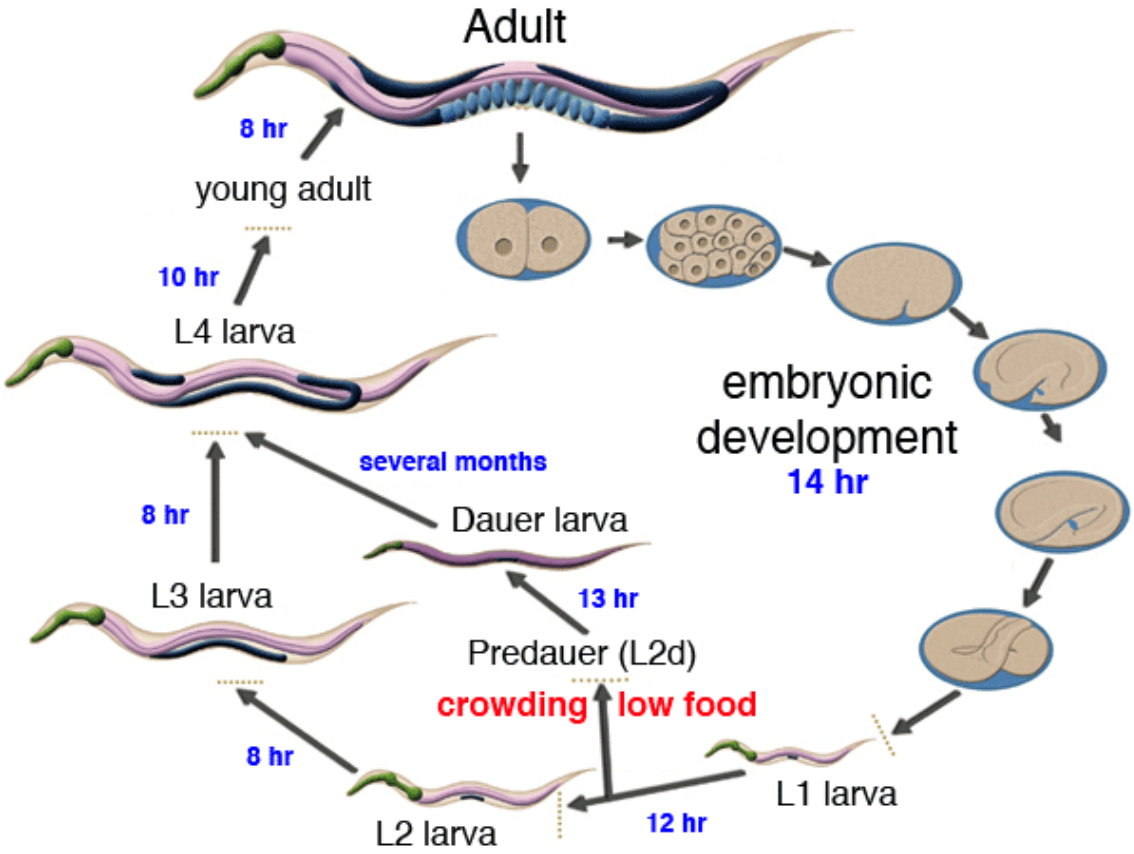


**Figure1.2.1 The *C. elegans* life cycle at 22°C**

The *C. elegans* life cycle starts when the egg of the hermaphrodite is fertilized. It takes approximately four days until the newborn hermaphrodite reaches adulthood and can lay eggs. Illustration from www.wormatlas.org

### 1.2.2 Vulval cell fate induction

During the L1 stage of *C. elegans* development, 12 epidermal cells P1.p to P12.p are generated in the ventral cuticle (Sulston and White, 1980). A WNT gradient coming from a group of cells at the posterior end of the L1 larva signals to these Pn.p cells and specifies P3.p to P8.p as competent to adopt a vulval cell fate (Eisenmann et al., 1998). This group of cells is thus called the vulva competence group, or the vulva precursor cells (VPCs). Dorsal to the VPCs, the somatic gonad develops, which will later form the uterus. In this somatic gonad, one of two uterine vu cells is specified by Delta/Notch lateral signaling, to adopt the anchor cell (AC) fate (Kimble and Hirsh, 1979). LIN-12 Notch activation regulates EGL-43 expression, a transcriptional repressor, which negatively regulates AC fate adoption(Hwang et al., 2007).
During the early-mid L2 larval stage, the specified AC starts to secrete LIN-3 EGF, which likely forms a gradient and induces distinct vulval cell fates in the adjacent VPCs. The LIN-3 receptor, LET-23 is predominantly localized to the basolateral membrane of the VPCs and thus enriched towards the signal sending AC. This localization is stabilized by a protein complex of LIN-7, LIN-2 and LIN-10 (Hoskins et al., 1996, Kaech et al., 1998; Whitfield et al., 1999).
As has been shown in mammalian cells, LIN-3 ligand mediated activation of its receptor, induces internalization and degradation of the receptor, while RAS/MAPK signalin promotes transcriptional upregulation of LET-23 and thus induces a positive feedback loop (Haag et al., 2014). The vulva inductive cue LIN-3 has been shown to act as a morphogen. At high concentration it promotes a 1° vulval cell fate and at lower concentrations it can lead to 2° vulval cell fate adoption (Katz et al., 1995). LET-23 is the sole ErbB family member in
*C. elegans* and thus forms a homodimer. Unlike in mammalian ErbB receptors, LET-23 forms a constitutive dimer, independent of ligand binding (Freed et al., 2015). LIN-3 binding induces minor structural rearrangements, which lead to trans-autophosphorylation by the receptor's tyrosine-kinase that can activate downstream effector pathways (Freed et al., 2015). During vulval induction, LET-23 has been shown to induce the LET-60 RAS/MPK-1 ERK pathway (Lackner and Kim, 1998, Han and Sternberg, 1990), which leads to upregulation of LIN-12 Notch ligands, such as LAG-2, DSL-1 and APX-1 (Huelsz-Prince and van Zon, 2017), which in turn activate Notch in the adjacent VPCs (Sternberg, 1988; Yochem et al., 1988). Notch activation through this lateral inhibition in turn promotes a 2° vulval cell fate and down-regulates LET-60 RAS signaling (Berset et al., 2001), whereas the increased RAS LET-60 signaling downregulates LIN-12 NOTCH expression (Shaye and Greenwald, 2002). This intricate interplay of RAS and NOTCH signaling in wild-type conditions, conveys the typical 2°-1°-2° vulval cell fate pattern, in which P6.p almost invariably takes the center (Braendle and Félix, 2008) (Fig. 1.2.2). The VPCs, which do not experience enough LIN-3 mediated LET-23 activation, adopt a non-vulva tertiary fate (3°), and after one round of cell division, fuse with the surrounding hypodermis. During this vulval cell fate coordination, basolateral LET-23 localization in the VPCs has been shown to significantly impair LIN-3 ligand spreading to more distal VPCs, as a method to control localized cell fate induction (Hajnal et al., 1997). This highly efficient ligand sequestering has also been observed for TGF-α in epithelial MDCK cells (Dempsey and Coffey, 1994). After the vulval cells have been specified, they undergo three rounds of cell division, generating a total of 22 cells, witch upon morphogenesis form a stack of seven toroids, which shape the vulval tube.
Excessive upregulation in signaling activity of any component in the LIN-3 mediated, LET-23

induced LET-60/MAPK pathway generates a typical phenotype, in which multiple VPCs adopt a vulval cell fate, promoting ectopic cell division and leading to a multivulva (Muv) phenotype. The opposite, in which RAS pathway signaling is reduced, generates less cell division, leading to a vulvaless (Vul) phenotype. Both these phenotypes are quite characteristic, and are used as readout in screens for regulators of the RAS pathway.

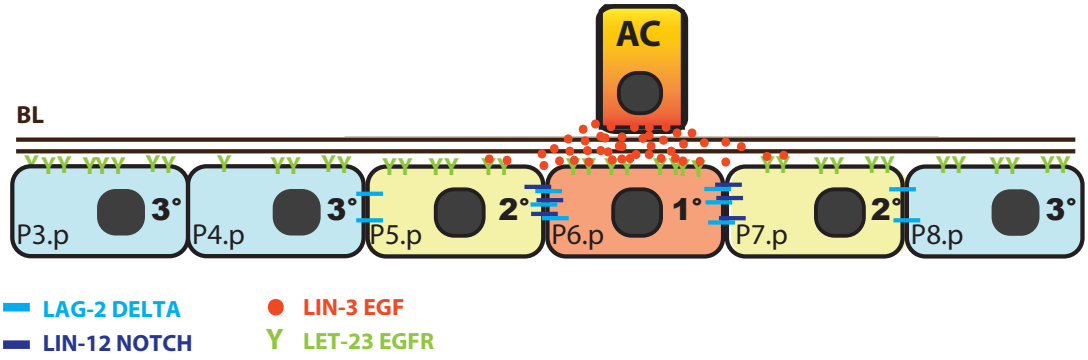


**Figure 1.2.2 Vulval cell fate induction**
Cartoon illustrates AC mediated vulval induction at the early L3 stage. The specific fate that reach VPC (P3.p-P8.p) adopts is shown. The basal lamina (BL) separates the AC from the VPCs. The involved signaling molecules are labeled in figure.

### 1.2.3 The AC mediates basal lamina breaching and uterine vulval connection

The uterine and the vulva epidermal tissue are each surrounded by an extracellular matrix, separating the two tissues. Since the hermaphrodite's uterus and vulva need to form a continuous lumen to allow future progeny to pass into the external environment, the barrior in form of the basement membrane or basal lamina needs to be removed.
The AC executes this process and in addition mediates and coordinates the connection of the two tissues. Differential signal interactions coordinate this process. As a prerequisite, the AC needs to be polarized, and form protrusions in the appropriate direction. The Netrin homolog UNC-6 is secreted from the ventral nerve cord (VNC) and directs its receptor, UNC-40, which is expressed in the AC, to relocate to the ventral membrane of the AC (Ziel et al., 2008). The ventral membrane of the AC is termed the invasive membrane, it is enriched with the phospholipid phosphatidylinositol 4,5-bisphosphate ($PIP_2$), which functions as scaffold for F-actin recruitment, association and regulation (Janmey and Lindberg, 2004; Mao and Yin, 2007; Yonezawa et al., 1990). Localization of the UNC-40 receptor is required for the AC to form a centralized, ventrally directed protrusion, which can invade the basal lamina (Hagedorn et al., 2013; Ziel et al., 2008). In *unc-6* mutants with no more directional cue, the UNC-40 receptor associates and dissociates in clusters, in a cyclic, but random manner within the AC. This random clustering is counteracted by the only known negative regulator of AC invasion, MADD-2 (Morf et al., 2013), which promotes UNC-40 cluster dissociation (Wang et al., 2014b). UNC-40 subcellular receptor localization is also regulated by the integrin receptor heterodimer INA-1/PAT-3, and in absence of UNC-40, the integrins can still promote actin recruitment, in a vulval cue dependent manner

(Hagedorn et al., 2013; Hagedorn et al., 2009; Lohmer et al., 2016; Ziel et al., 2008). This vulval cue is known to exist and is expressed from the 1° vulval cells, but so far, has not been identified.

In addition to the regulation of polarity and protrusion formation, the transcription factor FOS-1 plays a role during basal lamina breaching. FOS-1 activates transcription of metalloproteases, such as CDH-3 and ZMP-1, which are translocated to the invasive membrane, where they are secreted, allowing digestion of the basement membrane (Sherwood et al., 2005). The Ena/VASP ligand MIG-10 lamellipodin is a FOS-1 target, that has been shown to be recruited to the invasive membrane in an integrin dependent manner to promote basal lamina breaching (Wang et al., 2014a). These signaling combinations coordinate the AC basal lamina breaching process (Fig. 1.2.3).

The AC does not only induce the vulval cell fate, but also regulates π cell fate specification amongst a group of uterine cells (Newman et al., 1996). The AC later fuses with these π cells, to form the syncytium termed the utse. This fusion is necessary to clear the passage between uterine and vulval lumen.

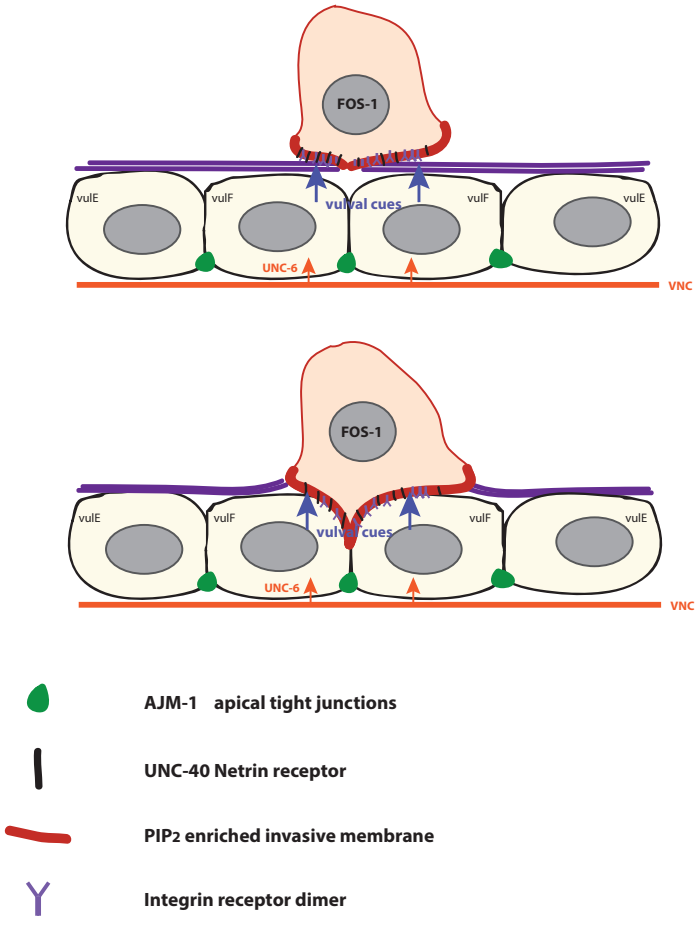


**Figure 1.2.3 Basal lamina breaching**

Cartoon illustrates basal lamina breaching by the AC at the mid to late L3 stage. Netrin UNC-6 secreted from the ventral nerve cord (VNC) together with the unknown vulva cue, polarize the ACs invasive membrane, enriched in $PIP_2$ and F-actin, via UNC-40 receptor and integrin recruitment, towards the basal lamina. The transcription factor FOS-1 activates upregulation of different metalloproteases and extracellular matrix components, promoting the removalf of the basal lamina.

### 1.2.4 Vulval morphogenesis

The vulval cells undergo three rounds of cell division, the first two are in a longitudinal, the last in either a transversal or a longitudinal direction. 1° cell division onset is at the mid L3, and within a few hours at the mid-late L3 stage, the second cell division occurs. At this point, the vulval cells adopt specific sub-fates, which are largely instructed by the AC. There are seven subfates, of which vulA, vulB1, vulB2, vulC and vulD are 2° specific, and vulE and vulF are 1° specific. The fate pattern presents a mirrored image, with the AC representing the point of reflection (Fig. 1.2.3). The vulF sub-fate adoption requires direct AC contact, and subsequent Wnt signaling between the proximal and distal 1° cells (Wang and Sternberg, 2000). The AC also sends Wnt signals, which reorient the cell fate pattern towards the AC in the 2° descendants of P7.p (Green et al., 2008). The vulva sub-fates have been shown to express distinct patterns in cell fate markers, for instance, the FGF homolog EGL-17 is initially a 1° cell fate marker (mid-late L3), and later (midL4) is specifically expressed in 2° vulC and vulD cells (Burdine et al., 1998), and
EGL-38, a Pax2/5/8 transcriptionfactor, is specific for the 1° vulF cells (Fernandes and Sternberg, 2007; Ririe et al., 2008). EGL-38 further induces vulF specific LIN-3 expression, which specifies the uterine uv1 cell fate (Chamberlin and Sternberg, 1994). The vulF cells also form the direct connection between the uterus and the vulva via junctions with the utse and uv1 cells (Newman et al., 1996). During the third round of cell division, the tissue takes on an additional plane, by dividing along a transversal axis in addition to the lateral division (Sharma-Kishore et al., 1999). At the same time, coordinated apical and lateral constriction events further convey a three-dimensional structure to the initial two-dimensional epidermal tissue (Yang et al., 2017).
To form the seven stacks that will shape the vulva, the 2° vulval cells of the same subfates migrate towards each other and form processes around the vulval cells more proximal to the AC. Having found their respective partners they either fuse or form junctions with them, forming toroids. These toroids give shape to the ventral lumen of the vulva (Sharma-Kishore et al., 1999). To form the dorsal vulval lumen, direct AC to vulF cell contact is required, which primes the vulF cells and enables them to from AC independent cell shape changes that expand the dorsal lumen (Estes and Hanna-Rose, 2009). Expression of EGL-26 in the adjacent vulE cells is required for this process (Hanna-Rose and Han, 2002) (Fig. 1.2.4).

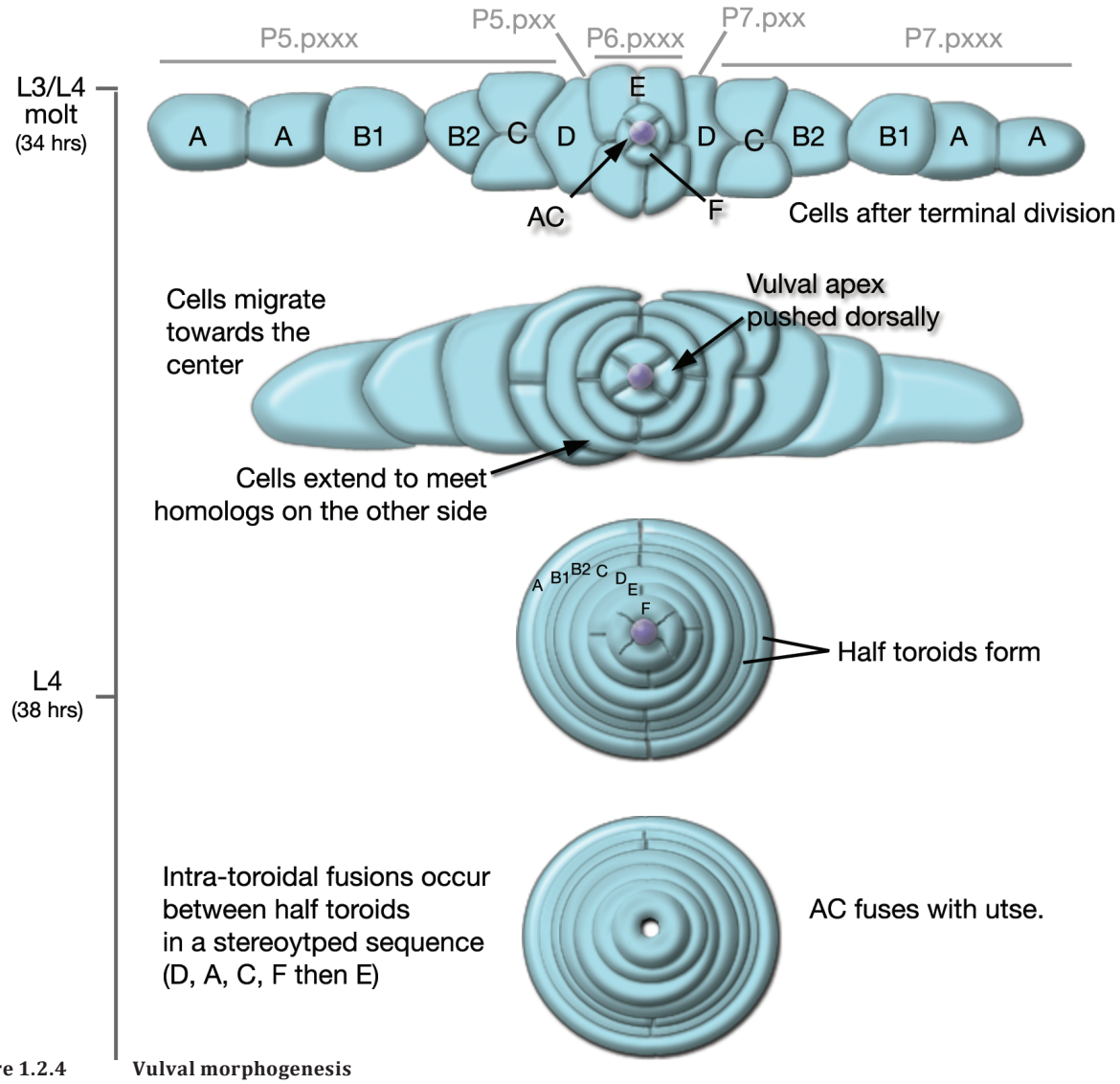


**Figure 1.2.4** **Vulval morphogenesis**

Figure show cell migration and cell shape alterations in the process of vulval morphogenesis. The figure is adapted from WormAtlas (www.wormatlas.org)

## 1.3 Cell polarity establishment

Cell polarity comprises the asymmetric distribution of cellular components, structures and organelles within a cell along one or more axes, which is required for asymmetric cell-division, cell differentiation, morphogenesis and cell migration. Epithelial cells are a type of highly polarized cells, which form tight junctions, connecting the individual cells into a tissue, which lines the cavities and compartments of organs and presents a barrier to the exterior environment. The Apical tight junction complexes are comprised of tight junctions and adherence junctions, and embody a physical barrier between the apical and the basolateral cell membranes (Hartsock and Nelson, 2008). They are composed of over 100 proteins, including scaffold proteins, kinases and phosphatases, transcription factors and actin binding factors, and can integrate extracellular signals into cytoskeletal rearrangement and even induce transcriptional activation (González-Mariscal et al., 2003; Quiros and Nusrat, 2014).
The E-cadherins are cell adhesion molecules involved in the establishment of the adherence junctions. E-cadherins are type I transmembrane proteins and localize to the lateral, but not to the apical membranes. Their extracellular domain form $Ca^{2+}$ dependent, homophilic contact with other E-cadherins in neighboring cells, initiating intercellular adherence (Takeichi, 1988). The intracellular domain of E-cadherins binds to β-catenin, which in turn binds α-catenin, which contacts the actin cytoskeleton. The adherence junctions are not static, but active and dynamic complexes. Their components are continuously recycled and adapted (Yap et al., 2007). The p120 catenin serves as a gatekeeper in E-cadherin regulation in mammalian cells. It contacts the cytoplasmic tail of E-cadherin, and promotes its retention at the membrane or its endocytosis and trafficking (Chen et al., 2003; Davis et al., 2003; Xiao et al., 2003).
Three major polarization complexes regulate apicobaslal cell-polarity, the Scribble/Discs Large/Lethal Giant Larvae, the CRB/PALS/PATJ and the PAR3/PAR6/atypical protein kinase C (aPKC) complex. These complexes are conserved from *Caenorhabditis elegans* to mammals (Roh and Margolis, 2003). The CRB and the PAR complexes promote apical membrane polarity, while the Large/Lethal Giant Larvae complex promotes basolateral membrane polarity, the basolateral and the apical complexes have antagonizing functions (Bilder, 2004).
CRB Crumbs are transmembrane proteins with conserved FERM- and PDZ-binding motifs in their cytoplasmic domain (Hollander et al., 1999; Hollander et al., 2001). The presence and composition of the extracellular CRB domain, is variable between species, and its importance is unclear, since truncated proteins lacking the extracellular membrane can rescue loss of endogenous CRB function in Drosophila (Wodarz et al., 1995). CRB expression is sufficient to determine apical membrane identity, and overexpression of CRB results in expansion of the apical domain (Wodarz et al., 1995). PALS1 Stardust, is a membrane-associated guanylate kinase protein and binds both CRB and PATJ, linking the two complex components (Roh et al., 2002), its N-terminal region can bind to Par6 (Wang et al., 2004). Loss in PALS1 function, leads to disruption of apical tight junctions, linked to induced defects in E-cadherin trafficking to the cell membrane (Wang et al., 2007). PATJ serves as a scaffold, and has multiple PDZ domains, which can interact with various components of the tight junction (TJ) complex. Loss of PATJ function, causes a delay in TJ formation and defects in cell polarity (Shin et al., 2005). The CRB and the PAR complexes rely on one another for proper localization, PALS1 can bind PAR6 and PAR3, and loss in PALS1 function leads to mislocalization of PAR3 in MDCK cells (Shin et al., 2005; Straight

et al., 2004).
The PAR proteins were first identified in *C. elegans*, where they were shown to be required for cytoplasmic localization in the newly formed zygote to confer asymmetric cell division for the establishment of the germ-cell lineage (Kemphues et al., 1988). PAR6 and PAR3 are scaffold proteins that form a tight complex with aPKC via their PDZ binding domains. The small GTPase Cdc42, a well-known regulator of polarity, is an effector of PAR6 and directly binds to its PDZ domain (Garrard et al., 2003; Johansson et al., 2000). Initially, PAR6 and aPKC form a precomplex with Lethal Giant Larvae (Lgl) (Yamanaka et al., 2003), active Cdc42-GTP binds to PAR6, inducing a conformational change and aPKC mediated phosphorylation of Lgl, upon which it dissociates from the pre-complex (Garrard et al., 2003). PAR3, which associates with components of the tight junctions (Ebnet et al., 2001), recruits PAR6 and aPKC, and the three factors form the PAR3/PAR6/aPKC complex. This process leads to exclusion of the LGL complex from the apical domain. EGFR signaling regulates PAR3 tyrosine phosphorylation, which induces negative interaction between Par3 and a LIM-kinase (LIMK2) (Wang et al., 2006). LIMK2 activates cofilin, an actin depolymerization factor, by phosphorylating it and promoting TJ assembly (Wang et al., 2006).
Thus, the cell polarity complexes regulate apical tight junction formation, and apical junctions likewise regulate cell polarity. It is thought that external information, such as cell-cell contact and contact to the extracellular matrixes, present cues that induce formation of the junction complexes acting as priming factors for cell polarity. However, many open questions to the exact causality of the regulation remain.

### 1.3.1 The membrane composition and cell polarity

The lipid composition of the cellular membranes likewise plays a role in the regulation of cell polarity. The phosphoinositides are specific phospholipids, with a phosphatidylinositol head group, which can be phosphorylated at locations 3,4 or 5 of the hexagonic ring. Different types of phosphoinositides are enriched at the cytoplasmic face of cellular membranes, and play a role in membrane identity and trafficking (Corvera et al., 1999).
In mammalian epithelial cells, phosphatidylinositol 4,5-bisphosphate ($PIP_2$) is enriched at the apical membrane and Phosphatidylinositol 3,4,5-bisphosphate ($PIP_3$) is enriched at the basolateral membrane. Imposing ectopic $PIP_2$ conversion or introduction into the basal membrane causes translocation of apical and tight junction proteins to the basal membranes, and the reverse causes protrusion formation at the apical side (Gassama-Diagne et al., 2006; Martin-Belmonte et al., 2007). $PIP_2$ affects many aspects of the actin cytoskeleton, mainly through its regulation of actin binding proteins. In general terms, it has been found that $PIP_2$ activates actin polymerizing factors, such as the WAVE/WASP complex, and inhibits actin depolymerizing factors such as cofilin (Saarikangas et al., 2010). $PIP_2$ has also been shown to recruit and activate talin, and promotes its binding to β-integrins, resulting in increased integrin clustering and activation (Cluzel et al., 2005) (Martel et al., 2001). The lipid phosphatase PTEN catalyzes the dephosphorylation of $PIP_3$ to $PIP_2$ (Maehama and Dixon, 1998), and it is localized predominantly to the apical plasma membrane in MDCK cells, where it controls $PIP_2$ segregation. $PIP_2$ then recruits Cdc42 via Anx2 to the apical plasma membrane, where it regulates the apical lumen

morphogenesis by reorganizing the actin cytoskeleton (Martin-Belmonte et al., 2007). Cdc42 further promotes apical polarity by binding and recruiting PAR6/aPKC (Garrard et al., 2003; Martin-Belmonte et al., 2007). In this way, the phosphoinositide (PI) composition of the cell membranes presents another link in the regulation of cell polarity, and consequently factors, which either synthesize or convert PIs likewise influence cell polarity. The lipid kinase, phosphoinositide 3-kinases (PI3Ks) is and antagonist of the tumor suppressor PTEN, and catalyzes $PIP_2$ to $PIP_3$ phosphorylation. PI3Ks mediated $PIP_3$ phosphorylation is known to activate the cell-cycle regulatory AKT/mTOR pathway, and other Akt induced pathways (Liu et al., 2009; Scheid and Woodgett, 2001). PI3Ks also establishes a basolateral $PIP_3$ gradient, required for the chemoattractant dependent directional sensing for cell polarization and migration of leukocytes (Sasaki et al., 2000). Class 1A PI3Ks can be activated by RAS or directly by receptor tyrosine kinases, such as EGFR (Liu et al., 2009). RAS is a likely upstream effector in PI3K mediated chemoattractant dependent directional sensing (Funamoto et al., 2002). Another connection between EGFR signaling and cell migration by PI regulation is mediated by the Phospholipase C (PLC). It was shown that EGF induces PLC mediated hydrolysis of $PIP_2$ and subsequent cofilin release (van Rheenen et al., 2007) could function as a mechanism in breast carcinoma cell migration along an EGF gradient (Mosadegh et al., 2008). EGFR ErbB1 signaling as a driving force during different types of cancer formation is well established and remains a field of extensive research. EGF induced ErbB1 EGFR signaling in cell polarity, migration and cancer cell invasion has been shown more than twenty years ago, but is still not well understood. Though, PLC activation as mediator is frequently involved (Barrandon and Green, 1987; Chen et al., 1994; Turner et al., 1996). It is clear that ErbB1 EGFR signaling can have an impact on the architecture of the PI membrane composition, through PLC, PI3K and possibly other factors, and the PI membrane composition in turn regulate cell polarity. This topic presents an interesting field for further investigations into the relationship of EGF signaling and cell polarity, migration and invasion.

# 2. Aim of this Thesis

In this thesis, there are two main projects, the first project follows up on the work of former PhD students, Matthias Morf and Peter Guttierez, who performed a sensitized whole genome RNAi screen to look for novel regulators of LIN-3 polarity in the AC and of LET-23 localization in the VPCs. My work was to characterize the function of the screen candidates in AC-specific LIN-3 polarization during vulval cell fate induction.
The second project investigates a putative novel function of LIN-3 as a directional cue for AC migration during vulval morphogenesis. This project was initiated during my master thesis in Prof. Dr. Alex Hajnal's group under the supervision of Matthias Morf. The common theme in both projects is AC polarity and its importance during vulval induction and vulval morphogenesis.

Hypothesis I
That the AC forms a LIN-3 EGF gradient during vulval induction has so far always been assumed, but never analyzed in detail. In a synthetic whole genome RNAi screen in a *gap-1(lf);rrf-3(lf)* background that had originally been constructed to identify regulators of LET-23 EGFR localization (Hajnal et al., 1997), known AC polarity regulators were identified, such as *unc-40*, the Netrin receptor and *madd-2*, a negative regulator of AC polarity. Upon these findings the hypothesis was formed that not only localization of the receptor in the signal receiving cells, but also localization of the secreted ligand in the signal sending cell is a factor that can modulate and shape the LIN-3 EGF gradient. As a result, Vulval induction is altered in a mildly hyper activated *let-60* RAS background.
The two identifies candidate genes are proposed to have a role in the LIN-3 EGF localization within the AC and thus in regulating its directed secretion. An area with increased ligand concentration within the AC is bound to influence the range of its secreted gradient.
The aim of this research project is to verify that LIN-3 is polarized in the AC during vulval induction and that the identified screen candidates regulate LIN-3 polarity, which shapes the ensuing LIN-3 gradient.

Hypothesis II
The only so far identified secreted or externally produced AC polarity cue is the Netrin homolog UNC-6 (Ziel et al., 2008). However it is clear that there are other cues, produced and likely secreted by the vulva, which are required for AC polarity, basal lamina breaching and directing AC protrusions towards the 1° vulval cell descendants (Ziel et al., 2008) (Hagedorn et al., 2009). The *C. elegans* EGF orthologue LIN-3 specifies the vulval cell fate and is essential for vulva development, it is therefore a challenge to determine whether it performs any succeeding functions during vulval morphogenesis. The aim of this research project is to determine the function of vulF specific LIN-3 EGF expression during vulval morphogenesis. Our hypothesis is that LIN-3 EGF expressed by the vulF cells during the late L3 larval stage, polarizes the AC and enables it to form directed protrusions around or in between the vulF cells, enabling their expansion and subsequent formation of the dorsal vulval lumen.

# 3. Projects

## 3.1 A sensitized whole genome RNAi screen identifies novel regulators of directed LIN-3 EGF secretion from the Anchor Cell

Manuscript draft

Louisa Mereu[1,2,*], Matthias Morf [*], Silvan Spiri[1,2], Juan M. Escobar-Restrepo, Peter Gutierrez, Michael Daube[1] & Alex Hajnal[1,°]

* These authors contributed equally to this work.

° Corresponding author: alex.hajnal@imls.uzh.ch

1 Institute of Molecular Life Sciences, University of Zurich, Winterthurerstrasse 190, Zurich, CH-8057, Switzerland.

2 Molecular Life Science PhD Program , University and ETH Zurich, CH-8057 Zurich

Key words: *C. elegans*, LIN-3, morphogen, gradient,

### 3.1.1 Abstract

Morphogens are signaling molecules, which in form of a gradient induce differential responses in the signal-receiving cells in a dose-dependent manner. In the nematode *C. elegans* there is a specialized uterine cell, the anchor cell (AC) that secrets the epidermal growth factor EGF homolog LIN-3, which is thought to form a gradient that acts as a morphogen and can induce either a 1° or a 2° vulval cell fate in the vulval competence group (VPCs). The existence of this gradient is generally assumed but has not been investigated extensively.
It has been shown that the presence of the LIN-3 receptor, LET-23, acts as a sink and limits the spreading of the signaling molecule. When LET-23 is largely dislocated to the apical membrane, the LIN-3 signal is able to spread to the more distal VPCs. In combination with a *gap-1(lf)* mutant, in which LET-60 RAS signaling is amplified, ectopic adoption of vulval cell fate occurs. We find that not only the localization of the receptor is important to shape the signaling gradient, but also the directed secretion of the signaling molecule itself. The AC is highly polarized and we observe that perturbation of its polarity also leads to spreading of the EGF signal to the more distally located VPCs. Based on this discovery, we conducted a genome-wide RNAi screen in a sensitized *gap-1(lf)* mutant background, the aim being to identify genes involved in the directional secretion of the EGF signal form the AC. We identified two novel candidates, *sra-9* and *nlp-26*, and our results show that both genes regulators of EGF polarity independent of general AC polarity.

### 3.1.2 Introduction

For a signal to act as a morphogen it has to form a gradient which requires the instructive signal to be sent from a single or a group of cells, and a group of receiving cells that are able to sense this signal. Attributes that are involved in the formation of a gradient have been assessed, and include signal production rate, the diffusion coefficient, the degradation rate, as well as time and space. These are variables that have been implemented in equations of models that act in the prediction of a gradients outcome (Wartlick et al., 2009). In a gradient generated by diffusion alone, the spreading is viewed to be non-directional. In the absence of modulating factors, such as degradation of the signal, the concentration steadily increases relative to time and space, as in the example of a Gaussian gradient that has no steady state (Berg, 1993). Modulations, such as ligand degradation or sequestering, are required to produce a steady state gradient, in addition to simple diffusion. Ligand degradation is non-linear if it depends on its own concentration, for example through an induced feed-back mechanism (Perrimon and McMahon, 1999). A corresponding example has been described in Hedgehog (Hh) and Patched (Ptc) signaling during Drosophila embryo patterning (Chen and Struhl, 1996). Ligand degradation is linear if the ligand is not degraded at a specific site, but everywhere at a constant level, as seen in the Wingless (Wg) gradient in Drosophila imaginal discs development (Entchev et al., 2000; Kicheva et al., 2007). In a biological context, signaling gradients are often implemented during morphogenesis and organogenesis. In vivo, factors that deplete or degrade the morphogens are proteases (DeLotto and DeLotto, 1998), receptors (Chen and Struhl, 1996) or extracellular matrixes. This aspect of gradient shaping has been studies widely and it is clear that they are important in maintaining and shaping a gradient (Bollenbach et al., 2007; Chen and Struhl, 1996; Hajnal et al., 1997). Examples, in which directed ligand diffusion, independently of receptor mediated reaction diffusion (Bozorgui et al., 2015), is involved in the shaping of a morphogen gradient, have so far not been encountered in vivo .

During *C. elegans* vulva formation, the vulval cell fate inducing cue, LIN-3 EGF is secreted from the gonadal anchor cell (AC) and forms a morphogen gradient that can induce either a 1° or a 2° vulval cell fate (Katz et al., 1995; Zand et al., 2011) in a group of adjacent Pn.p cells (P3.p through P8.p). These are all competent to adopt a vulval cell fate and are termed the vulva precursor cells (VPCs). This system presents a perfect model to study morphogen gradient formation. The LIN-3 EGF inductive signal binds to LET-23, the sole member of the EGFR/ErbB family of receptor tyrosine kinases, leading to an activation of the LET-60 RAS/MPK-1 ERK signaling pathway (Sternberg, 2005). In the maintenance of the LIN-3 morphogen gradient we find a further example of non-linear degradation, since internalization and degradation of ligand bound LET-23 receptor is dependent on the LIN-3 ligand concentration (Haag et al., 2014). LET-23 receptor localization presents another known factor that shapes in the LIN-3 gradient. In wild-type, the VPCs display a specific LET-23 receptor localization pattern, predominantly expressed on the basolateral surfaces (Kaech et al., 1998; Whitfield et al., 1999). Mislocalization of the receptor to the apical side of the VPCs leads to a strong reduction in vulval cell fate adoption. When hyperactivation in the LET-60 RAS pathway, caused by a *gap-1(lf)* mutation, is combined to LET-23 mislocalization, ectopic vulval induction is observed as a result (Hajnal et al., 1997). This finding has been attributed to an expansion of the LIN-3 EGF gradient range, caused by the manifold decrease of LET-23 EGFR mediated LIN-3 EGF sequestering. The added

mild LET-60 RAS hyper activation is enough to promote a vulval cell fate in the distally located VPCs in spite of the small amount of ligand endorsement. Inspired by this observation, a whole genome RNAi screen in a synthetic *gap-1(lf); rrf-3(lf)* background, to identify novel regulators of LET-23 EGFR localization was conducted. Interestingly, positive candidates included AC polarity regulators, such as MADD-2 (Morf et al., 2013) and UNC-40 (Ziel et al., 2008). This observation indicates that not only receptor, but also ligand localization within the ligand-secreting cell can be a requirement for gradient formation. The screen identified 50 primary candidates that showed reproducible ectopic vulval induction phenotypes. Of these we selected two candidates, *sra-9* and *nlp-26* that had defects in LIN-3 polarity, while their general AC polarity in terms of phospholipid PtdIns(4,5)$P_2$ ($PIP_2$) pattern remained unchanged. Our results demonstrate that *sra-9* and *nlp-26* are novel regulators of polarized LIN-3 secretion form the AC. Polarized LIN-3 EGF secretion presents a novel example of a type of directed diffusion.

## 3.1.3 Results

### Depolarization of the AC causes ectopic and shifted vulval induction

In wild-type *C. elegans* animals, three of six VPCs get induced to adopt a vulval cell fate. A mutation in the *let-60*/Ras *gap-1*/ GAP signaling pathway components enhances the strength of the inductive signal but not enough to cause a corresponding increase in the number of cells induced (Hajnal et al., 1997). It thus serves as a sensitizing background to detect changes in LIN-3 EGF distribution, among other things. When combining mutations in *gap-1* and the *C. elegans* Netrin homologue *unc-6,* responsible for guiding the AC during invasion, vulval induction is clearly increased above wild-type levels (Fig. 3.1.1, H). Similar phenotypes result from combining *gap-1* with other AC polarity associated mutations, such as in the Netrin receptor *unc-40* (Morrissey et al., 2013) or the negative AC polarity regulator *madd-2* (Morf et al., 2013) (Fig. 3.1.1, H ). To try and rule out potential effects of the RNAi on any other cells than the AC, we suppressed the *unc-40*, *gap-1* multivulva phenotype by expressing an *unc-40* transgene specifically in the AC (Fig. 3.1.1 H). This resulted in a slight rescue, but not complete suppression of the multivulva phenotype. When combining an AC polarity mutant like *unc-6(lf)* with a mutation that decreases vulval induction, for example the strong loss of function of *lin-3(e1417)*, it further enhances the *lin-3(rf)* vulvaless phenotype (Fig. 3.1.1, J).
We would argue that similar to the case of LET-23 EGFR mislocalization, AC polarity changes how secreted LIN-3 EGF is distributed along the VPCs and that it is this change that increases or decreases vulval induction depending on the genetic background. In the wild-type, the AC is almost invariably centered above P6.p (Braendle and Félix, 2008) which in consequence adopts a 1° vulval cell fate. In addition to the alterations in vulval induction we observed shifts from P6.p centered 1° cell fate to P5.p centered 1° vulval cell fate adoption (Fig. 3.1.1, G and I) in *unc-6* and *unc-40; gap-1* mutants. We attributed these shifts likewise to a disturbance in LIN-3 EGF gradient formation. (adapted from Matthias Morf Thesis, 2015)

### A whole-genome RNAi screen for negative regulators of vulval induction identifies anchor cell polarity genes

We performed a genome-wide synthetic multivulva screen, based on the observation that LET-23 EGFR mislocalization in a *gap-1* mutant background increases vulval induction (Hajnal et al., 1997), using the Ahringer RNAi library (Kamath et al., 2003) and a sensitized *rrf-3(pk1426); gap-1(ga133)* background. After the initial screen and multiple rounds of re-screening, we had 50 primary candidates that showed a persistent mutlivulva phenotype in the *gap-1* loss-of-function background (Table 3.1.1). A *gap-1(lf)* mediated multivulva phenotype can be caused by different mechanisms that lead to alterations in the LIN-3 gradient. Because we were interested in the particular role of the AC and LIN-3 secretion, we decided to check AC and LIN-3 polarity in a next step. We thought that there might be candidates directly controlling the manner, in which LIN-3 is secreted that would ideally leave general AC polarity unaltered. We thus checked AC polarity using a LIN- 3::GFP translational reporter and *mCherry::PLC*$\delta^{PH}$ (Ziel et al., 2008), a phosphatidylinositol-(4,5)-bisphosphate ($PIP_2$) (Janmey and Lindberg, 2004) associated reporter. Three of the 50 primary candidates (Table 3.1.1, orange) showed altered LIN-3, but not $PIP_2$ distribution in the AC upon RNAi knock-down. Those were *srh-247, nlp-26* and *sra-9.*

**Figure 3.1.1**

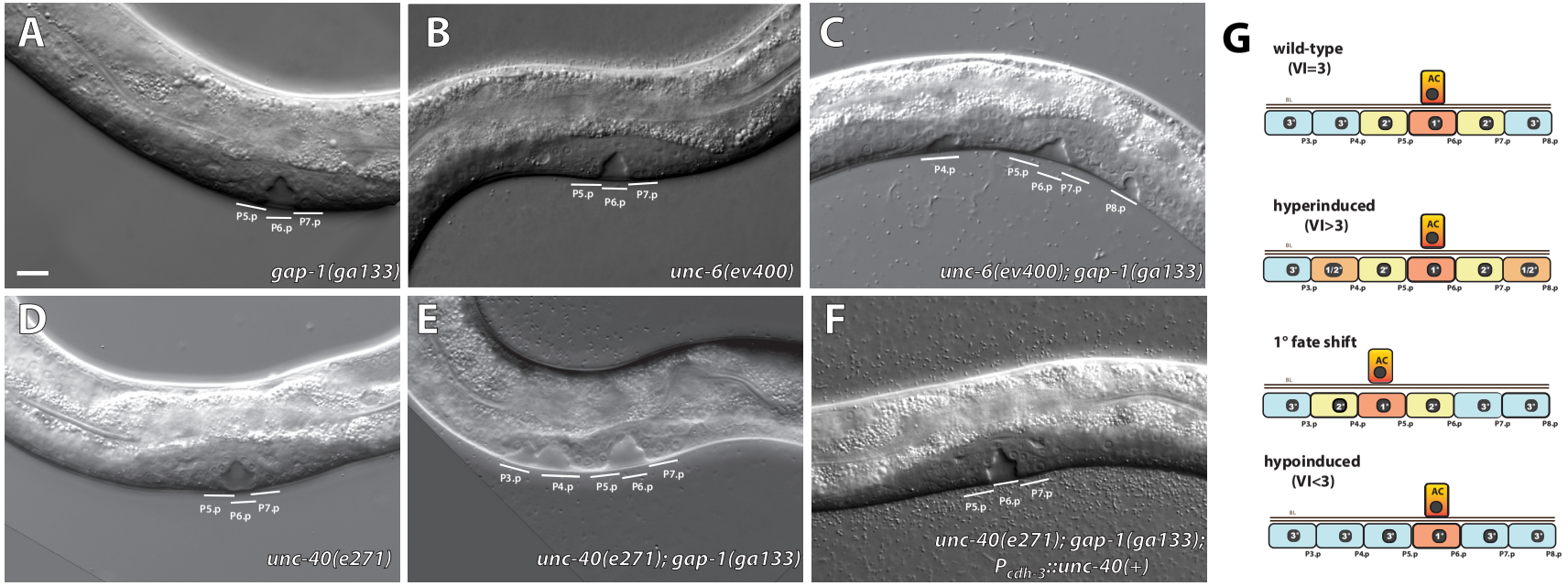
A
P5.p P6.p P7.p
gap-1(ga133)
B
P5.p P6.p P7.p
unc-6(ev400)
C
P4.p P5.p P6.p P7.p P8.p
unc-6(ev400); gap-1(ga133)
D
P5.p P6.p P7.p
unc-40(e271)
E
P3.p P4.p P5.p P6.p P7.p
unc-40(e271); gap-1(ga133)
F
P5.p P6.p P7.p
unc-40(e271); gap-1(ga133);
P cdh-3 ::unc-40(+)
G
wild-type
(VI=3)
hyperinduced
(VI>3)
1° fate shift
hypoinduced
(VI<3)
AC
P3.p P4.p P5.p P6.p P7.p P8.p

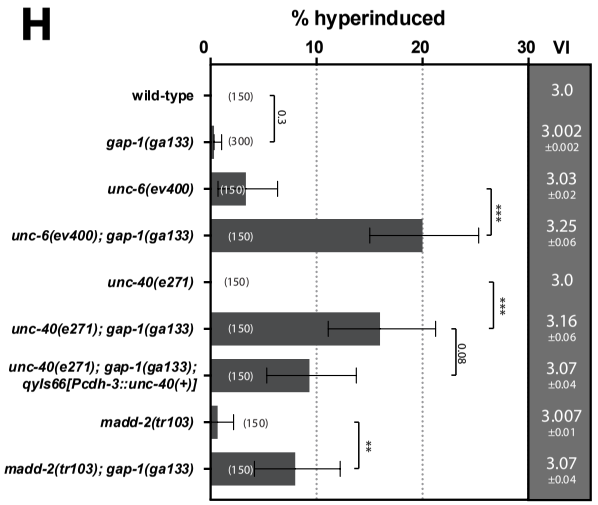
H
% hyperinduced
0 10 20 30 VI
wild-type (150) 3.0
gap-1(ga133) (300) 3.002 ±0.002
unc-6(ev400) (150) 3.03 ±0.02
unc-6(ev400); gap-1(ga133) (150) 3.25 ±0.06
unc-40(e271) (150) 3.0
unc-40(e271); gap-1(ga133) (150) 3.16 ±0.06
unc-40(e271); gap-1(ga133); qyIs66[Pcdh-3::unc-40(+)] (150) 3.07 ±0.04
madd-2(tr103) (150) 3.007 ±0.01
madd-2(tr103); gap-1(ga133) (150) 3.07 ±0.04
0.3
***
***
0.08
**

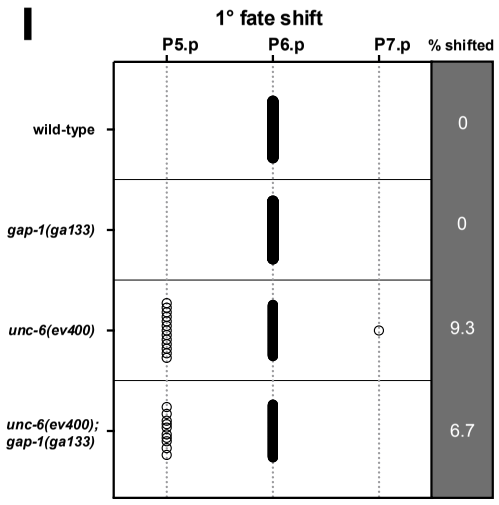
I
1° fate shift
P5.p P6.p P7.p % shifted
wild-type 0
gap-1(ga133) 0
unc-6(ev400) 9.3
unc-6(ev400); gap-1(ga133) 6.7

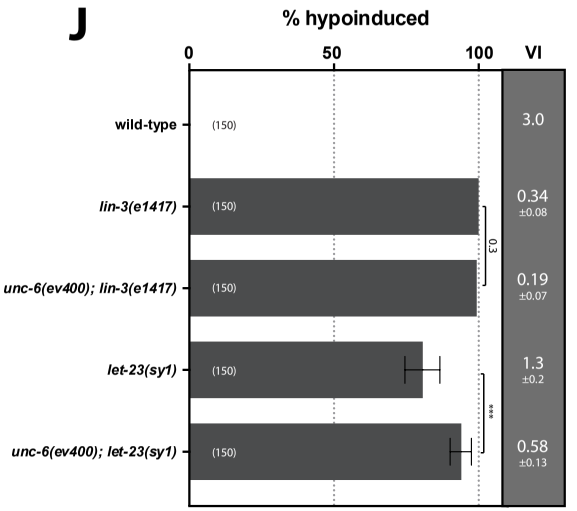
J
% hypoinduced
0 50 100 VI
wild-type (150) 3.0
lin-3(e1417) (150) 0.34 ±0.08
unc-6(ev400); lin-3(e1417) (150) 0.19 ±0.07
let-23(sy1) (150) 1.3 ±0.2
unc-6(ev400); let-23(sy1) (150) 0.58 ±0.13
0.3
***

From these candidates we selected *nlp-26* and *sra-9* for further, more detailed validation and analysis. (adapted from Matthias Morf Thesis, 2015).

**Figure 3.1.1 AC polarity modulates vulval induction strength (Data generated by Matthias Morf)**
(A-F) Nomarski sections show lateral view of mid L4 stage larvare, demonstrating (A, B, D and F) wild-type vulval induction and (C and E) hyperinduction phenotypes, in (A) gap-1(ga133), (B) *unc-6(ev400),* (C) *unc-6(ev400); gap-1(ga133),* (D) *unc-40(e271),* (E) *unc-40(e271); gap-1(ga133)* and (F) *unc-40(e271); gap-1(ga133);qyIs66[Pcdh-3>unc-40::gfp]* strains. P5.p, P6.p and P7.p vulval cell descendants are indicated by white line. Scale bar equals 10 µm.
(G) Cartoon illustrating observed vulval induction (VI) and AC to Pn.p alignment (1° fate shift) phenotypes that were scored. Vulval induction scoring: wild-type VI=3, hyperinduced VI > 3, hypoinduced VI < 3. AC to Pn.p alignment (1° fate shift) scoring: In wild-type P6.p is 1° fated. In a 1° fate shift, P5.p or P7.p are 1°fated.
(H) Plot shows percent of animals of indicated genotype with hyperinduced vulval induction (VI). Error bars show 95% percentile confidence interval, calculated by Bootstrapping with resampling size B=10000. P-values were generated by t-test for independent samples. ($p < 0.01$ = ** and $p < 0.001$ = ***). The sample size n for each genotype is displayed in plot. The mean VI, as well as the standard error of the mean are shown in the gray column for each genotype.
(I) Plot shows number of animas, in which a 1° fate shift was observed for each indicated genotype. The percent of animals, in which a 1° fate shift was observed is shown in gray column.
(J) Plot shows percent of animals of indicated genotype with hypoinduced vulval induction (VI). Error bars show 95% percentile confidence interval, calculated by Bootstrapping with resampling size B=10000. p-values were generated by t-test for independent samples. ($p < 0.001$ = ***). The sample size N for each genotype is displayed in plot.
The mean VI as well as the standard error of the mean are shown in the gray column for each genotype.

| cellular function | gene | WB identifier | brief description | LIN-3 polarity | AC polarity |
|---|---|---|---|---|---|
| **cell adhesion** | | | | | |
| | *dig-1* | WBGene00000998 | immunoglobulin superfamily | **P** | **n.d.** |
| **cell cycle** | | | | | |
| | *cdk-4* | WBGene00000406 | cyclin-dependent serine/threonine protein kinase | **P** | **n.d.** |
| | *cki-1* | WBGene00000516 | cyclin-dependent kinase inhibitor p27 | **P** | **n.d.** |
| | *cye-1* | WBGene00000871 | E-type cyclin | **n.d.** | **n.d.** |
| | *cdk-11.1* | WBGene00015203 | cyclin-dependent serine/threonine protein kinase | **P** | **n.d.** |
| | *cdk-2* | WBGene00019362 | cyclin-dependent serine/threonine protein kinase | **P** | **n.d.** |
| **cell signaling** | | | | | |
| | *lag-2* | WBGene00002246 | DSL family NOTCH ligand | **P** | **n.d.** |
| | *nlp-26* | WBGene00003764 | predicted neuropeptide | **D** | **P** |
| | *sra-9* | WBGene00005035 | G-protein coupled receptor | **D** | **P** |
| | *srd-36* | WBGene00005114 | G-protein coupled receptor | **P** | **n.d.** |
| | *srh-8* | WBGene00005234 | G-protein coupled receptor | **P** | **n.d.** |
| | *srh-247* | WBGene00005453 | G-protein coupled receptor | **D** | **P** |
| | *unc-40* | WBGene00006776 | netrin receptor | **D** | **D** |
| | *unc-73* | WBGene00006805 | guanine nucleotide exchange factor similar to Trio | **n.d.** | **n.d.** |
| | *madd-2* | WBGene00016539 | C1 subfamily of tripartite motif (TRIM) protein | **D** | **D** |
| | *toe-2* | WBGene00016971 | DEP domain containing protein | **P** | **n.d.** |
| **cellular iron ion homeostasis** | | | | | |
| | Y45F10D.4 | WBGene00012885 | iron-sulfur cluster assembly enzyme | **P** | **n.d.** |
| **chromosome organization** | | | | | |
| | *dpy-27* | WBGene00001086 | SMC4 subunit of mitotic condensin | **P** | **n.d.** |
| | *his-72* | WBGene00001946 | H3 histone | **P** | **n.d.** |
| | *hmg-3* | WBGene00001973 | Subunit of the heterodimeric FACT complex | **P** | **n.d.** |
| **immunity** | | | | | |
| | F26F12.5 | WBGene00017836 | antimicrobial protein | **P** | |
| **ion transport** | | | | | |
| | *acr-3* | WBGene00000043 | nicotinic acetylcholine receptor superfamily | **P** | **n.d.** |
| | *mca-1* | WBGene00003151 | plasma membrane Ca2+ ATPases | **P** | **n.d.** |
| **lipid transport** | | | | | |
| | *cav-2* | WBGene00000302 | caveolin | **P** | **n.d.** |
| | *acbp-3* | WBGene00009818 | acyl-CoA-binding binding domain | **D** | **D** |
| **protein modification** | | | | | |
| | *usp-48* | WBGene00009267 | ubiquitin specific peptidase | **D** | **D** |
| | *ugt-14* | WBGene00019233 | UDP glycosyltransferase | **P** | **n.d.** |
| | *gei-17* | WBGene00001574 | SUMO E3 ligase | **D** | **D** |
| | *ulp-1* | WBGene00006736 | SUMO protease | **D** | **D** |
| **regulation of transcription** | | | | | |
| | *lin-1* | WBGene00002990 | Ets-domain transcription factor | **P** | **n.d.** |
| | *lin-9* | WBGene00002998 | novel protein | **P** | **n.d.** |
| | *lin-14* | WBGene00003003 | novel protein | **P** | **n.d.** |
| | *mes-6* | WBGene00003224 | Polycomb-like chromatin repressive complex | **P** | **n.d.** |
| | *nhr-103* | WBGene00003693 | nuclear hromone receptors | **P** | **n.d.** |
| | *nhr-115* | WBGene00003705 | nuclear hromone receptors | **P** | **n.d.** |
| | *sdc-2* | WBGene00004746 | component of dosage compensation complex | **P** | **n.d.** |
| | *sem-4* | WBGene00004773 | zinc-finger transcription factor | **P** | **n.d.** |
| | *din-1* | WBGene00008549 | spen family transcriptional repressor | **P** | **n.d.** |
| | *hpo-11* | WBGene00010427 | nuclear receptor binding protein 2 | **P** | **n.d.** |
| **regulation of translation** | | | | | |
| | *fbf-2* | WBGene00001402 | Pumilio and FBF family translational regulator | **D** | **D** |
| | *puf-8* | WBGene00004244 | Pumilio and FBF family translational regulator | **n.d.** | **n.d.** |
| **small molecule metabolic process** | | | | | |
| | *cah-4* | WBGene00000282 | carbonic anhydrase | **D** | **D** |
| | *lact-9* | WBGene00012890 | beta-lactamase domain-containing protein | **P** | **n.d.** |
| | T22F3.3 | WBGene00020696 | glycogen phosphorylase isozymes | **P** | **n.d.** |
| **unknown functions** | | | | | |
| | C31H5.5 | WBGene00007856 | novel protein | **n.d.** | **n.d.** |
| | *clec-197* | WBGene00008202 | C-type lectin | **P** | **n.d.** |
| | T18D3.1 | WBGene00011820 | novel protein | **P** | **n.d.** |
| | Y69H2.3 | WBGene00013481 | novel protein | **P** | **n.d.** |
| | ZK795.2 | WBGene00014082 | novel protein | **P** | **n.d.** |
| | T20D4.11 | WBGene00020617 | novel protein | **P** | **n.d.** |
| | T02B11.9 | WBGene00044777 | novel protein | **D** | **D** |

**Table 3.1.1 The 50 primary candidates from synthetic whole-genome RNAi screen (M. Morf data)**

The table lists the positive candidates that showed multivulva phenotypes in the initial screen as well as in the four rounds of rescreening. The candidates are grouped into categories of cellular functions (first column). The 50 primary candidates were subject to a more detailed screening process, in which AC polarity, as well as LIN-3 polarity, was analyzed. The results are listed in the last (AC polarity) and second last (LIN-3 polarity) column of the table. P stands for polarized and D stands for defective polarity. In some cases the polarity could not be determined (n. d.). The candidates, in which RNAi lead to depolarization of LIN-3

but had no effect on AC polarity are highlighted in orange. The genes known to be regulators of AC polarity and AC positioning, which were positive hits in the screen are highlighted in green.

**EGF LIN-3 secretion is polarized in the AC throughout vulval induction**

From our results regarding the AC polarity and *gap-1* mutant analysis (Fig. 3.1.1, H and J), we concluded that AC polarity influences LIN-3 secretion and is a factor in the constitution of robust vulval induction in wild-type.

A method to influence and fine-tune LIN-3 distribution along the VPCs would be to directly adjust the manner of its secretion from the AC. To assess the LIN-3 localization pattern within the AC as accurately to the wild-type situation as possible, we constructed an endogenous reporter by inserting an *mNeongreen* encoding fluorophore element N-terminally to the EGF domain, employing the CRISPR/Cas9 System (Horvath and Barrangou; 2010, Friedland et al., 2013; Tzur et al., 2013; Dickinson et al., 2015). The reporter was expressed in the AC as expected and visible intracellularly in distinct foci as well as in the cytoplasma and at the cell-membrane (Fig 3.1.2, A, D and G). Although the overall expression pattern was variable between individuals and dependent on the developmental stage of the worm, the bulk of the signal was clearly enriched towards the ventral side of the AC from the mid L2 to the mid L3 larval stage in wild-type (Fig. 3.1.2, B, E and H). To quantify the LIN-3 distribution we took z-stacks of the AC expressing the *mNeongreen::lin-3* as well as the $PIP_2$ associated *mCherry::PLC*$\delta^{PH}$ reporter, made summed z-projections and measured the average intensity in equal areas in the ventral as well as the dorsal half of the AC. We divided the ventral by the dorsal value and thus obtained our polarity index (PI). We assigned a PI > 1.1 as our threshold for ventrally polarized LIN-3 expression. We measured the LIN-3 PI from the mid L2 to the mid L3 larval stages. The developmental stage was assigned according to the animal's gonad length (Kimble and Hirsh, 1979) and divided indo three groups, mid to late second larval stage (m-lL2), early third (eL3) and mid third (L3) larval stage.

If LIN-3 expression would be distributed uniformly or randomly within the AC, we would expect the PIs to be scattered around a value of 1, instead we observe that the PIs were grouped around a PI of 1.3 for all larval stages in wild-type, and very few outliers had a PI lower than 1 (Fig. 3.1.2, B,E and H). We also found that in each group 85% or more of the Animals had a PI higher than 1.1. (Fig. 3.1.2. J, K and L). Therefore LIN-3 reporter expression is polarized within the AC throughout vulval induction.

**LIN-3 polarity is reduced in *unc-6* mutants**

Our hypothesis is based on the discovery that AC depolarization causes ectopic vulval induction in a synthetic *gap-1* mutant background (Fig. 3.1.1, H). Since we now established that in wild-type LIN-3 is polarized during vulval induction, we next wanted to know how general AC depolarization, such as in *unc-6* mutants, affects LIN-3 polarity. UNC-6 Netrin is a secreted cue from the ventral nerve cord (VNC), known to direct its receptor UNC-40, F-actin regulators as well as $PIP_2$ towards the ventral side of the AC. This polarization is required for proper basal lamina breaching (Ziel et al., 2008). *unc-6(ev400)* is one of the strongest known general AC polarity mutants and therefore we chose it as positive control.

At the mid to late L2 larval stage, in approximately 50% of wild-type and *unc-6* mutant individuals, the subcellular $PIP_2$ (*mCherry::PLC*$\delta^{PH}$) distribution in the AC could not be determined accurately. In more than 95% of animals of the third larval stage, $PIP_2$ polarity in wild-type and *unc-6* mutants was clearly determinable (data not shown). We measured the *mCherry::PLC*$\delta^{PH}$ reporter expression pattern and determined the $PIP_2$ polarity index (PI) in the same manner as previously described for *lin-3* polarity. In wild-type we saw that the $PIP_2$ polarity index increased as the larval development progressed and was significantly decreased in *unc-6(ev400)* mutants from the early L3 stage on (Fig. 3.1.2. C, F and I). This corroborates the previous finding, in which UNC-6 is expressed in the VNC only from L2/L3 ecdysis on (Ziel et al., 2008). Regarding LIN-3 polarity, we observed a significantly smaller population of animals with a LIN-3 PI > 1.1, signifying polarized LIN-3 expression, in the *unc-6(ev400)* loss of function mutant strain compared to wild-type animals at the mid to late L2 and the early L3 larval stages (Fig. 3.1.2, J, K). At the early L3 stage, the distribution of the individual LIN-3 PIs in the *unc-6(ev400)* loss of function mutant strain was clearly different from wild-type. Later at the mid L3 larval stage there was no clear difference between the two groups, which could possibly be due to the smaller population size (Fig. 3.1.2, L).

When we looked at a possible correlation of LIN-3 and $PIP_2$ polarity on a single cell level we saw that they clearly coincided. There was a significant difference in the fraction of animals with both $PIP_2$ and LIN-3 depolarization in *unc-6(ev400)* animals compared to wild-type, from the mid L2 to the early L3 stage (Fig. 3.1.S1, B). Taken together we conclude that LIN-3 polarity depends on global AC polarity and thus global AC depolarization likewise causes LIN-3 depolarization.

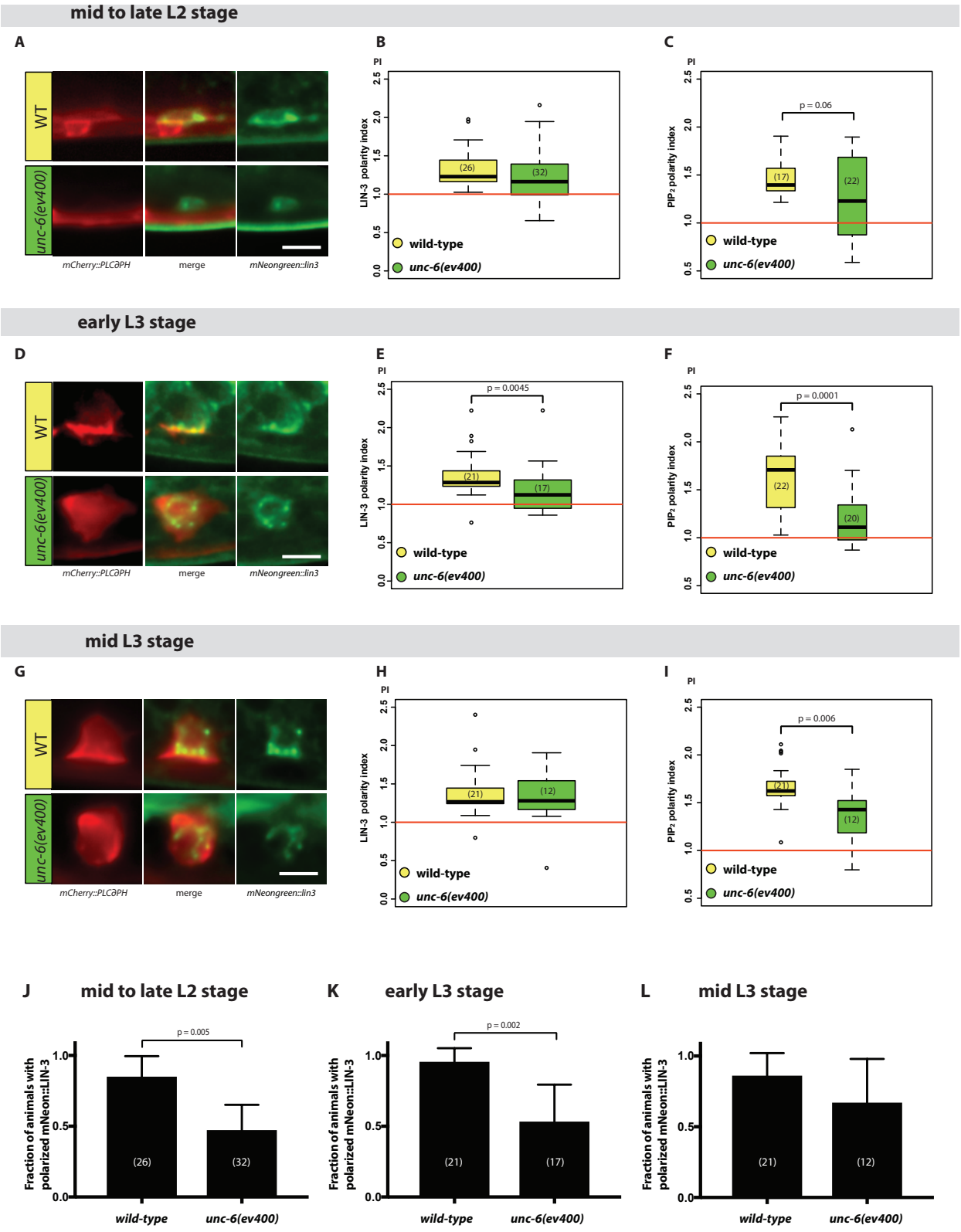


**Figure 3.1.2 LIN-3 secretions from the AC is polarized during vulval induction**

(A, D and G) AC expression pattern of summed z-projections of the $P_{cdh-3}$>*mCherry::PLCδ$^{PH}$* (left) and the endogenous *mNeongreen::lin-3* reporters (right) at the mid L2 larval stage in wild-type (top) and *unc-6(ev400)* mutants. Scale bar =5 µm. (A) mid to late L2 larval stages, (D) early L3 larval stages and (G) mid L3 larval stages.

(B, E and H) Boxplots showing the distribution of the measured dorsal to ventral LIN-3 polarity index (PI). The LIN-3 polarity index was calculated from summed z-projections of deconvolved stacks with 0.2 µm Z-spacing of ACs expressing the *mNeongreen::lin-3* reporter. The relative polarity index was calculated by dividing equal areas of the average intensity of the ventral by the average intensity of the dorsal half of the AC. PI > 1 indicates higher average intensity on ventral relative to the dorsal half of the AC. The sample size n for wild-type and *unc-6(ev400)*mutants at each larval stage is displayed in plot. (B) mid to late L2 larval stages, (E) early L3 larval stages and (H) mid L3 larval stages.
(C, F and I) Boxplot showing the distribution of the measured dorsal to ventral $PIP_2$ polarity index (PI). The $PIP_2$ polarity index was calculated from summed z-projections of stacks with 0.2 µm Z-spacing, in which the background was subtracted, of ACs expressing the $P_{cdh3}$*>mCherry::PLC*$\delta^{PH}$ reporter. The relative polarity index was calculated by dividing equal areas of the average intensity of the ventral by the average intensity of the dorsal half of the AC. PI>1 indicates higher average intensity on ventral relative to the dorsal half of the AC.
p-values were generated by t-test for independent samples of unequal variance, and are shown in figure. The sample size n for wild-type and *unc-6(ev400)* mutants at each larval stage is displayed in plot. (C) mid to late L2 larval stages, (F) early L3 larval stages and (I) mid L3 larval stages.
(J, K and L) Plot shows fraction of animals with polarized LIN-3 (PI > 1.1) expression pattern in wild-type and *unc-6(ev400)* mutants, error bars represent the 95% confidence interval. (J) mid to late L2 larval stages, (K) early L3 larval stages and (L) mid L3 larval stages. Statistical significance was calculated with Fisher's exact probability test, and p-values are displayed in figure.

**SRA-9 and NLP-26 modulate vulval induction**

We selected the candidates *sra-9* and *nlp-26* identified in the previous screen for further analysis. The genes encode a serpentine seven pass transmembrane receptor (Troemel et al., 1995) and a neuropeptide like protein respectively. *nlp-26* is classified as a neuropeptide like protein, and it is predicted to be secreted (Nathoo et al., 2001). There is very little previous knowledge about either of the genes, and they both have no human homologs. To be able to confirm or reject the previous RNAi data, mutant lines of the genes of interest were constructed. The generated *sra-9(zh108)* loss of function allele consists of a 2.5 kb deletion, spanning the entire gene, and it was generated by means of the CRISPR/Cas9 system (Arribere et al., 2014). The *nlp-26(zh113(gfp::3xFLAG))* allele has an inserted *gfp* element in the region encoding the predicted signaling peptide of the gene, generating a premature stop codon and subsequent null allele. The GFP::3xFlag sequence was inserted at the 5' region of the *nlp-26* locus by means of the CRISPR/Cas9 system according to the Dickinson protocol (Dickinson et al., 2015).

When we combined mutations in *gap-1* and *sra-9* or *nlp-26*, we observed both a hyper- and hypoinduction of the vulval cell fates (Fig. 3.1.3, D). In addition, we saw occurrences of 1° vulval cell fate shifts in *nlp-26* single as well as in *sra-9; gap-1* double mutants (Fig. 3.1.3, E). Although the penetrance is lower than what we see in combination with the *unc-6* mutants (Fig. 3.1.1, H), the difference is significant. This shows that both NLP-26 and SRA-9 are modulators of vulval induction.

**LIN-3 polarity is significantly reduced in *sra-9* and *nlp-26* mutants while general AC polarity remains unchanged from wild-type**

We next looked at LIN-3 and $PIP_2$ polarity in our generated mutant lines, to verify the RNAi screen results, in which LIN-3 was depolarized, but $PIP_2$ polarity was unaltered upon *sra-9* and *nlp-26* RNAi (Table 3.1.1). There was a significant change in the mean LIN-3 polarity index in *sra-9(zh108)* and *nlp-26(zh113)* mutants at the mid to late L2 larval stage compared to wild-type (Fig. 3.1.3, B). There was also a significantly smaller fraction of animals, in which the AC showed polarized LIN-3 (PI >1.1) expression in *sra-9(zh108)* mutants at the m-lL2 as well as at the eL3 larval stages, and in *nlp-26(zh113)* mutants at the lL2 stage (Fig. 3.1.3, F).

When we looked at general AC polarity on the other hand, we found no significant difference in the mean $PIP_2$ polarity indexes, either for *sra-9(zh108)* nor for *nlp-26(zh113)* mutants compared to wild-type at all analyzed larval stages (Fig. 3.1.3, C). Thus, general AC polarity is unaltered while LIN-3 polarity is reduced in *sra-9(zh108)* and *nlp-26(zh113)* mutants up to the early L3 stage. This comprises the time, in which the vulval cell fates are determined. Well into the mid L3 stage, most of the animals have already completed the first round of vulval cell division, and have determined vulval cell fates.

When we look at LIN-3 and $PIP_2$ polarity on a single cell level, we saw a significant increase in the fraction of animals with depolarized LIN-3, but polarized $PIP_2$ expression (Fig. 3.1.S1, B) for *sra-9(zh108)* (p=0.07) and *nlp-26(zh113)* (p=0.09) mutants at the mid to late L2 stage and for *sra-9(zh108)* (p=0.05) and *nlp-26(zh113)* (p=0.009) mutants at the early L3 stage. Thus, SRA-9 and NLP-26 are specifically involved in LIN-3 polarization, independently of general $PIP_2$ polarity.

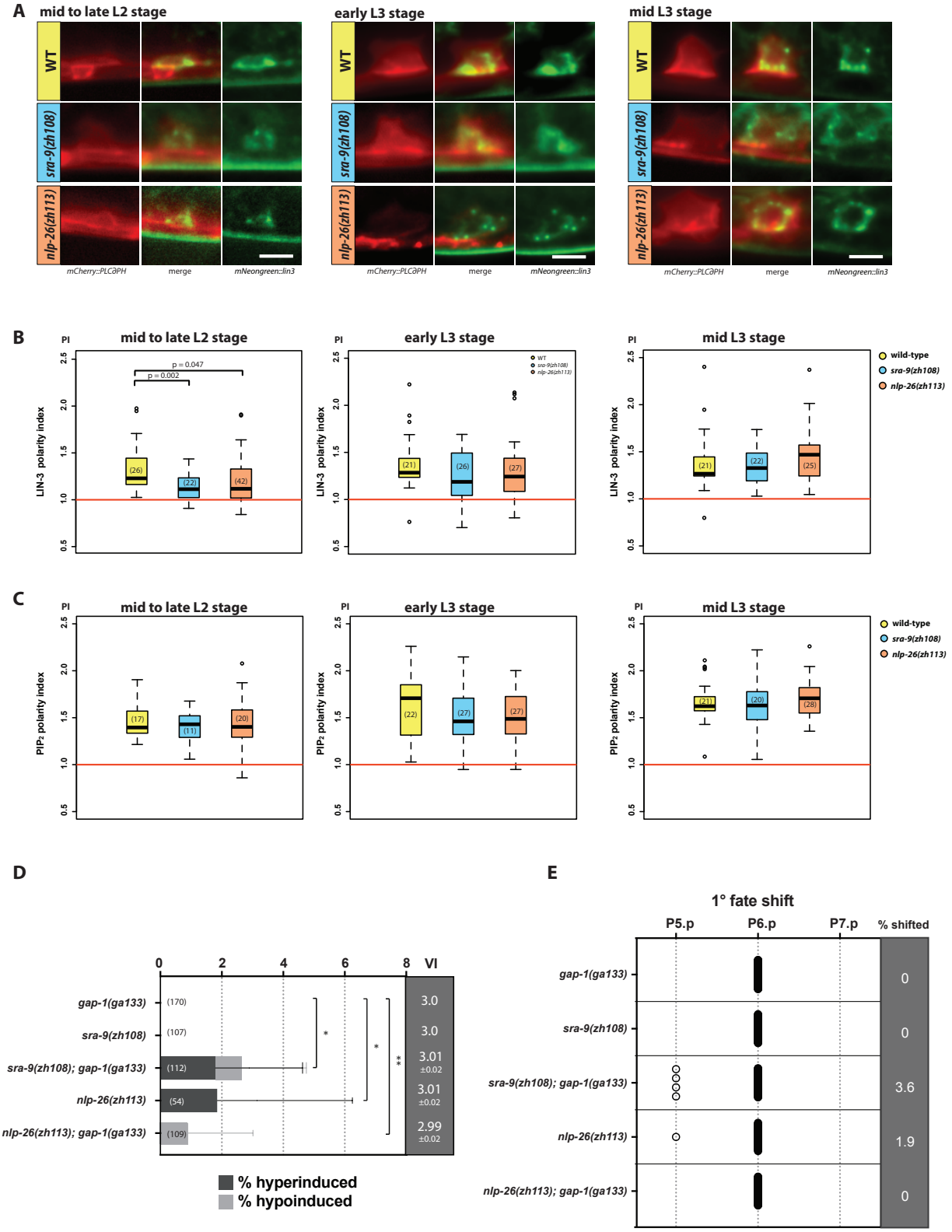


**Figure 3.1.3** **SRA-9 and NLP-26 are required for polarized LIN-3 secretion, independent of general $PIP_2$ polarity**

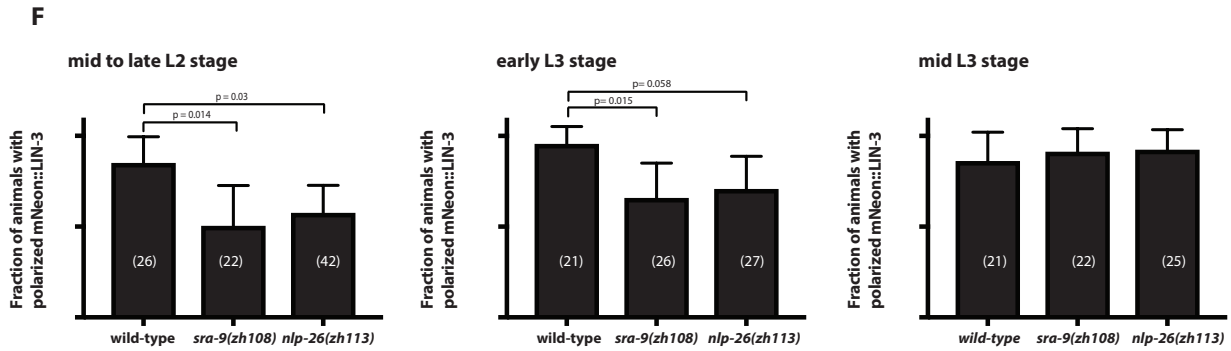


**Figure 3.1.3 SRA-9 and NLP-26 are required for polarized LIN-3 secretion, independent of general $PIP_2$ polarity**

(A) Images show summed z-projections of AC expression pattern of the $P_{cdh3}$*>mCherry::PLCδ$^{PH}$* (left) and the endogenous *mNeongreen::lin-3* reporter (right) at indicated larval stages in wild-type, *sra-9(zh108)* and *nlp-26(zh113)* mutants.
Scale bar = 5 µm.

(B) Boxplots showing the distribution of the measured dorsal to ventral LIN-3 polarity index (PI) at indicated larval stages. The LIN-3 polarity index was calculated from summed z-projections of deconvolved stacks with 0.2 µm Z-spacing of ACs expressing the *mNeongreen::lin-3* reporter. The relative polarity index was calculated by dividing equal areas of the average intensity of the ventral by the average intensity of the dorsal half of the AC. PI > 1 indicates higher average intensity on ventral relative to the dorsal half of the AC.
Students t-tests for independent samples of unequal variance was used to determine the statistical differences in the distribution of the polarity indexes of mutants compared to wild-type within the same larval stages. The corresponding p-values are indicated in figure.
The sample size for each genotype at given larval stage is displayed in plot.

(C) Boxplot showing the distribution of the measured dorsal to ventral $PIP_2$ polarity index (PI). The $PIP_2$ polarity index was calculated from summed z-projections of stacks with 0.2 µm Z-spacing, in which the background was subtracted, of ACs expressing the $P_{cdh3}$*>mCherry::PLCδ$^{PH}$* reporter. The relative polarity index was calculated by dividing equal areas of the average intensity of the ventral by the average intensity of the dorsal half of the AC.
PI > 1 indicates higher average intensity on ventral relative to the dorsal half of the AC. Boxplots showing the distribution of the measured dorsal to ventral LIN-3 polarity index (PI) at indicated larval stages. Student's t-tests for independent samples of unequal variance was used to determine the statistical differences in the distribution of the polarity indexes of mutants compared to wild-type within the same larval stages. The corresponding p-values are indicated in figure. The sample size for each genotype at given larval stage is displayed in plot.

(D) Plot shows percent of animals of indicated genotype with hyperinduced or hypoinduced vulval induction (VI). Error bars show 95% percentile confidence interval, calculated by Bootstrapping with resampling size B=10000.
P-values were generated by t-test for independent samples. ($p < 0.05$ = * and $p < 0.01$ = **). The sample size n for each genotype is displayed in plot. The mean VI, as well as the standard error of the mean are shown in the gray column for each genotype.

(E) Plot shows number of individuals indicated with circes, in which a 1° fate shift was observed for each indicated genotype. The percent of animals, in which a 1° fate shift was observed is shown in gray column. The sample size n is equal to the sample sized in E for all genotypes.

(F) Plot shows fraction of animals with polarized LIN-3 expression (PI > 1.1) at indicated larval stages. Error bars represent the 95% confidence interval. Statistical significance was analyzed with Fisher's exact probability test, and p-values are displayed in figure.

**AC to P6.p alignment is unequal to wild-type in *nlp-26* and *unc-6* mutants**

Vulval induction in wild-type is a highly robust process, in which among the six VPCs, P6.p consistently adopts a 1° vulval cell fate (Braendle and Félix, 2008). Considering the initially high variability in AC to P6.p alignment, it is interesting that at the termination of vulval induction (mid L3) the AC and P6.p are invariably aligned in wild-type (Grimbert et al., 2016). Recently, it was shown that an interplay of AC mediated LIN-3 gradient, LIN-3 dependent VPC migration towards the AC and Notch signaling between the VPCs competing for the 1° vulval cell fate are the required factors that result in an almost invariant alignment of the AC and the 1° fated P6.p (Grimbert et al., 2016; Huelsz-Prince and van Zon, 2017). Since our model focuses on the LIN-3 gradient formation, we wanted to see if our mutant candidates show alterations in AC to P6.p alignment. We measured the distance between the AC and P6.p along the basal lamina, from the center of the AC nucleus to the center of the P6.p nucleus in µm (Fig. 3.1.4, A) and plotted the measured distances for all analyzed mutants and larval stages (Fig. 3.1.4, B, C and D).

As in the mentioned previous studies we also observed initially high, but over time receding variability in wild-type (Fig. 3.1.4, B, C and D). In the wild-type we never observed that the AC was situated closer to either P5.p or P7.p throughout the analyzed larval stages. Also, the AC was never situated further than 15 µm from P6.p, nor was the AC ever situated equidistantly between P6.p and either P5.p or P7.p.

In *unc-6(ev400)* mutants the AC to P6.p alignment significantly varied from wild-type for all the analyzed larval stages (Fig. 3.1.4, B, C and D). In addition, we found a number of incidents, in which the AC was situated further than 15 µm from P6.p, and a highly significant fraction ($p < 0.001$ according to Chi-Squared test) had a distance greater than 10 µm during the m-lL2 as well the eL3 stages, compared to wild-type. We also found that in 9 out of 69 cases the AC was situated equidistantly between P6.p and either P5.p or P7.p (data not shown).

For *nlp-26(zh113)* mutants there was no significant difference compared to the overall wild-type alignment distribution. In a few incidents the AC was situated further than 15 µm from P6.p, and in one case the AC was closer to P7.p than to P6.p. When comparing the fraction of animals with an AC to P6.p distance greater than 10 µm, we found a significant increase in *nlp-26(zh113)* mutants compared to wild-type during the eL3 stage ($p= 0.037$, according to Chi-squared test).

In *sra-9(zh108)* mutants we observed one incident, in which the AC was situated further than 15 µm from P6.p (Fig. 3.1.4, B), but there was no significant alteration in alignment compared to wild-type.

Thus, there are detectable deviations from wild-type AC to P6.p alignment in *unc-6(ev400)* and *nlp-26(zh113)* mutants. The penetrance of these defects is comparable to the VI alterations (Fig. 3.1.1, H, Fig. 3.1.3, D) and especially the 1° vulval cell fate shifts we observed in the *gap-1* VI analysis (Fig. 3.1.1, I and Fig. 3.1.3, E).

**Endogenous NLP-26::GFP expression is detected in VPCs**

As mentioned previously, our *nlp-26(zh113)* mutant line was constructed by inserting a *gfp* element in the predicted signaling domain of the gene, introducing a frame shift and premature stop codon and in addition an endogenous reporter. We analyzed the reporter line at the early to mid L3 stage and found GFP expression in the VPCs (Fig. 3.1.4, E). The expression pattern intensity was quite weak, so we calculated the corrected total cell fluorescence (CTCF) (McCloy et al., 2014) for our NLP-26::GFP marker and did the same in wild-type animals carrying no reporter and compared the values (data not shown). The reporter had comparable values in between the measured VPCs of each genotype, but distinctly higher CTCF values in the NLP-26::GFP strain, compared to wild-type. Thus, NLP is expressed form the VPCs, and since neuropeptides are usually secreted, is likely secreted as well.

**LIN-3 polarity is directed towards P6.p along an AP axis in wild-type animals**

In the course of our analysis we noticed that the *mNeongreen::lin-3* reporter expression pattern in the AC appeared to have a biased polarity towards P6.p along the A/P axis (Fig. 3.1.4, F). So we measured the LIN-3 polarity along the anterior to posterior (A/P) axis, applying the same method as previously for the ventral to dorsal LIN-3 polarity analysis (Fig. 3.1.2), except that we divided the AC half situated proximal to P6.p by the half situated distal from it. Thus a PI > 1 indicates more relative intensity towards P6.p and less indicates the contrary. We measured the P6.p specific PI for wild-type, s*ra-9(zh108)* and *nlp-26(zh113)* mutants from the mid L2 to the mid L3 stage, for all individuals with an AC to P6.p distance greater than 2.5 µm (Fig. 3.1.4, G). This cutoff was made, due to the nature of the measurements, since the alignment were measured from AC nuclei to P6.p nuclei, we were lacking the context of the total cell volume and shape. When the distance between the two nucle was smaller than 2.5 µm, we could not make an accurate conclusion, whether the AC directs its LIN-3 expression towards the cell body of P6.p or not.

We found a significant bias in the mean LIN-3 polarity indexes towards P6.p in wild-type ($p < 0.001$, paired t-test), opposed to an unbiased PI mean of 1. In *sra-9(zh108)* and *nlp-26(zh113)* mutants, the mean PI was significantly reduced compared to wild-type (Fig. 3.1.4, G), and did not significantly differ from 1 (paired t-test $p > 0.16$). Interestingly, the mean PI in *unc-6(ev400)* mutants did not significantly differ from wild-type either (Fig. 3.1.4, G), but like in wild-type, was clearly different from a hypothetical unbiased mean PI of 1 ($p < 0.001$, paired t-test).

We next wanted to see how distance correlates to the P6.p directed LIN-3 polarity. We found a negative correlation of P6.p directed LIN-3 polarity with AC to P6.p. distances (Fig. 3.1.4, H). In wild-type, the number of individuals with a PI lower than 1 increased abruptly at an AC to P6.p distance greater than 5 µm. Neither in *sra-9(zh108)* nor in *nlp-26(zh113)* mutants such an abrupt increase was observed, and there was likewise no clear correlation to distance.

In *unc-6(ev400)* mutants, as in wild-type, the AC to P6.p distance correlated negatively with the PI value (Fig. 3.1.4, H). This suggests that a certain proximity is required for the AC to sense P6.p, which is disturbed in *sra-9(zh108)* and *nlp-26(zh113)* mutants. Possibly the AC can sense the location of P6.p or the closest VPC by some signaling mechanism, and as a result targets its LIN-3 secretion in that specific direction. This P6.p sensing is significantly perturbed in *sra-9(zh108)* and *nlp-26(zh113)* mutants, but not in *unc-6(ev400)* mutants.

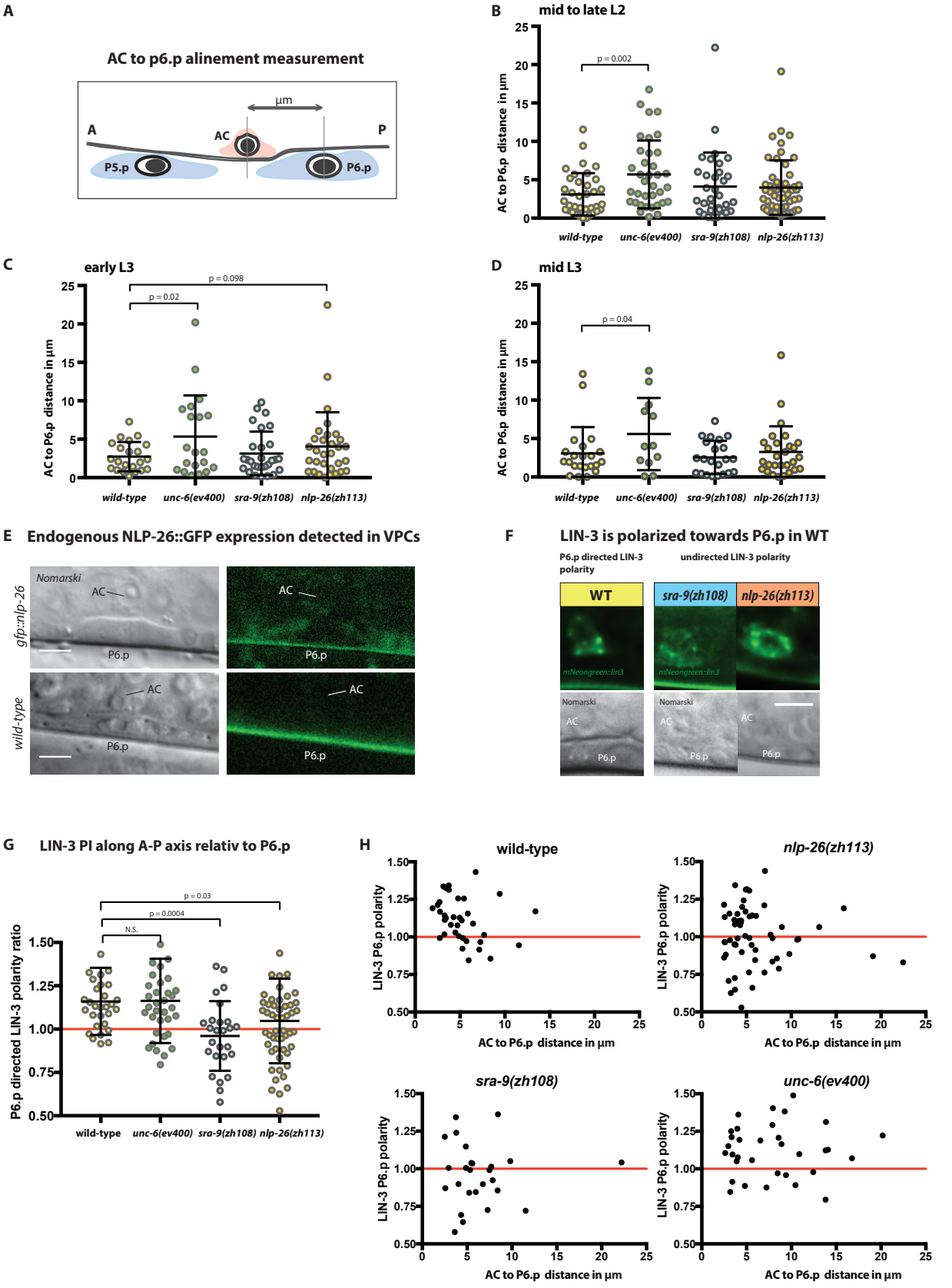


**Figure 3.1.4** AC to P6.p alignment is perturbed in *nlp-26(zh113)* and *unc-6(ev400)* mutants

**Figure 3.1.4 AC to P6.p alignment is perturbed in *nlp-26(zh113*) and *unc-6(ev400)* mutants**

(A) Cartoon illustrating the measurements taken for AC to P6.p distance quantification. The AC to P6.p distance was measured along the basal lamina from perpendicular intersections through the AC nucleus and the P6.p nucleus respectively.

(B-D) The plots shows distribution of the measured AC to P6.p distances in µm, as described in "A" for wild-type, *unc-6(ev400)*, *sra-9(zh108)* and *nlp-26(zh113*), at the mid to late L2 larval stage (B), the early L3 larval stage (C) and the mid L3 larval stage (D). t-tests for independent samples was used to determine the statistical significant differences between the wild-type and mutants at each developmental larval stage, the p-values are displayed in figure.

(E) Endogenous *gfp::nlp-26* reporter expression is detected in VPCs. Example Nomarski (left) and *gfp* excited (485nm) fluorescent (right) section of *nlp-26(zh113(gfp))* (top) and N2 animals. The same image microscope settings were used for both strains and background was substracted in example sections. The AC and P6.p are labeled. P6.p is outlines (white line). Scale bar = 5 µm.

(F) AC expression pattern of summed z-projections of the endogenous *mNeongreen::lin-3* reporter (top) and corresponding Nomarski images (bottom) of wild-type (top) *sra-9(zh108)* and *nlp-26(zh113)* mutants. The position of the AC and P6.p are labeled in Nomarski. Scale bar =5 µm.

(G) LIN-3 polarity index (PI) relative to P6.p was measured along the anterior posterior axis. The PI was calculated by making summed z-projections of the AC expressing the *mNeongreen::lin-3* reporter and dividing equal areas of average intensity of the proximal by the distal half of the AC relative to P6.p. The plots show the distribution of the PI for all individuals (mL2-mL3) with an AC to P6.p distance greater than 2.5 µm. t-tests for independent samples was used to determine the statistical significant differences between the polarity indexes in mutants and wild-type. The corresponding p-values are indicated in figure.

(H) The PI values from "G" were plotted against the corresponding individual AC to P6.p distances for wild-type, *unc-6(ev400)*, *sra-9(zh108)* and *nlp-26(zh113)* mutants.

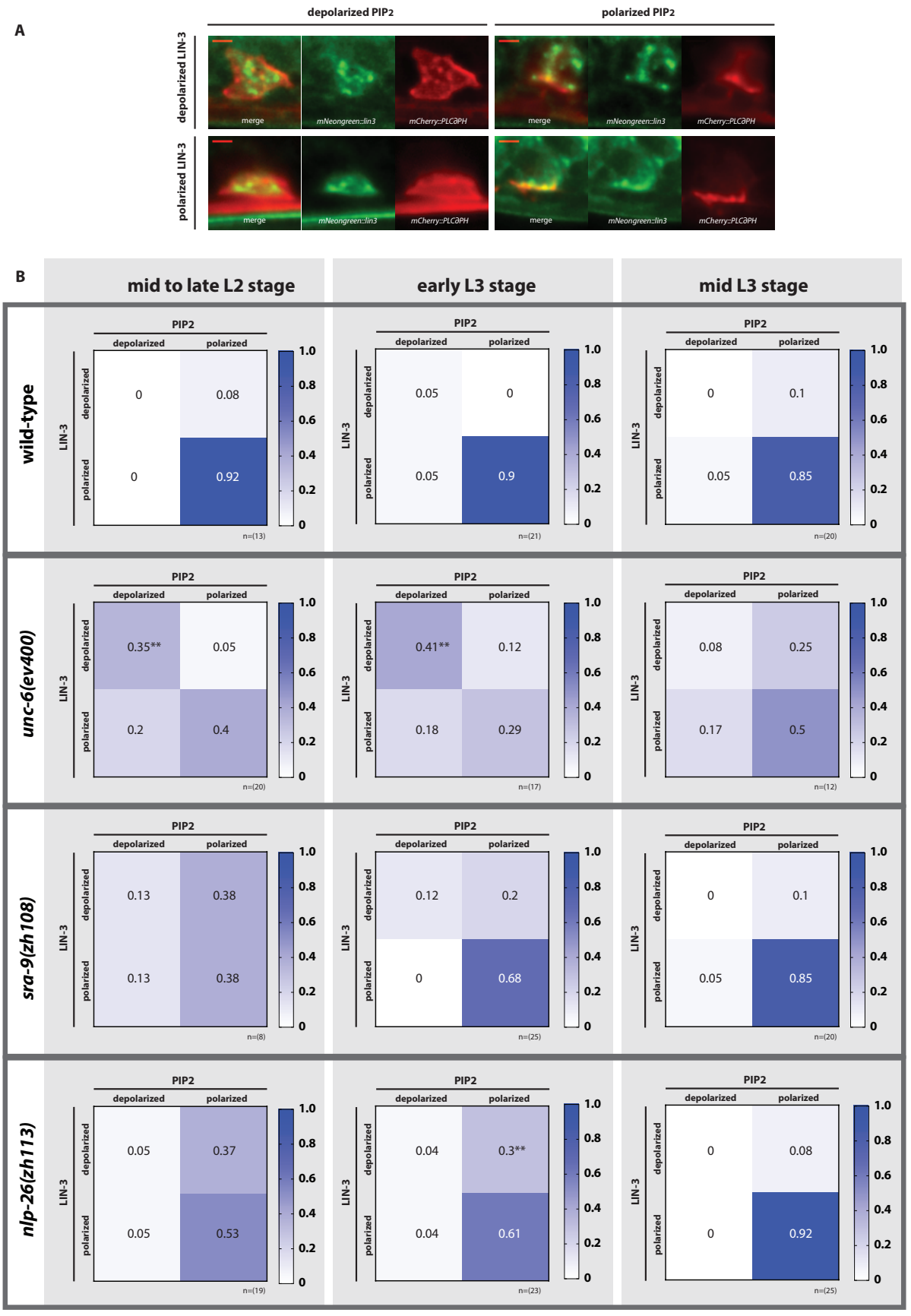
A
depolarized PIP2
polarized PIP2
depolarized LIN-3
polarized LIN-3
merge
mNeongreen::lin3
mCherry::PLCϑPH
B
mid to late L2 stage
early L3 stage
mid L3 stage
wild-type
unc-6(ev400)
sra-9(zh108)
nlp-26(zh113)
PIP2
LIN-3
depolarized
polarized
0
0.08
0
0.92
n=(13)
0.05
0
0.05
0.9
n=(21)
0
0.1
0.05
0.85
n=(20)
0.35**
0.05
0.2
0.4
n=(20)
0.41**
0.12
0.18
0.29
n=(17)
0.08
0.25
0.17
0.5
n=(12)
0.13
0.38
0.13
0.38
n=(8)
0.12
0.2
0
0.68
n=(25)
0
0.1
0.05
0.85
n=(20)
0.05
0.37
0.05
0.53
n=(19)
0.04
0.3**
0.04
0.61
n=(23)
0
0.08
0
0.92
n=(25)
1.0
0.8
0.6
0.4
0.2
0

**Figure 3.1.S1 Relative $PIP_2$ to LIN-3 polarity on an individual scale**

(A) Summed z-projections of ACs expressing the $P_{cdh3}$>*mCherry::PLC*$\delta^{PH}$ , the endogenous *mNeongreen::lin-3* reporter and merged images of wild-type animals depicting all observed combinations polarization and depolarized combinations for the two reporters. Scale bar =2.5 µm.

(B) Heat-maps show how the polarity combinations observed in "A" are distributed in fractions for wild-type, *sra-9(zh108)* and *nlp-26(zh113)* mutants at the mid to late L2, the early L3 and the mid L3 larval stages respectively. Sample size n is indicated for each group in figure. LIN-3 was scored as polarized for a PI > 1.1. The measured PI for the $PIP_2$ $P_{cdh3}$>*mCherry::PLC*$\delta^{PH}$ reporter has a higher mean than the LIN-3 PI and so the threshold for polarized $PIP_2$ PI was set higher. A $PIP_2$ PI > 1.2 was scored as polarized.

Statistical significance was calculated with Fisher's exact probability test, ($p < 0.05$ = * and $p < 0.01$ = **).

## LIN-3 Immunostaining coincides with the live LIN-3 expression pattern

Since we detect endogenous *mNeongreen::LIN-3* reporter expression mainly intracellularly and along the membrane, we did immunostaining to see if we could visualize the LIN-3 gradient. We used antibodies that recognize an inserted FLAG element in the endogenous lin-3 locus. To permeabilize the staged L2/L3 worms we used a freeze-cracking method (Miller and Shakes, 1995) and a light methanol/acetone fix. The FLAG staining proved to be strikingly less efficient than our MH27 control and we were only able to positively stain a small number of worms. These showed the same expression pattern we observe during our live imaging analysis for wild-type (Fig. 3.1.S2, A) and *unc-6* mutants (Fig. 3.1.S2, B), but no extracellular gradient formation could be visualized. We therefore did not investigate further with this method.

**A** *mNeongreen::lin3*

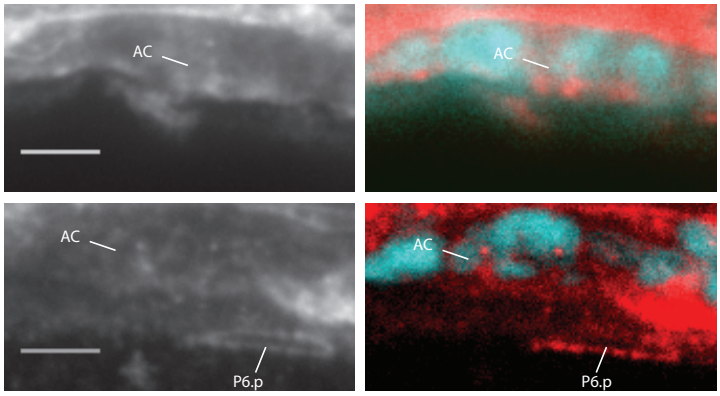


**Left:**
**1° antibody: α FLAG( mouse)**
**1° antibody: α AJM-1 MH27 (mouse)**
**2° antibody: α mouse, TRITC**

**Right:**
**Antibody Hoechst merge**

**B** *unc-6(ev400)***;** *mNeongreen::lin3; mCherry::PLC∂PH*

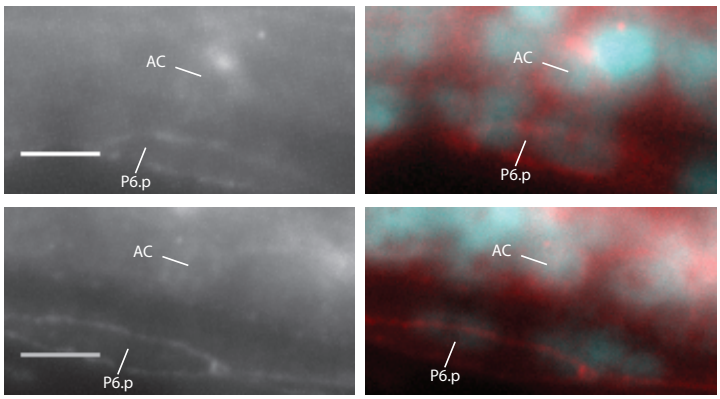


**C** N2

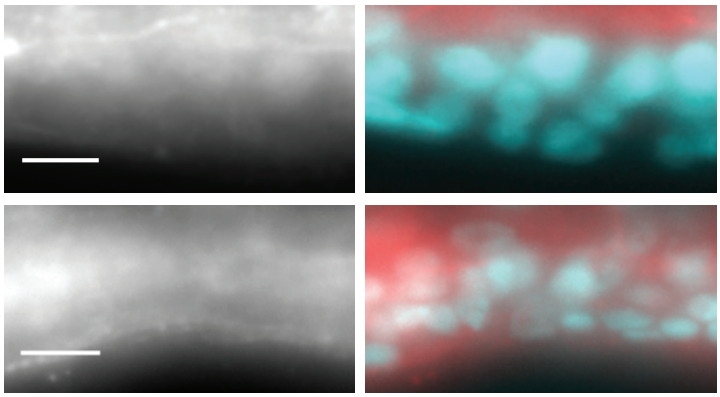

**Figure 3.1.S2 Immunostaining of LIN-3 resembles endogenous reporter expression**
(A) Examples of immunostained AC and VPC apical junctions in *mNeongreen::FLAG::lin-3* animals. The primary antibodies mark the LIN-3 transgene (anti FLAG) expressed in the AC and the apical junctions of the VPCs (MH27). The nuclei are visualized in the merge with Hoechst staining (right). The AC and P6.p are indicated by white line. Scale bar equals 5 µm.
(B) Examples of immunostained AC and VPC apical junctions in *unc-6(ev400); $P_{cdh3}$>mCherry::PLCδ$^{PH}$; mNeongreen::lin-3* animals. The primary antibodies mark the LIN-3 transgene (anti FLAG) expressed in the AC and the apical junctions of the VPCs (MH27). The nuclei are visualized in the merge with Hoechst staining (right). The AC and P6.p are indicated by white line. Scale bar equals 5 µm.
(C) Control staining in N2 animals. The primary antibodies mark the LIN-3 transgene (anti FLAG) expressed in the AC and the apical junctions of the VPCs (MH27). The nuclei are visualized in the merge with Hoechst staining (right). The AC and P6.p are indicated by white line. Scale bar equals 5 µm.

### 3.1.4 Discussion

It has been proposed that LIN-3 EGF secreted from the AC forms a gradient during vulval induction that acts in a dose-dependent manner on the underlying VPCs (Katz et al., 1995; Katz et al., 1996; Sternberg and Horvitz, 1986; Sternberg and Horvitz, 1989; Zand et al., 2011). Although these studies demonstrate evidence that clearly points to the existence of such a LIN-3 EGF gradient, the manner, in which the gradient is formed has not been studied extensively. So far the assumption is that the LIN-3 EGF gradient is formed by non-directional diffusion from a point source in terms of uniform LIN-3 secretion from the AC, in combination to non-linear degradation (Haag et al., 2014; Perrimon and McMahon, 1999) by LET-23 EGFR mediated sequestering (Aroian and Sternberg, 1991; Hajnal et al., 1997), internalization and subsequent degradation (Berset et al., 2005) in the adjacent VPCs. Our results demonstrate a novel example of a type of directional diffusion (Bollenbach et al., 2007) (Bozorgui et al., 2015; Wartlick et al., 2009), in the form of directed secretion of LIN-3 EGF by the AC as a factor in the formation of the morphogen gradient. The mentioned directional diffusion we propose is achieved by polarized LIN-3 EGF expression and secretion within and from the AC.

**Polarized LIN-3 EGF secretion shapes the morphogen gradient**

It is well established that LET-23 EGFR receptor mislocalization to the apical side of the VPCs excessively diminishes the efficacy of vulval cell fate adoption in VPCs. Upon loss of the RAS inhibitor GAP-1, and subsequent mild hyperactivation of RAS signaling, the former vulvaless phenotype results in the adoption of ectopic vulval cell fates and a multivulva Phenotype (Hajnal et al., 1997). This is due to the evoked distal spreading of the LIN-3 inductive cue, which under wild-type conditions is constricted in its diffusion by the presence of the LET-23 EGFR receptor. Our data concerning the endogenous *mNeongreen::lin-3* reporter clearly show that LIN-3 is significantly enriched on the ventral side of the AC, intracellularly as well as at the cell membrane (Fig. 3.1.2 (wild-type)). This highly suggests that increased amounts of the LIN-3 signal are secreted at the ventral side and towards the competing VPCs, opposed to a uniform secretion form the cellular membrane of the AC. We show that depolarization of the AC, determined by $PIP_2$ analysis, such as in *unc-6* mutants (Ziel et al., 2008), likewise leads to depolarization of LIN-3 (Fig. 3.1.2 and Fig. 3.1.S1). *unc-6* mutants also have significantly increased ectopic vulval induction in the *gap-1* mutant background (Fig. 3.1.1, H ), akin to the previous finding in *let-23(sy1); gap-1(ga133)*, where the receptor is mislocalized apically (Hajnal et al., 1997).
We show that AC depolarization in *unc-6* mutants also significantly increases the frequency of vulva hypoinduction in the *let-23(sy1)* mutant background, in which the LET-23 EGFR receptor is highly misslocalized to the apical side of the VPCs. Our results support the model that not only cellular receptor mislocalization such as in *let-23(sy1)* (Fig. 3.1.5, B) mutants (Hajnal et al., 1997), but also cellular ligand localization is involved in the regulation of the LIN-3 gradient formation (Fig. 3.1.5, C).

**SRA-9 and NLP-26 direct LIN-3 polarity independent of $PIP_2$**

From the 50 primary screen candidates (Table 3.1.1) we selected *sra-9* and *nlp-26*, the two candidates, which changed LIN-3 polarity independently of $PIP_2$ polarity when mutated (Fig. 3.1.3, Fig. 3.1.S1). This shows that one or more alternate pathways, independent of Netrin mediated

AC polarity (Morf et al., 2013; Ziel et al., 2008), must regulate LIN-3 polarity and that *sra-9* and *nlp-26* are likely components in this process. Although most neuropeptide-like proteins in *C. elegans* are members of two classes of gene families that have clear neuronal functions, *nlp-26* could not be placed into any of these two classes and was shown to be expressed in the hypodermis of the adult nematode (Nathoo et al., 2001). The proprotein convertase EGL-3 KPC-2 has been implicated as a processor of NLP-26, to mediate its secretion (Husson et al., 2006). EGL-3 is expresses in neurons of the ventral nerve cord, amongst other tissues. Mutants in *egl-3* are defective in their egg-laying ability, which indicates a function during vulva development. Our endogenous *gfp::nlp-26* reporter shows expression in the Pn.p cells (Fig. 3.1.4, G). We also find that *mNeongreen::lin-3* expression in the AC is not only enriched ventrally (Fig. (3.1.2, A,B and C (wild-tpye)), but also on the side of the AC facing P6.p (Fig. 3.1.4, G). This implies the presence of a sensing mechanism, in which the AC is able to perceive the location of the closest VPC, or possibly there is a feedback mechanism linked to 1° cell fate adoption. UNC-6 is secreted from the ventral nerve cord and polarizes $PIP_2$ and subsequently LIN-3 along thr D/V axis. The fact that *unc-6(ev400)* mutants have defects in dorsal to ventral LIN-3, but not in P6.p directed LIN-3 polarity, while *sra-9(zh108)* and *nlp-26(zh113)* mutants show defects in both polarities, indicates that SRA-9 and NLP-26 are necessary to direct LIN-3 along an additional axis, set by the location of P6.p. Together, the results indicate that NLP-26 expressed from the VPCs (Fig. 3.1.4, E) might function as a guidance cue to direct LIN-3 polarity, and canalize LIN-3 secretion towards the future 1° VPC, to limit spreading of the soluble ligand and avoid ectopic vulval cell fate adoption. SRA-9 is a member of the SRA family of chemosensory receptors, supposidly acting via a G-protein pathway, and has been shown to be expressed in the ASK amphid neurons (Troemel et al., 1995). These ASK neurons have functions in chemotaxis and sensory regulation of egg-laying. If SRA-9 would be expressed in the AC, we would postulate that NLP-26 could be its ligand. However this Hypothesis still needs to be investigated experimentally. SRA-13, a paralog of SRA-9, has been shown to negatively regulate RAS/MAPK signaling during vulval induction, as an integrator of environmental conditions, in response to starvation (Battu et al., 2003). It is therefore possible that SRA-9 likewise is a negative regulator of RAS/MAPK singaling and 1° cell fate adoption. This would explain the *gap-1(ga113)* vulva hyperinduction data. If SRA-9 does not functio in the AC, its impact on AC-specific LIN-3 polarity might be indirect, for instance by regulating NLP-26, directly or indirectly, in response to 1° cell fate upregulation. This hypothesis would support a model, in which NLP-26 might be upregulated in response to 1° vulval cell fate upregulation, and by reciprocal signaling would further promote directed LIN-3 secretion, to lock the 1° vulval cell fate in a positive feedback loop.

**Polarized LIN-3 secretion is a link in the robustness of *C. elegans* vulval induction**

In the absence of NLP-26 and SRA-9 function, there are no major defects on vulval induction or AC to P6.p alignment. Only in a sensitized background, such as a *gap-1* mutant, an increase in minor errors occurs (Fig. 3.1.3). Vulval induction is a robust mechanism, and directed LIN-3 secretion is merely another link in the constitution of the whole process. To see more striking effects, an additional sensitizing would likely be required.

A possible explanation for the small penetrance of defects found in the AC alignment and *gap-1* induced vulval induction alteration in the *sra-9* and *nlp-26* mutants can be found in the robustness of the *C. elegans* vulval induction mechanism that is secured through two pathways.

Recent publications have investigated this aspect of robustness in terms of dose dependent expression of the LIN-3 EGF and the Delta/Notch signaling pathways (Barkoulas et al., 2013). The authors in Barkoulas 2013 showed that a certain threshold of ectopic or reduced LIN-3 EGF and LIN-12 Notch expression on the mRNA level is required to alter the wild-type vulval cell fate pattern, and that the relative expression level of the two signals is decisive in the outcome of the cell fate pattern. This finding is comprehensible since the two pathways are known to regulate each other (Berset et al., 2001; Shaye and Greenwald, 2002). Another aspect of robustness in vulval cell fate patterning is the almost invariable centering of the 1° vulval cell fate on P6.p in the wild-tpye N2 strain under standard conditions (Braendle and Félix, 2008). Considering the initially large variability in AC to P6.p alignment, it is astounding that the AC comes to be situated above P6.p in 99.999% of the cases (Braendle and Félix, 2008). Two recent studies investigated the robust AC to P6.p alignment and found three factors that are authoritative in its execution (Grimbert et al., 2016; Huelsz-Prince and van Zon, 2017). Grimbert et al discovered that the VPCs align with the immobile AC and that the VPC motility is dependent on the LIN-3 EGF signal, and that the cell motility is reinforced in a positive correlation with 1° vulval cell fate adoption (Grimbert et al., 2016). The authors of Huelsz-Prince devised two mathematical models for AC to Pn.p cell alignment, one model based on LIN-3 induced VPC motility, in the second model LIN-12 Notch signaling was added as an additional factor, linking 1° vulval cell fate adoption to LIN-3 directed motility. They concluded that in principle LIN-3 EGF induced movement could correct for AC misplacement, but only within a certain range of LIN-3 expression levels. When they included LIN-12 Notch signaling into the mathematical model, the outcome in AC positioning matched their experimental observation for all the assumed LIN-3 EGF expression levels (Huelsz-Prince and van Zon, 2017).

Our results coincide with these previous findings, and in addition present a method, in which the LIN-3 EGF gradient is formed, presenting an additional link to the robust process of vulval cell fate induction. By polarized and directed LIN-3 EGF secretion towards the closest Pn.p cell, the chances that more than one VPC adopt a 1° vulval cell fate are minimized. In addition this directed secretion reinforces 1° vulval cell fate mediated migration towards the AC, which promotes proper AC to P6.p alignment.

In summary, we conclude that not only subcellular receptor polarization in the ligand receiving cells (Fig. 3.1.5, B) (Haag et al., 2014; Hajnal et al., 1997), but also subcellular localization of the ligand in the signal sending cell (Fig. 3.1.5, C), are factors that shape the LIN-3 EGF gradient during *C. elegans* vulval induction.

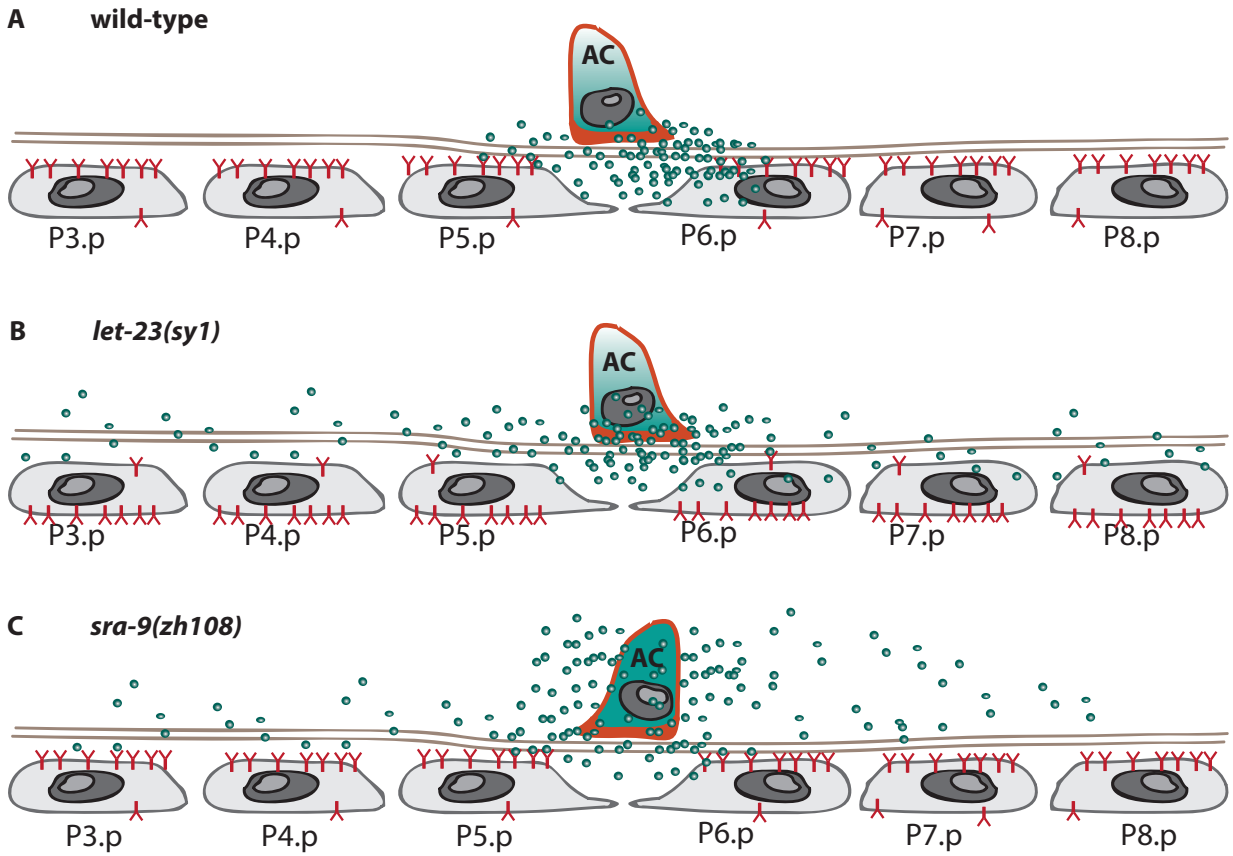


**Figure 3.1.5 Model for Polarized LIN-3 secretion**

The cartoon illustrates how the range of the LIN-3 gradient is expanded when either LIN-3 or its receptor LET-23 localization is depolarized.

(A) In wild-type the LIN-3 gradient is kept narrow, due to its being sequestered by its receptor LET-23, which is located predominantly on the basolateral side of the VPCs and is internalized upon LIN-3 binding.

(B) A *let-23(sy1)* mutation causes LET-23 mislocalization from basolatoral to the apical side of the VPCs. Since the LIN-3 ligand is no longer sequestered at a high rate by LET-23, the ligand is able to spread further to the distally located VPCs. This expands the range of the gradient.

(C) Mislocalization of LIN-3 such as in *sra-9(zh108)* or *nlp-26(zh113)* mutants results in uniform secretion of LIN-3 from the AC and allows the ligand to spread to more distal VPCs, since the sequestering by LET-23 can be bypassed to an extent. This expands the gradient range analogous to *let-23(sy1)*.

## 3.1.5 Materials and Methods

**General methods and strains used**

Unless specified otherwise, *C. elegans* strains were maintained at 20 °C on NGM (Nematode-Growth Medium) plates applying standard methods (Brenner, 1974).
The *C. elegans* Bristol variant N2, was used as wild-type (WT) reference and strains used for the experiments and generated crosses were derivates of N2.
The following alleles and transgenes were used:
LGI: *unc-40(e271)* (Hedgecock et al., 1990)
LG II: *qyIs23[[$P_{cdh-3}$>PLC∂$^{PH}$::mCherry, unc-119(+)]* (Ziel et al., 2008), *rrf-3(pk1426)* (Simmer et al., 2002), *let-23(sy1)* (Katz et al., 1996), ttTi5605 (Frøkjær-Jensen et al., 2008), *sra-9(zh108)*
LGIII: *unc-119(ed3)* , *madd-2(tr103)* (Alexander et al., 2010)
LG IV: *lin-3(e1417)* (Hwang, 2004), *lin-3(zh112[mNeongreen::LoxP::3xFlag])*
LG V: *fos-1(ar105)/nT1[sqIs51, let-XX(m435)], nlp-26(zh113[GFP::LoxP::3xFlag])*
LG X: *unc-6(ev400)* (Hedgecock et al., 1990), *gap-1(ga133)* (Hajnal et al., 1997), *bar-1(ga80)* (Eisenmann et al., 1998), *qyIs66[[$P_{cdh-3}$>unc-40::gfp, $P_{myo-2}$>yfp]*(Ziel et al., 2008)

**Microscopy and image analysis**

Images were acquired using an Olympus BX61 wide-field microscope equipped with a Cr.E.S.T. X-light spinning disc confocal system, a Lumencor SPECTRA X light engine and a Hamamatsu Orca CCD camera, controlled by the Visitron VisiView 2.1.1 software.
Other images were made with an iXon Ultra 888 ccd camera, or a QImaging Retiga 2000R. The *gap-1(ga133)* Nomarski exsample images were made using a Leica DMRA wide-field microscope with a Hamamatsu ORCA-ER camera controlled by Openlab 5.0.2.
Images were processed using Huygens Deconvolution (SVI) for Z-stacks where indicated, Fiji (ImageJ (NIH)) and Adobe Photoshop. (Image deconvolution was performed with the Huygens software provided by; the Center for Microscopy and Image Analysis, University of Zurich)
Injections were done on a Leica DM-IRB Injection microscope.

**AC polarity analysis**

The AC polarity index for LIN-3 as well as $PIP_2$ was calculated from summed z-projections of stacks with 0.2 µm Z-spacing, which had been deconvolved (*lin-3::mNeongreen)* or, in which the background had been subtracted (*$P_{cdh3}$>mCherry::PLCδ$^{PH}$*). The relative polarity index was calculated by dividing equal areas of the average intensity of the ventral by the average intensity of the dorsal half of the AC. PI > 1 indicates higher average intensity on ventral relative to the dorsal half of the AC. The same method was applied for the AC polarity index relative to P6.p, only instead of ventral to dorsal, the P6.p proximal was divided by the P6.p to distal part of the AC.

**Statistical analysis**

Statistical analyses for vulval induction (VI) was performed by bootstrapping. In this analysis, the data is resampled N times (N=10000), generating many bootstrap samples. The standard deviation within these bootstrap samples gives an estimate of the standard error of the mean and the 95% confidence interval.
Other statistical analysis was performed using Student's t tests or Fisher's exact tests

and calculated by Excel software (Microsoft), MATLAB (MathWorks®) or R.

**PCR**

PCR products used for genotyping of strains or RNAi clones, by fragment length analysis or by sequencing analysis, were performed according to the Taq-PCR protocol of ©2008 Invitrogen Corporation or using a PCR Protocol for LongAmp® Taq DNA Polymerase (M0323). For all PCR reactions performed, the annealing temperature was set at 58° or according to empirically tested optimum. All Fusion-PCR reactions were performed with the Phusion high-fidelity DNA polymerase according to the protocol of Finnzymes (Espoo, Finland). The DNA fragments generated by the PCR reactions were visualized using agarose gel electrophoresis and ethidium bromide staining.
The annealing temperatures were estimated with the Finnzyme Tm calculator (https://www.finnzymes.fi/tm_determination.html).

**CRISPR/Cas9 generated alleles**

*zh112* *mNeongreen::lin-3*

To insert the *mNeongreen::3xFlag* sequence in the 5` prime region of the *lin-3* locus, the CRISPR/Cas9 system (Jinek et al., 2012) according to the Dickinson protocol (Dickinson et al., 2015) was applied. The repair template plasmid pLM5 was injected at a concentration of 8 ng/µl, the two single guides with integrated CAS9 plasmids pLM12 and pLM13 at a concentration of 40 ng/µl together with the recommended Co-injectionmarkers pGH8 (Addgene 19359) at 10 ng/µl, pCFJ104 (Addgene 19328) at 5 ng/µl and pCFJ90 (19327) at 2.5 ng/µl. Further Selection was done according to the Dickinson protocol.

*zh113* *gfp::nlp-26*

To insert the *gfp::3xFlag* sequence in the 5` prime region of the *nlp-26* locus, the CRISPR/Cas9 system (Jinek et al., 2012) according to the Dickinson protocol (Dickinson et al., 2015) was applied. The repair template plasmid pLM7 was injected at a concentration of 10 ng/µl, the three single guides with integrated CAS9 plasmids pLM8, pLM9 and pLM10 at a concentration of 50 ng/µl together with the recommended Co-injectionmarkers pGH8 (Addgene 19359) at 10 ng/µl, pCFJ104 (Addgene 19328) at 5 ng/µl and pCFJ90 (19327) at 2.5 ng/µl. Further Selection was done according to the Dickinson protocol.

*zh108* *sra-9* deletion

The *sra-9(zh108)* deletion allele was generated according to the Arribere et al. 2014 (Arribere et al., 2014) protocol, with following single guide sequences: TTGGCAAAGTTCTAGTTAT, ACCAATTGAATTGCTGGAT.

**Plasmids**

pLM5 *zh112* repair template

The pDD268 (Dickinson et al., 2015) plasmid was digested with the AvrII and SpeI restriction digest enzymes, adding a linker to the 3' end of the fluorophore insertion site when recombined with the homology arms by means of the Gibson protocol (Gibson et al., 2009). The inserted

homology arms were amplified by Phusion PCR from genomic *lin-3* DNA with the following oligo combinations: HA1: 0.7 kb with OLM181
(ACGTTGTAAAACGACGGCCAGTCGCCGGCAGAAGAGGTCATACAGCAATGCACAG) and
OLM182
(CATCGATGCTCCTGAGGCTCCCGATGCTCCGAGACACGATTCTGAAACTTTTATTG)
and 0.46 kb with HA2:
OLM183
(CGTGATTACAAGGATGACGATGACAAGAGACCTTCGTGGTTTCGTCAAGAACGTAG)
OLM184
(GGAAACAGCTATGACCATGTTATCGATTTCCAGACCTAATCAAATGGCTACCTTTGC)

pLM6 *zh113* repair template
The pDD282 (Addgene #66823) plasmid was digested with the AvrII and SpeI restriction digest enzymes, adding a linker to the 3' end of the fluorophore insertion site when recombined with the homology arms by means of the Gibson protocol (Gibson et al., 2009). The inserted homology arms were amplified by Phusion PCR from genomic *nlp-26* DNA with the following oligo combinations: HA1: 0.6 kb with OSS3
(acgttgtaaaacgacggccagtcgccggcaTTGGCGGGAAATTCAATGTTTCAGTC) and
OSS4
(CATCGATGCTCCTGAGGCTCCCGATGCTCCtAGGGAGAAGATCACGAAGAAGTTC)
and 0.6 kb with HA2:
OSS5
(CGTGATTACAAGGATGACGATGACAAGAGACTTCTTGTTGGCCTTGTATCCGCAC)
OSS6
(ggaaacagctatgaccatgttatcgatttcCTGCTTGGTGTTATATTTGAAGGGTATCAC)

pLM8 SGN2 CCTTCTTGTTGGCCTTGTAT
Single guide N2 ATACAAGGCCAACAAGAAGG to insert a *gfp* into *nlp-26* locus with pLM6 as Donor template. The plasmid was cloned through NEB's Q5 Site-Directed Mutagenesis Kit into pDD162 (Addgene plasmid # 47549) with OSS7 (CCTTCTTGTTGGCCTTGTATGTTTTAGAGCTAGAAATAGCAAG)

pLM9 SGN3 TACAAGGCCAACAAGAAGGA
Single guide N3 ATACAAGGCCAACAAGAAGG to insert *gfp* into *nlp-26* locus with pLM6 as Donor template. The plasmid was cloned through NEB's Q5 Site-Directed Mutagenesis Kit into pDD162 (Addgene plasmid # 47549) with OSS8 (TACAAGGCCAACAAGAAGGAGTTTTAGAGCTAGAAATAGCAAG)

pLM10 SGN4 TCTTGTTGGCCTTGTATCCG
Single guide N4 sequence ATACAAGGCCAACAAGAAGG was cloned through NEB's Q5 Site-Directed Mutagenesis Kit into pDD162 (Addgene plasmid # 47549) with OSS9 (TCTTGTTGGCCTTGTATCCGGTTTTAGAGCTAGAAATAGCAAG), to insert a GFP into the *nlp-26* locus with pLM6 as Donor template.

pLM12 SG3A gttcttgacgaaaccacgaa
Single guide SG3A sequence gttcttgacgaaaccacgaa was cloned through NEB's Q5 Site-Directed Mutagenesis Kit into pDD162 (Addgene plasmid # 47549) with OLM177 (gttcttgacgaaaccacgaaGTTTTAGAGCTAGAAATAGCAAG), to insert a *mNeongreen* into the *lin-3* locus with pLM5 as Donor template.

pLM13 SG3B cagaatcgtgtctcccttcg
Single guide SG3A sequence cagaatcgtgtctcccttcg was cloned through NEB's Q5 Site-Directed Mutagenesis Kit into pDD162 (Addgene plasmid # 47549) with OSS1 (cagaatcgtgtctcccttcgGTTTTAGAGCTAGAAATAGCAAG), to insert a *mNeongreen* into the *lin-3* locus with pLM5 as Donor template.

**Immunocytochemistry**

Permeabillization by Freeze cracking

The freeze-cracking procedure was adapted from protocols described in (Shakes et al., 2012). The staged L2/L3 larvae were washed 5x in M9 buffer and 10 µl was mounted on 3x Poly-L-Lysin (0.1%, SIGMA) coated slides. The slides were frozen on a liquid Nitrogen cooled metal block and cracking was performed after 10 minutes.

Light Fixation

The slides were immediately immersed in -30°C cooled absolute Methanol for 2 minutes, following -30°C cooled absolute Acetone for 4 minutes. They were allowed to air-dry at RT for 5 minutes and then rehydrated for 15 minutes in 1x PBS buffer.

Antibody-staining

The staining was performed directly on the fixed slides with hydrophobic boundaries encircling the worms with a PAP-pen. Volume per slide ranged between 50ul-200ul.
Blocking was done for 30 minutes at RT with a 5% ABA buffer (1x PBS, 0.05% Triton, 5% BSA). The 1° Antibody MH27 was added at a dilution of (1:30) and FLAG antibody at a dilution of (1:100), in a 3% ABA buffer (1x PBS, 0.05% Triton, 3% BSA) and left over night at 4°C. All 2° Antibody were applied with a 1:200 dilution and left to incubated for 2 hours at RT.
Washing was performed with 0.05% PBS-T (0.05% Triton) buffer at RT 3x for 30 minutes (1°) and 3x 15 minutes (2°) respectively.

Hoechst staining

The Nuclei were visualized using Hoechst staining in a 1:1000 dilution from a Hoechst® dye stock of 10 mg/ml (ThermoFisher). Worms were incubated in dye for 5 minutes. And washed 3x in PBS-T buffer for 15 minutes.
Finally slides were mounted with 20-40 µl Mowiol (Aldrich, 4–88) mounting medium per slide and covered with a coverslip and let dry for one hour or kept at 4° for later analysis.

**Antibodies**
1° antibodies that were used: Monoclonal mouse ANTI-FLAG M2 (F3165, Sigma-Aldrich) and monoclonal mouse anti AJM-1 (MH27) (Francis and Waterston, 1991) serum.
2° Antibody: Tetramethyl Rhodamine lsothiocyanate (TRITC)-conjugated affinity pure Donkey Anti-Mouse lgG (H+L) (715-025-150, Jackson ImmunoReserJrch Laboratories, Inc.)

**RNAi**
RNA interference (RNAi) was performed using the feeding method as described (Kamath and Ahringer, 2003). P0 worms were synchronized at the L1 stage, transferred to NGM plates containing 3 mM IPTG and 50 ng/ml ampicillin seeded with the indicated RNAi bacteria and allowed to grow for 5-7 days at 20°C, after which the F1 progeny was analyzed.

**Vulval induction**
Vulval induction was scored by examining worms at the L4 stage under Nomarski optics as described in (Sternberg and Horvitz, 1986). The number of VPCs that had adopted a 1° or 2° vulval cell fate was counted for each animal and the vulval induction (VI) index was calculated by dividing the number of induced cells by the number of animals scored. The fraction of animals with more than three vulval cell fates induced was scored as VI > 3, and less than three cells induced was scored as VI < 3 was calculated. Statistical relevance was analyzed by bootstrapping. The compared allele combinations in the vulval induction assay were strains generated as progeny from the same cross.

### 3.1.6 References


**Alexander, M., Selman, G., Seetharaman, A., Chan, K. K. M., D'Souza, S. A., Byrne, A. B. and Roy, P. J.** (2010). MADD-2, a homolog of the Opitz syndrome protein MID1, regulates guidance to the midline through UNC-40 in Caenorhabditis elegans. *Developmental Cell* **18**, 961–972.

**Aroian, R. V. and Sternberg, P. W.** (1991). Multiple functions of let-23, a Caenorhabditis elegans receptor tyrosine kinase gene required for vulval induction. *Genetics* **128**, 251–267.

**Arribere, J. A., Bell, R. T., Fu, B. X. H., Artiles, K. L., Hartman, P. S. and Fire, A. Z.** (2014). Efficient marker-free recovery of custom genetic modifications with CRISPR/Cas9 in Caenorhabditis elegans. *Genetics* **198**, 837–846.

**Barkoulas, M., van Zon, J. S., Milloz, J., van Oudenaarden, A. and Félix, M.-A.** (2013). Robustness and Epistasis in the C. elegans Vulval Signaling Network Revealed by Pathway Dosage Modulation. *Developmental Cell* **24**, 64–75.

**Battu, G., Hoier, E. F. and Hajnal, A.** (2003). The C. elegans G-protein-coupled receptor SRA-13 inhibits RAS/MAPK signalling during olfaction and vulval development. *Development* **130**, 2567–2577.

**Berg, H. C.** (1993). *Random Walks in Biology*. Princeton University Press.

**Berset, T. A., Hoier, E. F. and Hajnal, A.** (2005). The C. elegans homolog of the mammalian tumor suppressor Dep-1/Scc1 inhibits EGFR signaling to regulate binary cell fate decisions. *Genes & Development* **19**, 1328–1340.

**Berset, T., Hoier, E. F., Battu, G., Canevascini, S. and Hajnal, A.** (2001). Notch inhibition of RAS signaling through MAP kinase phosphatase LIP-1 during C. elegans vulval development. *Science* **291**, 1055–1058.

**Bollenbach, T., Kruse, K., Pantazis, P., González-Gaitán, M. and Jülicher, F.** (2007). Morphogen transport in epithelia. *Phys Rev E Stat Nonlin Soft Matter Phys* **75**, 011901.

**Bozorgui, B., Teimouri, H. and Kolomeisky, A. B.** (2015). Theoretical analysis of degradation mechanisms in the formation of morphogen gradients. *J Chem Phys* **143**, 025102.

**Braendle, C. and Félix, M.-A.** (2008). Plasticity and errors of a robust developmental system in different environments. *Developmental Cell* **15**, 714–724.

**Brenner, S.** (1974). The genetics of Caenorhabditis elegans. *Genetics* **77**, 71–94.

**Chen, Y. and Struhl, G.** (1996). Dual roles for patched in sequestering and transducing Hedgehog. *Cell* **87**, 553–563.

**DeLotto, Y. and DeLotto, R.** (1998). Proteolytic processing of the Drosophila Spätzle protein by easter generates a dimeric NGF-like molecule with ventralising activity. *Mechanisms of Development* **72**, 141–148.

**Dickinson, D. J., Pani, A. M., Heppert, J. K., Higgins, C. D. and Goldstein, B.** (2015). Streamlined Genome Engineering with a Self-Excising Drug Selection Cassette. *Genetics* **200**, 1035–1049.

**Eisenmann, D. M., Maloof, J. N., Simske, J. S., Kenyon, C. and Kim, S. K.** (1998). The beta-catenin homolog BAR-1 and LET-60 Ras coordinately regulate the Hox gene lin-39 during Caenorhabditis elegans vulval development. *Development* **125**, 3667–3680.

**Entchev, E. V., Schwabedissen, A. and González-Gaitán, M.** (2000). Gradient formation of the TGF-beta homolog Dpp. *Cell* **103**, 981–991.

**Francis, R. and Waterston, R. H.** (1991). Muscle cell attachment in Caenorhabditis elegans. *J Cell Biol* **114**, 465–479.

**Friedland, A. E., Tzur, Y. B., Esvelt, K. M., Colaiácovo, M. P., Church, G. M. and Calarco, J. A.** (2013). Heritable genome editing in C. elegans via a CRISPR-Cas9 system. *Nature Methods* **10**, 741–743.

**Frøkjær-Jensen, C., Davis, M. W., Hopkins, C. E., Newman, B. J., Thummel, J. M., Olesen, S.-P., Grunnet, M. and Jorgensen, E. M.** (2008). Single-copy insertion of transgenes in Caenorhabditis elegans. *Nat. Genet.* **40**, 1375–1383.

**Gibson, D. G., Young, L., Chuang, R.-Y., Venter, J. C., Hutchison, C. A. and Smith, H. O.** (2009). Enzymatic assembly of DNA molecules up to several hundred kilobases. *Nature Methods* **6**, 343–345.

**Grimbert, S., Tietze, K., Barkoulas, M., Sternberg, P. W., Félix, M.-A. and Braendle, C.** (2016). Anchor cell signaling and vulval precursor cell positioning establish a reproducible spatial context during C. elegans vulval induction. *Developmental Biology* 1–13.

**Haag, A., Gutierrez, P., Bühler, A., Walser, M., Yang, Q., Langouët, M., Kradolfer, D., Fröhli, E., Herrmann, C. J., Hajnal, A., et al.** (2014). An in vivo EGF receptor localization screen in C. elegans Identifies the Ezrin homolog ERM-1 as a temporal regulator of signaling. *PLoS Genet* **10**, e1004341.

**Hajnal, A., Whitfield, C. W. and Kim, S. K.** (1997). Inhibition of Caenorhabditis elegans vulval induction by gap-1 and by let-23 receptor tyrosine kinase. *Genes & Development* **11**, 2715–2728.

**Hedgecock, E. M., Culotti, J. G. and Hall, D. H.** (1990). The unc-5, unc-6, and unc-40 genes guide circumferential migrations of pioneer axons and mesodermal cells on the epidermis in C. elegans. *Neuron* **4**, 61–85.

**Horvath, P. and Barrangou, R.** (2010). CRISPR/Cas, the immune system of bacteria and archaea. *Science* **327**, 167–170.

**Huelsz-Prince, G. and van Zon, J. S.** (2017). Canalization of C. elegans Vulval induction against Anatomical Variability. *Cell Systems* **4**, 219–230.e6.

**Husson, S. J., Clynen, E., Baggerman, G., Janssen, T. and Schoofs, L.** (2006). Defective processing of neuropeptide precursors in Caenorhabditis elegans lacking proprotein convertase?2 (KPC-2/EGL-3): mutant analysis by mass spectrometry. *Journal of Neurochemistry* **98**, 1999–2012.

**Hwang, B. J.** (2004). A cell-specific enhancer that specifies lin-3 expression in the C. elegans anchor cell for vulval development. *Development* **131**, 143–151.

**Janmey, P. A. and Lindberg, U.** (2004). Cytoskeletal regulation: rich in lipids. *Nat. Rev. Mol. Cell Biol.* **5**, 658–666.

**Jinek, M., Chylinski, K., Fonfara, I., Hauer, M., Doudna, J. A. and Charpentier, E.** (2012). A programmable dual-RNA-guided DNA endonuclease in adaptive bacterial immunity. *Science* **337**, 816–821.

**Kaech, S. M., Whitfield, C. W. and Kim, S. K.** (1998). The LIN-2/LIN-7/LIN-10 complex mediates basolateral membrane localization of the C. elegans EGF receptor LET-23 in vulval epithelial cells. *Cell* **94**, 761–771.

**Kamath, R. S. and Ahringer, J.** (2003). Genome-wide RNAi screening in Caenorhabditis elegans. *Methods* **30**, 313–321.

**Kamath, R. S., Fraser, A. G., Dong, Y., Poulin, G., Durbin, R., Gotta, M., Kanapin, A., Le Bot, N., Moreno, S., Sohrmann, M., et al.** (2003). Systematic functional analysis of the Caenorhabditis elegans genome using RNAi. *Nature* **421**, 231–237.

**Katz, W. S., Hill, R. J., Clandinin, T. R. and Sternberg, P. W.** (1995). Different levels of the C. elegans growth factor LIN-3 promote distinct vulval precursor fates. *Cell* **82**, 297–307.

**Katz, W. S., Lesa, G. M., Yannoukakos, D., Clandinin, T. R., Schlessinger, J. and Sternberg, P. W.** (1996). A point mutation in the extracellular domain activates LET-23, the Caenorhabditis elegans epidermal growth factor receptor homolog. *Mol. Cell. Biol.* **16**, 529–537.

**Kicheva, A., Pantazis, P., Bollenbach, T., Kalaidzidis, Y., Bittig, T., Jülicher, F. and González-Gaitán, M.** (2007). Kinetics of morphogen gradient formation. *Science* **315**, 521–525.

**Kimble, J. and Hirsh, D.** (1979). The postembryonic cell lineages of the hermaphrodite and male gonads in Caenorhabditis elegans. *Developmental Biology* **70**, 396–417.

**McCloy, R. A., Rogers, S., Caldon, C. E., Lorca, T., Castro, A. and Burgess, A.** (2014). Partial inhibition of Cdk1 in G 2 phase overrides the SAC and decouples mitotic events. *Cell Cycle* **13**, 1400–1412.

**Miller, D. M. and Shakes, D. C.** (1995). Immunofluorescence microscopy. *Methods Cell Biol.* **48**, 365–394.

**Morf, M. K., Rimann, I., Alexander, M., Roy, P. and Hajnal, A.** (2013). The Caenorhabditis elegans homolog of the Opitz syndrome gene, madd-2/Mid1, regulates anchor cell invasion during vulval development. *Developmental Biology* **374**, 108–114.

**Morrissey, M. A., Hagedorn, E. J. and Sherwood, D. R.** (2013). Cell invasion through basement membrane: The netrin receptor DCC guides the way. *Worm* **2**, e26169.

**Nathoo, A. N., Moeller, R. A., Westlund, B. A. and Hart, A. C.** (2001). Identification of neuropeptide-like protein gene families in Caenorhabditiselegans and other species. *Proc. Natl. Acad. Sci. U.S.A.* **98**, 14000–14005.

**Perrimon, N. and McMahon, A. P.** (1999). Negative feedback mechanisms and their roles during pattern formation. *Cell* **97**, 13–16.

**Shakes, D. C., Miller, D. M. and Nonet, M. L.** (2012). Immunofluorescence microscopy. *Methods Cell Biol.* **107**, 35–66.

**Shaye, D. D. and Greenwald, I.** (2002). Endocytosis-mediated downregulation of LIN-12/Notch upon Ras activation in Caenorhabditis elegans. *Nature* **420**, 686–690.

**Sherwood, D. R. and Sternberg, P. W.** (2003). Anchor Cell Invasion into the Vulval Epithelium in C. elegans. *Developmental Cell* **5**, 21–31.

**Simmer, F., Tijsterman, M., Parrish, S., Koushika, S. P., Nonet, M. L., Fire, A., Ahringer, J. and Plasterk, R. H. A.** (2002). Loss of the putative RNA-directed RNA polymerase RRF-3 makes C. elegans hypersensitive to RNAi. *Current Biology* **12**, 1317–1319.

**Sternberg, P. W.** (2005). Vulval development. *WormBook* 1–28.

**Sternberg, P. W. and Horvitz, H. R.** (1986). Pattern formation during vulval development in C. elegans. *Cell* **44**, 761–772.

**Sternberg, P. W. and Horvitz, H. R.** (1989). The combined action of two intercellular signaling pathways specifies three cell fates during vulval induction in C. elegans. *Cell* **58**, 679–693.

**Troemel, E. R., Chou, J. H., Dwyer, N. D., Colbert, H. A. and Bargmann, C. I.** (1995). Divergent seven transmembrane receptors are candidate chemosensory receptors in C. elegans. *Cell* **83**, 207–218.

**Tzur, Y. B., Friedland, A. E., Nadarajan, S., Church, G. M., Calarco, J. A. and Colaiácovo, M. P.** (2013). Heritable custom genomic modifications in Caenorhabditis elegans via a CRISPR-Cas9 system. *Genetics* **195**, 1181–1185.

**Wartlick, O., Kicheva, A. and González-Gaitán, M.** (2009). Morphogen gradient formation. *Cold Spring Harb Perspect Biol* **1**, a001255–a001255.

**Whitfield, C. W., Bénard, C., Barnes, T., Hekimi, S. and Kim, S. K.** (1999). Basolateral localization of the Caenorhabditis elegans epidermal growth factor receptor in epithelial cells by the PDZ protein LIN-10. *Mol. Biol. Cell* **10**, 2087–2100.

**Zand, T. P., Reiner, D. J. and Der, C. J.** (2011). Ras Effector Switching Promotes Divergent Cell Fates in C. elegans Vulval Patterning. *Developmental Cell* **20**, 84–96.

**Ziel, J. W., Hagedorn, E. J., Audhya, A. and Sherwood, D. R.** (2008). UNC-6 (netrin) orients the invasive membrane of the anchor cell in C. elegans. *Nat Cell Biol* **11**, 183–189.

## 3.2 LIN-3 EGF directs AC polarity and invasion during vulval morphogenesis

Manuscript draft

Louisa Mereu[1,2,*], Silvan Spiri[1,2], Matthias Morf , Erika Fröhli and Alex Hajnal[1,°]

° Corresponding author: alex.hajnal@imls.uzh.ch

1 Institute of Molecular Life Sciences, University of Zurich, Winterthurerstrasse 190, Zurich, CH-8057, Switzerland.

2 Molecular Life Science PhD Program , University and ETH Zurich, CH-8057 Zurich

Key words: *C. elegans*, LIN-3, morphogen, gradient,

### 3.2.1 Abstract

During animal development, the epidermal growth factor (EGF) acts in multiple tissues as stimulator of cell proliferation, growth, differentiation and survival. Cancer cells take advantage of EGF signaling by expressing increased levels of EGF receptors. EGF receptor signaling is implicated in controlling the invasiveness of metastatic cancer cells. AC invasion during *Caenorhabditis elegans* vulval morphogenesis is an excellent in vivo model to study the signaling processes utilized by invasive cells in their physiological environment.
During the *C. elegans* larval development, a specialized uterine cell, the anchor cell (AC), invades through two basal lamina into the ventrally situated vulval tissue in order to connect the prospective uterus with the developing vulva. AC invasion embodies a robustly regulated process, secured by redundant signaling events that have not all been elucidated yet. Vulva specific *lin-3* depletion as well as ectopic *lin-3* expression caused defects in AC polarity, AC mispositioning and vulval morphogenesis defects. Defects in vulF mediated LIN-3 expression in a mutant of the encoded *egl-38* Pax2/5/8 transcriptionfactor, significantly increased the *unc-6(ev400)* mutant basal lamina breaching defect. Our data indicate a novel function of the *C. elegans* EGF homolog LIN-3 as an AC polarity and guidance cue during AC mediated vulval morphogenesis.

### 3.2.2 Introduction

Cell polarity is essential for cell migration, which is a key factor required for cancer cells to form metastases. As time progresses, the primary tumor associated stroma can become more reactive and acquires features characteristic of a state of wound-healing or inflammation (Grivennikov et al., 2010). This environment promotes the upregulation of pro-invasive features in the carcinoma cells, which hijack innate cellular responses, and invade novel tissues for secondary growth. To enable metastasis formation, the cancer cells have to invade through barriers like the extracellular matrix (ECM) and the basement membrane, to enter the stroma. It has previously been shown that EGF gradients can function as a chemoattractant and direct cell motility (Kedrin et al., 2007; Price et al., 1999; Sun et al., 2005; Wyckoff et al., 2004), in metastatic rat mammary adenocarcinoma cell cultures (MTLn3)(Goswami et al., 2005). The authors found that macrophages secrete an EGF gradient, which activates EGFR in neighboring carcinoma cells, promoting their directed motility and invasiveness along the formed EGF gradient (Goswami et al., 2005). Almost all previous studies, investigating EGF gradient induced cell motility, were performed in cell culture assays and with different cell lines (Bailly et al., 2000; Barrandon and Green, 1987; Blay and Brown, 1985; Price et al., 1996; Sun et al., 2005). There are also contradictory reports, stating that EGF merely promotes cell migration, but does not function as a chemoattractant on its own, only in cooperation with other chemoattractant gradients, such as SDF-1α (Kim et al., 2013). The authors explained that these contradicting results could arise from the differences in the set-up of the cell-culture assays. Especially, cell migration in 2D cultures is fundamentally different from cell migration ins 3D cell cultures and therefore differential prerequisites in the experimental models could produce different results (Kim et al., 2013). It is difficult to mimic the innate environment of a cellular organism in a cell culture assay, therefore in-vivo studies can be very useful to corroborate cell-culture experiments. There are only few previous in-vivo studies linking EGF gradients to cell polarity and cell migration (Duchek and Rørth, 2001; Wyckoff et al., 2000; Wyckoff et al., 2004). In our study, we show further evidence that loss in localized EGF signaling affects cell polarity and subsequent cell migration in an in vivo context. The formation of the uterine to vulval lumen connection during *C. elegans* development, in which a single cell is involved in its orchestration, presents a comprehensible model for regulated cell invasion. During *C. elegans* hermaphrodite vulval development, six epidermal cells are competent to adopt a vulval cell fate and are termed VPCs. The somatic gonad is localized dorsal to the VPCs, and from within this tissue, a specialized uterine cell, the anchor cell (AC) secretes an inductive LIN-3 EGF signal, in a graded manner. This LIN-3 EGF signal specifies a 1° or a 2° vulval cell fate in three of the VPCs (P5.p. P6.p and P7.p), in a dose dependent manner (Katz et al., 1995; Zand et al., 2011). The LIN-3 EGF ligand binds to its receptor LET-23 EGFR, leading to an activation of the LET-60 RAS/MPK-1 ERK signaling pathway (Sternberg, 2005). Induction of LET-60 RAS signaling promotes a primary (1°) vulval cell fate and upregulates LIN-12 Notch ligands, which induce a 2° vulval cell fate and downregulate 1° vulval cell fate regulators in the adjacent cells, leading to a 2°-1°-2° pattern (Greenwald, 2005; Shaye and Greenwald, 2002; Shaye and Greenwald, 2005; Sternberg, 1988; Wang and Sternberg, 2001; Yochem et al., 1988). The fates are set by the end of the early L3 larval stage. To generate the vulva organ, the cells undergo three rounds of cell division, completed by the end of the late L3 larval stage. The vulval cell descendants are further pat-

terned through a combination of signaling events, including AC mediated LET-60 RAS (Wang and Sternberg, 2000) and Wnt signaling (Inoue et al., 2004), to from a mirrored pattern of subfates termed vulA, vulB1, vulB2, vulC and vulD, descendants of the 2° fated vulval cells, as well as vulE and vulF, descendants of the 1° fated vulval cell (Gupta et al., 2012). The following morphogenesis events, including cell migration and fusion produces a stack of seven toroids, surrounding the ensuing ventral vulval lumen at the mid L4 larval stage (Sharma-Kishore et al., 1999). The continuous connection of the vulva and the uterine lumen is coordinated by the AC through a series of events. First, the AC breaches the two basal lamina separating the two tissues, the vulva and the developing uterus, at the mid to late L3 larval stage. To achieve this, the invasive membrane of the AC is directed ventrally towards the developing vulva through UNC-6 Netrin signaling, secreted by the ventral nerve cord (VNC), which directs the UNC-40 Netrin receptor ventrally within the AC. This leads to an increased phosphatidylinositol-4,5-bisphosphate ($PIP_2$) accumulation at the ventral membrane that functions as a scaffold for F-actin recruitment, and subsequently enables and directs the AC's invasive protrusion formation (Ziel et al., 2008). The integrin heterodimer INA-1/PAT-3 is likewise recruited to the invasive membrane and coordinates AC polarity upstream of UNC-40, in response to the unknown vulva cues (Hagedorn et al., 2009; Lohmer et al., 2016). These vulva cues are secreted from the 1° vulval cells and further enhance the AC's ability to breach the basal lamina and direct its invasive protrusions towards them (Ziel et al., 2008). Following basal lamiane breaching, the AC is required to contact the central 1° vulval cell descendants (vulF). This process initiates dorsal lumen expansion and is a requisite for the continuous uterine lumen connection (Estes and Hanna-Rose, 2009; Yang et al. 2017).

We demonstrate a novel function of EGL-38-dependent LIN-3 signaling form the vulF cells at an earlier developmental stage than previously reported (Chang et al., 1999). The evidence we provide, in which deregulation of vulva specific *lin-3* expression affects AC polarity of $PIP_2$, and enhances basal lamina breaching in *unc-6* mutants, suggests that vulF induced *lin-3* expression functions as a novel AC polarity and protrusion formation regulator (Ziel et al., 2008) promoting wild-type dorsal vulval lumen morphogenesis.

### 3.2.3 Results

**Vulva specific *lin-3* RNAi causes defects in dorsal lumen formation**

LIN-3 is expressed from the vulF cells during vulval morphogenesis at the early to mid L4 stage (Hwang, 2004). VulF-specific LIN-3 expression is activated by the EGL-38 transcription factor (Chang et al., 1999). So far, this EGL-38 dependent LIN-3 expression has been shown to be required for the determination of the uterine uv1 cell fate (Chang et al., 1999; Rajakumar and Chamberlin, 2007). If EGL-38 function is reduced or lost, this leads to a lack in uv1 cell fate determination (Chang et al., 1999) and also to a defect in dorsal lumen formation of the vulva, a phenotype that so far has not been accounted for entirely.

To further analyze putative functions of LIN-3 secreted by the vulF cells, we knocked down LIN-3 specifically in the VPCs by means of tissue-specific RNAi (Qadota et al., 2007), and found that this lead to defects in dorsal lumen expansion (Fig. 2.3.1, B and B') in around 10% of the animals (Fig. 2.3.1, D). To quantify this finding, we measured the inner diameter between the vulF/vulE apical toroidal junctions (Fig. 3.2.1, E), and found a significant decrease in the mean vulF/vulE diameter of *lin-3* RNAi treated animals compared to empty control (Fig. 3.2.1, F). Another phenotype we observed upon *lin-3* knock-down was an elongation of the dorsal vulval lumen height (Fig. 3.2.1, E and F). In addition, we analyzed a strain with *lin-3* shRNA expression specifically in the VPCs (*zhEx518[*$P_{lin\text{-}31}$*>lin-3i;* $P_{myo\text{-}2}$*>mcherry*) (Dutt et al., 2004). In this strain, we also observed slight reduction in mean dorsal lumen expansion and a significant increase in mean dorsal lumen height (Fig. 3.2.1. G). As a control, we compared individuals of the same extrachromosomal strain, with co-injectionmarker expression ($P_{myo\text{-}2}$*>mCherry* ) to those without. These results indicate that LIN-3 expressed by the vulval cells is involved in formation of wild-type dorsal vulval lumen expansion.

**AC ablation until the P6.p 8-cell stage causes morphogenesis defect**

It has been shown that the AC is required not only for basal lamina breaching, but also to initiate dorsal lumen formation by directly contacting and invading inbetween the 1° vulF cells (Estes and Hanna-Rose, 2009; Yang et al., 2017). We suspect that this AC invasion process is disturbed upon VPC specific *lin-3* RNAi, leading to the observed dorsal lumen expansion defect. To estimate the permissive time-frame, in which the AC is required for wild-type dorsal lumen expansion we performed an AC ablation series at progressing developmental stages and analyzed the effect on dorsal vulval lumen expansion at the mid L4 X-tree stage. Six of eight animals had defect in dorsal lumen expansion (Fig. 3.2.2, A-B' and E rows 1-3) upon AC ablation between the P6.p 2-4 cell stages (mid-late L3). Upon AC ablation at the P6.p 8-cell stage, four of seven animals had defects in dorsal lumen formation (Fig. 3.2.2, E row 4). Ablation of the AC at the triangle early L4 stage of vulval morphogenesis had no effect on dorsal lumen expansion and produced a wild-type vulva in eight out of eight cases (Fig. 3.2.2, C–D' and E row 5). This shows that the AC is only required until the last round of 1° vulval cell division for dorsal lumen opening. However, the exact function the AC performs in this process still needs to be determined. It is possible that it is linked to a recent finding occurring at the coinciding developmental stage, in which the AC was described to form circumferal protrusions around the vulF-vulF lateral membrane and thus induce lateral membrane constriction and vulval lumen expansion (Yang et al., 2017).

**Ectopic *lin-3* expression at the mid L3 stage depolarizes $PIP_2$ in the AC**

Our AC ablation experiment showes that the permissive developmental stage, in which the AC regulates dorsal lumen expansion can be narrowed down to the P6.p 4-8cell (late L3) larval stage. To establish a link between LIN-3 signaling and AC mediated vulF invasion we expressed *lin-3* ectopically from a heat-shock inducible promoter at the L2/L3 stage and analyzed the worms 12 hours later at the P6.p 4-8 cell (late L3) stage. We analyzed the $P_{cdh3}$*>mCherry::PLC∂*$^{PH}$ reporter expression pattern (Ziel et al., 2008) that marks the Phospholipid phosphatidylinositol-4,5-bisphosphate ($PIP_2$), specifically in the AC. In mammalian cells, $PIP_2$ is enriched at the apical cellular membrane and $PIP_3$ at the basolateral cellular membrane (Martin-Belmonte et al., 2007). In the AC, $PIP_2$ is enriched towards the ventral side of the AC, which comprises the basolateral side per definition, as it faces the basement membrane. We compared AC polarity by means of the $P_{cdh3}$*>mCherry::PLC∂*$^{PH}$ reporter expression pattern in wild-type (Fig. 3.2.3, A) and in a *syIs11[*$P_{hs}$*>lin-3soluble]* strain (Fig. 3.2.3, C), in which LIN-3 can be expressed ectopically by a heat-shock promoter. We compared wild-type animals with and without heat-shock treatment to *syIs11* animals, with and without heat-shock treatment (Fig. 3.2.3, B and D). AC $PIP_2$ polarity was established by measuring the relative $PIP_2$ reporter intensity profile in the AC, and a polarity index was assigned by means of a custom written R script, which calculates the standard deviation of an individual intensity profile, from its average intensity, and the statistical significance was assessed by bootstrapping (Morf et al., 2013). We found a significant decrease in the mean $PIP_2$ polarity index of heat-shock treated *syIs11[*$P_{hs}$*>lin-3soluble]* animals compared to the same strain without heat-shock induction. The mean $PIP_2$ polarity index of heat-shock induced *syIs11* animals was also significantly decreased compared to wild-type animals with and without heat-shock induction (Fig. 3.2.3, F). There was no significant difference between wild-type and *syIs11[*$P_{hs}$*>lin-3soluble]* animals without heat-shock treatment. Interestingly, heat-shock subjected wild-type animals showed a significant increase in $PIP_2$ polarity index compared to all other groups. Heat-shock induction presents an immense stress factor for the worms and comprehensibly induces a stress response (Morimoto, 2011). Possibly, upregulation of heat shock response proteins, such as HSF-1 and chaperons have a positive effect on AC polarity. This would confer higher significance to the reduction in AC polarity observed in response to ectopic LIN-3 expression. We further analyzed the *let-60(n1046gf)* strain and found a significant decrease in $PIP_2$ polarity index compared to wild-type control without heat-shock induction (Fig. 3.2.3, F). This points to a putative downstream regulator of $PIP_2$ polarity.

The results show that ectopic LIN-3 expression has a negative effect on AC $PIP_2$ polarity at the mid-late L3 stage. These results suggest that LIN-3 expression from a localized source might promote enrichment of $PIP_2$ at the cell membrane of the AC, and subcellular ventral $PIP_2$ enrichment in the AC is required for AC invasion and basal lamina breaching. The fact that constitutively active LET-60 likewise causes $PIP_2$ depolarization indicates that LET-60 RAS acts as a possible downstream effector in the process and implies that localized LET-23 EGFR activation under wild-type conditions might recruit and activate LET-60 (Fig. 3.2.3, F).

**VPC specific *lin-3* shRNA expression cause aberrant AC polarity, positioning and dorsal lumen expansion phenotypes**

From the ectopic LIN-3 expression results we hypothesize that, if LIN-3 acts as a directional cue for AC polarity, loss in LIN-3 signaling from the vulF cells might likewise cause defects in

AC polarity. We therefore looked at AC $PIP_2$ polarity in a strain expressing a VPC specific *lin-3* shRNA ($P_{cdh-3}$*>PLC∂$^{PH}$::mCherry; ajm-1::gfp; zhEx518*[$P_{lin-31}$*>lin-3i;* $P_{myo-2}$*>mCherry* ]), and found an increase in the occurrence of depolarized ACs (Fig. 3.2.4, B and D) compared to the control (*$P_{cdh-3}$>PLC∂$^{PH}$::mCherry; ajm-1::gfp)* strain. We also found occurences of AC mispositioning in this strain (Fig. 3.2.4, C, D). In addition, the strain contained a significant population of animals with a defect in dorsal lumen morphogenesis at the mid L4 X-tree stage (Fig. 3.2.4, E, F and G). These results suggest that loss in localized LIN-3 expression from the vulF cells leads to defects in dorsal lumen formation, likely due to AC depolarization and erratic AC positioning.
The only known LIN-3 receptor is LET-23, the sole *C.elegans* EGFR/ErbB1 family member. If LIN-3 signals to the AC, it is more than likely that the LET-23 receptor is activated in response. We examined the *let-23::gfp* reporter (Haag et al., 2014) expression pattern at the mid-late L3 stage and found it expressed in the AC at the permissive stage (Fig. 3.2.4, H). The LET-23 expression in the AC especially come to light upon VPC specific *let-23* knock-down (Fig. 3.2.4, I). This shows that LIN-3 expressed from the vulF cells could be perceived by the AC within the time-frame, in which AC invasion has shown to be required for dorsal lumen expansion (Fig. 3.2.2).

**_egl-38_(_ne578_) mutants have defects in AC polarity and dorsal lumen formation**

The EGL-38 transcription factor has been shown to drive *lin-3* transcription in the vulF cells at the early to mid L4 larval stage (Hwang, 2004). Earlier *egl-38* transgene expression has so far not been reported, but genetic evidence for EGL-38 mediated *lin-3* expression at the time of vulval induction exists (Dutt et al., 2004). Our results so far show that the dorsal lumen expansion phenotype is linked to AC invasion and disturbances in AC positioning and polarity, and that these are likely causes of the observed vulval morphogenesis defect.
The *egl-38(n578)* allele has been shown to disrupt *lin-3::gfp* expression from the vulF cells and in addition has defects in dorsal lumen expansion and uterin uv1 cell fate adoption (Rajakumar and Chamberlin, 2007; Chang et al., 1999). We quantified the reported dorsal lumen expansion defect and found a concordant significant reduction in the average vulF toroid diameter in *egl-38(n578)* animals compared to wild-type (Fig. 3.2.5, A-D). We then looked at AC polarity in *egl-38(n578)* animals and found a significantly decrease in the mean $PIP_2$ polarity index at the P6.p four cell stage (mid-late L3) (Fig. 3.2.5, F-G) compared to wild-type control. We conclude that the AC polarity defect in e*gl-38(n578)* animals might arise from loss in vulF specific LIN-3 expression and possibly contribute to the dorsal lumen expansion defect observed in this strain. Thus, LIN-3 from the vulF cells does not only act via uv1 specification but also by polarizing the AC.

**The _egl-38(ne578)_ allele significantly increases the _unc-6(ev400)_, but not the _unc-40(e271)_ mediated invasion defect**

Since *egl-38(n578)* mutants have very similar phenotypic defects compared to the defects we observed upon VPC specific *lin-3* knock–down, we used the allele as a tool for further investigation of putative LIN-3 functions in vulval morphogenesis. As shown above, the ACs of *egl-38(n578)* mutants have defects in $PIP_2$ polarity. Another known AC polarity regulator is UNC-6, the Netrin homolog. UNC-6 is a secreted cue from the ventral nerve cord (VNC), which is known to direct its receptor UNC-40, $PIP_2$ and F-actin regulators to the ventral side of the AC, which

is required for proper polarization and basal lamina breaching (Ziel et al., 2008). *unc-6(ev400)* mutants accordingly have defects in AC polarity and delayed basal lamina breaching. We found that the *egl-38(n578)* mutant allele significantly increased the *unc-6(ev400)* mediated basal lamina breaching defect during the early to mid L4 stage (Fig. 3.2.6, G). However, prior to the L3/L4 molting stage, there was no significant difference in percent of basal lamina breaching between the two strains (Fig. 3.2.6, G), suggesting that LIN-3 mediates late invasion in *unc-6(ev400)* mutants. To test if the *unc-40(e271)* mediated basal lamina breaching defect is also enhanced by the *egl-38(n578)* allele, we crossed the two alleles together. We scored basal lamina breaching by mito-tracker staining at the early L4 (Fig. 3.2.S1, A-B') and the mid L4 (Fig. S1, C-D') larval stages, but found no significant difference between the two strains (Fig. 3.2.S1, E).
These results suggest that EGL-38 is involved in AC dependent basal lamina breaching in parallel to UNC-6, but in the same pathway or at the level of the UNC-40 receptor.

**The AC 's ability to identify the 1° fated P8.p after P3-7.p ablation is decreased in *egl-38(n578)* mutants**

In a wild-type situation, LIN-3 EGF signaling from the AC induces P6.p to adopt a 1° vulval cell fated at the early L3 stage. Upon laser ablation of the P3.p-P7.p cells at the mid L2 stage, the remaining P8.p cell adopts a 1° vulval cell fate. During the course of the mid to late L3 stage the AC extends a protrusion towards the 1° fated P8.p descendants (Fig. 3.2.7, A to C). In *unc-6(ev400)* mutants, the AC fails to extend a protrusion towards P8.pxx (Ziel et al., 2008). We ablated P3.p-P7.p at the mid L2 stage in wild-type and *egl-38(n578)* mutants and found that the AC failed to extend a process towards the 1° fated P8.pxx descendants in 50 percent of the cases, which was a significant decrease compared to the wild-type control (Fig. 3.2.7, D and E). In addition, the AC processes and polarity were frequently not directed towards P8.pxx in *egl-38(n578)* mutants, but rather in a random orientation (Fig. 3.2.7, F and G).
These results indicate that EGL-38 is involved in the regulation of a signal secreted from the 1° vulval cells that acts as a directional cue for AC polarity and protrusion formation. To conclude whether this AC directing cue is LIN-3, still needs further investigation.

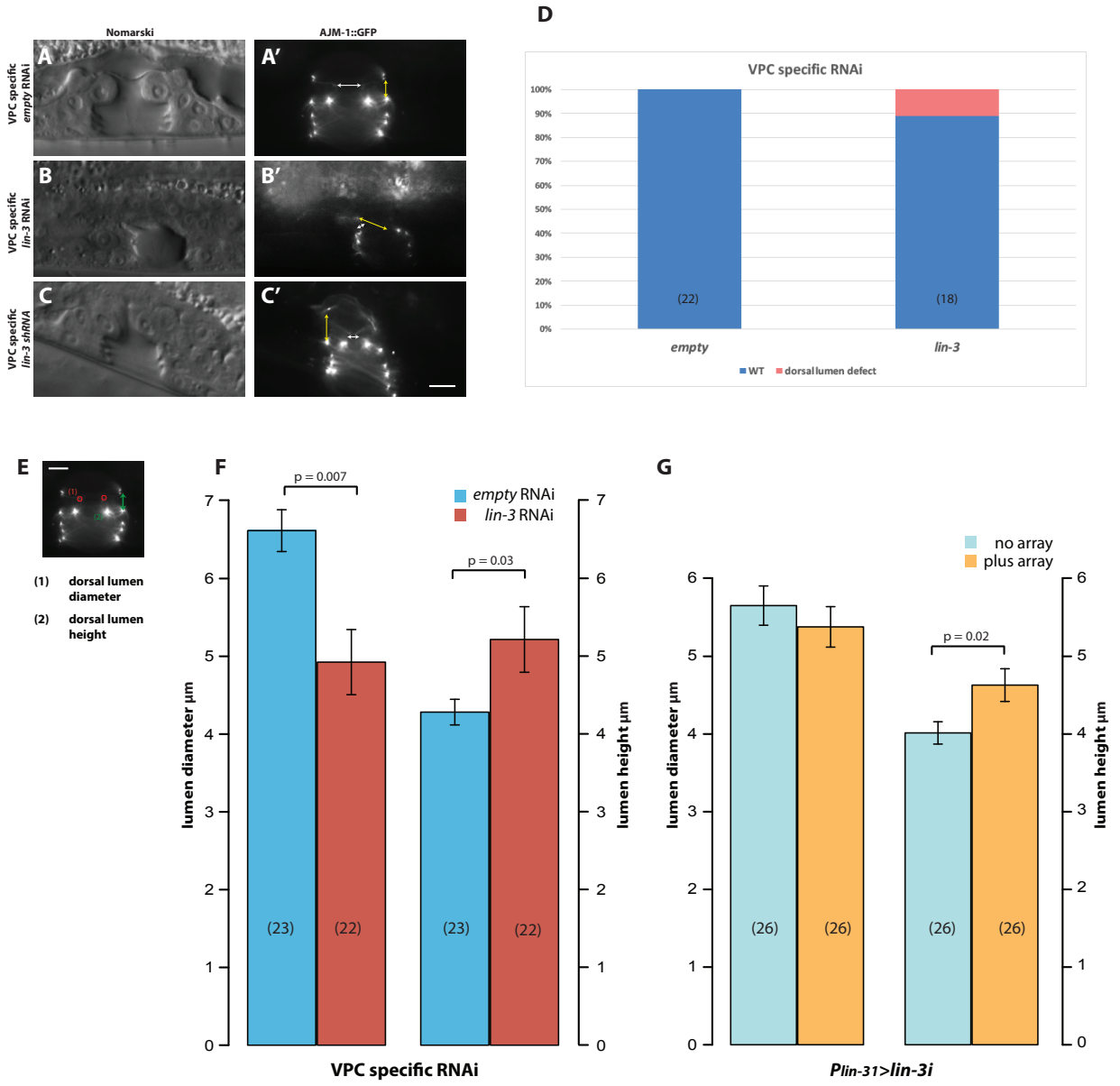


**Figure 3.2.1. Vulva-Specific LIN-3 depletion leads to defects in dorsal lumen formation**

(A, B and C) Nomarski and (A', B' and C') *ajm1::gfp* fluorescence sections of lateral view mid L4 stage vulvas:
(A and B) *rrf-3(pk1426); rde-1(ne219); ajm-1::gfp;* $P_{lin-31}$*>rde-1(+)* animals, treated with (A) empty vector control, (B) *lin-3* RNAi treated as well as (C) $P_{cdh3}$*>mCherry::PLC*$\delta^{PH}$; *ajm-1::gfp; zhEx518[*$P_{lin-31}$*>lin-3i;* $P_{myo-2}$*>mcherry]* animals, expressing a vulva specific *lin-3* shRNA transgene ($P_{lin-31}$*>lin-3i*). (A) Shows a vulva with phenotypically wild-type dorsal lumen expansion, (B and C) show vulvas with defects in dorsal lumen expansion (white arrow) and dorsal lumen height (yellow arrow). Scale bar equals 5 µm.
(D) Stacked chart showing the percentage of cases, in which a dorsal lumen expansion defect was observed, in empty and *lin-3* RNAi treated *rrf-3(pk1426); rde-1(ne219);* $P_{lin-31}$*>rde-1(+)* animals. Animals were scored at the mid L4 stage.
(E) The dorsal lumen expansion phenotype was characterized by measuring (1) the inner diameter of the vulF toroid, based on the distance of the vulF/vulE apical junctions, marked by a the translational gfp reporter, *ajm-1::gfp*, as well as by measuring (2) the height of the vulE and vulF toroid. Scale bar indicates 5 µm.
(F) Plot shows average of the measurements taken as described in C, for animals treated with VPC specific RNAi. Error bar indicates standard error of the mean. According to independent students t-test of unequal sample size and variance, there is a significant decrease between the dorsal lumen diameter ((1); p = 0.007) and increase of dorsal lumen height ((2); p = 0.03), in *lin-3* RNAi treated animals compared to empty control.

(G) Quantification of measurements as indicated in C for $P_{cdh3}$>*mCherry::PLCδ*$^{PH}$; *ajm1::gfp* strains with extrachromosomal expression of VPC specific *lin-3* shRNA *zhEx518[*$P_{lin-31}$>*lin-3i;* $P_{myo-2}$>*mcherry]* (plus array), compared to $P_{cdh3}$>*mCherry::PLCδ*$^{PH}$; *ajm-1::gfp* strain with no extrachromosomal *lin-3* shRNA transgene (no array). Error bar indicates standard error of the mean. According to independent students t-test of unequal variance, there is no significant decrease between the dorsal lumen diameter (1), but a significant increase in dorsal lumen height ((2); p = 0.02), in animals expressing the VPC specific *lin-3* shRNA compared to control.

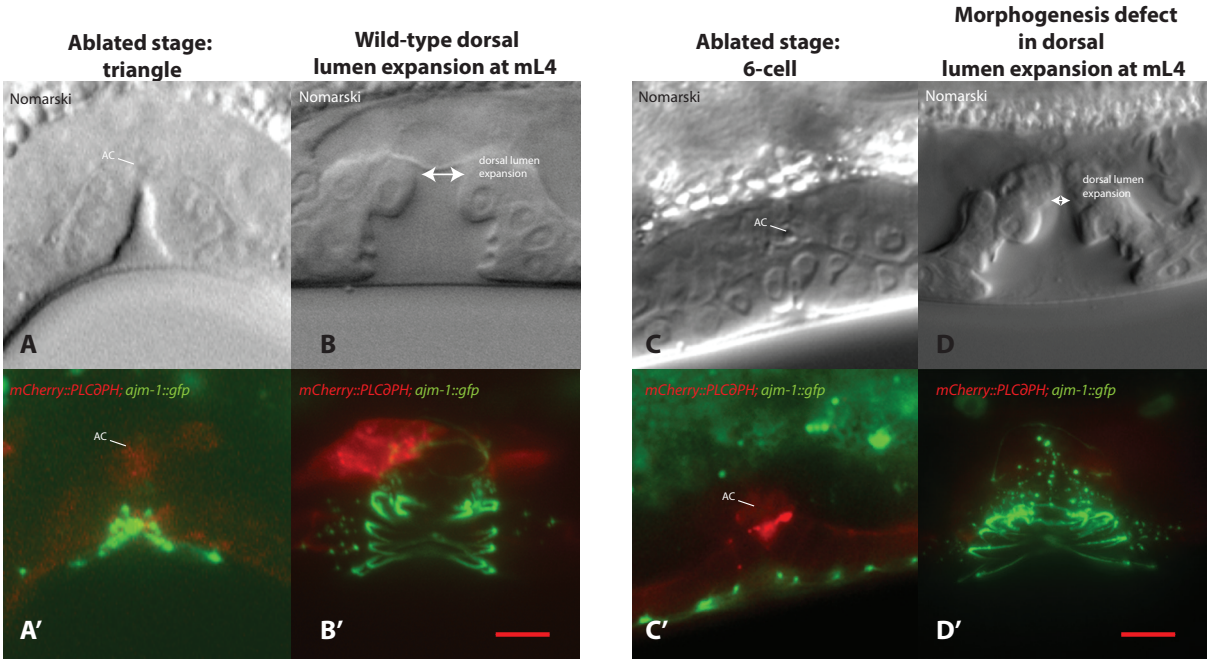


E

| | 1° cell divison progression at AC ablation timepoint | X-tree Phenotype at mL4 stage | |
|---|---|---|---|
| | | WT | Morph. Def. |
| 1 | 2-4 cell | 0 | 2 |
| 2 | 4 cell | 1 | 3 |
| 3 | 6 cell | 1 | 1 |
| 4 | 8 cell | 3 | 4 |
| 5 | triangle | 8 | 0 |
| | N | 13 | 10 |

**Figure 3.2.2. AC ablation after P6.p 8-cell stage causes no vulval morphogenesis defect**
(A and A') Images show examples of AC and vulva at the L3/L4 triangle stage, immediately after AC ablation, and the vulva of the same animal (B and B') at the mid L4 X-tree stage, which developed a wild-type dorsal lumen expansion. (A and B) Nomarski, section images of lateral view vulva. (A' and B') Show expression pattern of summed z-projections of the AC expressing $P_{cdh3}$>*mCherry::PLCδ*$^{PH}$ (red), merged with the *ajm-1::gfp* reporter (green) that marks the apical junctions between the vulva toroids. AC is labeled and dorsal lumen expansion diameter is indicated by double-headed arrow. Scale bar equals 5 µm.
(C and C') Images show examples of AC and vulva at the late L3 6-cell stage, immediately after AC ablation,
(D and D') show the vulva of the same animal at the mid L4 X-tree stage, which developed a defective dorsal lumen expansion. (C and D) Nomarski section images of lateral view animals, (C' and D') Show expression pattern of summed z-projections of the AC expressing $P_{cdh3}$>*mCherry::PLCδ*$^{PH}$ (red), merged with the *ajm-1::gfp* reporter (green) that marks the apical junctions between the vulva toroids. The AC is labeled and the dorsal lumen expansion diameter is indicated by double-headed arrow. Scale bar equals 5 µm.
(E) Table shows the number of animals, which developed a wild-type or a defective dorsal lumen expansion at the mid L4 X-tree stage, after AC ablation at the indicated developmental larval stage.

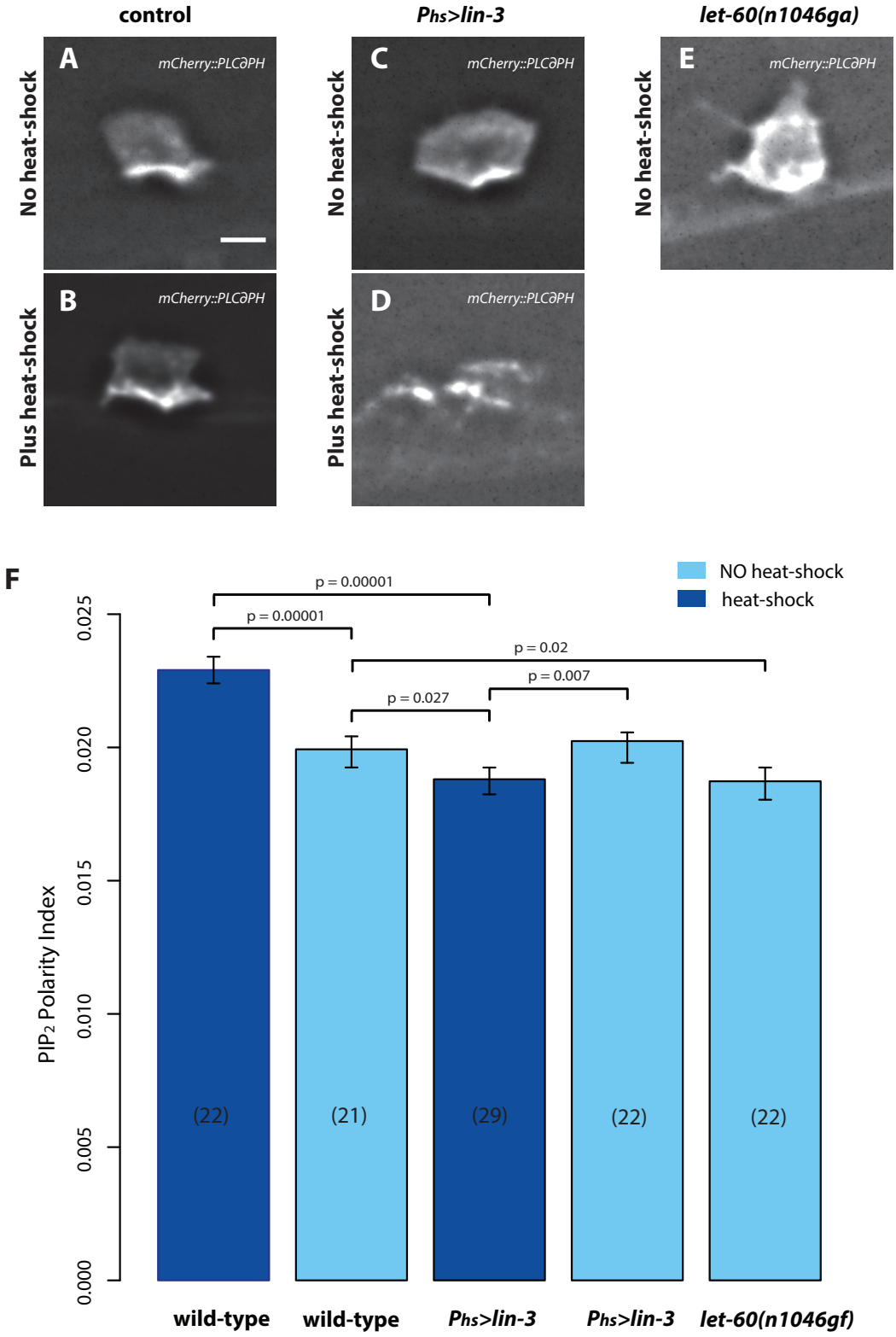


**Figure 3.2.3. Ectopic *lin-3* expression at the mid L3 stage depolarized $PIP_2$ in the AC**

(A-E) Examples of deconvolved, summed-intensity z-projections of ACs at the p6.pxx cell (late L3) stage. All analyzed strains carry the integrated $P_{cdh3}$>*mCherry::PLCδ*$^{PH}$ transgene, which is expressed in the AC and marks the phospholipid $PIP_2$. Scale bar is equal 5 µm.

(A) Control animal without heat-shock treatment and (B) with heat-shock treatment.

(C and D) Examples of a strain with an integrated heat-shock inducible *lin-3* transgene ($P_{hs}$>*lin-3EGF*); (C) without heat-shock treatment and (D) with heat-shock treatment.
(E) Example of a strain carrying a gain of function mutation in the *let-60(n1046)* locus, without heat-shock treatment.
(F) Plot shows the $PIP_2$ AC polarity index of the strains (A-E). The $PIP_2$ polarity index was calculated with a custom written script (Morf et al., 2013) that measures the degree of polarization by the deviation of the relative polarity profile along the dorsal to ventral axis of the AC from its mean intensity. 0 = no deviation from the mean and is a hypothetical total depolarization, 1 = maximum deviation from the mean and is a hypothetical total polarization. Statistical analysis was done by Bootstrapping and the relative p-values are displayed in the plot.

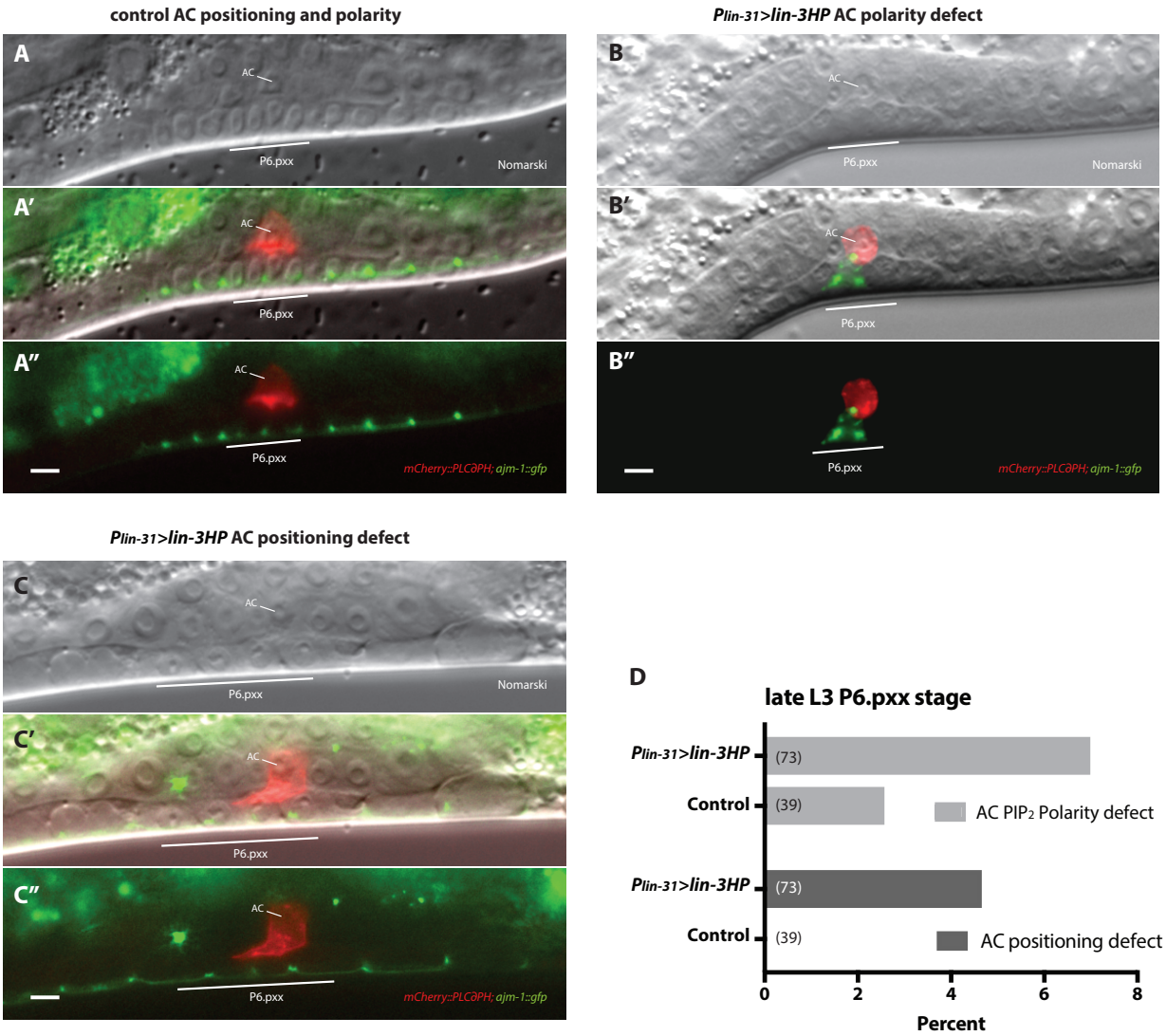


**Figure 3.2.4. VPC specific *lin-3* shRNA expression cause AC positioning and dorsal lumen expansion defects**

(A-C) Example of (A) wild-type AC polarity and AC positioning, (B) AC polarity defect, (C) AC positioning defect in a strain expressing the VPC specific *lin-3* shRNA. The AC as well as the P6.pxx position are labeled with a white line.

(A, B and C) Nomarski, (A'', B''and C'') $P_{cdh3}$>*mCherry::PLCδ*$^{PH}$; *ajm-1::gfp* and (A', B'and C') merged section images, showing the labeled AC and P6.pxx cells. Scale bar equals 5 µm.

(D) Plot shows percent of animals expressing a VPC specific *lin-3* shRNA transgene with a defect in AC polarity or a defect in AC positioning compared to control ($P_{cdh3}$>*mCherry::PLCδ*$^{PH}$; *ajm-1::gfp*) animals. According to Fisher's exact probability test there is no significant difference.

Example of (E-E'') wild-type dorsal lumen expansion and (F-F'') dorsal lumen expansion defect in a strain expressing the VPC specific *lin-3* shRNA, at the mid L4 X-tree larval stage. The dorsal lumen expansion diameter is marked by a double-headed arrow.

(E and F) Nomarski, (E'' and F'') $P_{cdh3}$>*mCherry::PLCδ*$^{PH}$; *ajm-1::gfp* and (E' and F' ) merged section images, showing the marked AC syncytium and the mid L4 X-tree toroidal apical junctions. Scale bar equals 5 µm.

(G) Plot shows percent of animals expressing a VPC specific *lin-3* shRNA transgene with a defect in dorsal lumen expansion, compared to control ($P_{cdh3}$>*mCherry::PLCδ*$^{PH}$; *ajm-1::gfp*) animals. Statistical significance was calculated according to Fisher's exact probability test and p-value is displayed in plot.

(H and I) Example images of the *let-23::gfp* reporter expression pattern in a VPC specific RNAi strain (*rde-1(ne219); rrf-3(pk1426);zhIs038[let-23::gfp, unc-119(+)]; zhEx418[*$P_{lin-31}$*>rde-1;* $P_{myo-2}$*>mCherry]*).

(H and I) Nomarski, (H'' and I'') *let-23::gfp* and (H' and I') merge images of VPC specific RNAi treated animals with (H) empty vector and (I) *let-23* at the P6.pxx mid-late L3 larval stage.

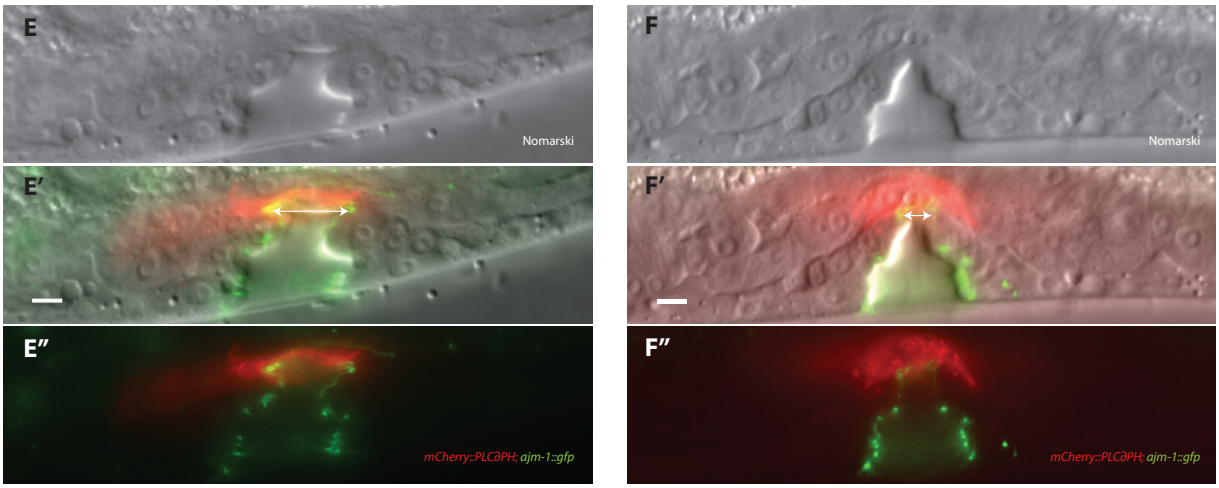


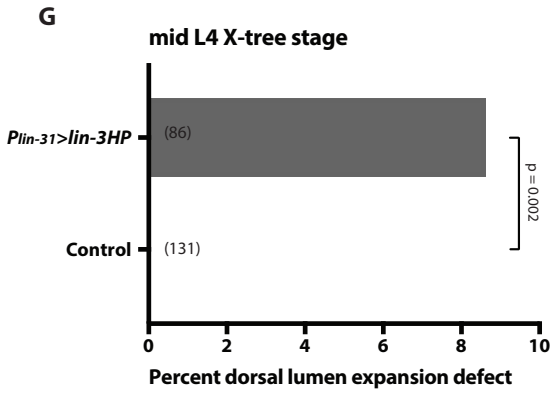


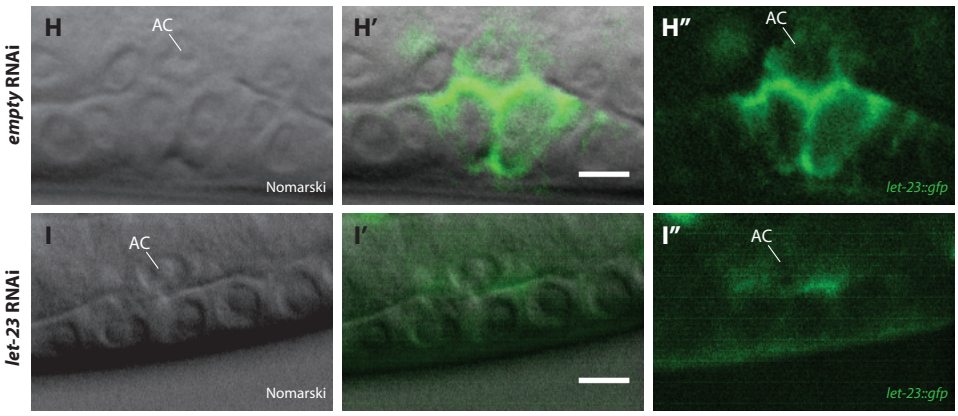


*rde-1(ne219); rrf-3(pk1426)zhIs038[let-23::gfp, unc-119(+)]; zhEx418[Plin-31>rde-1; Pmyo-2>mcherry]*

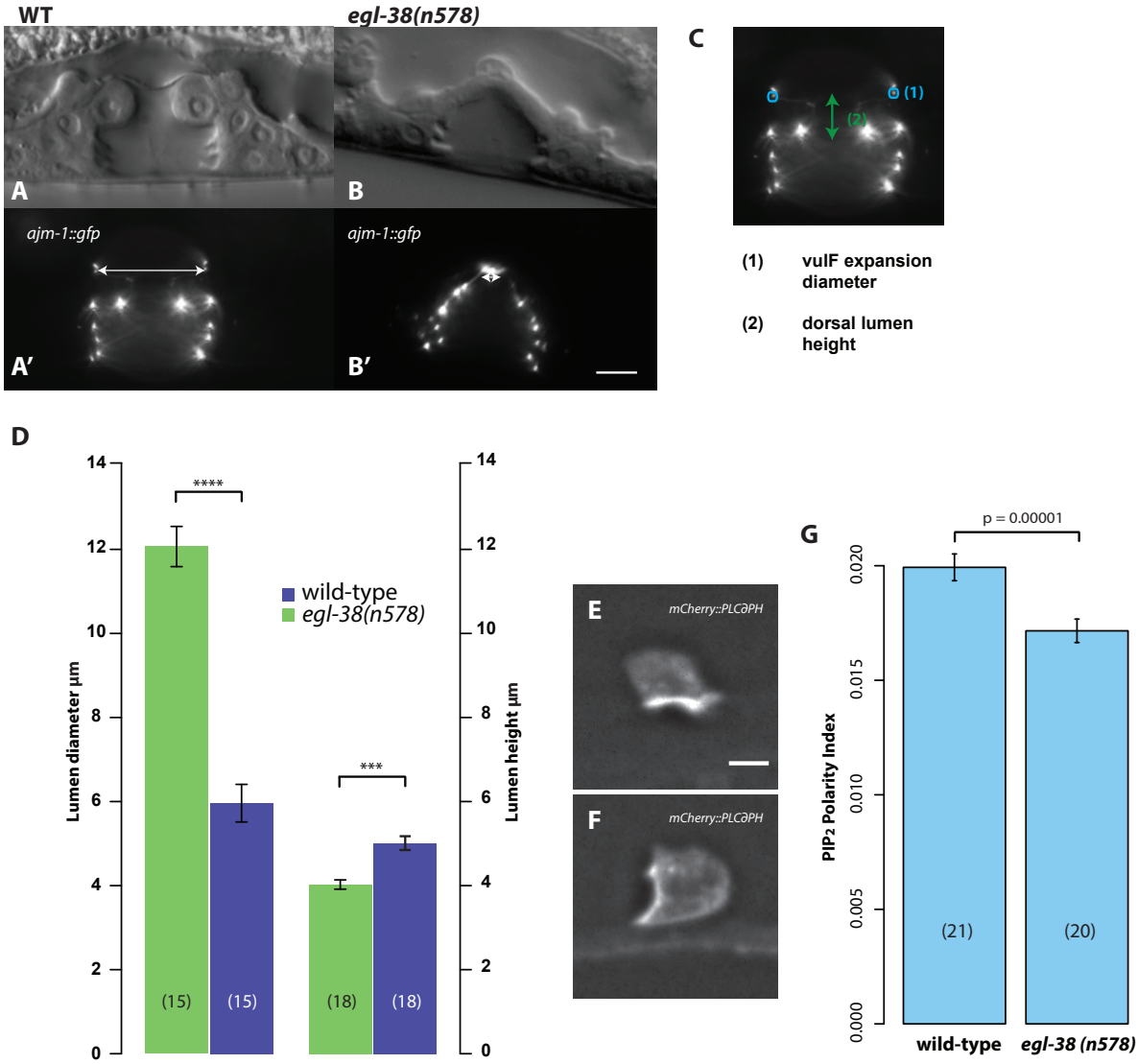


**Figure 3.2.5. *egl-38* mutants have defects in $PIP_2$ polarity and dorsal lumen expansion**
(A) (A and B) Nomarski and (A' and B') fluorescence section images showing the *ajm-1::gfp* reporter that marks the apical junctions between the vulva toroids. Images show a lateral view of the mid L4 X-tree stage vulva of (A and A') wild-tpye and (B and B') *egl38(n578)* mutants. Dorsal lumen expansion diameter is marked by double-headed arrow. Scale bar is equal 5 µm. (C) Demonstration of the measurements taken for quantification: (1) distance between inner AC/vulF toroidal junctions were taken to measure the dorsal lumen expansion, (2) height of vulE and vulF toroids was measured. (D) Plot shows mean values and standard error of the mean of measurements taken as described in "C" for wild-tpye and *egl38(n578)* mutants. P-values were calculated by Bootstrapping; p < 10^-6 = **** and p = 0.00001=***. (E and F) Deconvolved Summed-intensity z-projections of ACs at the mid-lat L3 p6.pxx cell stage expressing the $P_{cdh3}$>*mCherry::PLCδ*$^{PH}$ transgene that marks the Phospholipid $PIP_2$, in (E) wild-type and (F) *egl38(n578)* mutants. Scale bar is equal 5 µm. (G) Plot shows the $PIP_2$ AC polarity index calculated with a custom written script (Morf et al., 2013) that measures the degree of polarization by the deviation of the relative polarity profile along the dorsal to ventral axis of the AC's from the mean . 0 = no deviation from the mean and is a hypothetical total depolarization, 1 = maximum deviation from the mean and is a hypothetical total polarization. Statistical analysis was done by Bootstrapping and p = 0.00001.

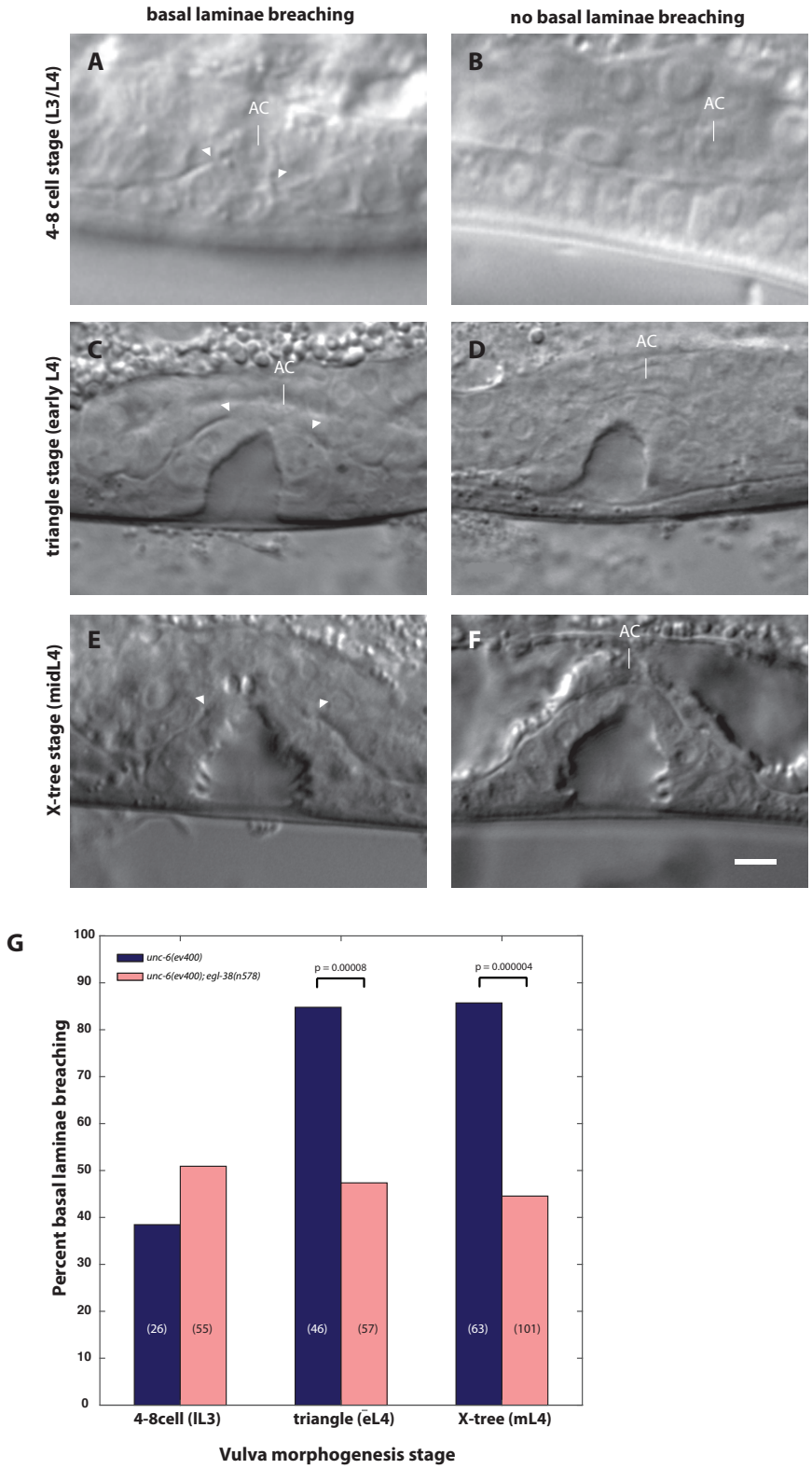


**Figure 3.2.6. The egl-38(n578) allele significantly increases the unc-6(ev400) invasion defect**

(A-F) Nomarski section images showing the lateral view of (A and B) 4-8 cell (L3/L4) stage, (C and D) triangle stage (early L4) and (E and F) X-tree (midL4) stage animals with an *unc-6(ev400)* mutant background. (A, C and E) Demonstrate examples of basal lamina breaching, the breached edges of the basal lamina are indicated by white triangles. (B, D and F) Demonstrate examples, in which no basal lamina breaching occurs. White lines and text point to the AC when present in the section. Scale bar is equal 5 µm. (G) Plot shows percent of animals with basal lamina breaching at indicated developmental stages, of *egl-38(n578);unc-6(ev400)*

double compared to control *unc-6(ev400)* single mutants. Statistical significance was analyzed with Fisher's exact probability test, and p-values are displayed in figure.

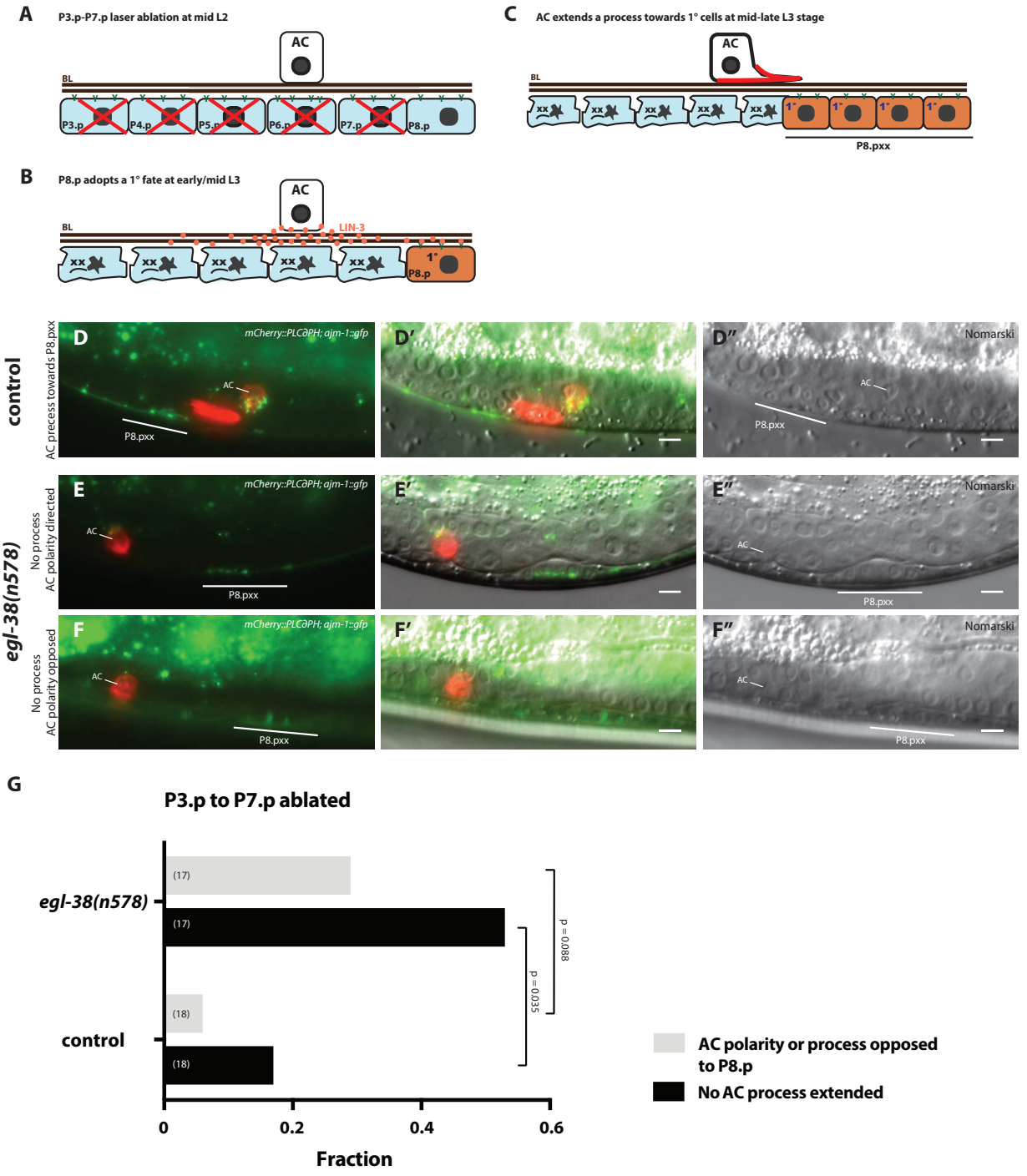


**Figure 3.2.7. The AC 's ability to identify the 1° fated P8.pxx cell descendants after P3-7.p ablation is decreased in *egl-38(n578)* mutants**

(A) Cartoon illustrates P3.p to P7.p laser ablation at the mid L2 stage, (B) P8.p adoption of the 1° vulval cell fate at the early-mid L3 stage and (C) the AC extending a protrusion towards P8.pxx at the mid/late L3stage.

(D-F) Images show examples of AC and P8.pxx (late L3), 12h after P3.p to P7.p ablation occurred. AC and P8.pxx are labeled and indicated by white lines. (D, E and F) Shows expression pattern of summed z-projections of the $P_{cdh3}$>*mCherry::PLCδ$^{PH}$;ajm-1::gfp* reporters (D'', E'' and F'') show Nomarski sections and (D', E' and F') show merged images.

(D, D' and D'') Shows wild-type example of an AC sending a directed protrusion towards the 1° fated P8.pxx cells.

(E, E' and E'') *egl-38(n578)* mutant example of an AC with no Protrusion extended, but polarized towards P8.pxx cells.

(F, F' and F'') *egl-38(n578)* mutant example of an AC with no Protrusion extended, and AC polarity is directed opposite to the P8.pxx cells. Scale bar =5 μm.
(G) Plot shows fraction of ablated animals, with ACs that had no process extended towards P8.pxx and ACs that had processes or polarity directed opposite to P8.pxx, in wild-type and *egl-38(n578)* mutants. Statistical significance was analyzed with Fisher's exact probability test, and p-values are displayed in figure.

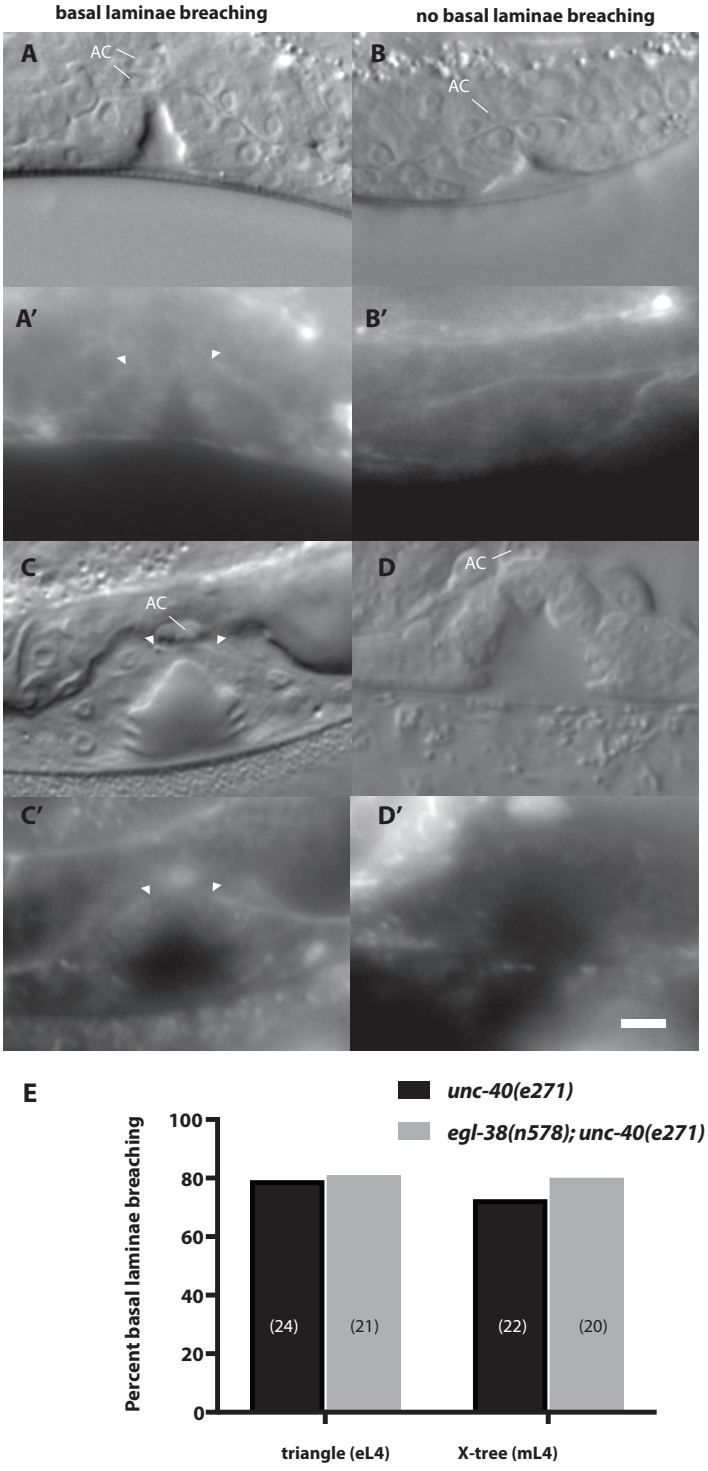


**Figure 3.2.S1. The *egl-38(n578)* allele does not enhance the *unc-40(e271)* induced basal lamina breaching defect**
(A-D) Nomarski and (A'-D') MitoTracker staining example images of (A, A', C and C') basal lamina breaching and (B, B', D and D') no basal lamina breaching in the *unc-40(e271)* mutant background. Sections show lateral view of (A, A', B and B') early L4 triangle stage vulvas and (C, C', D and D') mid L4 X-tree stage vulvas. The edge of the breached basal lamina is indicated by white triangles. The AC nucleus is labeled when present in the image. Scale bar equals 5 µm. (E) Plot shows percent of animals with basal lamina breaching at indicated developmental stage, for *egl-38(ne578); unc-40(e271)* double compared to control *unc-40(e271)* single mutants. According to Fisher's exact probability test there is no significant difference in basal lamina breaching between double and single mutants at any stage.

### 3.2.4 Discussion

Our results present new in-vivo evidence linking localized EGF signaling to cell polarity, basal lamina breaching and morphogenesis. The AC invasion model supports previous findings, in which EGF gradients directed cell motility (Bailly et al., 2000; Goswami et al., 2005), and provides an ideal tool to investigate downstream effectors and parallel pathways of EGF gradient directed cell polarity and protrusion formation in an in-vivo context. Regarding *C. elegans* vulval morphogenesis, we show that EGL-38-dependent LIN-3 EGF expression from the vulF cells plays a role earlier than previously reported (Chang et al., 1999; Rajakumar and Chamberlin, 2007). The evidence we provide, in which deregulation of vulva specific *lin-3* expression affects AC polarity and enhances defects in basal lamina breaching in *unc-6* mutants, suggests that vulF induced *lin-3* expression functions as a novel AC polarity regulator (Ziel et al., 2008).

**AC depolarization causes defects in dorsal vulval lumen expansion**

LIN-3 EGF expression form the vulF cells has been shown to be dependent on the Pax 2/5/8 transcription factor EGL-38 (Chang et al., 1999; Rajakumar and Chamberlin, 2007; Ririe et al., 2008), and is detectable by fluorescent reporter analysis from the early L4 stage on (Hwang, 2004). Genetic evidence of EGL-38-mediated *lin-3* expression indicates that it has a function earlier in development during vulval induction at the early-mid L3 stage (Dutt et al., 2004). Our results regarding dorsal lumen expansion defects in VPC specific *lin-3* RNAi treated animals (Fig. 3.2.1, F) as well as *egl-38(n578)* mutants (Fig. 3.2.5, G), strongly suggest that vulF specific *lin-3* expression regulates dorsal lumen expansion during vulval morphogenesis. We narrowed the susceptible period, during which the AC initiates dorsal vulval lumen expansion (Estes and Hanna-Rose, 2009), to the last round of vulval cell division at the L3/L4 larval stage (Fig. 3.2.2, E). A recent publication found that the AC extends circumferential processes around the vulF lateral membrane, which is required for lateral vulF constriction, and wild-type vulval lumen morphogenesis, at the coinsiding developmental stage (Yang et al., 2017). The only known LIN-3 EGF receptor in *C. elegans* is LET-23, and it is expressed in the AC at the submissive developmental stage, in which the AC mediates dorsal lumen expansion (Fig. 2.3.4, A and B). So far, it has never been reported that LET-23 is expressed in the AC, and likewise no putative function of such has been described. We thus conclude that LIN-3 expressed from the vulF cells signals to the AC, likely by binding its receptor LET-23 EGFR, which promotes wild-type dorsal lumen expansion. The occurrence of defects in dorsal vulval lumen expansion have previously been shown in *unc-6* mutants in spite of successful basal laminea breaching (Singh and Harris, 2005). Since UNC-6 is a prominent regulator of AC polarity (Ziel et al., 2008), it stands to argue that directed AC polarity is a requisite for dorsal vulval lumen expansion.

**LIN-3 expressed from the vulF cells likely regulates AC polarity in parallel to UNC-6, but at the level of UNC-40**

There have been previous reports that systemic *lin-3* RNAi or vulvaless *lin-3* mutant alleles cause defects in AC polarity and basal lamina breaching (Lohmer et al., 2016; Ziel et al., 2008). But since vulval cell fate induction is dependent on LIN-3 signaling, the fact was explained by a loss in expression of the unknown 1° vulval cue. Our results show that ectopic LIN-3

expression through heat-shock induction (Fig. 2.3.3, F) as well as vulva tissue specific *lin-3* depletion by VPC specific *lin-3* shRNA expression (Fig. 2.3.4, H) or from loss in EGF-38 function (Fig. 3.2.5, G) all produced defects in AC polarity. This evidence clearly indicates that vulF specific LIN-3 expression is a regulator of
PtdIns(4,5)$P_2$ ($PIP_2$) polarity in the AC. UNC-6 Netrin is a directional AC polarity cue, conveying ventral to dorsal polarity. Loss in UNC-6 function conveys a highly penetrant AC polarity defect, and so far it is the only known secreted cue that directs AC polarity (Ziel et al., 2008). Previous evidence has shown that there must be other secreted cues from the 1° vulval cell descendants, which direct AC polarity and basal lamina breaching (Ziel et al., 2008), but so far these cues have not been identified.
The initial basal lamina breach during AC cell invasion is regulated by invadopodia, F-actin-rich membrane associated cellular protrusions, which are dynamically recycled through the endolysosome (Hagedorn et al., 2014). The UNC-40 receptor is localized at the site of breaching, and directs the formation of a focused larger protrusion, as well as inhibiting further random invadopodia formation (Hagedorn et al., 2013). In the absence of this bundling force, basal lamina breaching driven by invadopodia formation sill occurs, but it is delayed significantly (Wang et al., 2014).
We found that the basal lamina breaching defect in *unc-6* mutants is significantly enhanced by the *egl-38(n578)* allele (Fig. 3.2.6, G), however only from the early L4 triangle stage on, not earlier. These findings indicate that vulF specific LIN-3 possibly acts in parallel to the UNC-6 Netrin cue, for instance as a regulator of invadopodia formation. Interestingly, the *egl-38(n578)* allele does not enhance the *unc-40(lf)* mediated basal lamina breaching defect at any analyzed stage (Fig. 2.3.S1). These results suggest that EGL-38 is involved in AC dependent basal lamina breaching in parallel to UNC-6, but in the same pathway or on the level of the UNC-40 receptor. In terms of polarization it makes a difference whether a receptor is mislocalized or not present within a cell. Actin localization in the AC of *unc-40(lf)* mutants is similar to wild-type and significantly different from *unc-6(lf)* mutants (Wang et al., 2014). When no UNC-6 directing signal is present, the UNC-40 receptor subcellular localization in the AC is random, but shows a dynamic reassociation pattern over time. UNC-40 tends to aggregates in clusters, which recruit $PIP_2$ and F-actin to these sites. These cluster are continuously resolved and counteracted by MADD-2 signaling, a negative regulator of AC invasion (Morf et al., 2013; Wang et al., 2014). UNC-40 localization is further regulated by the integrin heterodimer INA-1/PAT-3 (human integrin homologs α6/β1), which can likewise organize F-actin polarity. Integrins present a possible link between UNC-40 and LIN-3 signaling. It has been found that the integrin heterodimer INA-1/PAT-3 targets the netrin receptor UNC-40 to the AC plasma membrane during AC invasion (Hagedorn et al., 2009). There exists evidence showing that EGF induced cell migration is dependent of integrin signaling (Azimifar et al., 2012; Boscher and Nabi, 2013), and in carcinoma cells EGF Stimulation has been shown to regulate cell migration and chemotaxis by recruiting α6β4 integrin localization to the lamellipodia. The authors further showed that EGFR co-localizeed with α6β4 integrins and promoted their phosphorylation through Protein Kinase C (PKC) activation (Rabinovitz et al., 1999). Other reports showed that locally attached EGF ligands recruited EGFR, RAS and phosphor-ERK to the site of the bound EGF ligand, in NIH3T3 cells, and that β1 integrins were enriched in these clusters likewise. Anchored EGF ligand induced EGFR signaling further recruited F-actin in a phosphoinositide (PIP) dependent manner,

which stabilized the formed complexes (Holowka and Baird, 2017; Singhai et al., 2014). Thus, previous findings support the possibility that LIN-3 might direct AC polarity and protrusion formation or migration during vulval morphogenesis, by directing integrin localization. Loss of integrin function does not essentially interfere with $PIP_2$ polarity, however depolarization of integrin likewise depolarizes $PIP_2$ (Hagedorn et al., 2009). The $PIP_2$ depolarization is dependent on UNC-40 and integrins can recruit UNC-40. Therefore, we propose that localized LIN-3 signaling from the vulF cells, could recruit the integrin hetero-dimer INA-1/PAT-3, to the AC membrane facing the vulF cells, which further promotes UNC-40 and $PIP_2$ accumulation at the site. This fits to our results, since ectopic EGF expression as well as constitutively active RAS causes $PIP_2$ polarity defects in the AC (Fig. 2.3.3, F).
Our results also show that in a situation, in which the AC is displaced relative to the 1° fated vulval cell descendants, the *egl-38(n578)* allele significantly impairs the AC's ability to form a protrusion towards the vulval cells (Fig. 2.3.7, G). UNC6/UNC40 netrin signaling is required for the AC to form a directed protrusion, however the unknown vulval cue or cues directs the process towards the 1° vulval cell descendants (Ziel et al., 2008). Integrin signaling via the INA-1/PAT-3 heterodimer directs the UNC-40 receptor to the invasive membrane, and is likewise required for the AC to extend a protrusion towards the mislocalized 1° fated vulval cells (Hagedorn et al., 2009). This indicates that vulF specific LIN-3 signaling might control the subcellular integrin localization in the AC upstream of UNC-40 to direct AC cell polarity. This polarization is likely required for the AC to form protrusions around or between the vulF cells, to regulate dorsal lumen expansion (Yang et al., 2017).

**Possible model**

The $P_{cdh\text{-}3}$*>PLCδ*$^{PH}$*::mCherry* transgene causes a mild basal lamina breaching defect (Ziel et al., 2008). We argue that this is caused by interference with Phospholipase C (PLC) signaling, by ectopic expression of its $PIP_2$ specific PH domain, fused to mCHerry, causing a sequestering or mild dominant negative effect, since it associates with $PIP_2$, but has no catalytic ability. Systemic *lin-3* RNAi has been shown to cause defects in $PIP_2$ as well as F-actin polarity in the AC (Lohmer et al., 2016). PLC-$\gamma$ is a direct downstream target of EGFR signaling that interacts via its SH2 domains with the tyrosine kinase (Meisenhelder et al., 1989). PLCs function as phospholipases and hydrolyze $PIP_2$, producing the second messengers IP3 and DAG (Banno et al., 1992; Goldschmidt-Clermont et al., 1991). The membrane phospholipid phosphatidylinositol (4,5)-bisphosphate ($PIP_2$) is a key regulator of actin cytoskeleton dynamics and regulates proteins that promote actin cytoskeleton anchoring to the plasma membrane (Mao and Yin, 2007; Sechi and Wehland, 2000). Cofilin is an F-actin depolymerizing factor (ADF), and inhibits F-actin repolymerization, and is important in the regulation of actin dynamics (Fechheimer and Zigmond, 1993). $PIP_2$ and cofilin have been shown to bind at the same site (Yonezawa et al., 1990), and $PIP_2$ inhibits actin binding to cofilin (Yonezawa et al., 1991). It has been shown in rat carcinoma cell lines (MTLn3) that localized EGF signaling induces PLC mediated $PIP_2$ hydrolysis, which in turn causes local cofilin release from the plasma membrane, leading to changes in actin polymerization and protrusion formation (van Rheenen et al., 2007). These results provide a putative mechanism for EGF directed cell migration (Kedrin et al., 2007; Wyckoff et al., 2004). UNC-60, the *C. elegans* cofilin orthologue, is expressed in the AC and enriched at the invasive membrane dependent on the integrin INA-1/PAT-3. Moreover, UNC-60 is required for

AC invasion (Hagedorn et al., 2014). To form a model from our results in the context of current literature, we speculate that localized LIN-3 EGF signaling, possibly in a membrane-bound from (Hill and Sternberg, 1992), could indirectly recruit the integrin heterodimer INA-1/PAT-3 to the site of invasion (Singhai et al., 2014), as well as reorganize actin polymerization, by PLC mediated $PIP_2$ hydrolysis and cofilin UNC-60 release (van Rheenen et al., 2007), thus regulating directed cellular protrusion formation. LET-23 activates the *C. elegans* PLC-γ homolog PLC-3, which has so far been implicated in ovulation in the hermaphrodite spermatheca (Clandinin et al., 1998; Kariya et al., 2004), and for neuronal functions regulating behavior (Van Buskirk and Sternberg, 2007). A role of PLC-3 mediated LET-23 signaling has so far not been described for vulval morphogenesis.
LET-60(gf) likewise caused $PIP_2$ depolarization in the AC (Fig. 3.2.3). In mammalian cells, localized PI3K activity and $PiP_3$ production has been shown to control cell polarity and migration in response to chemotaxis (Sadhu et al., 2003; Sasaki and Firtel, 2006; Sasaki et al., 2007). Thus, locally activated LET-60 RAS could regulate PI3K activation and subsequently the ACs $PIP_2/PIP_3$ membrane composition and AC polarity.

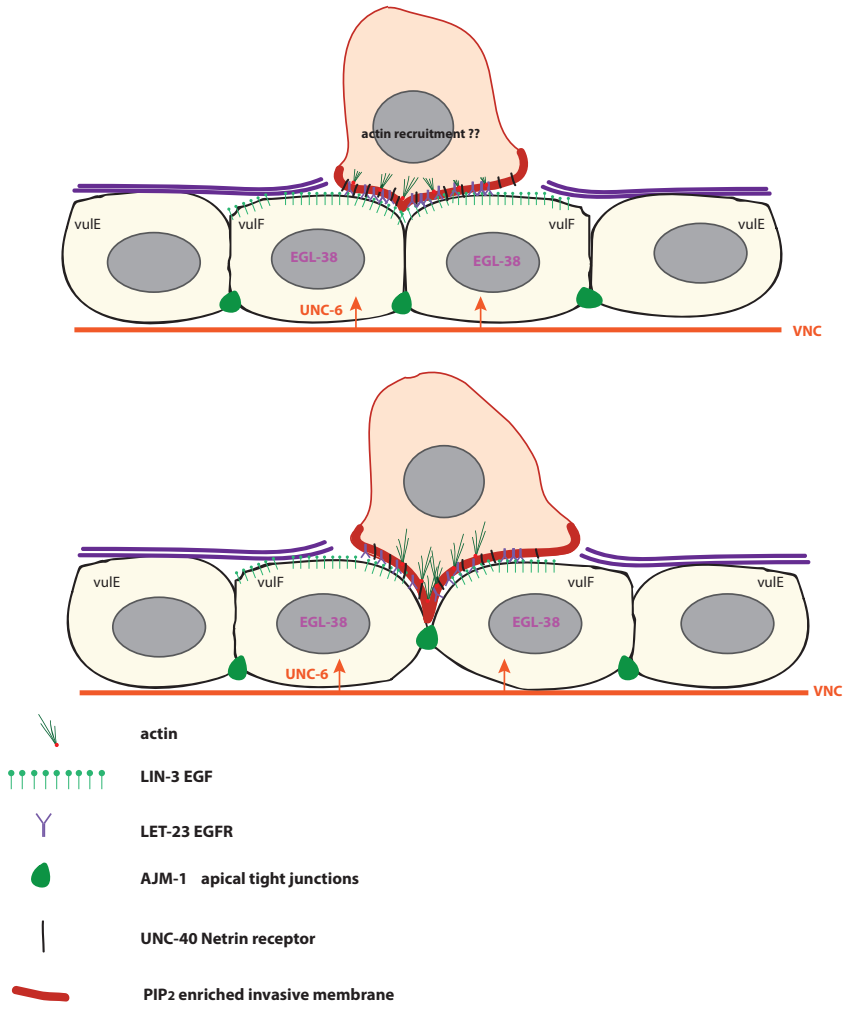


**Figure 3.2.8. Illustration for LIN-3 directed AC protrusion formation**

## 3.2.5 Materials and Methods

**General methods and strains used**

Unless specified otherwise, *C. elegans* strains were maintained at 20 °C on NGM (Nematode-Growth Medium) plates applying standard methods (Brenner, 1974).
The *C. elegans* Bristol variant N2, was used as wild-type (WT) reference and strains used for the experiments and generated crosses were derivatives of N2.
The following alleles and transgenes were used:
LG II: *qyIs23[$P_{cdh-3}$>PLC∂$^{PH}$::mCherry, unc-119(+)]* (Ziel et al., 2008), *rrf-3(pk1426)* (Simmer et al., 2002)
LG IV: *egl-38(n578)* (Zhang et al., 2005), *let-60(n1046)* (Han and Sternberg, 1990), *zhIs061[$P_{cdh-3}$>let-23(dom-rf)::gfp; $P_{myo-2}$>mcherry], zhIs038[let-23::gfp, unc-119(+)]* (Haag et al., 2014)
LG V: *rde-1(ne219)* (Tabara et al., 1999), *swIs79[ajm-1::gfp, seamcell::gfp, unc-119(+)]* (Mohler et al., 2002)
LG X: *unc-6(ev400)* (Hedgecock et al., 1990), *syIs11[$P_{hs}$>lin-3EGF]* (Katz et al., 1995)
Extra chromosomal arrays and integrated transgenes:
*zhEx418[$P_{lin-31}$>rde-1; $P_{myo-2}$>mcherry], zhEx518[$P_{lin-31}$>lin-3hairpin; Pmyo-2>mcherry]*

**Microscopy and image analysis**

Most images were acquired using an Olympus BX61 wide-field microscope equipped with a Cr.E.S.T. X-light spinning disc confocal system, a Lumencor SPECTRA X light engine and a Hamamatsu Orca CCD camera, controlled by the Visitron VisiView 2.1.1 software.
Other images were made using a Leica DMRA wide-field microscope with a Hamamatsu ORCA-ER camera controlled by Openlab 5.0.2.
Images were processed using Huygens Deconvolution (SVI) for z-stacks where indicated, Fiji (ImageJ (NIH)) and Adobe Photoshop.

**Cell ablations**

The AC was ablated between the late L3 up to the early L4 larval stages, as specified in results. The VPC ablations of P3.p to P7.p were performed at the late L2 larval stage. The worms were mounted on 3-4% agarose pads and ablated using a Leica DMR wide-field microscope equipped with MicroPoint Laser system (Photonic Instruments) as described in (Farooqui et al., 2012).

**AC polarity analysis**

General AC polarity quantification, referring to the *qyIs23*[$P_{cdh-3}$*>mCherry::PH; unc-119(+)*] reporter expression pattern was done by using a custom written, semi-automated scripts in ImageJ and R applied to deconvolved wide-field z-stacks with a Z-spacing of 0.13 µm (Morf et al., 2013). (Image deconvolution was performed with the Huygens software provided by; the Center for Microscopy and Image Analysis, University of Zurich). For AC polarity analysis in the *zhEx518*[$P_{lin-31}$*>lin-3i; $P_{myo-2}$>mcherry* ] strain, the AC was scored as depolarized upon phenotypic characteristics of the $PIP_2$ expression pattern.

**AC positioning scoring**
The AC was scored as mispositioned when at least half of the AC nucleaus was centered over one of the vulE cells at the P6.pxx cell stage.

**Basal lamina breaching scoring**
The basal lamina breaching by the AC was scored in Nomarski optics at the indicated larval and Pn.p cell-divisional stage. The scoring was determined form the P6.pxx stage on, after the 1° fated vulF cells start apical constriction and invagination. This allowed a reliable scoring in the *unc-6* mutant background. For the tissue specific RNAi the basal lamina breaching was scored with the *qyIs10[lam-1::gfp]* marker according to Hagedorn et al. 2009 (Hagedorn et al., 2009).

**Statistical analysis**
Statistical analyses for the general AC quantification were performed by bootstrapping using a custom written script for R (Morf et al., 2013). Chi-Square, Fisher's exact test or t-tests were performed in excel or R.

**PCR**
PCR products used for genotyping of strains or RNAi clones, by fragment length analysis or by sequencing analysis, were performed according to the Taq-PCR protocol of ©2008 Invitrogen Corporation or using a PCR Protocol for LongAmp® Taq DNA Polymerase (M0323). For all PCR reactions performed, the annealing temperature was set at 58° or according to empirically tested optimum. All Fusion-PCR reactions were performed with the Phusion high-fidelity DNA polymerase according to the protocol of Finnzymes (Espoo, Finland). The DNA fragments generated by the PCR reactions were visualized using agarose gel electrophoresis and ethidium bromide staining.
The annealing temperatures were estimated with the Finnzyme Tm calculator (https://www.finnzymes.fi/tm_determination.html).

**Heat shock treatment**
The worms grown on 60mm diameter NGM plates and sealed with parafilm. The sealed plates were submerged in a 33°C warm water bath and incubated for 30min. Then they were recovered, unsealed and left to recover at 20°C.

**Worm bleaching and staging**
Two to four NGM plates, confluent with not starved adult worms were transferred with $H_2O$ to a 15 ml falcon tube. The falcon tube was centrifuged for 1 minute at 1'100 rpm and the supernatant was discarded, leaving 1ml solution and worms reamining. After adding 200 µl of 10-15% sodium hypochloride and 100 µm 5M NaOH, the worms were vortexed until no floating bodies were detected. The bleach was attenuated to 14 ml with $H_2O$ and washed four times with $H_2O$. The eggs were left to hatch overnight on a shaker at RT and plated on NGM plates grown with OP50 e. Coli.

**Mitotracker staining**
The basement membrane was stained by MitoTracker Red CMXRos, from Thermo Fisher, ac-

cording to the manufacturers protocol. The worms were incubated in a solution of 10 µM MitoTracker Red in M9 buffer (Brenner, 1974) at RT for 2 hr, under exclusion of light sources. The worms were then allowed to recover for 30 min on NGM agar plates.

**Microinjection**

Microinjection for the generation of extrachromosomal lines was performed as described in (Mello et al., 1991) using purified plasmid or PCR DNA at a concentration of 50 ng/µl or 30 ng/µl respectively. The transformation markers pCFJ90 ($P_{myo-2}$>*mCherry*) and pTG96 ($P_{sur-5}$>*gfp*) were used at a concentration of 2.5 ng/µl (Frøkjær-Jensen et al., 2008) or 30 ng/µl respectively, and pBluescript-KS plasmid was used to achieve a final DNA concentration of 150 ng/µl in a total volume of 15µl.

For CRISPR/Cas9 or Mosci injections the injection mix was prepared as described in Arribere et al 2014, Dickinson et al., 2015 and Frokajer et al 2008 respectively (Dickinson et al., 2015; Frøkjær-Jensen et al., 2008).

**RNAi**

RNA interference (RNAi) was performed using the feeding method as described (Kamath et al., 2003). P0 worms were synchronized at the L1 stage, transferred to NGM plates containing 3 mM IPTG and 50 ng/ml ampicillin seeded with the indicated RNAi bacteria and allowed to grow for 5-7 days at 20°C, after which the F1 progeny was analyzed.

The used clones (*lin-3, egl-38, pas-6, empty*) were taken from the Ahringer library (Kamath and Ahringer, 2003) the *let-23* clone was cloned from genomic DNA.

**RNAi clone construction**

pLM16 was transformed into the HT115(DE3) RNAi strain, an RNase III-deficient *E. coli* strain with IPTG-inducible T7 polymerase activity.

**Generated alleles and inserted transgenes and Extrachromosomal arrays**

*zhEx418* $Pl_{in-31}$*::rde-1;* $P_{myo-2}$*>mcherry*

The extrachromosomal array was generated by fusion of two PCR fragments. Fusion templates were 2.3kb of the *lin-31* promoter, amplified from PB253 (Tan et al., 1998) with OPG309(ACGAGGAGCGGTGGTGTGGCCAGC) and OMMO86(GCACAGGGAGAAAGAGCATG) and 3.9 kb of the *rde-1* gene amplified from genomic DNA with OLM1 (atgtcctcgaattttcccgaattggaaaaagg) and OLM2 (ggcaattgtttcagcatgaaacaagc), making a fusion product of 6.2 kb. The purified fusion PCR was injected at 20 ng/µl , ($P_{myo-2}$>*mcherry*) 8 ng/µl and filled up with bluescript DNA to a total of 150 ng/µl. The extrachromosomal array was later spontaneously integrated.

*zhEx518* $P_{lin-31}$*>lin-3i;* $P_{myo-2}$*>mcherry*

The array was generated by injecting the *lin-3::hairpin* pLM12,13 and 15 at each 25 ng/µl and the plasmid *Phs>cas-9* pMB67 (Addgene plasmid # 47947) at 50 ng/µl as well as pCFJ90 ($P_{myo-2}$>*mcherry*) at 2.5 ng/µl.

## Plasmids

pLM16 *let-23* genomic DNA in L4440
The RNAi clone plasmid was generated by amplifying 2kb of genomic *let-23* DNA OLM36 (TTTTAGATCTgctatggaggatgtaagcag), and OIN129 (catttctcggattctttccg). The PCR product as well as the insertion vector L4440 were digested with EcoRI and BglII and the PCR was ligated into the L4440 (a gift from Andrew Fire (Addgene plasmid # 1654)).

## 3.2.6 References


**Azimifar, S. B., Böttcher, R. T., Zanivan, S., Grashoff, C., Krüger, M., Legate, K. R., Mann, M. and Fässler, R.** (2012). Induction of membrane circular dorsal ruffles requires co-signalling of integrin-ILK-complex and EGF receptor. *J. Cell. Sci.* **125**, 435–448.

**Bailly, M., Wyckoff, J., Bouzahzah, B., Hammerman, R., Sylvestre, V., Cammer, M., Pestell, R. and Segall, J. E.** (2000). Epidermal growth factor receptor distribution during chemotactic responses. *Mol. Biol. Cell* **11**, 3873–3883.

**Banno, Y., Nakashima, T., Kumada, T., Ebisawa, K., Nonomura, Y. and Nozawa, Y.** (1992). Effects of gelsolin on human platelet cytosolic phosphoinositide-phospholipase C isozymes. *J. Biol. Chem.* **267**, 6488–6494.

**Barrandon, Y. and Green, H.** (1987). Cell migration is essential for sustained growth of keratinocyte colonies: the roles of transforming growth factor-alpha and epidermal growth factor. *Cell* **50**, 1131–1137.

**Blay, J. and Brown, K. D.** (1985). Epidermal growth factor promotes the chemotactic migration of cultured rat intestinal epithelial cells. *J. Cell. Physiol.* **124**, 107–112.

**Boscher, C. and Nabi, I. R.** (2013). Galectin-3- and phospho-caveolin-1-dependent outside-in integrin signaling mediates the EGF motogenic response in mammary cancer cells. *Mol. Biol. Cell* **24**, 2134–2145.

**Brenner, S.** (1974). The genetics of Caenorhabditis elegans. *Genetics* **77**, 71–94.

**Chang, C., Newman, A. P. and Sternberg, P. W.** (1999). Reciprocal EGF signaling back to the uterus from the induced C. elegans vulva coordinates morphogenesis of epithelia. *Current Biology* **9**, 237–246.

**Clandinin, T. R., DeModena, J. A. and Sternberg, P. W.** (1998). Inositol trisphosphate mediates a RAS-independent response to LET-23 receptor tyrosine kinase activation in C. elegans. *Cell* **92**, 523–533.

**Dickinson, D. J., Pani, A. M., Heppert, J. K., Higgins, C. D. and Goldstein, B.** (2015). Streamlined Genome Engineering with a Self-Excising Drug Selection Cassette. *Genetics* **200**, 1035–1049.

**Duchek, P. and Rørth, P.** (2001). Guidance of cell migration by EGF receptor signaling during Drosophila oogenesis. *Science* **291**, 131–133.

**Dutt, A., Canevascini, S., Froehli-Hoier, E. and Hajnal, A.** (2004). EGF Signal Propagation during C. elegans Vulval Development Mediated by ROM-1 Rhomboid. *PLoS Biol* **2**, e334–16.

**Estes, K. A. and Hanna-Rose, W.** (2009). The anchor cell initiates dorsal lumen formation during C. elegans vulval tubulogenesis. *Developmental Biology* **328**, 297–304.

**Farooqui, S., Pellegrino, M. W., Rimann, I., Morf, M. K., Mereu, L., Fröhli, E. and Hajnal, A.** (2012). Coordinated Lumen Contraction and Expansion during Vulval Tube Morphogenesis in Caenorhabditis elegans. *Developmental Cell* **23**, 494–506.

**Fechheimer, M. and Zigmond, S. H.** (1993). Focusing on unpolymerized actin. *J Cell Biol* **123**, 1–5.

**Frøkjær-Jensen, C., Davis, M. W., Hopkins, C. E., Newman, B. J., Thummel, J. M., Olesen, S.-P., Grunnet, M. and Jorgensen, E. M.** (2008). Single-copy insertion of transgenes in Caenorhabditis elegans. *Nat. Genet.* **40**, 1375–1383.

**Goldschmidt-Clermont, P. J., Kim, J. W., Machesky, L. M., Rhee, S. G. and Pollard, T. D.** (1991). Regulation of phospholipase C-gamma 1 by profilin and tyrosine phosphorylation. *Science* **251**, 1231–1233.

**Goswami, S., Sahai, E., Wyckoff, J. B., Cammer, M., Cox, D., Pixley, F. J., Stanley, E. R., Segall, J. E. and Condeelis, J. S.** (2005). Macrophages promote the invasion of breast carcinoma cells via a colony-stimulating factor-1/epidermal growth factor paracrine loop. *Cancer Res.* **65**, 5278–5283.

**Greenwald, I.** (2005). LIN-12/Notch signaling in C. elegans. *WormBook* 1–16.

**Grivennikov, S. I., Greten, F. R. and Karin, M.** (2010). Immunity, inflammation, and cancer. *Cell* **140**, 883–899.

**Gupta, B. P., Hanna-Rose, W. and Sternberg, P. W.** (2012). Morphogenesis of the vulva and the vulval-uterine connection. *WormBook* 1–20.

**Haag, A., Gutierrez, P., Bühler, A., Walser, M., Yang, Q., Langouët, M., Kradolfer, D., Fröhli, E., Herrmann, C. J., Hajnal, A., et al.** (2014). An in vivo EGF receptor localization screen in C. elegans Identifies the Ezrin homolog ERM-1 as a temporal regulator of signaling. *PLoS Genet* **10**, e1004341.

**Hagedorn, E. J., Kelley, L. C., Naegeli, K. M., Wang, Z., Chi, Q. and Sherwood, D. R.** (2014). ADF/cofilin promotes invadopodial membrane recycling during cell invasion in vivo. *J Cell Biol* **204**, 1209–1218.

**Hagedorn, E. J., Yashiro, H., Ziel, J. W., Ihara, S., Wang, Z. and Sherwood, D. R.** (2009). Integrin Acts Upstream of Netrin Signaling to Regulate Formation of the Anchor Cell•s Invasive Membrane in C. elegans. *Developmental Cell* **17**, 187–198.

**Hagedorn, E. J., Ziel, J. W., Morrissey, M. A., Linden, L. M., Wang, Z., Chi, Q., Johnson, S. A. and Sherwood, D. R.** (2013). The netrin receptor DCC focuses invadopodia-driven basement membrane transmigration in vivo. *J Cell Biol* **201**, 903–913.

**Han, M. and Sternberg, P. W.** (1990). let-60, a gene that specifies cell fates during C. elegans vulval induction, encodes a ras protein. *Cell* **63**, 921–931.

**Hedgecock, E. M., Culotti, J. G. and Hall, D. H.** (1990). The unc-5, unc-6, and unc-40 genes guide circumferential migrations of pioneer axons and mesodermal cells on the epidermis in C. elegans. *Neuron* **4**, 61–85.

**Hill, R. J. and Sternberg, P. W.** (1992). The gene lin-3 encodes an inductive signal for vulval development in C. elegans. *Nature* **358**, 470–476.

**Holowka, D. and Baird, B.** (2017). Mechanisms of epidermal growth factor receptor signaling as characterized by patterned ligand activation and mutational analysis. *Biochim. Biophys. Acta* **1859**, 1430–1435.

**Hwang, B. J.** (2004). A cell-specific enhancer that specifies lin-3 expression in the C. elegans anchor cell for vulval development. *Development* **131**, 143–151.

**Inoue, T., Oz, H. S., Wiland, D., Gharib, S., Deshpande, R., Hill, R. J., Katz, W. S. and Sternberg, P. W.** (2004). C. elegans LIN-18 is a Ryk ortholog and functions in parallel to LIN-17/Frizzled in Wnt signaling. *Cell* **118**, 795–806.

**Kamath, R. S. and Ahringer, J.** (2003). Genome-wide RNAi screening in Caenorhabditis elegans. *Methods* **30**, 313–321.

**Kariya, K.-I., Bui, Y. K., Gao, X., Sternberg, P. W. and Kataoka, T.** (2004). Phospholipase Cepsilon regulates ovulation in Caenorhabditis elegans. *Developmental Biology* **274**, 201–210.

**Katz, W. S., Hill, R. J., Clandinin, T. R. and Sternberg, P. W.** (1995). Different levels of the C. elegans growth factor LIN-3 promote distinct vulval precursor fates. *Cell* **82**, 297–307.

**Kedrin, D., van Rheenen, J., Hernandez, L., Condeelis, J. and Segall, J. E.** (2007). Cell motility and cytoskeletal regulation in invasion and metastasis. *J Mammary Gland Biol Neoplasia* **12**, 143–152.

**Kim, B. J., Hannanta-anan, P., Chau, M., Kim, Y. S., Swartz, M. A. and Wu, M.** (2013). Cooperative roles of SDF-1α and EGF gradients on tumor cell migration revealed by a robust 3D microfluidic model. *PLoS ONE* **8**, e68422.

**Lohmer, L. L., Clay, M. R., Naegeli, K. M., Chi, Q., Ziel, J. W., Hagedorn, E. J., Park, J. E., Jayadev, R. and Sherwood, D. R.** (2016). A Sensitized Screen for Genes Promoting Invadopodia Function In Vivo: CDC-42 and Rab GDI-1 Direct Distinct Aspects of Invadopodia Formation. *PLoS Genet* **12**, e1005786–29.

**Mao, Y. S. and Yin, H. L.** (2007). Regulation of the actin cytoskeleton by phosphatidylinositol 4-phosphate 5 kinases. *Pflugers Arch.* **455**, 5–18.

**Martin-Belmonte, F., Gassama, A., Datta, A., Yu, W., Rescher, U., Gerke, V. and Mostov, K.** (2007). PTEN-mediated apical segregation of phosphoinositides controls epithelial morphogenesis through Cdc42. *Cell*

**128**, 383–397.

**Meisenhelder, J., Suh, P. G., Rhee, S. G. and Hunter, T.** (1989). Phospholipase C-gamma is a substrate for the PDGF and EGF receptor protein-tyrosine kinases in vivo and in vitro. *Cell* **57**, 1109–1122.

**Mello, C. C., Kramer, J. M., Stinchcomb, D. and Ambros, V.** (1991). Efficient gene transfer in C.elegans: extrachromosomal maintenance and integration of transforming sequences. *EMBO J.* **10**, 3959–3970.

**Mohler, W. A., Shemer, G., del Campo, J. J., Valansi, C., Opoku-Serebuoh, E., Scranton, V., Assaf, N., White, J. G. and Podbilewicz, B.** (2002). The type I membrane protein EFF-1 is essential for developmental cell fusion. *Developmental Cell* **2**, 355–362.

**Morf, M. K., Rimann, I., Alexander, M., Roy, P. and Hajnal, A.** (2013). The Caenorhabditis elegans homolog of the Opitz syndrome gene, madd-2/Mid1, regulates anchor cell invasion during vulval development. *Developmental Biology* **374**, 108–114.

**Morimoto, R. I.** (2011). The heat shock response: systems biology of proteotoxic stress in aging and disease. *Cold Spring Harb. Symp. Quant.* Biol. 76, 91–99.

**Price, J. T., Tiganis, T., Agarwal, A., Djakiew, D. and Thompson, E. W.** (1999). Epidermal growth factor promotes MDA-MB-231 breast cancer cell migration through a phosphatidylinositol 3'-kinase and phospholipase C-dependent mechanism. *Cancer Res.* **59**, 5475–5478.

**Price, J. T., Wilson, H. M. and Haites, N. E.** (1996). Epidermal growth factor (EGF) increases the in vitro invasion, motility and adhesion interactions of the primary renal carcinoma cell line, A704. *Eur. J. Cancer* **32A**, 1977–1982.

**Qadota, H., Inoue, M., Hikita, T., Köppen, M., Hardin, J. D., Amano, M., Moerman, D. G. and Kaibuchi, K.** (2007). Establishment of a tissue-specific RNAi system in C. elegans. *Gene* **400**, 166–173.

**Rabinovitz, I., Toker, A. and Mercurio, A. M.** (1999). Protein kinase C-dependent mobilization of the alpha6beta4 integrin from hemidesmosomes and its association with actin-rich cell protrusions drive the chemotactic migration of carcinoma cells. *J Cell Biol* **146**, 1147–1160.

**Rajakumar, V. and Chamberlin, H. M.** (2007). The Pax2/5/8 gene egl-38 coordinates organogenesis of the C. elegansegg-laying system. *Developmental Biology* **301**, 240–253.

**Ririe, T. O., Fernandes, J. S. and Sternberg, P. W.** (2008). The Caenorhabditis elegans vulva: a post-embryonic gene regulatory network controlling organogenesis. *Proc. Natl. Acad. Sci. U.S.A.* **105**, 20095–20099.

**Sechi, A. S. and Wehland, J.** (2000). The actin cytoskeleton and plasma membrane connection: PtdIns(4,5)P(2) influences cytoskeletal protein activity at the plasma membrane. *J. Cell. Sci.* **113 Pt 21**, 3685–3695.

**Sharma-Kishore, R., White, J. G., Southgate, E. and Podbilewicz, B.** (1999). Formation of the vulva in Caenorhabditis elegans: a paradigm for organogenesis. *Development* **126**, 691–699.

**Shaye, D. D. and Greenwald, I.** (2002). Endocytosis-mediated downregulation of LIN-12/Notch upon Ras activation in Caenorhabditis elegans. *Nature* **420**, 686–690.

**Shaye, D. D. and Greenwald, I.** (2005). LIN-12/Notch trafficking and regulation of DSL ligand activity during vulval induction in Caenorhabditis elegans. *Development* **132**, 5081–5092.

**Simmer, F., Tijsterman, M., Parrish, S., Koushika, S. P., Nonet, M. L., Fire, A., Ahringer, J. and Plasterk, R. H. A.** (2002). Loss of the putative RNA-directed RNA polymerase RRF-3 makes C. elegans hypersensitive to RNAi. *Current Biology* **12**, 1317–1319.

**Singh, A. B. and Harris, R. C.** (2005). Autocrine, paracrine and juxtacrine signaling by EGFR ligands. *Cell. Signal.* **17**, 1183–1193.

**Singhai, A., Wakefield, D. L., Bryant, K. L., Hammes, S. R., Holowka, D. and Baird, B.** (2014). Spatially defined EGF receptor activation reveals an F-actin-dependent phospho-Erk signaling complex. *Biophys. J.* **107**, 2639–2651.

**Sternberg, P. W.** (1988). Lateral inhibition during vulval induction in Caenorhabditis elegans. *Nature* **335**, 551–554.

**Sternberg, P. W.** (2005). Vulval development. *WormBook* 1–28.

**Sun, R., Gao, P., Chen, L., Ma, D., Wang, J., Oppenheim, J. J. and Zhang, N.** (2005). Protein kinase C zeta is required for epidermal growth factor-induced chemotaxis of human breast cancer cells. *Cancer Res.* **65**, 1433–1441.

**Tabara, H., Sarkissian, M., Kelly, W. G., Fleenor, J., Grishok, A., Timmons, L., Fire, A. and Mello, C. C.** (1999). The rde-1 gene, RNA interference, and transposon silencing in C. elegans. *Cell* **99**, 123–132.

**Tan, P. B., Lackner, M. R. and Kim, S. K.** (1998). MAP kinase signaling specificity mediated by the LIN-1 Ets/LIN-31 WH transcription factor complex during C. elegans vulval induction. *Cell* **93**, 569–580.

**Van Buskirk, C. and Sternberg, P. W.** (2007). Epidermal growth factor signaling induces behavioral quiescence in Caenorhabditis elegans. *Nat. Neurosci.* **10**, 1300–1307.

**van Rheenen, J., Song, X., van Roosmalen, W., Cammer, M., Chen, X., Desmarais, V., Yip, S.-C., Backer, J. M., Eddy, R. J. and Condeelis, J. S.** (2007). EGF-induced PIP2 hydrolysis releases and activates cofilin locally in carcinoma cells. *J Cell Biol* **179**, 1247–1259.

**Wang, M. and Sternberg, P. W.** (2000). Patterning of the C. elegans 1 degrees vulval lineage by RAS and Wnt pathways. *Development* **127**, 5047–5058.

**Wang, M. and Sternberg, P. W.** (2001). Pattern formation during C. elegans vulval induction. *Curr. Top. Dev. Biol.* **51**, 189–220.

**Wang, Z., Linden, L. M., Naegeli, K. M., Ziel, J. W., Chi, Q., Hagedorn, E. J., Savage, N. S. and Sherwood, D. R.** (2014). UNC-6 (netrin) stabilizes oscillatory clustering of the UNC-40 (DCC) receptor to orient polarity. *J Cell Biol* **206**, 619–633.

**Wyckoff, J. B., Jones, J. G., Condeelis, J. S. and Segall, J. E.** (2000). A critical step in metastasis: in vivo analysis of intravasation at the primary tumor. *Cancer Res.* **60**, 2504–2511.

**Wyckoff, J., Wang, W., Lin, E. Y., Wang, Y., Pixley, F., Stanley, E. R., Graf, T., Pollard, J. W., Segall, J. and Condeelis, J.** (2004). A paracrine loop between tumor cells and macrophages is required for tumor cell migration in mammary tumors. *Cancer Res.* **64**, 7022–7029.

**Yang, Q., Roiz, D., Mereu, L., Daube, M. and Hajnal, A.** (2017). The Invading Anchor Cell Induces Lateral Membrane Constriction during Vulval Lumen Morphogenesis in C. elegans. *Developmental Cell* **42**, 271–285.e3.

**Yochem, J., Weston, K. and Greenwald, I.** (1988). The Caenorhabditis elegans lin-12 gene encodes a transmembrane protein with overall similarity to Drosophila Notch. *Nature* **335**, 547–550.

**Yonezawa, N., Homma, Y., Yahara, I., Sakai, H. and Nishida, E.** (1991). A short sequence responsible for both phosphoinositide binding and actin binding activities of cofilin. *J. Biol. Chem.* **266**, 17218–17221.

**Yonezawa, N., Nishida, E., Iida, K., Yahara, I. and Sakai, H.** (1990). Inhibition of the interactions of cofilin, destrin, and deoxyribonuclease I with actin by phosphoinositides. *J. Biol. Chem.* **265**, 8382–8386.

**Zand, T. P., Reiner, D. J. and Der, C. J.** (2011). Ras Effector Switching Promotes Divergent Cell Fates in C. elegans Vulval Patterning. *Developmental Cell* **20**, 84–96.

**Zhang, G., Sleiman, S. F., Tseng, R.-J., Rajakumar, V., Wang, X. and Chamberlin, H. M.** (2005). Alteration of the DNA binding domain disrupts distinct functions of the C. elegans Pax protein EGL-38. *Mechanisms of Development* **122**, 887–899.

**Ziel, J. W., Hagedorn, E. J., Audhya, A. and Sherwood, D. R.** (2008). UNC-6 (netrin) orients the invasive membrane of the anchor cell in C. elegans. *Nat Cell Biol* **11**, 183–189.

## 3.3 Additional Experiments not included in the manuscript drafts

### 3.3.1 *lin-3* transgene expressed in the vulF cells does not rescue the *egl-38(n578)* dorsal lumen expansion defect

We wanted to know if the dorsal lumen defect observed in the *egl-38(n578)* mutants is caused by loss in *lin-3* expression from the vulF cells. To investigate this, we constructed a rescue transgene driving *lin-3::gfp* expression from the *vab-23* promoter and injected it into the *egl-38(n578); ajm-1::gfp; $P_{cdh3}$>mCherry::PLCδ$^{PH}$* mutant strain (*zhEx544[$P_{vab-23}$>lin-3::gfp; $P_{sur-5}$>gfp]*). *vab-23* is expressed in the AC and the 1° cell descendants from the early L3 stage on (Pellegrino et al., 2011). We looked at AC polarity, AC positioning and dorsal lumen expansion in animals expressing the transgene, compared to control animals of the same strain without transgene expression (Fig. 3.3.1, A and B). There was no significant difference in the frequency of the analyzed phenotypes between the group expressing the rescue transgene compared to control group at any developmental stage (Fig. 3.3.1, C). This suggests that LIN-3 expressed from the vulF cells under control of the *vab-23* promoter is not sufficent to rescue the *egl-38(n578)* defects.

Conclusion

This result indicates that either the *egl-38(n578)*-specific mutant phenotypes, such as the dorsal lumen expansion defect, are not caused by the loss in *lin-3* expression from the vulva, or that a precise *lin-3* source or dose is required to direct AC mediated vulF invasion. With our rescue construct we wanted to generate a mosaic expression pattern and select animals, in which *lin-3* expression was rescued in the 1° vulval cells, but not in the AC. We discriminated according to the *sur-5::gpf* co-injection marker expression pattern (Yochem et al., 1998). Our generated zhEx544 line was very stable in its expression such that almost no individuals could be found, which showed transgene expression only in the vulval cells. This shows that the rescue transgene more likely resembles an ectopic *lin-3* expression line. Ideally, the *egl-38* promoter would have been selected to drive the *lin-3* rescue transgene. However EGL-38 drives its own expression and in the reduction of function n578 allele *egl-38* expression is lost (Ririe et al., 2008). In view of the subsequently generated AC ablation results (Fig. 3.2.2), in retrospect the *egl-17* promoter would have been preferable for this experiment. Though, at the time of the zhEx544 strain construction, we hypothesized that LIN-3 expression from the vulF cells at the P6.pxxx early to mid L4 stage is required for vulF expansion. At this developmental stage *egl-17* expression shifts from vulE and vulF to vulC and vulD (Burdine et al., 1998).

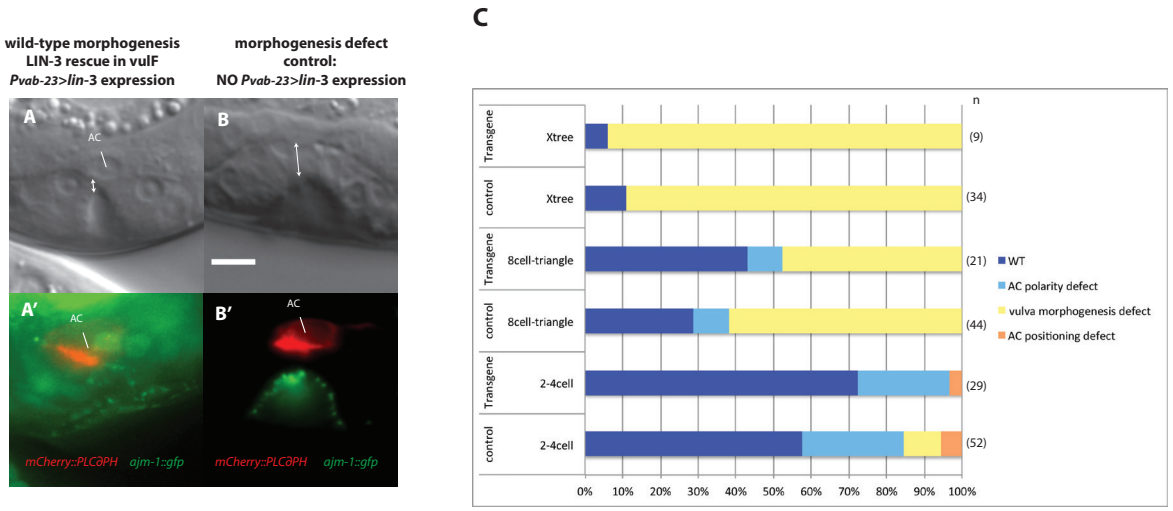


**Figure 3.3.1. A *lin-3* rescue transgene expressed in the vulF cells does not rescue the egl-38(n578) dorsal lumen expansion defect**

Examples of (A) wild-type and (B) a typical *egl-38(n578)* dorsal lumen defective vulva at the triangle (early L4) stage.
(A and B) Nomarski and (A' and B') fluorescent expression of the *ajm-1::gfp* and $P_{cdh3}$*>mCherry::PLCδ*$^{PH}$; *ajm-1::gfp* transgenes in *egl-38(n578)* mutants (A') without and (B') with *zhEx544[*$P_{vab-23}$*>lin-3::gfp; sur-5::gfp] lin-3* rescue expression. AC is labeled and indicated by white line and vulF lateral constriction morphogenesis is indicated by white double-headed arrow. Scale bar equals 5 µm.
(C) Plot shows percent of animals with distinct phenotypes at the indicated developmental stages with and without rescue *lin-3* expression in the vulva. According to Fisher's exact probability test there is no significant difference in dorsal lumen expansion, AC polarity or positioning between *lin-3* rescue expression or none for all stages.

### 3.3.2 AC specific *let-23(dom-rf)::gfp*, with reduced kinase activity promotes defects in AC positioning and dorsal lumen

To look at possible LET-23 functions in the AC, we constructed a strain, in which a dominant-reduction of function *let-23::gfp* transgene is expressed from an AC specific promoter (*zhIs061[$P_{cdh-3}$>let-23(dom-rf)::gfp; $P_{myo-2}$>mCherry]*). The introduced *let-23* mutation represents a Tyrosine to Cystein exchange at position Y1064. We analyzed AC positioning in this strain and found that a low percentage of animals displayed an AC mispositioning phenotype (Fig. 3.3.2, B-C). In addition, we observed a significant percent of animals with a dorsal lumen expansion defects in the *zhIs061* strain compared to control (Fig. 3.3.2, D and F).

Conclusion

Originally, it was intended to construct a *let-23dominant-negative* transgene and express it in the AC. It was thus intended to exchange a T to A, introducing a *sy16* mutation, resulting in a Threonine to Isoleucine exchange at the T1065 location, leading to a complete loss of Kinase function resulting from structural conformational changes (Aroian and Sternberg, 1991; Aroian et al., 1994). Erroneously, we introduced an A to G nucleotide exchange and a subsequent tyrosine to cysteine transformation at position Y1064 in the LET-23 tyrosine kinase domain, which is a conserved tyrosine in the EGFR kinase domain (Bae et al., 2012). Thus, the *zhIs061[$P_{cdh-3}$>let-23(dom-rf)::gfp; $P_{myo-2}$>mCherry]* transgene only encodes a dominant-reduction of function protein, because a mistake in the design of for the cloning of the plasmid was made, and unfortunately only discovered later. Since we do not know the exact function of Y1064, we cannot predict the impact it has when exchanged to Cysteine on LET-23 induced signaling. We can only postulate that it likely presents a major deviation from wild-type signaling. The fact that we see some defects upon expression of this transgene indicates that a proper constructed LET-23(dn) transgene in the AC, or an AC specific *let-23* knock-out very likely would have a much greater impact on AC positioning and dorsal vulval lumen expansion. We are currently setting up experiments to confirm this data with an introduced excisable FLP/FRT system in the endogenous *let-23* locus.

**Figure 3.3.2. AC specific *let-23(dom-rf)::gfp* , with reduced functionality promotes defects in AC positioning and dorsal lumen**

(A-A'') Example of wild-type AC positioning and defects in (B-B'') AC positioning defect, in a strain expressing the AC specific *let-23(dom-rf)::gfp* transgene, at the P6.pxx mid-late L3 larval stage. The AC, as well as the P6.pxx position is labeled with a white line.

(A) Nomarski, (A'') $P_{cdh3}$>*mCherry::PLC*$\delta^{PH}$; *ajm-1::gfp* section images, showing the labeled AC and P6.pxx cells. (B) Nomarski, (B'') AC specific *let-23(dom-rf)::gfp* (*zhIS61*) section images, showing the labeled AC and P6.pxx cells. Scale bar equals 5 µm.

(C) Plot shows percent of animals, expressing an AC specific *let-23(dom-rf)::gfp* transgene, with a defect in AC positioning compared to control animals. Statistical significance was calculated according to Fisher's exact probability test and p-values are displayed in plot.

Example of (E) wild-type dorsal lumen expansion and (F) dorsal lumen expansion defect in the zhIS61 strain, at the mid L4 X-tree larval stage. The dorsal lumen expansion diameter is marked by a double-headed arrow.

(E) Nomarski and (E'') $P_{cdh3}$>*mCherry::PLC*$\delta^{PH}$; *ajm-1::gfp* section images, showing the marked AC syncytium and the mid L4 X-tree toroidal apical junctions. (F) Nomarski and (F'') AC specific *let-23(dom-rf)::gfp* transgene (*zhIS61*) expression section images, showing the labeled AC syncytium of the mid L4 X-tree stage vulva. Scale bar equals 5 µm.

(D) Plot shows percent of zhIS61 animals with a defect in dorsal lumen expansion, compared to control. Statistical significance was calculated according to Fisher's exact probability test and p-values are displayed in plot.

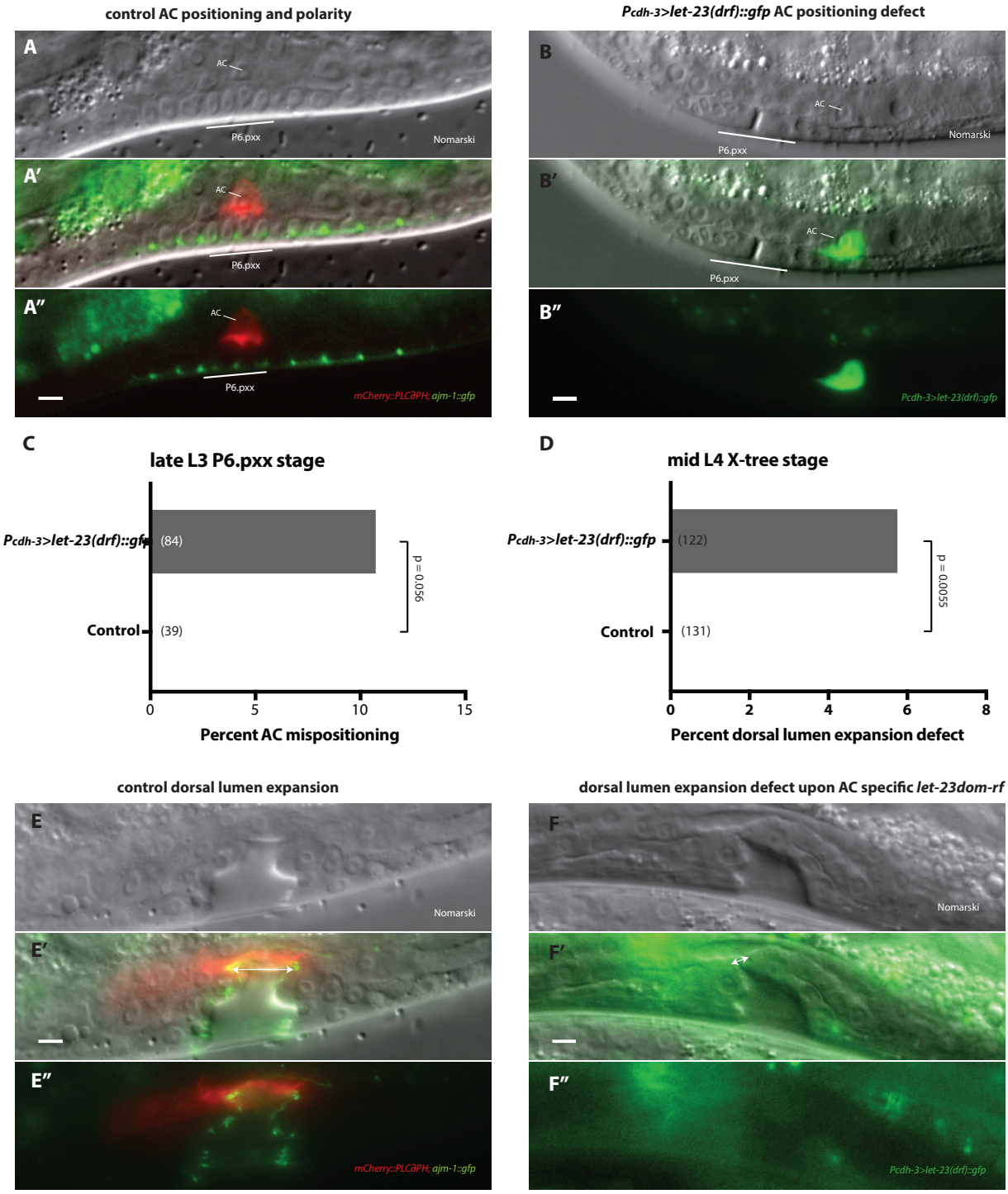


**Figure 3.3.2. AC specific *let-23(dom-rf)::gfp* , with reduced functionality promotes defects in AC positioning and dorsal lumen**

### 3.3.3 AC-specific *let-23* and *let-60* RNAi do not cause significant alterations in dorsal lumen expansion

To gain further insight into the putative function of LET-23 signaling in the AC, we knocked down *let-23* and *let-60* by AC specific RNAi and looked at dorsal lumen expansion at the mid L4 stage (Fig. 3.3.3, A-C) (Hagedorn et al., 2009; Qadota et al., 2007). We found a slight increase in dorsal lumen expansion defects upon *let-23* knock-down, but not for *let-60* (Fig. 3.3.3, D). For better quantification, we measured the vulE/vulF lumen toroid diameter in an AC specific RNAi strain with integrated *ajm-1::gfp* reporter expression (Fig. 3.3.3, E-F'). We found no significant decrease in vuleE/vulF diameter upon AC specific *let-60* RNAi compared to *empty* vector control. AC-specific *let-23* RNAi, in a strain carrying the *ajm-1::gfp* reporter had a sterilizing effect on the P0 RNAi treated animals, which had no progeny and so the F1 generation could not be analyzed in this experiment.

Conclusion

The AC-specific RNAi strain produced a high percentage of defects in dorsal lumen expansion in the empty vector control. From this we speculate that *rde-1* and *rrf-3* have functions that are required for wild-type dorsal lumen morphogenesis. Due to the high rate of defect in dorsal lumen expansion in the control group, the experiment was not repeated for AC specific *let-23* RNAi.

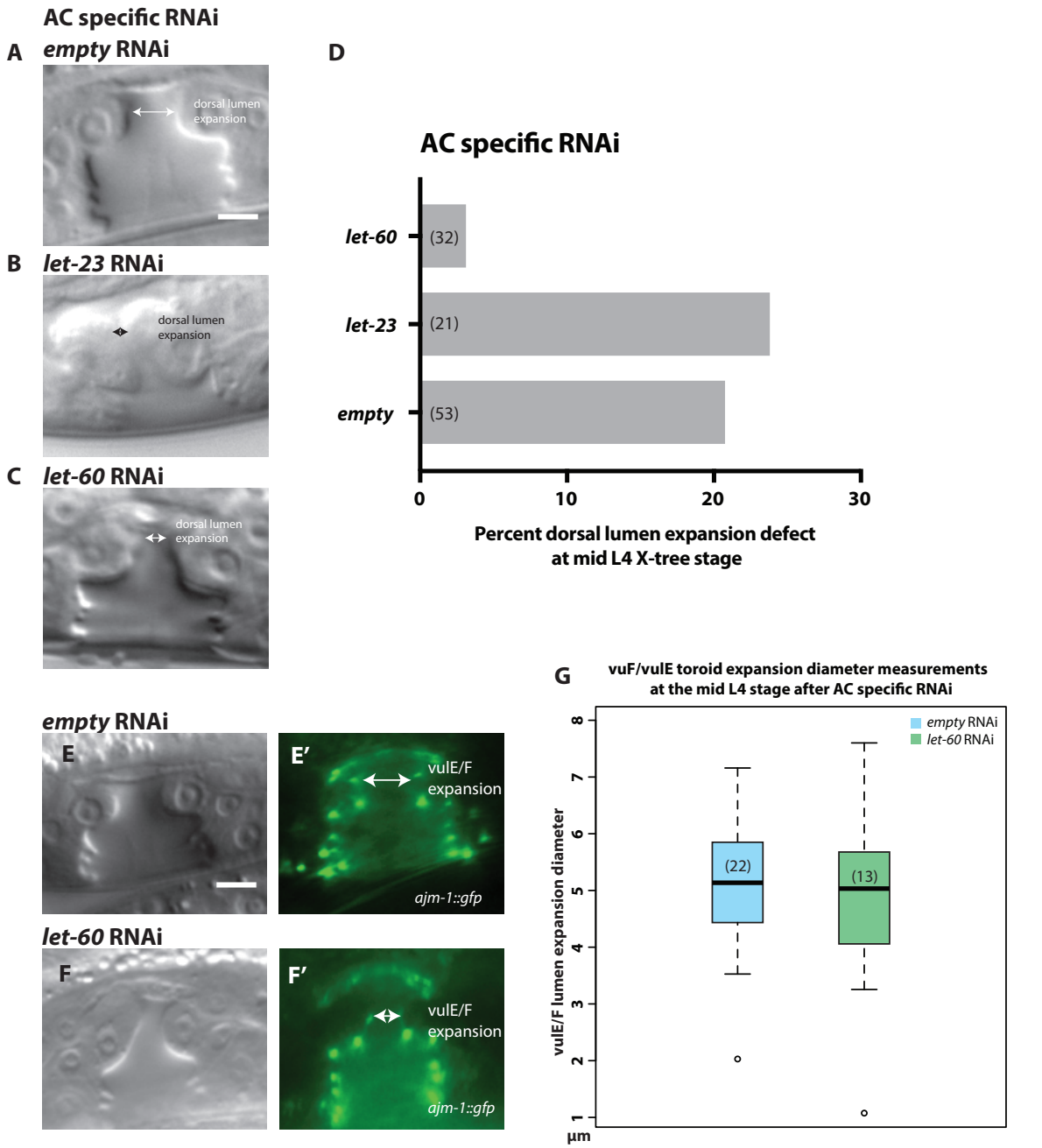


**Figure 3.3.3. AC specific *let-23* and *let-60* RNAi do not cause significant alterations in dorsal lumen expansion**

(A, B and C) Nomarski sections of lateral view mid L4 stage X-tree vulvas of *rrf-3(pk1426); rde-1(ne219); $P_{fos-1}$>rde-1(+)* strain, treated with (A) empty vector control, (B) *let-23* or (C) *let-60* RNAi. Images show examples of (A) wild-type dorsal lumen expansion and (B and C) dorsal lumen expansion defects. Dorsal lumen expansion is indicated by double-headed arrow.

(D) Plot shows the percentage of cases, in which a dorsal lumen expansion defect was observed, upon AC specific RNAi of empty vector control, *let-23* or *let-60*.

According to Fisher's exact probability test there is no significant difference in the frequency of dorsal lumen expansion defects between empty, *let-23* or *let-60*.

(E and F) Nomarski and (E' and F') *ajm1::gfp* fluorescence sections of lateral view mid L4 stage vulvas. Examples show a strain with *ajm1::gfp* transgene expression, in which AC specific RNAi can be performed (*ajm-1::gfp*; *rrf-3(pk1426); rde-1(ne219); $P_{fos-1}$>rde-1(+)*), treated with (E and E') empty vector control or (F and F') *let-60* RNAi. The measured vulE/vulF diameter is indicated by double-headed arrow. Scale bar equals 5 µm.

(G) Plot shows range of measured vulE/vulF diameters in µm for empty vector control and *let-60* RNAi. According to an independent test of unequal variance there is no significant difference in dorsal lumen expansion between the two groups.

### 3.3.4 Systemic *lin-3* RNAi in *let-23(sa62)* causes slightly increased dorsal lumen expansion defects

EGL-38 regulates *lin-3* transcription in the vulF cells, which is required for the specification of the uterine uv1 cell fate (Chang et al., 1999). *egl-38(n578)* mutants have defects in uv1 cell fate specification and dorsal vulval lumen expansion. When the gain-of-function *let-23(sa62)* allele is comined with the *egl-38(n578)* mutant, this leads to a rescue in uv1 cell fate specification, but not of the dorsal lumen expansion phenotype (Chang et al., 1999). The *sa62* allele encodes a gain of function mutation, with a cysteine to tyrosine exchange at position Y359 in the first Cysteine-rich domain in the extracellular part of LET-23. The mutated LET-23 allele can signal in a LIN-3 EGF ligand independent manner, but still remains sensitive to LIN-3 binding, which enhances vulval induction in the *let-23(sa62)* allele upon ectopic expression of LIN-3 (Moghal and Sternberg, 2003). We hypothesize that if the LIN-3 signal from the vulF cells indeed directs AC polarity and AC migration, a gain-of-function *let-23* allele would not rescue the *egl-38(n578)* caused dorsal lumen expansion defect, as the directional cue would still be missing in the *let-23(sa62)*; *egl-38(n578)* double mutant. As a preview to exclude that the uv1 cell fate specification is required for wild-type dorsal lumen formation, we performed systemic *lin-3* RNAi in the *let-23(sa62)* mutant background and scored defects in dorsal lumen expansion. Animals with hypoinduced vulvas due to the *lin-3* RNAi were not scored as having defects in dorsal lumen formation. We found a mild increase in the number of animals with defects in dorsal vulval lumen expansion (Fig. 3.3.4, B) upon *lin-3* RNAi compared to control (Fig. 3.3.4, C).

Conclusion

Since we performed systemic RNAi, we can exclude putative defects from loss in *rde-1* and *rrf-3* function as supposed from the tissue specific RNAi, but we loose the directional aspect of LIN-3 signaling, and thus cannot argue that loss in *lin-3* signaling from the vulva caused dorsal lumen defects. What we can conclude from this result is that other factors than uv1 cell fate specifications can cause dorsal lumen expansion defects upon *lin-3* RNAi.

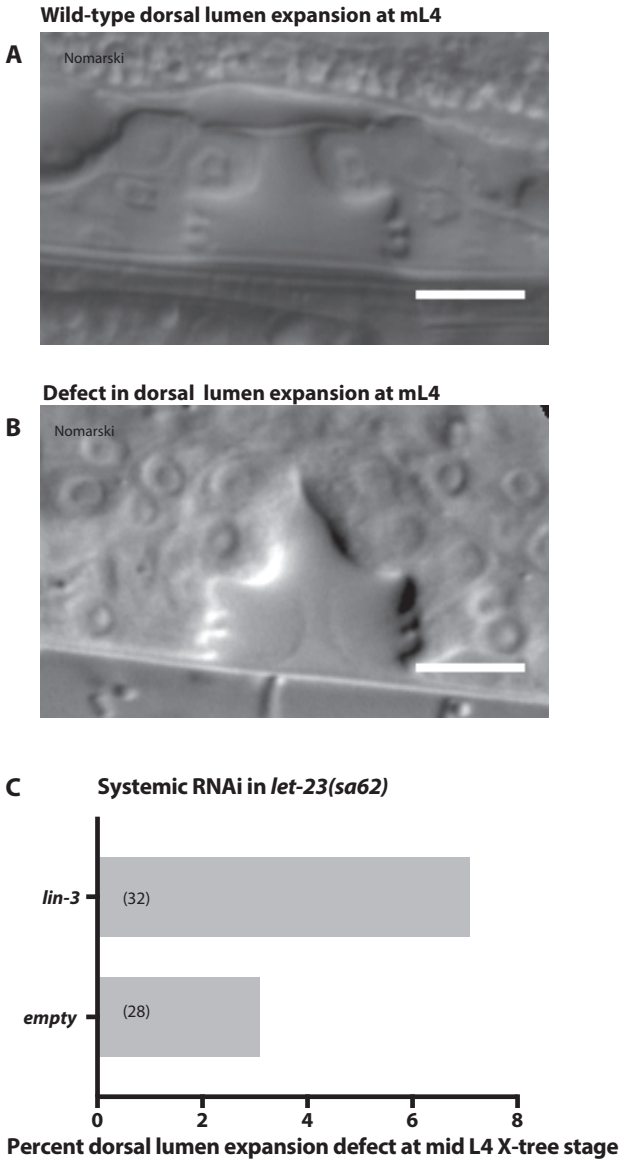


**Figure 3.3.4. Systemic *lin-3* RNAi in *let-23(sa62)* causes slightly increase in dorsal lumen expansion defect occurrence**
Nomarski section images of lateral view mid L4 stage vulvas, showing an example of a (A) wild-type dorsal lumen expansion and a (B) dorsal lumen expansion defect. Scale bar equals 10 µm. Images show a strain carrying the *let-23(sa62)* gain of function allele, treated with systemic (A) empty vector control or (B) *lin-3* RNAi.
(C) Plot shows the percentage of cases, in which a dorsal lumen expansion defects was observed, upon systemic empty vector control, *lin-3* RNAi in the *let-23(sa62)* background. According to Fisher's exact probability test there is no significant difference in the frequency of dorsal lumen expansion defects between empty control and *lin-3* RNAi.

### 3.3.5 HS induction of LIN-3 at the early L4 stage causes dorsal lumen expansion defects

To establish a link between LIN-3 signaling and dorsal lumen expansion we expressed *lin-3* ectopically from a heat-shock inducible promoter within a staged larval population at the approximate early L4 stage and analyzed the worms 5 hours later at the mid L4 stage. We looked at dorsal vulval lumen expansion and scored vulF expansion defects by means of Nomarski microscopy. We analyzed heat-shock treated wild-type and *syIs11[$P_{hs}$>lin-3soluble]* animals with and without heat-shock treatment, both expressing the *syIs51[$P_{cdh-3}$>cfp, unc-119(+)]* reporter, marking the 1° vulval cell fate descendants (Fig. 3.3.5, A-B'). Surprisingly, we found that wild-type control animals, which had been subjected to heat-shock treatment generated a higher percentage of animals with abnormal dorsal lumen expansion compared to *syIs11[$P_{hs}$>lin-3soluble]* animals with and without heat-shock induction. But, there was no significant difference between any of the groups. This shows that exposure to heat-shock can impair wild-type vulval morphogenesis.

Conclusion

We know that the AC does not affect vulval morphogenesis after the L3/L4 transition stage (Fig. 3.2.2). Therefore, the dorsal lumen expansion defect observed in this experiment is likely due to other factors than ectopic *lin-3* expression. Animal that are subjected to sheet-shock treatment undergo a stress-response. This response leads to the transcription of heat shock proteins (HSPs), which are molecular chaperones, and are upregulated during stress conditions to prevent the aggregation of nonnative proteins, modulate the structure of newly synthesized proteins and stabilize the stress-damaged proteins (Snutch and Baillie, 1983). This alters the protein composition in the cells and likely leads to further unknown alterations in cell signaling. It is therefore not surprising that heat-shock can have an effect on vulval morphogenesis.

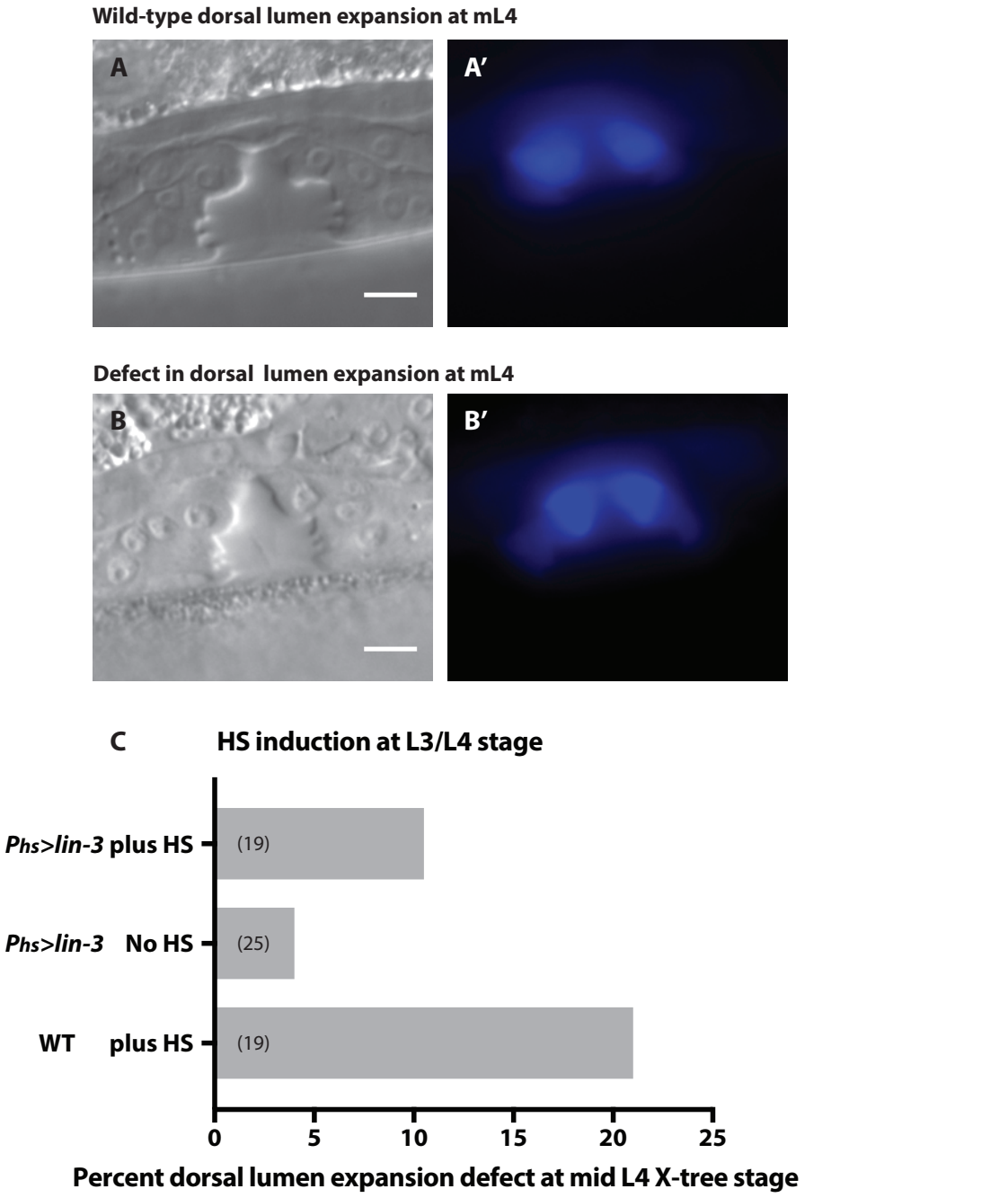


**Figure 3.3.5. HS induction at the L3/L4 stage caused dorsal lumen expansion defects**

(A and B) Nomarski and fluorescent $P_{cdh-3}$>*cfp* reporter images of lateral view mid L4 stage vulvas, showing an example of a (A and A') wild-type dorsal lumen expansion and a (B and B') a dorsal lumen expansion defect. Scale bar equals 10 µm. Images show a (A) wild-type strain and (B) a strain carrying the $P_{hs}$*::lin-3EGF*.

(C) Plot shows the percentage of cases, in which a dorsal lumen expansion defects was observed, in indicated wild-type and $P_{hs}$*::lin-3EGF*, with and without heat-shock induction.

According to Fisher's exact probability test there is no significant difference in the frequency of dorsal lumen expansion defects between any of the genotypes with and without heat-shock induction.

### 3.3.6 Time-course analysis of dorsal lumen expansion from the early L4 to the mid L4 stage in wild-type

To gain a deeper understanding of dorsal vulval lumen morphogenesis, we performed time-lapse imaging in wild-type and *egl-38(n578)* animals, using reporters, marking AC polarity ($P_{cdh\text{-}3}$*>mCherry::PLCδ*$^{PH}$) and the apical junctions between the vulval toroids (*ajm-1::gfp*).
We generated four time-lapse movies of wild-type larvae, which successfully developed from the early L4 until the mid L4 larval stage. Under standard laboratory conditions (Brenner, 1974), the developmental progression from the early to mid L4 larval stage takes approximately 5h at 20°C. The animals developed significantly slower under the microscope, such that the same developmental progression lasted twice this time (app. 11h). For quantification and analysis, we measured the individual toroidal diameters (Fig. 3.3.6. C) at each generated time-point for all four movies. As zero time-point we specified the turning point, in which the vulA diameter expands again after having contracted (Fig. 3.3.6, D (red arrow)), to correct for differences in developmental progression at the onset of the time-lapse imaging.
We then plotted the average diameter and standard error of the mean for the measured toroid diameter or height at each time-point (Fig. 3.3.6, E).
Conclusion
The resolution of the time-lapse images is relatively low because the exciting laser intensity had to be kept low as well. The analysis was thought to support additional time-course data, which can be generated at much higher resolution, but has a higher error rate in the exact ascertainment of the developmental stage, since it is difficult to exactly stage a larval population. The time-lapse assay was thought to present a scaffold for the alignment of the time-course assay. With the two together, we wanted to investigate how the AC expands the dorsal lumen. However, from our AC ablation experiment (Fig. 3.2.2) we concluded that at the onset of the early L4 larval stage, when the movies were taken, the AC no longer has a function in dorsal lumen expansion. In consequence, we revised our experimental approach and set its focus on the late L3 larval stage. We generated time-lapse movies of vulva development at the mid-late L3 larval stage. One of these movies is published in a manuscript of another lab member who investigated AC mediated lateral vulF constriction, a process required for wild-type vulval morphogenesis (Yang et al., 2017). This process very likely encompasses the ACs function in wild-type dorsal lumen formation.

**Figure 3.3.6. Time-course analysis of dorsal lumen expansion from the early L4 to the mid L4 stage in wild-type**
(A, B and C) Nomarski section images and (A', B' and C') deconvolved fluorescence images of summed z-projections showing expression pattern of the AC in red ($P_{cdh3}$*>mCherry::PLCδ*$^{PH}$), merged with the *ajm-1::gfp* reporter (in green), marking the apical junctions between the vulva toroids, for (A and A') the early L4, (B and B') early to mid L4 and (C and C') mid L4 stages.
(D) Cartoon showing the color-coded measurements taken for the wild-type vulva toroid morphogenesis characterization.
(E) Plot shows the progression of the individual measurements taken in "D", relative to time. The measurements were taken in µm and the mean value for four individuals and the standard error of the mean is shown in plot. The exact larval developmental stage at onset of time-lapse imaging varies for each measured individual. To correct for this in the average values, the measured time points were aligned according to the "vulA turning point", described in detail in the results section, which was set as point 0.

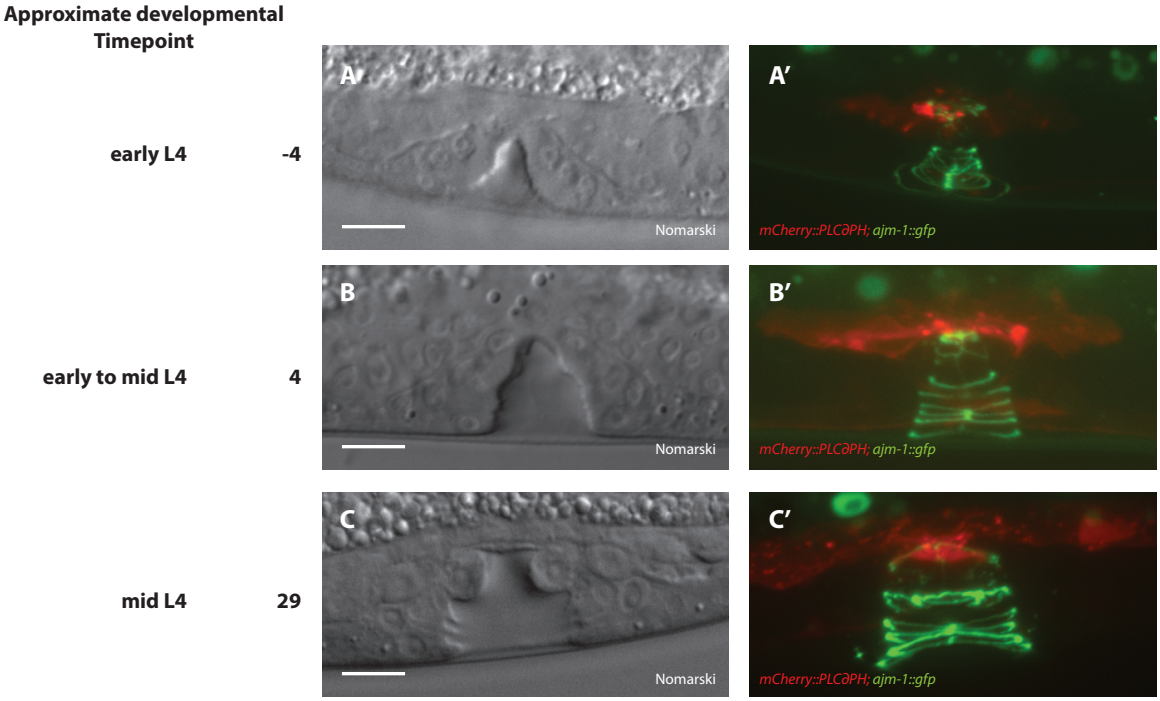
Approximate developmental Timepoint
early L4
-4
A
Nomarski
A′
mCherry::PLCϑPH; ajm-1::gfp
early to mid L4
4
B
Nomarski
B′
mCherry::PLCϑPH; ajm-1::gfp
mid L4
29
C
Nomarski
C′
mCherry::PLCϑPH; ajm-1::gfp

D

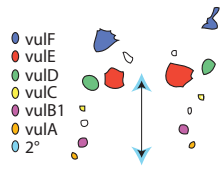
vulF
vulE
vulD
vulC
vulB1
vulA
2°

E

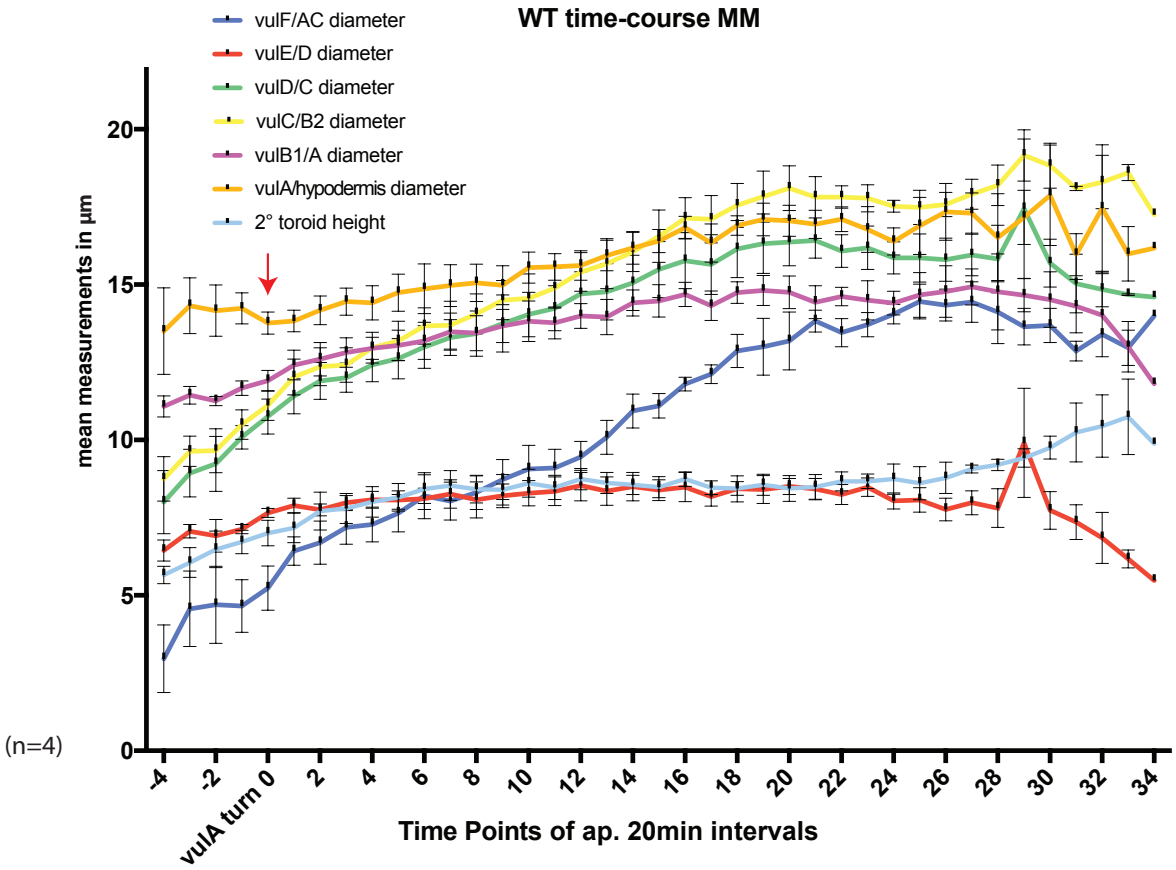
WT time-course MM
vulF/AC diameter
vulE/D diameter
vulD/C diameter
vulC/B2 diameter
vulB1/A diameter
vulA/hypodermis diameter
2° toroid height
mean measurements in µm
0
5
10
15
20
-4
-2
vulA turn 0
2
4
6
8
10
12
14
16
18
20
22
24
26
28
30
32
34
Time Points of ap. 20min intervals

(n=4)

### 3.3.7 An *FRT::lin-3::gfp::FRT* reporter leads to ectopic vulval induction and does not rescue the *lin-3(n1059)* null allele

To confirm our tissue-specific *lin-3* RNAi dorsal lumen expansion phenotype (Fig. 3.3.1), we wanted to generate an integrated *lin-3::gfp* MoSCI (Zeiser et al., 2011) reporter, flanked by FRT sites, which would rescue a loss of function *lin-3(n1059)* mutant allele. This compilation would give us a system, in which *lin-3* could be excised by means of the FLP/FRT system in a temporal or tissue-specific manner (Voutev and Hubbard, 2008).
We successfully constructed the MoSCI integrated *zhIs83[frt::lin-3::gfp::frt, unc-119(+)]* reporter (Fig. 7, A). The reporter showed *lin-3* expression in the AC and the vulF cells as reported (Hwang, 2004), but in the vulF cells no signal was observed before the early L4 stage. Interestingly, the strain had a highly penetrant vulva hyperinduction phenotype (Muv) (Fig. 7, B-D'). We crossed the *zhIs83* reporter to the *lin-3(n1059)* mutant background, which is balanced with nT1. The *zhIs83[frt::lin-3::gfp::frt, unc-119(+)]* transgene did not rescue the *n1059* allele. No animals developed further than the L1 stage without carrying the balancer.
In an alternative approach, we wanted to generate an endogenous *lin-3* reporter and FLP/FRT excisable strain with the CRISPR/Cas9 tool (Horvath and Barrangou, 2010), applying the Co-CRISPR method (Arribere et al., 2014). Unfortunately, we were never able to isolate a positively verified *lin-3* insertion strain with this method. We found a line, in which a *lin-3::citrin::lin-3* plasmid (pLM2) had been used as a repair template, which showed citrin expression in the AC, but could not positively verify endogenous integration by PCR, and the strain could not be maintained (Fig. 3.3.7, E-E'').
Conclusion
An explanation why the *zhIs83* integration generated a vulva hyperinduction phenotype could be attributed to the site of the MoSCI integration. A previous MoSCI integrated plasmid (pMMO10), which was used as template for the inserted *frt::lin-3::gfp::frt* plasmid (pLM1), did not produce ectopic vulval induction, and had been integrated in a MoSCI site on Chromosome II. The *zhIs83* integration is on chromosome I. It is possible that an enhancer element is located near the MoSCI insertion site on Chromosome I (ocTI185). The phenotype is not completely penetrant, which could be due to epigenetic modification of the putative enhancer near the MoSCI insertion site on Chromosome I.
The *zhIs83* strain failed to rescue the *lin-3(n1059)* mutant allele. We sequenced the strain allegedly carrying the *n1059* allele, but could not confirm the published Trp to STOP codon substitution in the EGF domain (G to R (Liu et al., 1999)) by PCR and sequencing. Since we could not genotype the background allele and the transgene could not rescue the mutant allele anyway, and in the light of newly emerging CRISPR/Cas9 techniques at the time, we decided to leave off from further attempts at an excisable rescue construct.
Subsequently we successfully engineered the *lin-3* locus with the SEC CRISPR protocol (Dickinson et al., 2015), and generated an endogenous *mNeongreen::lin-3(zh108)* and an endogenous *lin-3::FRT::EGF::FRT(zh114)* strain (Master Thesis Silvan Spiri, October 2016), and the former was used for the LIN-3 polarity analysis in the "A sensitized whole genome RNAi screen identifies novel regulators of directed LIN-3 EGF secretion from the Anchor Cell" unpublished manuscript.

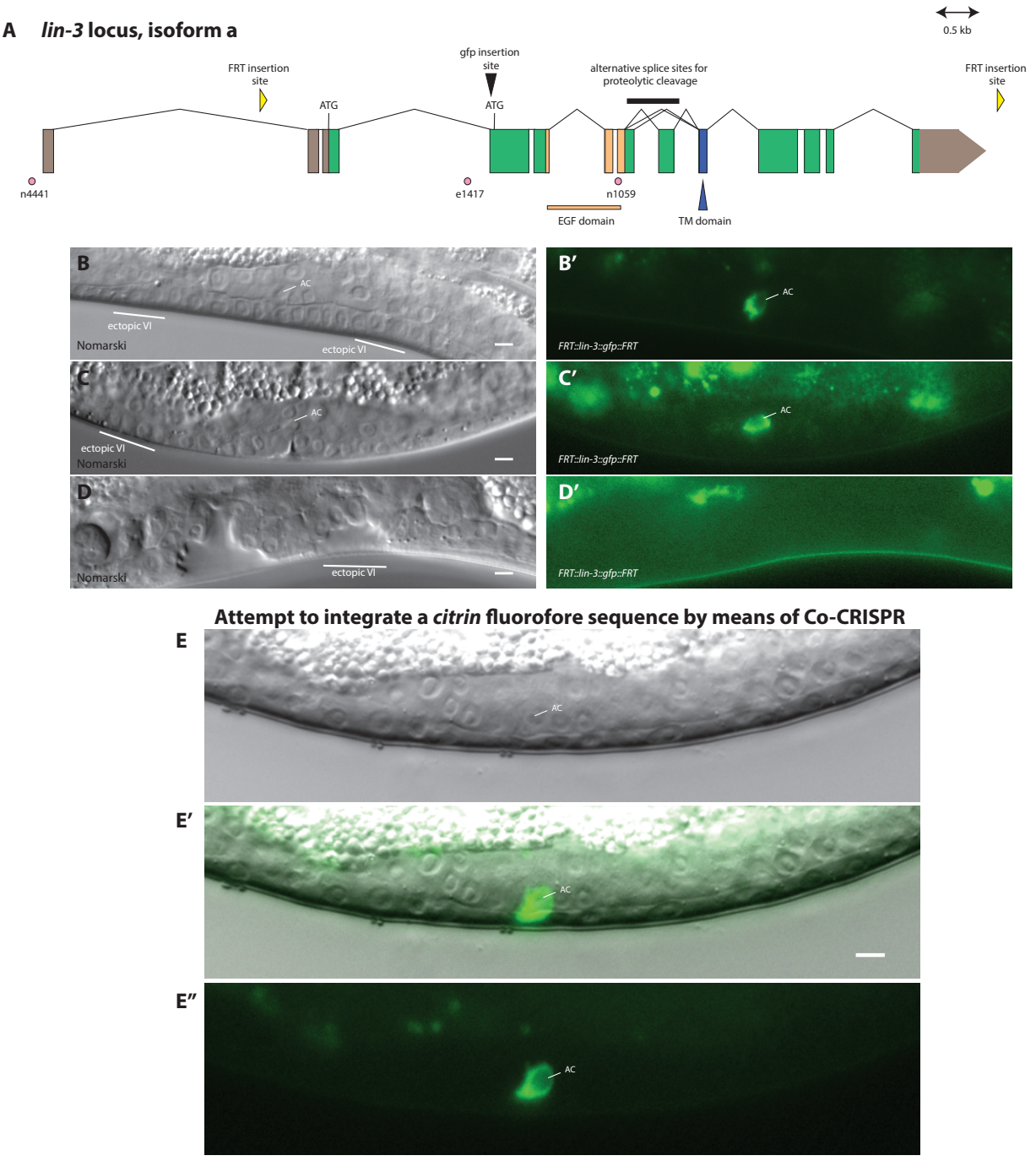


**Figure 3.3.7. *FRT::lin-3::gfp::FRT* reporter leads to ectopic vulval induction and does not rescue the *lin-3(n1059)* null allele**

(A) Cartoon shows elements of the genomic *lin-3* locus; (brown) the 5' and 3' UTR regions, (green) the translated exon regions, (orange) the EGF domain, (blue) the transmembrane (TM) domain and (black bar) the splice region that produces alternative proteolytic cleavage sites as well as (red circle) three known *lin-3* alleles. In addition, (black triangle) the inserted *gfp* sequence and (yellow triangle) the inserted FRT sites, which were cloned into the MoSCI recombination plasmid, are marked.
(B, C and D) Nomarski and (B', C' and D') fluorescence section images of a MoSCI integrated *FRT::lin-3::gfp::FRT* strain, with *gfp* expression in the AC, (B and B') at the P6.pxx cell stage (late L3), (C and C') the P6.pxxx stage (L3/L4) and (C and C') the X-tree stage (mid L4). The AC and ectopic vulval inductions are labeled and indicated by white line. Scale bar equals 5 µm.
(E) Nomarski, and (E') fluorescence and (E'') merged section images of the AC expressing *lin-3::citrin* (pLM2) at the mid-late L3 stage. A white line indicates the AC. Scale bar equals 5 µm.

### 3.3.8 Heat-shock induced, somatic CRISPR/Cas9 mediated *lin-3* knock-out

We explored the possibility of applying tissue-specific CRISPR/Cas9 mediated knock out and tested this based on the *lin-3* example. To this end, we injected a plasmid mix containing heat-shock inducible Cas9 (pMB67), a *lin-3* specific single guide (pLM15) as well as a co-injection marker into N2 worms. Of the generated two extrachromosomal strains (*zhEx584*), one line appeared more efficient and we analyzed this one in more detail. We submitted a late L2 staged larval population to a 30 minute heat-shock and analyzed the worms at the mid L4 larval stage. We found that approximately 30 percent of the analyzed worms with positive co-injection marker expression showed a vulva phenotype (Fig. 3.3.8, A-D). The observed vulval phenotypes consisted in hypoinduced (Fig. 3.3.8, D), vulvaless or dorsal lumen expansion defects. This shows that tissue-specific CRISPR/Cas9 mediated gene knock-out presents an additional tool for the analysis of essential gene functions.

Conclusion

From this experiment we can conclude that the tissue-specific CRISPR/Cas9 *lin-3* knock-out efficiency is at least 30 percent. A few factors contribute to the diminishing of the perceived efficiency. First, the $P_{hs}$*::cas-9* is expressed from an extrachromosomal (*zhEx584*) array. Thus, in case of mosaic array expression (Stinchcomb et al., 1985), in which the AC lost the array during development, several individuals could have been scored as wild-type, which should not have been taken into account at all. Second, although the heat-shock induced larval population was staged largely at the mid L2 developmental stage, it is almost impossible to have a tight confinement in the range of larval developmental progression. Thus, the exact developmental progression likely varied vastly. A staged population could possibly range from mid L1 to the mid L3 stage at the time of heat-shock induction. From this follows that *lin-3* might have been knocked-out within the time of duct cell formation at the L1 stage, leading to early larval lethality, due to impaired duct-cell development (Abdus-Saboor et al., 2011; Ferguson and Horvitz, 1985). A number of dead or arrested L1 larvae had been observed after the heat-shock, but had not been scored.

The observed dorsal lumen expansion defect (Fig. 3.3.8, C) might be caused by *lin-3* knock out at the mid L3 stage after successful vulval induction, due to loss in LIN-3 signaling from the vulF cells.

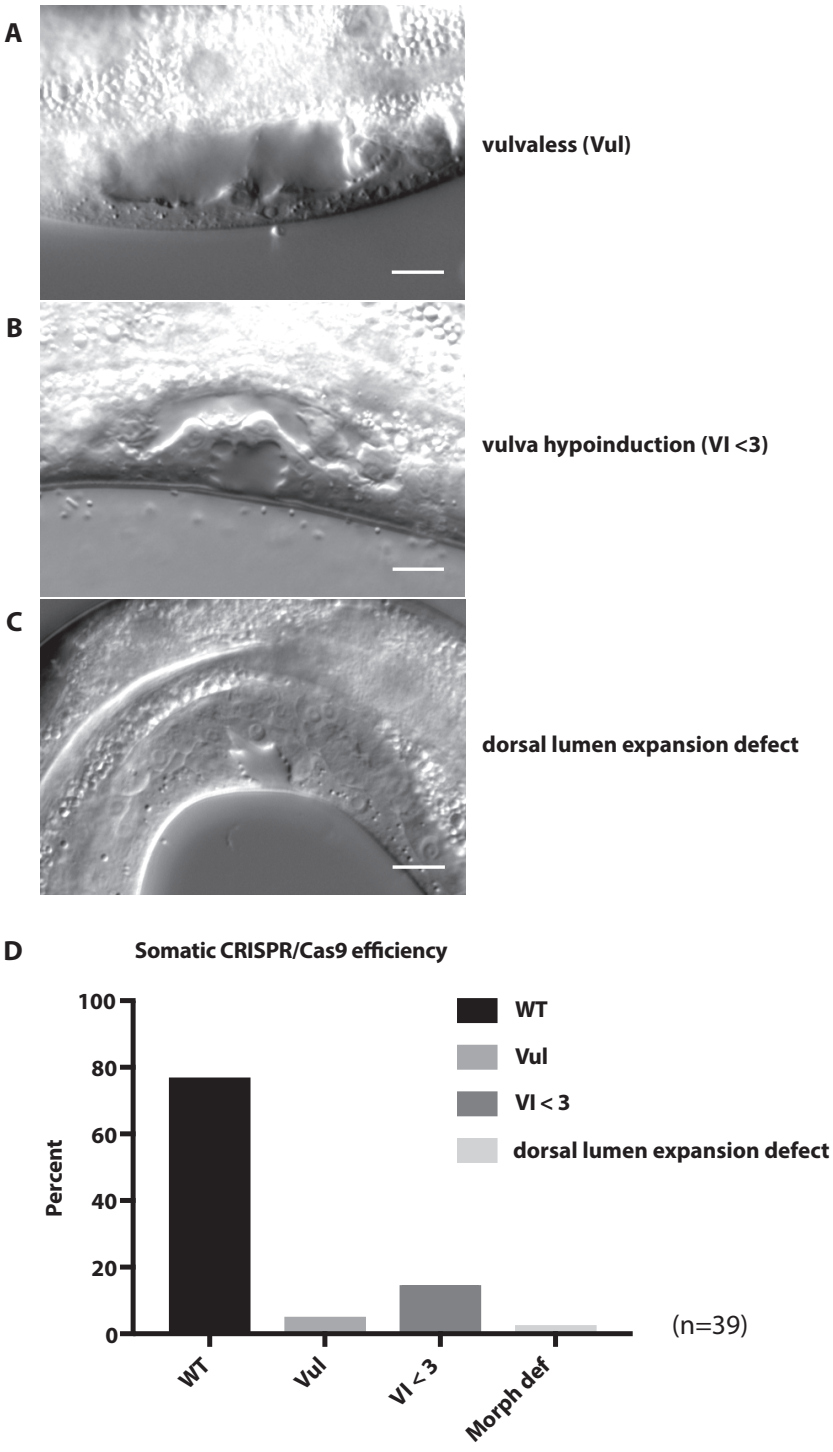


**Figure 3.3.8. Heat-shock induced, somatic CRISPR/Cas9 mediated *lin-3* knock-out produces known *lin-3* mutant phenotypes**

Nomarski sections of *zhEx584[$P_{hs}$>cas-9; sglin3; $P_{myo-2}$>mCherry]* strain, showing examples of phenotypes generated after heat-shock induced CAS9 expression together with lin-3 specific single guide RNAs. The heat-shock, as described in materials and methods, was performed on a staged larval (late L2) population, and worms were analyzed at the mid L4 larval stage. Images are of animals with, (A) Vulvaless (Vul), (B) vulva hypoinduction (VI < 3) and (C) dorsal lumen expansion defect phenotypes. Scale bar equals 10 µm.

(D) Plot shows percent of animals with defects (A-C) at the mid L4 stage, after heat-shock induction at the early L3 stage.

### 3.3.9 Loss of *mpk-1* ERK function in the AC does not cause increased dorsal lumen expansion defects

As a possible downstream component to the putative AC-specific LET-23 EGFR signaling in the process of dorsal lumen formation, we investigated MPK-1 ERK function in the AC. For this purpose, we analyzed an *mpk-1(lf)* strain, in which MPK-1 function is rescued by a VPC-specific *mpk-1* rescue transgene (*mpk-1(ga117)/qc1; gaIs47[*$P_{lin\text{-}31}$*>mpk-1(gf),* $P_{lin\text{-}31}$*>dmek(gf)]*) (Lackner and Kim, 1998). We compared homozygous *mpk-1(lf)* mutants to the balanced control and scored dorsal lumen expansion defects (Fig. 3.3.9, A and B). We found that dorsal lumen expansion defects in the vulva of mid L4 animals occurred at approximate equal frequency in both groups (Fig. 3.3.9, C).

Conclusion

Although there is no significant difference between the control and the *mpk-1(ga117)* mutant group, it is possible that the genotypes were not always associated correctly. The *mpk-1(ga117)* allele is linked to the *unc-32(e189)* and *dpy-17(e164)* markers that when homozygous, generates small, dumpy, coiler phenotypes. The qc1 balancer carries the *dpy-19(e1259)* temperature sensitive (20-25°C) marker, causing a dumpy phenotype and sterility, but has no inserted fluorescent marker in this specific strain (Edgley et al., 2006). Therefore, for the untrained eye it is difficult to differentiate the *mpk-1(ga117)* homozygous from the qc1 homozygous animals. We did not continue with the analysis of this strain.

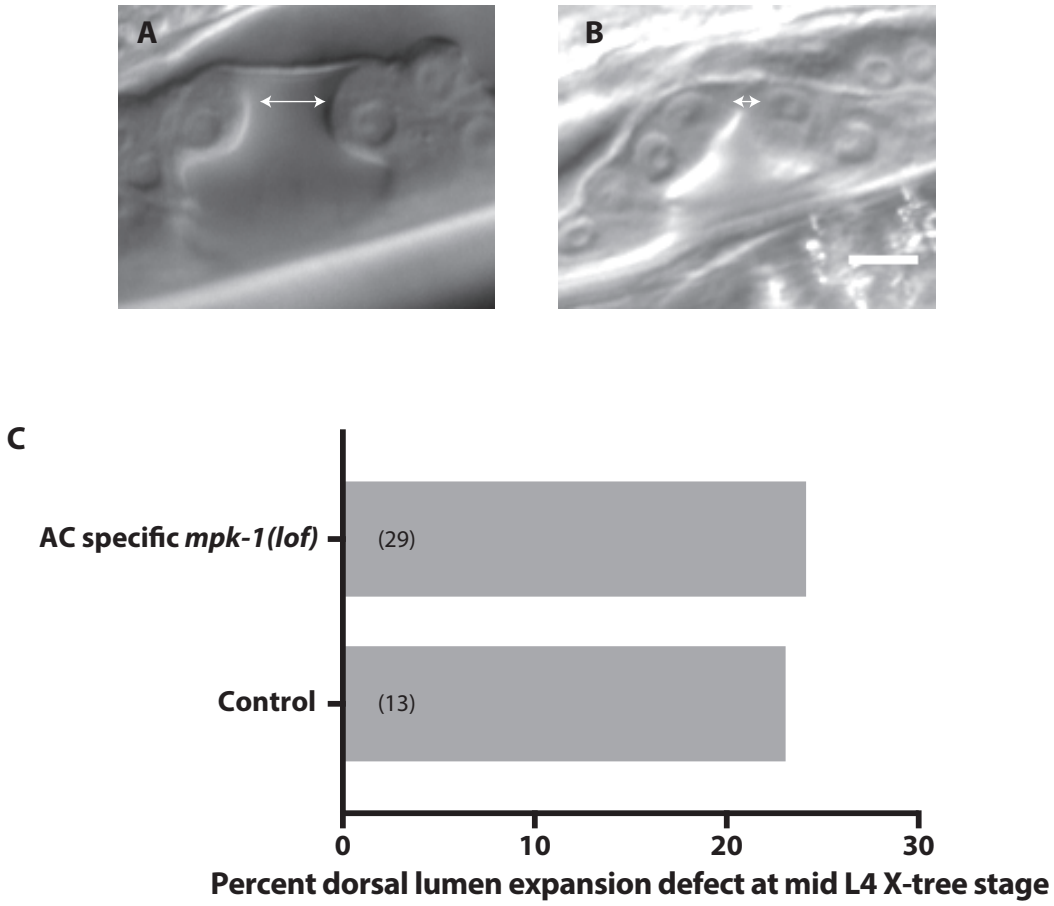


**Figure 3.3.9. Loss of *mpk-1* ERK function in the AC does not cause increased dorsal lumen expansion defects**
Dorsal lumen expansion analysis in *mpk-1(ga117)* loss of function mutants with VPC specific rescue of MPK-1 function (*gaIs47[$P_{lin-31}$>mpk-1(gf), $P_{lin-31}$>dmek(gf)]*) compared to balanced control, in which MPK-1 function is restored in AC.
(A) Nomarski section of wild-type dorsal lumen expansion (double headed arrow) of a mid L4 stage vulva of control *mpk-1(ga117)/qc1*; *gaIs47[$P_{lin-31}$>mpk-1(gf), $P_{lin-31}$>dmek(gf)]* animals.
(B) Nomarski section of dorsal lumen expansion defect (double headed arrow)of a mid L4 stage vulva of homozygous *mpk-1(ga117)*; *gaIs47[$P_{lin-31}$>mpk-1(gf), $P_{lin-31}$>dmek(gf)]* animals. Scale bar equals 5 µm.
(C) Plot shows Percent of animals with dorsal vulval lumen expansion defect at the mid L4 larval stage for control and *mpk-1(ga117)* mutants.

### 3.3.10 VPC-specific *lin-3* RNAi does not significantly enhance the *unc-6(ev400)* mediated basal lamina breaching defect

The *egl-38(n578)* allele significantly enhances the *unc-6(ev400)* mediated basal lamina breaching defect (Fig. 3.2.6). To determine whether loss in vulF specific *lin-3* expression is responsible for the basal lamina breaching enhancement, we performed VPC specific *lin-3* RNAi in an *unc-6(ev400); lam-1::gfp* background. We found that there is no significant defect in basal lamina breaching (Fig. 3.3.10, B) upon VPC specific *lin-3* knock-down compared to empty control at any developmental stage (Fig. 3.3.10, C). This suggests that VPC specific *lin-3* expression is not involved in promoting AC invasion.

We further wanted to test, whether perturbed LET-23 signaling in the AC enhances the *unc-6(ev400)* mutant mediated basal lamina breaching defect, and scored the latter in a strain expressing ectopic LET-23(rf) in the AC specific ($P_{cdh-3}$*>let-23(dom-rf)::gfp; unc-6(ev400))*. We found that the transgene causes a significant decrease in basal lamina breaching compared to the *unc-6(ev400)* single mutant at the mid L4 stage, but not compared to the $P_{cdh-3}$*>PLC∂$^{PH}$::mCherry; unc-6(ev400)* control (Fig. 3.3.10, J), which also showed a significant decrease in basal lamina breaching compared to the *unc-6(ev400)* single mutant. The $P_{cdh-3}$*>PLC∂$^{PH}$::mCherry* transgene was used as a control for *let-23(dom-rf)* transgene, since it is expressed form the same promoter and translates into a cell membrane associated protein.

Conclusion

Although there is no significant decrease in basal lamina breaching upon VPC specific *lin-3* RNAi, the result is not completely conclusive. In our mutant analysis of basal lamina breaching (Fig. 3.3.10, J), the percent of *unc-6(ev400)* single mutant animals, in which basal lamina breaching occurred was approximately 90 percent at the mid L4 stage. In our *unc-6(ev400)* VPC specific RNAi strain (*unc-6(ev400);rrf-3(pk1426); rde-1(ne219); lam-1::gfp;* $P_{lin-31}$*>rde-1(+))* basal lamina breaching only occurred in approximately 60 percent of the animals treated with empty RNAi. This is a significant decrease according to Fisher's exact probability test (p=0.0004). Thus, RNAi insensitive alleles (*rrf-3(pk1426); rde-1(ne219))* can have an amplifying effect on phenotypes generated from other mutant alleles, which must be taken into account when analyzing the data. It is therefore recommendable to have additional results that confirm one's hypothesis.

The basal lamina breaching results observed in the $P_{cdh-3}$*>let-23dom-rf::gfp; unc-6(ev400)* strain can be looked at from two angles (Fig. 3.3.10, J). First, since there is no significant difference in basal lamina breaching efficiency compared to the $P_{cdh-3}$*>PLC∂$^{PH}$::mCherry; unc-6(ev400)* control, it can be concluded that ectopic expression of any translational transgene can impair basal lamina breaching in an unspecific manner, merely by functioning perturbing regulation of the invasive membrane.

Another explanation can be drawn if we look at the specific transgene utilized in this experiment. $P_{cdh-3}$*>PLC∂$^{PH}$::mCherry,* is basically the PH domain of phospholipase C, which conveys binding specificity to the phosphoinositide PI(4,5)$P_2$, with the addition of an mCherry fluorophore. PLC-*∂* is a type of phospholipase C. All PLCs function by hydrolyzing PI(4,5)$P_2$, releasing the second messengers IP3 and DAG (Lemmon et al., 1995). The differences between the individual PLC types is given by their regulatory elements. Mammalian PLC-γ, the *C. elegans* PLC-3 homolog, has been shown to act directly downstream of ErbB (Anderson et al., 1990; Chattopadhyay et al., 1999) and LET-23 (Kariya et al., 2004) signaling. And PLC signaling has

been implicated in $PIP_2$ hydrolysis dependent cofilin release (van Rheenen et al., 2007). It is thus possible that $P_{cdh-3}$*>PLCϑ$^{PH}$::mCherry* expression conveys a specific basal lamina breaching impediment by sequestering putative access of PLC-3 to $PIP_2$. Ectopic $P_{cdh-3}$*>let-23dom-rf::gfp* expression might disturbe localized PLC-3 signaling and thus convey a specific defect in the organization of AC polarity and protrusion formation, rather than just a general disturbance.

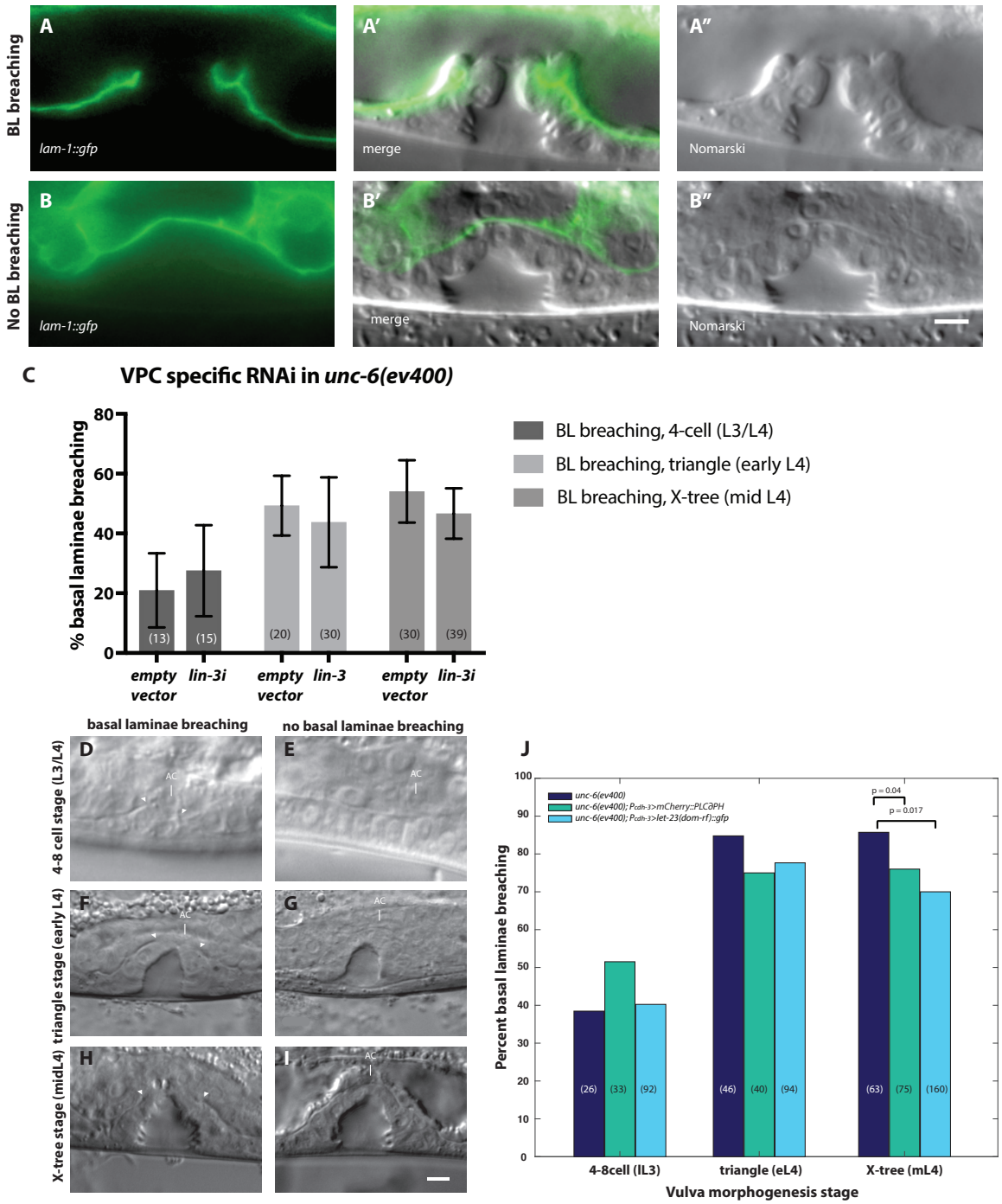


**Figure 3.3.10. VPC specific *lin-3* RNAi does not enhance the *unc-6(ev400)* mediated basal lamina breaching defect but aberrant LET-23 signaling effects it at a late stage**

**Figure 3.3.10. VPC specific *lin-3* RNAi does not enhance the *unc-6(ev400)* mediated basal lamina breaching defect but aberrant LET-23 signaling effects it at a late stage**

(A and B) *lam-1::gfp* fluorescence, (A'' and B'') Nomarski and (A' and B') merged section images of lateral view mid L4 stage X-tree vulvas, of *unc-6(ev400); rrf-3(pk1426); rde-1(ne219); lam-1::gfp;* $P_{lin-31}$*>rde-1(+)* animals treated with empty or *lin-3* RNAi. Examples of (A) basal lamina breaching and (B) no basal lamina breaching. Scale bar equals 5 µm.

(C) Plot shows average percent of animals with basal lamina breaching at indicated developmental stages, for the *unc-6(ev400); rrf-3(pk1426); rde-1(ne219); lam-1::gfp;* $P_{lin-31}$*>rde-1(+)* strain treated with empty or *lin-3* RNAi. The error bars are the standard error of the mean, calculated from three RNAi replica experiments. The average sample size is indicated in plot. According to Fisher's exact probability test there is no significant difference between empty and *lin-3* RNAi at any stage.

(D-I) Nomarski section images showing the lateral view of (D and E) 4-8 cell (L3/L4) stage, (F and G) triangle stage (early L4) and (H and I) X-tree (midL4) stage animals with an *unc-6(ev400)* mutant background. (D, F and H) Demonstrate examples of basal lamina breaching, the breached edges of the basal lamina are indicated by white triangles. (E, G, and I) Demonstrate examples, in which no basal lamina breaching occurs. White lines and text point to the AC when present in the section. Scale bar is equal 5 µm.

(J) Plot shows percent of animals with basal lamina breaching at indicated developmental stages, in the *[*$P_{cdh-3}$*> let-23(dom-rf)::gfp]; unc-6(ev400)* strain compared to *[*$P_{cdh-3}$*>mCherry::PLC*$\delta^{PH}$*]; unc-6(ev400)* control and *unc-6(ev400)* single mutant control. Statistical significance was analyzed with Fisher's exact probability test, and p-values are displayed in figure.

### 3.3.11 The ACs in *srh-247(tm6072)* mutants have no significant defect in *mNeongreen::lin-3* polarity

At the onset of the LIN-3 polarity study, we had found three interesting candidates (Table 3.1.1). The third candidate, *srh-247,* encodes a serpentine 7-pass-transmembrane receptor. RNAi against *srh-247* in the *gap-1(ga133)* background resulted in hypo- and hyperinduced vulval phenotypes (Matthias Morf Thesis). Moreover, this gene had been selected due to its *lin-3::gfp* and $PIP_2$ AC polarity phenotype upon RNAi (unpublished data, Matthias Morf).
To confirm these data, we performed mutant analysis of the *srh-247(tm6072)* allele, which showed a weak hyperinduced phenotype, as well as 1° vulval cell fate shift in combination with the *gap-1(ga133)* allele (Fig. 3.3.11, J and K), at a low penetrance. These data coincide with the RNAi data, except that no underinduced phenotype was observed.
Next, we looked at LIN-3 polarity in the *srh-247(tm6072)* allele to verify the RNAi screen results, in which LIN-3 was depolarized, but $PIP_2$ polarity remained. We found no significant change in the mean LIN-3 polarity index in *srh-247(tm6072)* mutants compared to control animals at any of the analyzed larval stages (Fig. 3.3.11, C, F and I). We therefore did not further investigate this candidate gene.

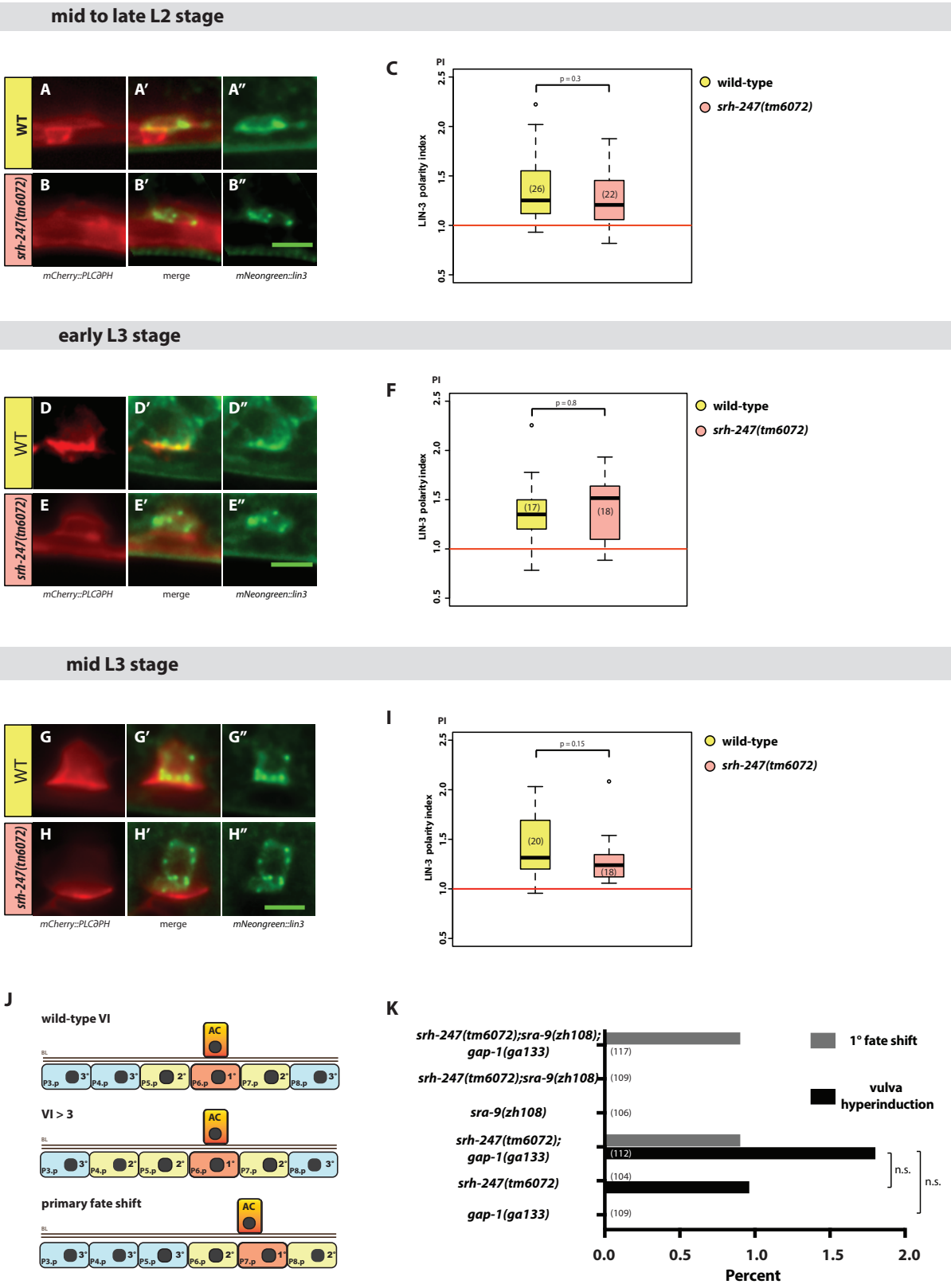


**Figure 3.3.11. The ACs in *srh-247(tm6072)* mutants have no defect in *mNeongreen::lin-3* polarity**

(A-B'') AC expression pattern of summed z-projections of (A and B) $P_{cdh-3}$>*mCherry::PLCδ*$^{PH}$ and (A'' and B'') the endogenous *mNeongreen::lin-3* reporter at the mid L2 larval stage in (A) wild-type and (B) *srh-247(tm6072)* mutants. Scale bar equals 5 µm. Images were taken of (A-B'') mid to late L2 larval stage, (D-E'') early L3 larval stage and (G-H'') mid L3 larval stage animals.

(C, F and I) Boxplots show the distribution of the measured dorsal to ventral LIN-3 polarity indexes (PI). The LIN-3 polarity index was calculated from summed z-projections of deconvolved stacks with 0.2 µm Z-spacing of ACs expressing the *mNeongreen::lin-3* reporter. The relative polarity index was calculated by dividing equal areas of the average intensity of the ventral by the average intensity of the dorsal half of the AC. PI > 1 indicates higher average intensity on ventral relative to the dorsal half of the AC.
(C) mid to late L2 larval stages, (F) early L3 larval stages and (I) mid L3 larval stages. According to independent t-test of unequal variance, there is no significant diferrence between wild-type and *srh-247(tm6072)* mutants, p-values are indicated in Figure.
(J) Cartoon illustrating observed vulval induction (VI) and AC to Pn.p alignment (1° fate shift) phenotypes that were scored. Vulval induction scoring: wild-type VI=3 and hyperinduced VI > 3. AC to P6.p alignment (1° fate shift) scoring: In wild-type P6.p is 1° fated. In a 1° fate shift, P5.p or P7.p are 1°fated.
(K) Plot shows percent of animals of indicated genotype with vulva hyperinduction or 1° fate shift phenotype. The sample size n for each genotype is displayed in plot. According to Fisher's exact probability test there is no significant difference between the different genotypes.

## 3.3.12 References


**Abdus-Saboor, I., Mancuso, V. P., Murray, J. I., Palozola, K., Norris, C., Hall, D. H., Howell, K., Huang, K. and Sundaram, M. V.** (2011). Notch and Ras promote sequential steps of excretory tube development in C. elegans. *Development* **138**, 3545–3555.

**Anderson, D., Koch, C. A., Grey, L., Ellis, C., Moran, M. F. and Pawson, T.** (1990). Binding of SH2 domains of phospholipase C gamma 1, GAP, and Src to activated growth factor receptors. *Science* **250**, 979–982.

**Aroian, R. V. and Sternberg, P. W.** (1991). Multiple functions of let-23, a Caenorhabditis elegans receptor tyrosine kinase gene required for vulval induction. *Genetics* **128**, 251–267.

**Aroian, R. V., Lesa, G. M. and Sternberg, P. W.** (1994). Mutations in the Caenorhabditis elegans let-23 EGFR-like gene define elements important for cell-type specificity and function. *EMBO J.* **13**, 360–366.

**Arribere, J. A., Bell, R. T., Fu, B. X. H., Artiles, K. L., Hartman, P. S. and Fire, A. Z.** (2014). Efficient marker-free recovery of custom genetic modifications with CRISPR/Cas9 in Caenorhabditis elegans. *Genetics* **198**, 837–846.

**Bae, Y.-K., Sung, J. Y., Kim, Y.-N., Kim, S., Hong, K. M., Kim, H. T., Choi, M. S., Kwon, J. Y. and Shim, J.** (2012). An in vivo C. elegans model system for screening EGFR-inhibiting anti-cancer drugs. *PLoS ONE* **7**, e42441.

**Brenner, S.** (1974). The genetics of Caenorhabditis elegans. *Genetics* **77**, 71–94.

**Burdine, R. D., Branda, C. S. and Stern, M. J.** (1998). EGL-17(FGF) expression coordinates the attraction of the migrating sex myoblasts with vulval induction in C. elegans. *Development* **125**, 1083–1093.

**Chang, C., Newman, A. P. and Sternberg, P. W.** (1999). Reciprocal EGF signaling back to the uterus from the induced C. elegans vulva coordinates morphogenesis of epithelia. *Current Biology* **9**, 237–246.

**Chattopadhyay, A., Vecchi, M., Ji, Q. S., Mernaugh, R. and Carpenter, G.** (1999). The role of individual SH2 domains in mediating association of phospholipase C-gamma1 with the activated EGF receptor. *J. Biol. Chem.* **274**, 26091–26097.

**Dickinson, D. J., Pani, A. M., Heppert, J. K., Higgins, C. D. and Goldstein, B.** (2015). Streamlined Genome Engineering with a Self-Excising Drug Selection Cassette. *Genetics* **200**, 1035–1049.

**Edgley, M. L., Baillie, D. L., Riddle, D. L. and Rose, A. M.** (2006). Genetic balancers. *WormBook* 1–32.

**Ferguson, E. L. and Horvitz, H. R.** (1985). Identification and characterization of 22 genes that affect the vulval cell lineages of the nematode Caenorhabditis elegans. *Genetics* **110**, 17–72.

**Hagedorn, E. J., Yashiro, H., Ziel, J. W., Ihara, S., Wang, Z. and Sherwood, D. R.** (2009). Integrin Acts Upstream of Netrin Signaling to Regulate Formation of the Anchor Cell•s Invasive Membrane in C. elegans. *Developmental Cell* 17, 187–198.

**Horvath, P. and Barrangou, R.** (2010). CRISPR/Cas, the immune system of bacteria and archaea. *Science* **327**, 167–170.

**Hwang, B. J.** (2004). A cell-specific enhancer that specifies lin-3 expression in the C. elegans anchor cell for vulval development. *Development* **131**, 143–151.

**Kariya, K.-I., Bui, Y. K., Gao, X., Sternberg, P. W. and Kataoka, T.** (2004). Phospholipase Cepsilon regulates ovulation in Caenorhabditis elegans. *Developmental Biology* **274**, 201–210.

**Lackner, M. R. and Kim, S. K.** (1998). Genetic analysis of the Caenorhabditis elegans MAP kinase gene mpk-1. *Genetics* **150**, 103–117.

**Lemmon, M. A., Ferguson, K. M., O'Brien, R., Sigler, P. B. and Schlessinger, J.** (1995). Specific and high-affinity binding of inositol phosphates to an isolated pleckstrin homology domain. *Proc. Natl. Acad. Sci. U.S.A.* **92**, 10472–10476.

**Liu, J., Tzou, P., Hill, R. J. and Sternberg, P. W.** (1999). Structural requirements for the tissue-specific and tissue-general functions of the Caenorhabditis elegans epidermal growth factor LIN-3. *Genetics* **153**, 1257–1269.

**Moghal, N. and Sternberg, P. W.** (2003). Extracellular domain determinants of LET-23 (EGF) receptor tyrosine kinase activity in Caenorhabditis elegans. *Oncogene* **22**, 5471–5480.

**Qadota, H., Inoue, M., Hikita, T., K ppen, M., Hardin, J. D., Amano, M., Moerman, D. G. and Kaibuchi, K.** (2007). Establishment of a tissue-specific RNAi system in C. elegans. *Gene* 400, 166–173.

**Ririe, T. O., Fernandes, J. S. and Sternberg, P. W.** (2008). The Caenorhabditis elegans vulva: a post-embryonic gene regulatory network controlling organogenesis. *Proc. Natl. Acad. Sci. U.S.A.* **105**, 20095–20099.

**Snutch, T. P. and Baillie, D. L.** (1983). Alterations in the pattern of gene expression following heat shock in the nematode Caenorhabditis elegans. *Can. J. Biochem. Cell Biol.* **61**, 480–487.

**Stinchcomb, D. T., Shaw, J. E., Carr, S. H. and Hirsh, D.** (1985). Extrachromosomal DNA transformation of Caenorhabditis elegans. *Mol. Cell. Biol.* **5**, 3484–3496.

**van Rheenen, J., Song, X., van Roosmalen, W., Cammer, M., Chen, X., Desmarais, V., Yip, S.-C., Backer, J. M., Eddy, R. J. and Condeelis, J. S.** (2007). EGF-induced PIP2 hydrolysis releases and activates cofilin locally in carcinoma cells. *J Cell Biol* **179**, 1247–1259.

**Voutev, R. and Hubbard, E. J. A.** (2008). A "FLP-Out" system for controlled gene expression in Caenorhabditis elegans. *Genetics* **180**, 103–119.

**Yochem, J., Gu, T. and Han, M**. (1998). A new marker for mosaic analysis in Caenorhabditis elegans indicates a fusion between hyp6 and hyp7, two major components of the hypodermis. *Genetics* 149, 1323–1334.

**Zeiser, E., Frøkjær-Jensen, C., Jorgensen, E. and Ahringer, J.** (2011). MosSCI and Gateway Compatible Plasmid Toolkit for Constitutive and Inducible Expression of Transgenes in the C. elegans Germline. *PLoS ONE* **6**, e20082–6.

## 3.4 Contributions to previous Publications

### 3.4.1 Coordinated Lumen Contraction and Expansion during Vulval Tube Morphogenesis in *Caenorhabditis elegans*

My contribution to the publication was by performing a cross, generating the AH2338 (*qyIs23[$P_{cdh\text{-}3}$>mCherry::PLC$\delta^{PH}$] II;swIs79[ajm-1::gfp, seamcell::gfp, pUnc-119] IV*) strain, used in Figure 7 and S1.

Developmental Cell
Article

# Coordinated Lumen Contraction and Expansion during Vulval Tube Morphogenesis in *Caenorhabditis elegans*

Sarfarazhussain Farooqui,[1,2] Mark W. Pellegrino,[1,3] Ivo Rimann,[1,4] Matthias K. Morf,[1,2] Louisa Müller,[1] Erika Fröhli,[1] and Alex Hajnal[1,*]
[1]University of Zürich, Institute of Molecular Life Sciences, Winterthurerstrasse 190, CH-8057, Switzerland
[2]Molecular Life Sciences PhD Program, Uni ETH Zürich, CH-8057, Switzerland
[3]Present address: Memorial Sloan Kettering Cancer Center, Rockefeller Research Laboratories, RRL 617B, 430 East 67th Street, New York, NY 10065, USA
[4]Present address: The Scripps Research Institute, 10550 North Torrey Pines Road, La Jolla, CA 92037, USA
*Correspondence: alex.hajnal@imls.uzh.ch
http://dx.doi.org/10.1016/j.devcel.2012.06.019

## SUMMARY

**Morphogenesis is a developmental phase during which cell fates are executed. Mechanical forces shaping individual cells play a key role during tissue morphogenesis. By investigating morphogenesis of the *Caenorhabditis elegans* hermaphrodite vulva, we show that the force-generating actomyosin network is differentially regulated by NOTCH and EGFR/RAS/MAPK signaling to shape the vulval tube. NOTCH signaling activates expression of the RHO kinase LET-502 in the secondary cell lineage through the ETS-family transcription factor LIN-1. LET-502 induces actomyosin-mediated contraction of the apical lumen in the secondary toroids, thereby generating a dorsal pushing force. In contrast, MAPK signaling in the primary lineage downregulates LET-502 RHO kinase expression to prevent toroid contraction and allow the gonadal anchor cell to expand the dorsal lumen of the primary toroids. The antagonistic action of the MAPK and NOTCH pathways thus controls vulval tube morphogenesis linking cell fate specification to morphogenesis.**

## INTRODUCTION

Organogenesis requires the differentiation of selected cells followed by tissue morphogenesis, which involves cell shape changes, cell-cell interactions, and coordinated cell movements. Tubes are the basic building blocks of most epithelial organs. Tube morphogenesis is therefore an essential process in various developmental processes such as embryonic development, tissue vascularization, and the development of most epithelial organs (Andrew and Ewald, 2010; Rodríguez-Fraticelli et al., 2011). During tissue morphogenesis, mechanical forces generated between cells are necessary to determine the proper size and shape of an organ. With a high degree of mechanical coupling between cells, tissue morphogenesis could be governed by forces from a few cells pushing or pulling all other cells (Gov, 2007). Major challenges are therefore to identify the cells that exert physical forces and the molecular pathways that control the generation of forces. In vivo models used to address these questions include vascular sprouting and branching in vertebrates, neuroblast migration during lateral line formation in the Zebrafish embryo, border cell migration in *Drosophila* ovaries, and tracheal morphogenesis in the *Drosophila* embryo (Rodríguez-Fraticelli et al., 2011; Schottenfeld et al., 2010). In most cases, ''leader cells'' at the front of an advancing group of cells generate forces that are transmitted rearward from cell to cell and thus act to pull along the ''follower cells'' (Gov, 2007; Omelchenko et al., 2003; Poujade et al., 2007; Vaughan and Trinkaus, 1966). However, forces that arise predominately within follower cells and extend over several cell rows to cells at the leading edge have been observed during the collective migration of cultured MDCK cells (Xavier Trepat et al., 2009).

Here, we are investigating morphogenesis of the *Caenorhabditis elegans* hermaphrodite vulva, a tubular organ that connects the uterus to the outside and permits egg laying. While the molecular mechanisms that regulate cell fate specification during vulval induction have been characterized in great detail, much less is known about the signaling pathways controlling vulval morphogenesis (Sternberg, 2005). During vulval induction, the interplay between the EGFR/RAS/MAPK and NOTCH pathways determines the two vulval cell fates. The gonadal anchor cell (AC) induces the primary (1°) cell fate in the adjacent vulval precursor cell (VPC) P6.p by activating the EGFR/RAS/MAPK pathway. High levels of MAPK activity in P6.p result in the phosphorylation and inactivation of the LIN-1 ETS transcription factor that represses 1° cell fate specification in the remaining VPCs (Beitel et al., 1995). P6.p then induces via a lateral DELTA/NOTCH signal the neighboring VPCs P5.p and P7.p to adopt the secondary (2°) cell fate (Greenwald, 2005). The three induced VPCs—P5.p, P6.p, and P7.p—go through three rounds of cell divisions to generate 22 vulval cells with seven distinct subfates. The seven descendants of each P5.p and P7.p adopt the VulA, VulB1, VulB2, VulC, and VulD subfates, while the eight 1° descendants of P6.p adopt the VulE and VulF subfates (Figure 1I) (Sharma-Kishore et al., 1999). During the subsequent phase of morphogenesis, the vulval cells invaginate and move dorsal (i.e., from the ventral midline toward the dorsal uterus) to form the vulval lumen. At the same time, the cells extend

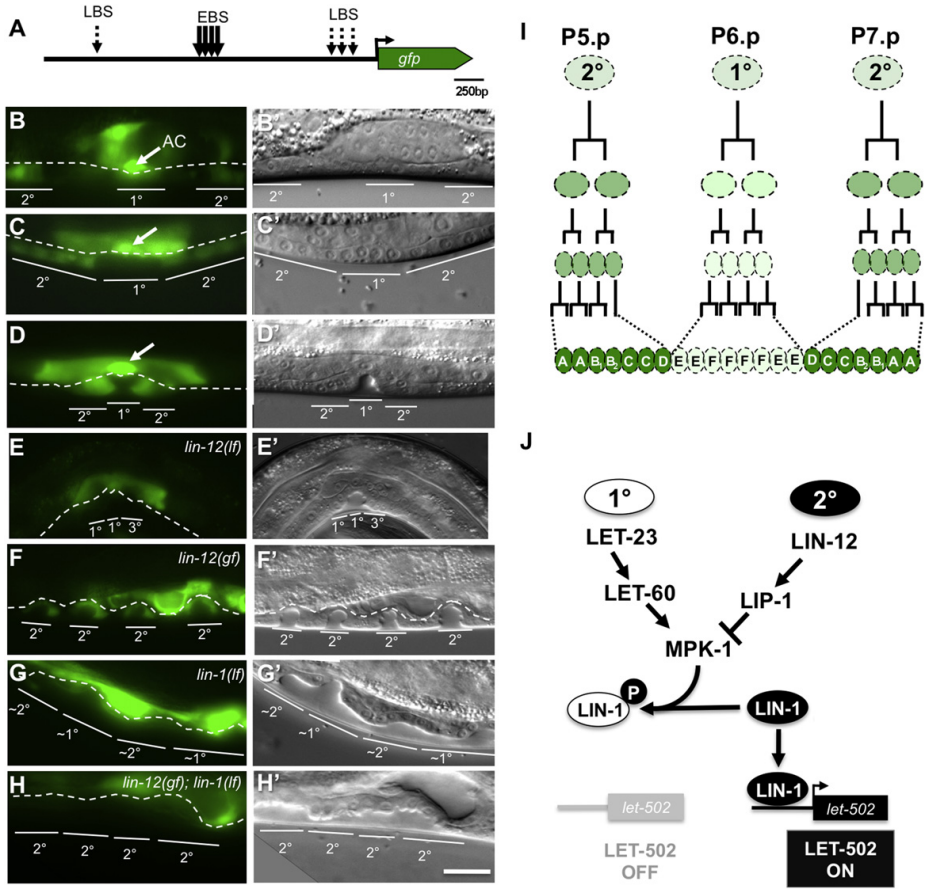


**Figure 1. LIN-12 NOTCH Induces LET-502 Expression in the 2° Vulval Lineage via LIN-1 ETS**

(A) Structure of the transcriptional $P_{let\text{-}502}$*::gfp* reporter. The locations of the four LBS and EBS sites are indicated.

(B–H') Time-course analysis of $P_{let\text{-}502}$*::gfp* expression from the L2 until the L4 stage with, in (B') through (D'), the corresponding Nomarski images. (E) $P_{let\text{-}502}$*::gfp* expression and (E') the corresponding Nomarski image in *lin-12(lf)*, (F and F') *lin-12(gf)*, (G and G') *lin-1(lf)*, and (H and H') *lin-12(gf); lin-1(lf)* mutants. In all panels, anterior is to the left and ventral is to the bottom, and the dotted lines represent the uterine-vulval boundary. Scale bar, 5 μm.

(I) Summary of the *let-502* expression pattern in the vulval cell lineage. The VulA through VulF subfates are indicated.

(J) Model for the transcriptional regulation of *let-502* by LIN-12, LET-23 EGFR, MPK-1 MAPK, and LIN-1. Alleles used: *lin-12(n137 gf)*, *lin-12(n137 gf n720lf)*, *lin-1(n301)*, and *sIs1078*.

circumferentially toward the vulval midline, where they make homotypic contacts with their contralateral partner cells of the same subfate, thereby forming seven concentric epidermal rings called *vulval toroids* (Figure 7K). In a final step, the AC expands the dorsal lumen of VulF (Estes and Hanna-Rose, 2009) and fuses with the uterine-seam cell (utse) syncytium.

We have found that NOTCH signaling in the 2° cells positively regulates via the LIN-1 transcription factor expression of the Rho-kinase LET-502, which induces a contractile force on the apical surface of the 2° toroids and thereby generates a dorsal pushing force. EGFR/RAS/MAPK signaling, on the other hand, prevents contraction of the 1° toroids by repressing LET-502 expression, allowing the AC to expand the 1° toroid lumen and connect the toroids to the uterus. Thus, the antagonistic NOTCH and RAS/MAPK signaling pathways coordinate actomyosin-induced forces to shape the toroids.

## RESULTS

### LET-502 Is Differentially Expressed in the 1° and 2° Vulval Cell Lineages

We identified *let-502*, which encodes a Rho-activated kinase (Wissmann et al., 1997), as a gene specifically expressed in the 2° vulval lineage in an in silico screen for genes containing at

least three conserved LAG-1 binding sites (LBSs) (Christensen et al., 1996) in their regulatory regions (dashed arrows in Figure 1A) (S.F. and A.H., unpublished data). To analyze the expression pattern of *let-502* during vulval development, we examined the expression of a $P_{let\text{-}502}$*::gfp* transcriptional reporter containing 2.8 kilobase (kb) pairs upstream of the *let-502* translational start site fused to a *gfp* cassette (a kind gift of the *C. elegans* Gene Expression Consortium). $P_{let\text{-}502}$*::gfp* was expressed at equal levels in P3.p–P8.p before vulval induction in early to mid-L2 larvae (Figure 1B; data not shown). During vulval induction, $P_{let\text{-}502}$*::gfp* was downregulated in the 1° descendants of P6.p, while expression gradually increased in the P5.p and P7.p descendants that form the 2° lineage (Figures 1C and 1I). *let-502* expression peaked at the onset of vulval morphogenesis, when highest expression was observed in the 2° cells (Figures 1D and 1I; Figure S1A available online). Thus, *let-502* transcription is upregulated in the 2° cells and downregulated in the 1° cells after the vulval cell fates have been specified.

## LET-502 Expression Is Regulated by LIN-12 NOTCH Signaling via LIN-1 ETS

Since the 2° lineage-specific expression of *let-502* is characteristic of LIN-12 target genes, we tested if LIN-12 controls *let-502* transcription. $P_{let\text{-}502}$*::gfp* was expressed in the ectopic 2° cells induced in *lin-12(gf)* mutants, while vulval *let-502* expression was absent in *lin-12(lf)* mutants, in which P5.p and P7.p adopt the 1° or 3° instead of the 2° cell fate (Figures 1E and 1F) (Greenwald, 2005). To test if LIN-12 directly regulates *let-502* transcription, we created the $P_{let\text{-}502}$ *ΔLBS::gfp* reporter, in which all four LBSs had been mutated from RTGGGAA to RAGGGAA. Surprisingly, the $P_{let\text{-}502}$ *ΔLBS::gfp* mutant reporter did not show any change in the expression pattern (Figure 2A; Figure S1B), suggesting that *let-502* is an indirect LIN-12 target. Deletion analysis of the *let-502* regulatory region identified an enhancer element required for 2°-specific expression in a 300 bp region between positions −1800 and −1400 containing a cluster of four putative ETS binding sites (EBS) defined by the motif $GGA^{A}/_{T}$ (Figure 2A) (Sementchenko and Watson, 2000; Zhang and Greenwald, 2011). The *lin-1* gene encodes an ETS family transcription factor that was originally identified as a repressor of vulval development (Beitel et al., 1995). We thus examined *let-502* expression in *lin-1(n304lf)* mutants, in which all six VPCs adopt an alternating pattern of 1° and 2° cell fates. Even though P5.p and P7.p execute a normal 2° cell lineage in *lin-1(lf)* mutants, no vulval expression of the $P_{let\text{-}502}$*::gfp* reporter was observed in *lin-1(lf)* mutants (Figure 1G). To determine the epistatic relationship between *lin-12* and *lin-1*, we analyzed $P_{let\text{-}502}$*::gfp* expression in *lin-12(gf); lin-1(lf)* double mutants, in which all VPCs adopt a 2° cell fate. Similar to *lin-1(lf)* single mutants, no vulval $P_{let\text{-}502}$*::gfp* expression was detected in *lin-12(gf); lin-1(lf)* double mutants (Figure 1H), indicating that LIN-12 regulates *let-502* expression indirectly via LIN-1. Since LIN-1 activity is negatively regulated by MAPK phosphorylation in 1° cells and LIN-12 signaling blocks MAPK activation in 2° cells by inducing inhibitors of the RAS/MAPK pathway such as the MAPK phosphatase LIP-1 (Berset et al., 2001; Greenwald, 2005), we hypothesized that the nonphosphorylated form of LIN-1 may act downstream of LIN-12 as a positive regulator of *let-502* transcription in the 2° cell lineage (Figure 1J).

## The Nonphosphorylated Form of LIN-1 Activates *let-502* Transcription in the 2° Vulval Cells

To test the model shown in Figure 1J, we generated the $P_{let\text{-}502}$ *ΔEBS::gfp* reporter, in which the four putative EBS were deleted (Figure 2A). In two of three transgenic $P_{let\text{-}502}$ *ΔEBS::gfp* lines, no reporter expression was detected in the vulval cells, and a third line showed weak expression (Figures 2A and S1C). We then examined whether LIN-1 binds to the *let-502* enhancer region by performing chromatin immunoprecipitation (ChIP) experiments (Mukhopadhyay et al., 2008). Since LIN-1 activity is negatively regulated by MPK-1-mediated phosphorylation at the C terminus, we generated a nonphosphorylatable version of LIN-1 by truncating 90 amino acids from the C terminus, analogous to the mutation in the *lin-1(e1790)* gain-of-function allele (Jacobs et al., 1998). This constitutively active LIN-1 (LIN-1ΔCT) was tagged with hemagglutinin-streptavidin (HA) at the N terminus and expressed under control of the heat shock promoter (*hs::HA::lin-1ΔCT*). In *hs::HA::lin-1ΔCT* animals analyzed 4 hr after a brief heat shock by ChIP, we detected strongest binding to region B (positions −1518 to −1660 bp) that spans the four EBS and weaker binding to regions A and C (Figures 2A and 2B). In *hs::HA::lin-1ΔCT* animals that had not been heat shocked, binding to region B was still above background levels, probably because of basal activity of the heat shock promoter at the standard growth temperature (Figure 2B).

Next, we investigated whether induction of LIN-1ΔCT after cell fate specification has occurred was sufficient to induce *let-502* expression. In *hs::lin-1ΔCT;* $P_{let\text{-}502}$*::gfp* animals that had been heat shocked at the Pnp.x stage, *let-502* expression was upregulated in the 1° and 2° cells at the onset of invagination (Figures 2C and 2D). However, if LIN-1ΔCT expression was induced later during the Pn.pxx or Pn.pxxx stages, elevated *let-502* expression was only detected in the 2° toroids of L4 larvae, suggesting that, at later stages, LIN-1 is not sufficient to induce *let-502* in the 1° lineage (Figures 2E and 2F). We also examined *lin-31*, which encodes a Forkhead transcription factor that represses the 1° vulval cell fate in P6.p together with LIN-1 (Tan et al., 1998; Miller et al., 1993). *let-502* continued to be expressed in *lin-31(lf)* mutants, both in the descendants of the ectopically induced distal VPCs and in the P5.p and P7.p descendants (Figure 2G). Thus, LIN-1 does not require LIN-31 to induce *let-502* expression.

Since the MAP kinase MPK-1 inactivates LIN-1 via phosphorylation, we hyperactivated MPK-1 using a heat-shock-inducible *mpk-1* transgene (*hs::mpk-1*) to temporally control LIN-1 activity (Lackner and Kim, 1998). Consistent with the model shown in Figure 1J, an increase in MPK-1 activity at the Pn.px-to-Pnp.xx stage resulted in the loss of *let-502* expression at the late L4 (Pn.pxxx) stage (Figure 2I).

Taken together, the binding of LIN-1ΔCT to EBS sites that are required for vulval *let-502* expression and the changes in *let-502* reporter expression after activation or inactivation of LIN-1 indicate that the LIN-1 positively regulates *let-502* transcription in the 2° cell lineage.

## LET-502 Is Required for Toroid Contraction during Vulval Morphogenesis

To investigate the role of LET-502 during vulval morphogenesis, we examined the apical cell junctions of the toroids using a DLG-1::RFP reporter (Diogon et al., 2007). In addition, we

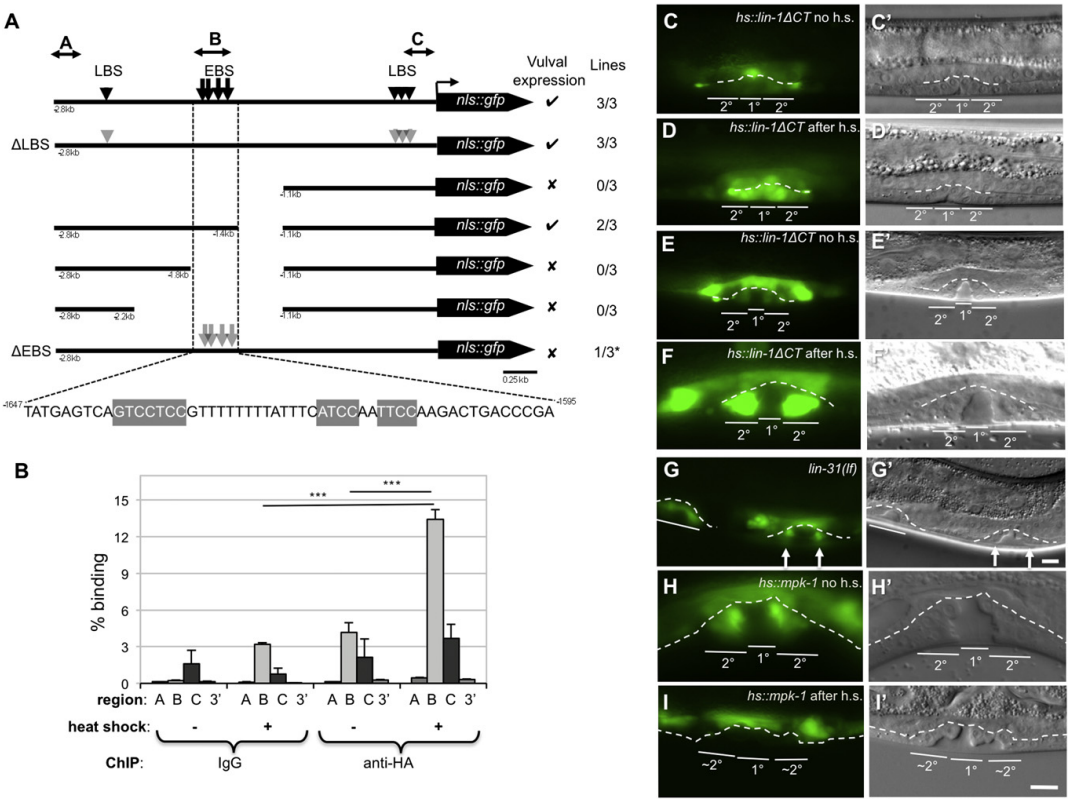


**Figure 2. Nonphosphorylated LIN-1 Induces *let-502* Transcription in the 2° Vulval Cells**

(A) Structure of reporter constructs used to assay *let-502* promoter activity. Three independent lines were analyzed for each construct. Arrows indicate the positions of the putative ETS binding sites (EBS) and arrowheads indicate the LAG-2 binding sites (LBS). Gray arrowheads in the ΔLBS construct indicate the point mutations changing the LBS from RTGGGAA to RAGGGAA. Grey arrows in the ΔEBS construct indicate the deletions of the EBS and the deleted nucleotides are shaded in gray. The double-headed arrows indicate regions A, B, and C used as probes for ChIP.

(B) Binding of LIN-1ΔCT to the *let-502* 5′ regulatory region detected by ChIP followed by Q-PCR. A, B, and C refer to the probe regions shown in (A) and 3′ to a probe at the 3′ end of the gene. Error bars indicate the SDs of three experiments. **p ≤ 0.01, ***p ≤ 0.001, two-tailed t tests.

(C–I') $P_{let\text{-}502}$*::gfp* expression and the (C') corresponding Nomarski image in a *hs::lin-1ΔCT* larva at the onset of invagination (late Pn.pxx to early Pn.pxxx stage) without heat shock, and in (D) and (D'), the same stage after heat shock at the Pn.px stage. (E), (E'), (F), and (F') show $P_{let\text{-}502}$*::gfp* expression in a *hs::lin-1ΔCT* larva at the late L4 (Pn.pxxx) stage without and after heat shock at the late Pn.pxx stage, respectively. (G) and (G') show $P_{let\text{-}502}$*::gfp* expression in a *lin-31(lf)* L4 larva. Note that expression was detected in the P.5 and P7.p descendant (arrows) as well as in the ectopically induced P3.p and P4.p descendants (underlined). (H) and (H') show $P_{let\text{-}502}$*::gfp* expression in a *hs::mpk-1* larva without and, in (I) and (I') after heat shock at the Pn.pxx stage. In all panels, anterior is to the left and ventral is to the bottom, and the dotted lines represent the uterine-vulval boundary. Scale bars, 5 μm. Alleles used in (A): *zhEx393, 398, 399, 401-405*, (B): *zhEx394*, (C through I): *lin-31(n301), gaIs36, zhEx395, sIs10781*.

See also Figure S1.

visualized filamentous actin (F-actin) microfilaments (MFs) using a reporter, in which the actin-binding domain of Abp140 (first 17 amino acids) had been fused to GFP and expressed under control of the pan-epithelial *dlg-1* promoter ($P_{dlg\text{-}1}$*::LifeAct::gfp*) (Pohl and Bao, 2010).

In the 2° VulA, VulB1, and VulB2 toroids of wild-type L4 larvae, actin MFs were arranged in circumferential rings, which localized in proximity to DLG-1::RFP outlining the apical junctions on the luminal side of the toroids (Figures 3A and 3C). In contrast, the MFs in the 1° VulE and VulF toroids formed a pyramid-shaped meshwork oriented along the dorsoventral (D/V) axis, thereby connecting VulE and VulF on the dorsal side to the ventral uterus and on the ventral side to the 2° toroids. Weak LifeAct::GFP staining was also visible in the cell bodies of VulB1 and VulB2 (asterisks in Figure 3A).

We next examined the toroids in *let-502(ok1283)* null mutants, which carry a 1,435 bp deletion removing the Rho binding and pleckstrin-homology (PH) domains and causing a frameshift in the remaining exons, which results in a zygotic adult sterile phenotype as reported for other *let-502(lf)* alleles (Figure S3A)

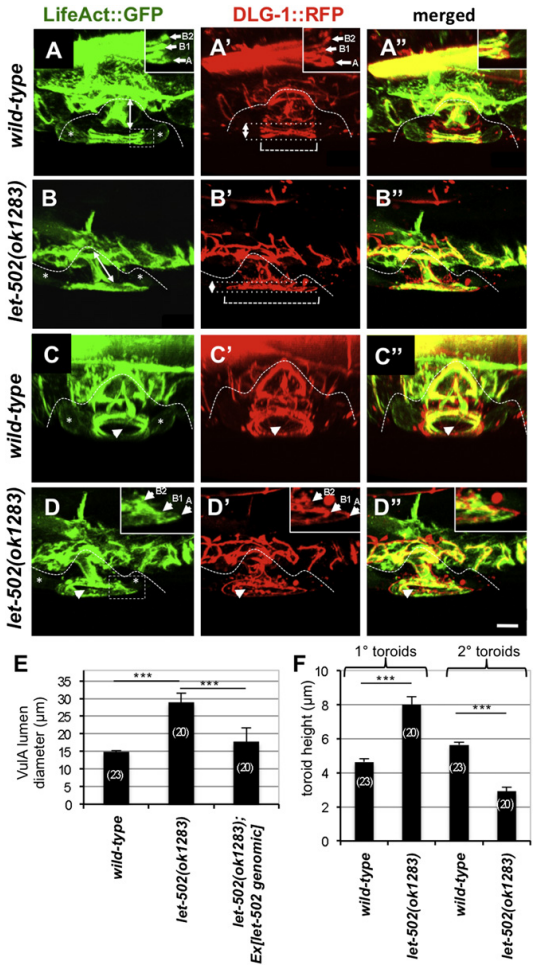


**Figure 3. LET-502 Is Required for Toroid Contraction during Vulval Morphogenesis**

(A–D") 3D reconstructions of LifeAct::GFP expression to visualize polymerized actin, (A') DLG-1::RFP to visualize the apical junctions and (A") the merged images in the toroids of a wild-type L4 and (B through B") a *let-502(lf)* L4 larva. (C) through (D") show ventrolateral projections of the same animals. The dashed lines in all panels indicate the uterine-vulval boundary. The double arrows in (A) and (B) indicate the height of 1° toroids, and in (A') and (B') the 2° toroid height between the dotted lines. The dashed bracket indicates the VulA lumen diameter. The dashed boxes in (A) and (D) indicate the regions magnified in the insets showing midsagittal sections. The asterisks in (A), (B), (C), and (D) indicate LifeAct staining in the cell bodies. The arrowheads in (C) through (D") indicate the vulval lumen.

(E) Average VulA lumen diameter in wild-type, *let-502(lf)*, and *let-502(lf)* mutants rescued with a 12.8-kb *let-502* genomic fragment. For details on the measurement points used to quantify each parameter, see Figure S5.

(G) Average 1° and 2° toroid heights in wild-type and *let-502(lf)* mutants. The numbers in brackets indicate the number of animals analyzed, and the error bars indicate SDs. $^{**}p \leq 0.01$, $^{***}p \leq 0.001$, two-tailed t tests. Scale bar, 5 µm. Alleles used: *let-502(ok1283), mcIs46,* and *zhIs396*.

See also Figure S2.

(Wissmann et al., 1999). In *let-502(ok1283)* larvae, we did not observe an obvious change in cell fate marker expression (Figure S2) or the number of vulval toroids, although the overall shape of the toroids appeared to be distorted (Figures 3B and 3D). The average diameter of the 2° VulA toroid lumen diameter was increased about 2-fold, while the combined height of the 2° toroids was decreased (Figures 3E and S3A). The 1° VulE and VulF toroids, on the other hand, were stretched along the D/V axis, and their combined height was increased (Figures 3B and 3G). Moreover, actin MFs in the 2° VulA, VulB1, and VulB2 toroids of *let-502(ok1283)* mutants appeared to be slightly disorganized, even though they still formed circumferential rings (Figure 3D). A 12.8 kb genomic fragment spanning the entire *let-502* locus and including the downstream gene C10H11.8, which may be in an operon together with *let-502*, rescued the toroid morphogenesis defects of *let-502(ok1283)* mutants (Figure 3F; Figure S3A). Finally, a translational LET-502::GFP reporter showed expression near the apical lumen of the 2° toroids and weak or undetectable expression in 1° toroids (Figure S3B).

Taken together, the increased diameter and decreased height of the 2° toroids in *let-502* mutants together with the circumferential localization of actin MFs near the apical junctions of the 2° toroids suggested that actomyosin-mediated contraction on the luminal side of the 2° toroids is essential to shape the vulval toroids.

## LET-502 Regulates 1° and 2° Toroid Diameters by Inducing Actomyosin Contraction

We visualized myosin MFs either by staining L4 larvae with antibodies against non-muscle myosins NMY-1 and NMY-2 (Piekny et al., 2003) or by observing expression of a myosin light chain MLC-4 reporter containing 2.83 kbp of 5′ regulatory sequences (Figure 4A; Figures S3D and S3E). Here, we observed localization of an MLC-4$R_{17}A_{18}$::GFP nonphosphorylatable mutant, although the same localization was observed with the constitutively active MLC-4$D_{17}D_{18}$ mutant (Gally et al., 2009; data not shown). MLC-4 and the nonmuscle myosins were localized similar to actin MFs near the apical junctions. However, while NMY-1 and NMY-2 were equally expressed in all toroids, MLC-4(RA)::GFP was only detected in the VulA, VulB1, and VulB2 toroids (Figure 4A). During eversion in the final phase of vulval morphogenesis, MLC-4::GFP was detected in all toroids (data not shown). Thus, the VulA, VulB1, and VulB2 toroids contain actin-myosin bundles organized in circumferential rings, while the VulC, VulD, VulE, and VulF toroids contain lower amounts of MLC-4 and no circumferential actin MFs.

Since LET-502 Rho Kinase phosphorylates MLC-4 to induce actomyosin contraction (Diogon et al., 2007), we examined whether expression of the constitutively active MLC-4DD mutant rescued the enlarged diameter of the 2° toroids in *let-502(ok1283)* mutants. Since *let-502(ok1283); mcEx402[$P_{mlc-4}$::mlc-4DD::gfp]* animals were inviable for unknown reasons, we used RNAi to knock down *let-502* function. While *let-502* RNAi caused approximately a 40% increase in 2° toroid diameter in nontransgenic controls, no significant increase in lumen diameter was observed in the transgenic *[$P_{mlc-4}$::mlc-4DD::gfp]* siblings treated with *let-502* RNAi on the same plates (Figure 4D). Thus, LET-502 induces actomyosin-mediated contraction of the 2° toroids via MLC-4.

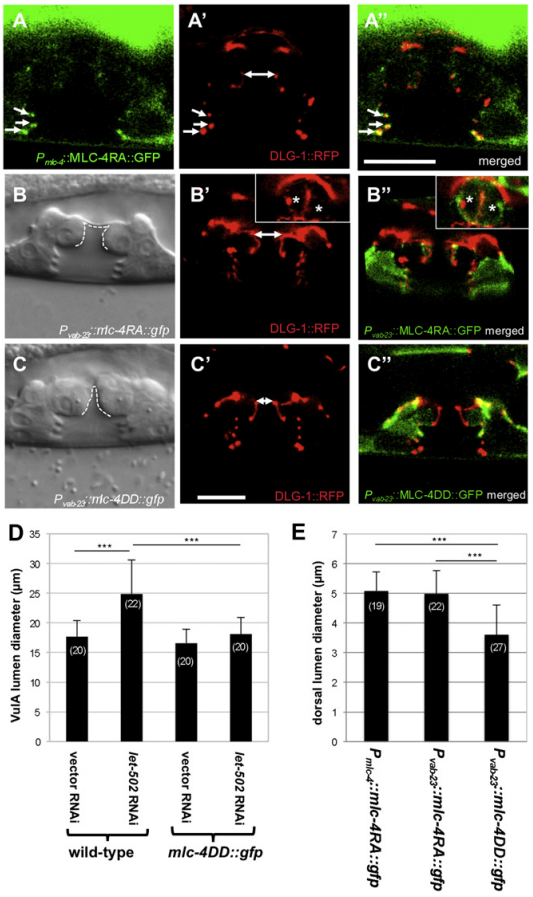


**Figure 4. Localization of MLC-4 and Ectopic Expression in 1° Toroids**

(A) Confocal midsagittal section of MLC-4RA::GFP (A') DLG-1::RFP and (A'') the merged images in the toroids of an L4 larva. The arrows point at MLC-4RA::GFP localized near the apical junctions of the VulA, VulB1, and VulB2 toroids.

(B–B'') Nomarski image of a $P_{vab-23}$*::mlc-4RA::gfp* L4 larva showing normal expansion of the dorsal lumen outlined with a dashed line. (B') DLG-1::RFP and (B'') the merged MLC-4::GFP and DLG-1::RFP images of the same animal. The insets show an upper plane with 1° VulE and VulF toroids expressing MLC-4RA::GFP labeled with asterisks.

(C–C'') Nomarski image of a $P_{vab-23}$*::mlc-4DD::gfp* L4 larva showing incomplete expansion of the dorsal lumen. (C') DLG-1::RFP and (C'') the merged images of the same animal are shown. Scale bars, 10 μm.

(D) Average VulA lumen diameter in wild-type and *mlc-4::DD::gfp* L4 larvae treated with *let-502* RNAi or empty vector control. *mlc-4::DD::gfp* transgenic animals were compared to nontransgenic siblings on the same RNAi plates.

(E) Average dorsal lumen diameter in $P_{mlc-4}$*::mlc-4RA::gfp*, $P_{vab-23}$*::mlc-4RA::gfp*, and $P_{vab-23}$*::mlc-4DD::gfp* L4 larvae measured at the VulE/VulF junctions as described in Figure S5. The numbers in brackets indicate the number of animals analyzed, and the error bars indicate the SDs. p-values obtained in two-tailed t tests are indicated as $^{**}p \leq 0.01$, $^{***}p \leq 0.001$. Alleles used: *mcIs46, zhEx437, zhEx438, zhEx439*, and *mcEx402*.

See also Figures S3 and S4.

During the mid-L4 stage, the AC invades and expands the dorsal lumen formed by the 1° toroids (Estes and Hanna-Rose, 2009). We therefore examined the role of actomyosin MFs in dorsal toroid lumen expansion by expressing constitutively active MLC-4DD in the 1° VulF and VulE toroids under control the *vab-23* promoter ($P_{vab-23}$*::mlc-4DD::gfp*), and as negative control the nonphosphorylatable MLC-4RA mutant ($P_{vab-23}$*::mlc-4RA::gfp*; Figures 4B and 4C) (Pellegrino et al., 2011). The diameter of the dorsal toroid lumen in $P_{vab-23}$*::mlc-4DD::gfp* animals was significantly reduced compared to $P_{vab-23}$*::mlc-4RA::gfp* or $P_{mlc-4}$*::mlc-4RA::gfp* controls (Figure 4E). A similar phenotype was observed after RNAi knockdown of the *mel-11* phosphatase, which inhibits actomyosin contraction by dephosphorylating MLC-4 (Figures S3F and S4) (Wissmann et al., 1999).

We conclude that ectopic actomyosin contraction in the 1° toroids prevents proper expansion of the dorsal toroid lumen. Hence, RAS/MAPK signaling represses *let-502* expression in the 1° toroids to permit dorsal lumen expansion by the AC.

## LIN-1 Regulates Multiple Aspects of Vulval Morphogenesis

Since LIN-1 directly activates *let-502* transcription in the 2° vulval cells, we examined if loss of *lin-1* function may cause similar vulval morphogenesis defects as *let-502(lf)*, in addition to the ectopic vulval induction caused by loss of the inhibitory LIN-1 function during fate specification. We first examined vulval toroid formation in *lin-1(n304lf)* mutants at the L4 stage by staining the apical junction marker AJM-1. Although P5.p, P6.p, and P7.p adopt a normal 2°-1°-2° pattern of cell fates based on cell lineage analysis (Beitel et al., 1995), their descendants failed to form ring-like structures characteristic of vulval toroids (Figure 5B). Instead, the vulval cells retained a square shape and failed to extend the circumferential processes containing actin bundles that were observed in the wild-type (Figure 5F). In contrast, in animals carrying a gain-of-function mutation in *let-60 ras*, P5.p, P6.p, and P7.p formed toroids with a similar morphology as in the wild-type (Figure 5C) (Sharma-Kishore et al., 1999), indicating that hyperactivation of the RAS pathway per se does not disrupt vulval morphogenesis.

To further investigate the role of LIN-1 during vulval morphogenesis, we inactivated LIN-1 after vulval fate specification by providing a pulse of MPK-1 activity in all vulval cells. When *hs::mpk-1* animals were heat shocked at the Pnp.xx-Pnp.xxx stage (Figure 5A), we observed not only a loss of *let-502* expression as shown in Figure 2I but also an abnormal toroid formation (Figure 5E). Except for the VulF cells, no toroid-like structures were formed by the P5.p, P6.p, and P7.p descendants at the L4 stage, similar to *lin-1(n304)* mutants. Moreover, the diameter of the vulval lumen was increased to a similar extent as in *let-502(ok1283)* mutants (Figure 5G).

Thus, inactivation of LIN-1 after vulval induction almost completely disrupts vulval toroid formation, suggesting that LIN-1 regulates vulval morphogenesis by controlling additional target genes besides *let-502*.

## Contraction of the 2° Toroids and Expansion of the 1° Toroids by the AC Shape the Vulval Tube

The increased lumen diameter and reduced height of the 2° toroids in *let-502* mutants suggested that the contraction of

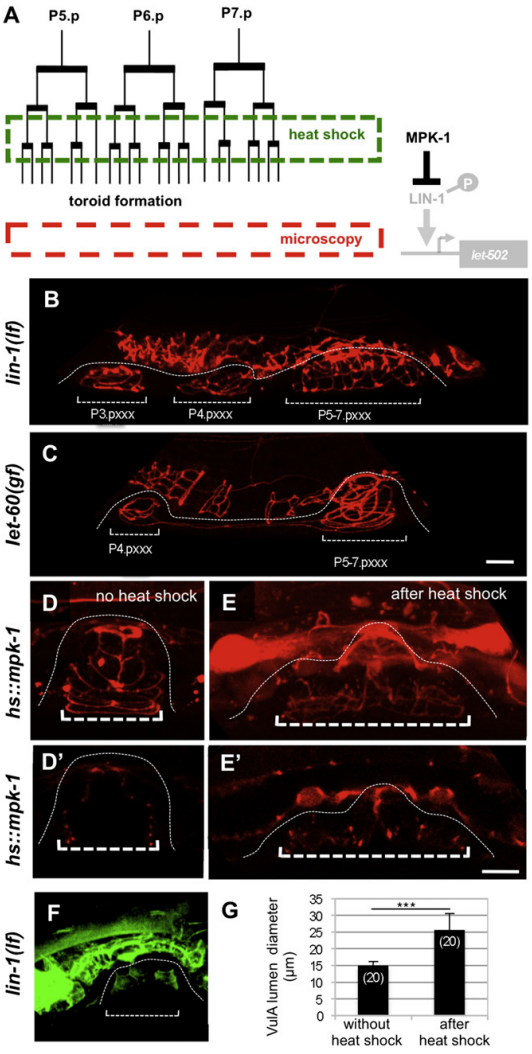


**Figure 5. LIN-1 Regulates Multiple Aspects of Vulval Morphogenesis**

(A) Lineage diagram showing the timing of *mpk-1* induction by heat shock and observation by 3D microscopy.

(B and C) Vulval toroid junctions visualized by MH27 antibody staining in (B) a *lin-1(lf)* and (C) a *let-60(gf)* mutant L4 larva.

(D–E') Vulval toroid junctions at the L4 stage visualized by DLG-1::RFP expression (D) without and (E) after heat shock induction of MPK-1 at the Pn.pxx stage. (D') and (E') show midsagittal sections of the animals shown in (D) and (E), respectively.

(F) Polymerized actin visualized with LifeAct::GFP expression in a *lin-1(lf)* L4 larva. Note the absence of circumferential actin rings formed in 2° cells as shown for the wild-type in Figure 3A. The dashed lines indicate the vulval-uterine boundary and the dashed brackets the diameters of the multiple invaginations. Scale bars, 5 µm.

(G) Average VulA diameter without and after heat-shock induction of MPK-1 measured as described in Figure S5. The numbers in brackets indicate the number of animals analyzed, and the error bars indicate the SDs.

the 2° toroids might generate a dorsal (i.e., from ventral toward dorsal) pushing force during vulval invagination. To test this hypothesis, we performed cell ablation experiments removing the 2° descendants of P5.p and P7.p at the Pn.pxx stage before the onset of vulval invagination. Ablation of the 2° vulval cells alone did not block invagination of the remaining 1° cells but rather caused an increase in the height of the 1° toroids (Figures 6B and 6E; n = 11). The residual invagination and increased height of the 1° toroids in the absence of 2° cells suggested the existence of tension created by the attachment of the dorsal toroids to the uterus. We therefore ablated the AC before the onset of invagination at the Pn.pxx stage. AC ablation prevented dorsal lumen expansion and caused an increase of the 1° and a simultaneous decrease of the 2° toroid height despite the normal contraction of the 2° toroids (Figures 6C and 6E; n = 10). Interestingly, AC ablation increased the height of the 1° VulF but not the VulE toroid, while ablation of the 2° cells increased the height of both the VulF and VulE toroids (Figure 6F). Finally, simultaneous ablation of the AC and the 2° cells resulted in the formation of a very small vulval lumen without a connection between the uterus and the cuticle (Figure 6D; n = 10). The height of the remaining 1° toroids could not be reliably quantified due to their small size and severely distorted morphology. Taken together, the ventral contraction of the 2° toroids by the actomyosin MFs and the lateral expansion of the 1° toroids by the AC are both required to shape the vulval tube and form a normal invagination.

## Quantitative Analysis of Shape Changes during Toroid Morphogenesis

To quantify the dynamic shape changes of the toroids, we followed vulval morphogenesis in wild-type L4 larvae expressing the apical junction marker AJM-1::GFP (Köppen et al., 2001) by time-lapse (four-dimensional; 4D) microscopy and measured the changes in toroid diameter and height over time. As the diameter of the ventral-most VulA toroid lumen decreased to its final size of less than 15 µm, the height of the 2° toroids increased, while 1° toroid height remained more or less constant (Figures 7A, 7F, and 7G; Movie S1). After the 2° toroids had fully contracted in mid-L4 larvae, we observed how the invading AC expanded the diameter of the dorsal toroid lumen (Figures 7B and 7H; Movie S1). The height of the 2° toroids further increased during this final phase of dorsal toroid lumen expansion (Figure 7I). In AC-ablated animals, on the other hand, the dorsal toroid lumen did not expand and the 1° toroid lumen remained small (Figure 6C). We also observed the vulval cell bodies during ventral lumen contraction and dorsal lumen expansion using a CED-10::GFP reporter, which labels the plasma membranes (Lundquist et al., 2001). Despite the changes in lumen size, the positions of the vulval cell bodies during ventral toroid contraction and dorsal expansion remained constant relative to the uterine cells (Movie S2; data not shown), indicating that vulval invagination is driven predominantly by changes in toroid shape rather than by active cell migration.

**p ≤ 0.01, ***p ≤ 0.001, two-tailed t tests. Alleles used: *lin-1(n301), mcIs46, gaIs36*, and *zhIs96*.

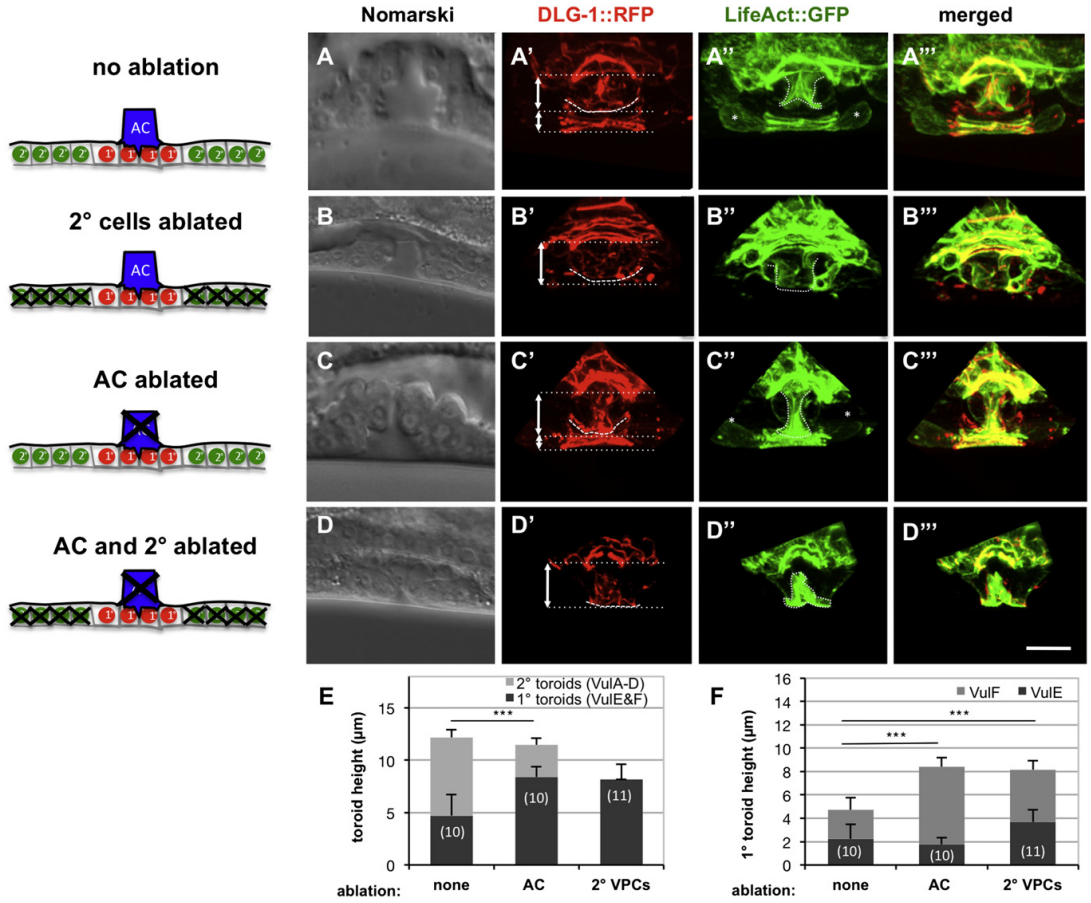


**Figure 6. 2° Toroid Contraction and 1° Toroid Expansion Shape the Vulval Tube**

(A–D''') (A–A''') Nomarski image, DLG-1::RFP-labeled junctions, polymerized actin visualized with LifeAct::GFP, and merged images in a wild-type L4 larva at the Pn.pxxx stage without ablation, (B–B''') after ablation of the 2° P5.p and P7.p descendants at the Pn.pxx stage, (C–C''') after ablation of the AC at the Pn.pxx stage, and (D–D''') after simultaneous ablation of the AC and the 2° P5.p and P7.p descendants. Double-headed arrows and the dotted lines indicate the height of the 1° and 2° toroids. Dashed curved lines indicate the junction between VulD and VulE or, in (B) and (D), the ventral epidermis and VulE. Scale bar, 5 µm.

(E and F) (E) Average height of the 1° and 2° toroids and (F) VulF and VulE after the different ablations measured as described in Figure S5. The numbers in brackets indicate the number of animals analyzed, and the error bars indicate the SDs. The p values obtained in two-tailed t tests comparing 2° toroid heights in (E) and 1° toroid heights in (F) are indicated as **p ≤ 0.01 and ***p ≤ 0.001. Alleles used: *mcIs46* and *zhIs396*.

Based on the dynamic changes in toroid height and diameter, we conclude that ventral 2° toroid contraction followed by lateral expansion of the 1° toroids are both required to achieve the proper height of the vulval toroids (Figure 7K).

## The Ventral Toroids and the AC/Utse Syncytium Create Tension in the Toroids

Finally, we investigated the tensions as an estimate for the forces generated during toroid morphogenesis by measuring toroid recoil velocities in laser-cutting experiments. First, we tested whether the vulval lumen in L4 larvae represents a closed compartment, to which pressure is being applied during morphogenesis. For this purpose, we punctured the ventral epidermis separating the vulval lumen from the outside. This intervention caused a rapid efflux of fluids and a ventral recoil of the toroids (Figure 7C; Movie S3). The morphology of the vulva after this induced collapse of the lumen was remarkably similar to the vulva in young adult animals after vulval eversion had occurred. As an estimate for the forces involved, we measured the peak recoil velocity of the VulD toroids (Figures 7C and 7J). Next, we cut the ventral VulA, VulB1, and VulB2 toroids, which caused an instant ventral recoil of the remaining toroids, indicating that ventral toroid contraction provides support for the remaining dorsal toroids (Figure 7D; Movie S4). In the presence

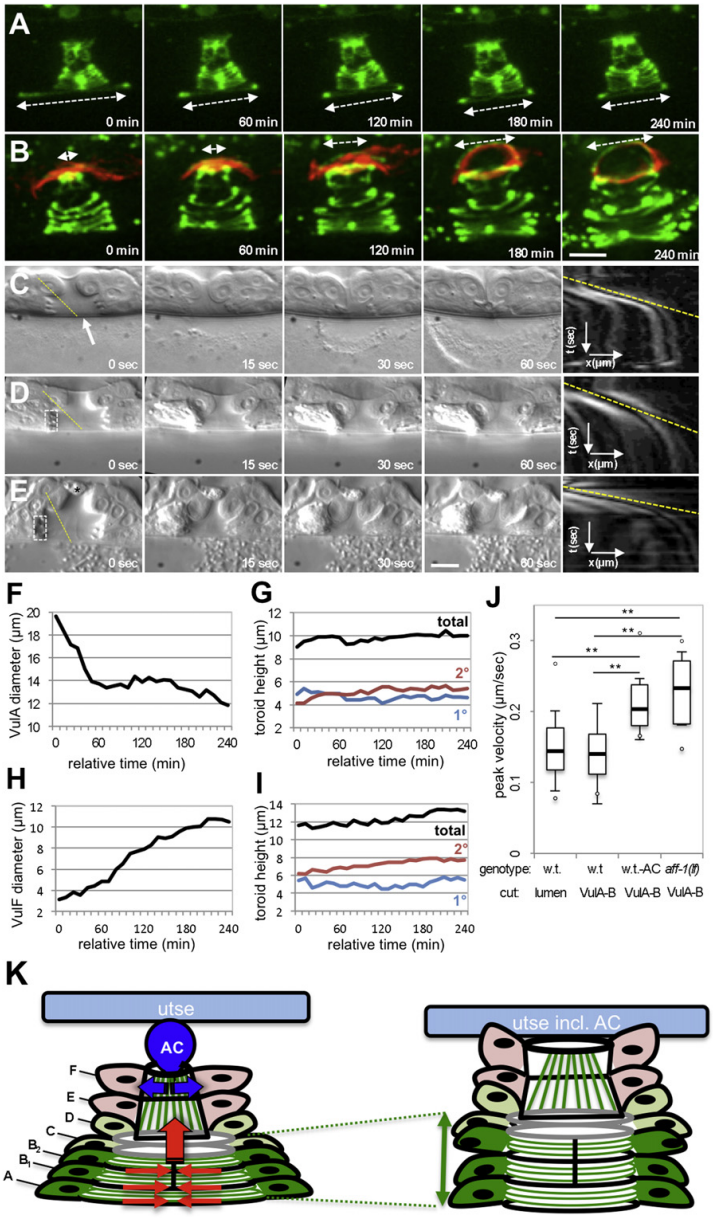


**Figure 7. Quantitative Analysis of Vulval Toroid Morphogenesis**

(A) Time-lapse recording of 2° toroid contraction in an early L4 larva using the AJM-1::GFP marker in green (Movie S1).

(B) Time-lapse recording of 1° toroid expansion in an L4 larva after the 2° toroids had contracted (Movie S1). The ventral plasma membrane of the AC is labeled in red using a PLC∂PH::mCherry marker (Ziel et al., 2009).

(C) Puncturing of the vulval lumen in L4 larvae results in a rapid lumen collapse and vulval eversion (Movie S3). The arrow in the first frame indicates the site in the ventral epidermis where the lumen was laser punctured. The animals were mounted in a suspension of 100 nm latex beads to visualize the efflux of fluids.

(D and E) Cutting of the VulA, VulB1, and VulB2 toroids in the (D) presence and (E) absence of the AC (Movie S4). The dashed box in the first frames outline the regions where the toroids were cut and the asterisk in (E) labels the AC corpse. The yellow dashed lines indicate the axes of VulD movement used to generate the kymograph shown in the rightmost panels and measure the peak recoil velocities. Scale bars, 5 µm.

(F and G) Quantification of the reduction in VulA (F) lumen diameter and (G) toroid height during 2° toroid contraction in the animal shown in (A).

(H and I) Quantification of the increase in VulF lumen diameter (H) and toroid height (I) during dorsal toroid lumen expansion in the animal shown in (B). Measurements on the recordings shown in (A) and (B) were performed on one out of three to five movies obtained for each stage as described in Figure S5.

(J) Box plot of the peak velocities measured in the lumen puncturing and toroid cutting experiments. The numbers in brackets indicates the number of animals analyzed, and the error bars indicate the SDs. $^{**}p \leq 0.01$, $^{***}p \leq 0.001$, two-tailed t tests.

(K) Toroid contraction and expansion during vulval morphogenesis. Cell bodies of 1° VulF and VulE toroids are shown in light red, cell bodies of 2° VulD and VulC toroids in light green, and of VulB2, VulB1, and VulA in dark green. Green lines indicate actomyosin MFs and black and gray lines the apical cell junctions. LET-502-mediated apical contraction of VulA, VulB, and VulB2 toroids result in a dorsal pushing force (red arrows), while invasion of the AC (dark blue) into the 1° toroids laterally expands the dorsal toroid lumen (blue arrows). Finally, the AC fuses with the utse (light blue) allowing the attachment of the toroids to the utse. Alleles used: *aff-1(ty4), swIs79*, and *qyIs23*.

of the AC, we measured a similar recoil velocity as in the lumen-puncturing experiments (Figures 7D and 7J). However, if the AC was ablated at the early Pn.pxxx stage at the onset of dorsal toroid expansion, after the π cells had been specified, the recoil velocity after toroid cutting was increased by around 50% (Figures 7E and 7J; Movie S4). To further dissect the role of the AC in toroid morphogenesis, we measured recoil velocities in *aff-1(ty4)* mutants, in which the AC normally expands the dorsal lumen but does not fuse with the overlying utse syncytium formed by eight π cells (Sapir et al., 2007). Dorsal lumen diameter in *aff-1(ty4)* was 5.1 ± 1.0 µm and 5.0 ± 0.69 µm in the wild-type; n = 20 each. We observed a similar increase in recoil velocity in *aff-1(ty4)* mutants as in AC-ablated wild-type animals (Figure 7J; Movie S4).

We conclude that actomyosin-driven contraction of the 2° toroids first generates a dorsal pushing force. Then, dorsal toroid expansion followed by fusion of the AC to the utse allows the formation of a continuous connection between the dorsal toroids, the uterine uv1 cells, and the utse/AC syncytium, which anchors the toroids to the lateral seam cells and thereby generates a tension in the dorsal toroids (Figure 7K) (Lints and Hall, 2009).

## DISCUSSION

### LIN-1 Links Cell Fate Specification with Morphogenesis

Our data point at a direct link between the cell fate specification pathways determining the 1° and 2° vulval fates and the force-generating actomyosin network during vulval morphogenesis. Rho kinase *let-502* transcription is directly induced by the ETS-family transcription factor LIN-1 (Figure 1J). High levels of NOTCH signaling in the 2° vulval cells prevent activation of the MAPK and thus keep LIN-1 in its active, unphosphorylated state, while high levels of MAPK signaling in the 1° cells result in the phosphorylation and inactivation of LIN-1. In this manner, a differential expression of RHO kinase LET-502 is established during the subsequent phase of vulval morphogenesis, such that high levels of LET-502 are maintained in the 2° cells, whereas LET-502 expression gradually fades in the 1° cells. In contrast to LET-502, the RHO-1 GTPase and the RHO guanine exchange factor ECT-2 (S. Canevascini and A.H., unpublished data), as well as the MEL-11 phosphatase, are uniformly expressed in 1° and 2° vulval toroids, suggesting that LET-502 is a limiting factor necessary to overcome the inhibitory activity of MEL-11 and induce actomyosin contraction. Our results also indicate that continuous RAS/MAPK and NOTCH signaling are required to maintain the differential LET-502 expression, as activation or inactivation of LIN-1 after vulval fate specification altered LET-502 expression levels and perturbed vulval morphogenesis. Hence, expression of both the EGFR ligand by the AC and the NOTCH ligands by the 1° vulval cells are maintained until the final stage of vulval development.

It has recently been reported that RAS and NOTCH signaling regulate different steps in the development of the *C. elegans* excretory system (Abdus-Saboor et al., 2011). Also in this organ, RAS and NOTCH signaling control not only the specification of the different cell fates but also the morphogenesis of the excretory tube. However, the target genes regulated by LIN-1 during excretory tube morphogenesis are not known.

Interestingly, LIN-1 appears to control multiple aspects of vulval morphogenesis besides regulating LET-502 expression and independent of its earlier inhibitory role during VPC fate specification. Even though the VPCs in *lin-1(lf)* mutants adopt an alternating pattern of 1° and 2° cell fates (Beitel et al., 1995), vulval toroids are largely absent and actin MFs do not organize in circumferential bundles in the 2° toroids. Therefore, LIN-1 appears to be necessary for the formation of circumferential cell extensions and homotypic cell contacts during vulval toroid formation. The opposing effects of the NOTCH and RAS/MAPK signaling pathways on LIN-1 activity thus orchestrate the cell shape changes during vulval tube formation.

### Contraction of the 2° Toroids Generates a Dorsal Pushing Force

The 2° vulval toroids differ from the 1° toroids not only by higher LET-502 expression levels but also by a different orientation of the actomyosin network (Figure 7K). While actin MFs are organized in circumferential bundles near the apical surface of the 2° VulA, VulB1, and VulB2 toroids, actin MFs in the 1° VulE and VulF toroids are aligned along the dorsoventral axis. Moreover, the regulatory myosin light chain MLC-4 was detected exclusively near the apical junctions of the 2° VulA, VulB1, and VulB2 toroids. Thus, only the three ventral-most toroids are capable of contracting in response to LET-502 activation, while the MLC phosphatase MEL-11 prevents contraction of the remaining toroids. It is not known how the different orientation of the actin fibers in 1° and 2° toroids is established. However, loss of *let-502* function did not change the overall orientation or organization of actin MFs.

The generation of a dorsal pushing force by 2° toroid contraction requires that the vulval lumen represents a closed compartment to which pressure can be applied. Indeed, when the vulval lumen was punctured in L4 larvae, this resulted in an almost instantaneous collapse of the vulval lumen and vulval eversion, indicating that the luminal space does represent a closed compartment that is under pressure. Mutations in the *sqv* genes, which encode proteins required for the biosynthesis or secretion of glycoproteins, cause a drastic reduction in the size of the vulval lumen (Herman et al., 1999; Herman and Horvitz, 1999; Hwang et al., 2003). It was proposed that hygroscopic proteoglycans secreted into the vulval lumen cause fluids to gradually increase the volume of the lumen and build up osmotic pressure. Therefore, a reduction in the radius of the lumen on the ventral side will cause an elongation of the lumen dorsally and thereby generate a dorsal pushing force (Figure 7K).

### Lateral Expansion of the 1° Toroids by the AC and Attachment to the Seam

Estes and Hanna-Rose (2009) have reported that invasion of the AC into the vulval tissue is necessary for dorsal lumen morphogenesis. We found that after the contraction of the ventral 2° toroids has been completed, the lateral expansion of the dorsal 1° toroid lumen by the invading AC is accompanied by a further increase in 2° toroid height. Accordingly, early ablation of the AC before vulval invagination (at the Pn.pxx stage) resulted not only in a reduced diameter and increased length of the 1° toroids but also a decrease in 2° toroid height. On the other hand, the diameter of the 2° toroids did not increase after AC ablation as long as the LET-502 induced actomyosin contraction was normal. Thus, AC ablation probably increases the pressure on the ventral toroids, which is counteracted by the actomyosin force. This results in the flattening of the 2° toroid and the stretching of the 1° toroid, as in the absence of the AC the 1° toroids remain attached to the basement membranes between uterus and vulva. The AC may increase the diameter of the 1° lumen by inducing lateral sliding of the basement membranes between the uterine and vulval cells (Ihara et al., 2011); it may mechanically stretch the VulF toroid or induce remodeling of the cytoskeleton in VulF through direct cell-cell interaction. In either case, continuous RAS/MAPK signaling must repress *let-502* transcription in the 1° VulE and VulF toroids to inhibit

actomyosin contraction and permit the AC to expand the dorsal lumen.

The increased toroid recoil velocity in the absence of the AC or, more specifically, in the absence of fusion between the AC and utse, points at a second function of the AC that is independent of its first role during dorsal lumen expansion, as the dorsal lumen was expanded in *aff-1(lf)* mutants. The removal of the AC through fusion may make room necessary for the attachment of the overlying utse to the dorsal toroids and the uv1 cells (Sapir et al., 2007; Lints and Hall, 2009). In this manner, AC fusion allows the establishment of a continuous connection between the vulva and the uterus to anchor the vulval toroids via the utse syncytium to the lateral epidermis, which creates a lateral tension in the dorsal toroids (Figure 7K).

### Regulation of Cell Shape Changes by NOTCH and RAS Signaling

Tissue morphogenesis depends on collective cell movements and the transmission of mechanical forces between different cell types. In many examples of collective cell migration, specific leader cells have been identified that generate in response to extracellular signals a mechanical force, which is transmitted to follower cells through cell-cell interactions (Caussinus et al., 2008). For example, RAS and NOTCH signaling are interlinked in a similar fashion during *Drosophila* tracheal tube morphogenesis to regulate the ETS transcription factors Pnt and Yan and differentiate between leader and follower cells (Schottenfeld et al., 2010). However, in contrast to the *Drosophila* trachea, there exists no clear distinction between leaders and followers during *C. elegans* vulval morphogenesis since not only the AC/utse/seam cell connection but also the 2° cells contribute forces to shape the vulval tube. Finally, we show that the RAS and NOTCH signaling pathways first used to specify the vulval cell fates are again used during vulval morphogenesis to differentially regulate actomyosin activity. Vulval fate specification and morphogenesis are therefore tightly coupled processes.

## EXPERIMENTAL PROCEDURES

### General Methods and Strains

*C. elegans* strains were maintained at 20°C on standard nematode growth media as described previously (Brenner, 1974). The wild-type strain of *C. elegans* used was Bristol N2. Strains used were as follows: LGI: *dpy-5(e907), let-502(ok1283)/hT2[bli-4(e937) let(q782) qIs48] (I;III)*, LGII: *aff-1(ty4), unc-4(e120), LGIII: dpy-19(e1259), lin-12(n137)/unc-32(e189) lin-12(n137n720), lin-1(n304), lin-31(n301)*, LGIV: *let-60(n1046)*. Extrachromosomal and integrated arrays: *gaIs36[hs::mpk-1(+), Dmek-2(wt)]* (Lackner and Kim, 1998), *swIs79[ajm-1::gfp,P$_{scm-1}$::gfp, unc-119(+)], mcIs46[dlg-1::rfp, unc-119(+)]* (Diogon et al., 2007), *sIs10781[rcesC10H11.9::gfp, pCeh361], qyIs23[P$_{cdh-3}$::PLC∂PH::mCherry; unc-119(+)]* (Ziel et al., 2009), *zhEx401 [P$_{let-502}$::nls::gfp::lacz::unc-54 3′utr, P$_{lin-48}$::gfp], zhEx402[P$_{let-502}$ LBS Δ1-4:: nls::gfp::lacz::unc-54 3′utr, P$_{lin-48}$::gfp], zhEx399[-1.1P$_{let-502}$::nls::gfp::lacz:: unc-54 3′utr, P$_{lin-48}$::gfp], zhEx403[-2.8P$_{let-502}$ Δ1.1-1.4 kb::nls::gfp::lacz::unc-54 3′utr, P$_{lin-48}$::gfp], zhEx404[-2.8P$_{let-502}$ Δ1.1-1.8 kb::nls::gfp::lacz::unc-54 3′utr, P$_{lin-48}$::gfp], zhEx405[-2.8P$_{let-502}$ Δ1.1-2.2 kb::nls::gfp::lacz::unc-54 3′utr, P$_{lin-48}$::gfp], zhEx393[-2.8P$_{let-502}$ ΔEBS::nls::gfp::lacz::unc-54 3′utr, P$_{lin-48}$:: gfp], zhEx395[hs::lin-1ΔCT, P$_{lin-48}$::gfp], zhEx394[hs::3xHA::strep::lin-1ΔCT, P$_{lin-48}$::gfp], zhIs396[P$_{dlg-1}$::lifeact::gfp::unc-54 3′utr, P$_{lin-48}$::gfp], mcEx402 [P$_{mlc-4}$::gfp::mlc-4DD + P$_{pie-1}$::gfp::mlc-4(wt), rol-6(gf)]* (Gally et al., 2009), *zhEx398[let-502 genomic, C10H11.8::gfp, P$_{lin-48}$::gfp], zhEx436[let-502::gfp], sbEx133[P$_{mel-11}$::gfp, rol-6(su1006)]* (Wissmann et al., 1999), *zhEx439[P$_{mlc-4}$:: mlc-4RA::gfp], zhEx437[P$_{vab-23}$::mlc-4RA::gfp], zhEx438[P$_{vab-23}$::mlc-4DD::gfp].*

All constructs were microinjected into the gonad arms of adult worms at concentrations between 2 and 50 ng/μl along with the coinjection marker *P$_{lin-48}$::gfp* at 50 ng/μl and pBluescript added to a final concentration of 150 to 200 ng/μl to generate stable transgenic lines (Mello et al., 1991). Sequences of primers used and details on the construction of plasmids can be found in the Supplemental Experimental Procedures.

### RNA Interference

RNA interference (RNAi) was performed using the feeding method as described (Kamath et al., 2001). P0 worms were synchronized at the L1 stage, transferred to nematode growth media plates containing 3 mM IPTG and 50 ng/ml ampicillin seeded with the desired RNAi bacteria, and allowed to grow for 3–5 days at 20°C, after which the surviving F1 progeny was analyzed.

### Microscopy and Laser Cutting

Immunostaining was performed as described previously (Miller and Shakes, 1995). In brief, worms were permeabilized using the freeze-crack method and immediately fixed in methanol at −20°C. Samples were blocked with 3% bovine serum albumin, first incubated with primary antibody (1:25 MH27 and 1:1,000 anti NMY-1 or NMY-2) for 2 hr at room temperature, then incubated with secondary antibody (1:100 anti-mouse TRITC and anti-rabbit CY-5), and washed and mounted in Mowiol. Fluorescent images were obtained using a Leica DMRA wide-field microscope, equipped with a cooled CCD camera (Hamamatsu ORCA-ER). Images were analyzed using Openlab 3.0 software package (Improvision). For three-dimensional (3D) reconstructions, GFP and RFP images of larvae animals were recorded with an Olympus FV1000 confocal microscope with a stack size of 0.3 to 0.5 μm. For 4D recordings of vulval toroid morphogenesis, animals were mounted on 4% agarose pads containing 2.5 mM tetramisole and immobilized with 100 nm latex beads (Polysciences Inc.). Images were recorded on an Olympus BX61 DSU spinning disc microscope at 10-min time intervals taking 30 to 40 z-stacks of 0.4 μm per time point. Laser ablation and cutting experiments were performed with a micropoint dye laser (Photonics Instruments) attenuated to around 70% maximal intensity at a pulse rate of 10 Hz aimed at the nucleoli for cell ablations or at the cell extensions to cut the toroids.

### Image Analysis

3D reconstructions were made using Imaris software (7.1), and 4D movies were analyzed using Image J. Measurements of toroid height and diameters were conducted on midsagittal sections through the toroids of late L4 larvae, after the VulF lumen had expanded and the AC had fused with the utse. For each parameter, the distances shown in Figure S5 were measured, and the averages and SDs were calculated. Measurements of peak velocities of the VulD recoil were done with Image J using the "kymograph" and "read velocity" macros written by J. Rietdorf and A. Seitz (EMBL Heidelberg).

### ChIP Analysis

For ChIP analysis, chromatin was prepared from *hs::HA::lin-1ΔCT* animals and precipitated with anti-HA antibodies (Roche) as described (Mukhopadhyay et al., 2008). As negative control, a mock precipitation using immunoglobulin G as primary antibody was performed in parallel. In each experiment, samples were processed in triplicates. Binding was quantified by Q-PCR with the probes shown in Figure 2A. The primers used for probes are shown in Supplemental Experimental Procedures. For each sample, the signal was normalized to the input DNA (Δct) and the percentage of bound DNA relative to 5% of the input signal was plotted.

## SUPPLEMENTAL INFORMATION

Supplemental Information includes five figures, four movies, and Supplemental Experimental Procedures and can be found with this article online at http://dx.doi.org/10.1016/j.devcel.2012.06.019.

## ACKNOWLEDGMENTS

We thank Juan Escobar, Stefan Luschnig, Shoib Siddiqui, and Michael Walser for comments on the manuscript, all present and past group members for critical discussion, and Dr. Oleg Georgiev for technical help during cloning. We are

also grateful to Paul Mains and Ken Kemphues for providing NMY antibodies and the *C. elegans* Genetics Centre, S. Mitani (Japan Knockout Consortium), and the Gene Expression Consortium for providing strains and Andrew Fire for vectors. S.F. was the recipient of a Forschungskredit grant from the University of Zürich and travel grants from the Julius Klaus Stiftung and Molecular Life Science PhD Program, Zürich. This research was also supported by the Kanton Zürich and by grants from Swiss National Science Foundation to A.H.

Received: October 7, 2011
Revised: April 6, 2012
Accepted: June 29, 2012
Published online: September 10, 2012

## REFERENCES

Abdus-Saboor, I., Mancuso, V.P., Murray, J.I., Palozola, K., Norris, C., Hall, D.H., Howell, K., Huang, K., and Sundaram, M.V. (2011). Notch and Ras promote sequential steps of excretory tube development in *C. elegans*. Development *138*, 3545–3555.

Andrew, D.J., and Ewald, A.J. (2010). Morphogenesis of epithelial tubes: Insights into tube formation, elongation, and elaboration. Dev. Biol. *341*, 34–55.

Beitel, G.J., Tuck, S., Greenwald, I., and Horvitz, H.R. (1995). The *Caenorhabditis elegans* gene *lin-1* encodes an ETS-domain protein and defines a branch of the vulval induction pathway. Genes Dev. *9*, 3149–3162.

Berset, T., Hoier, E.F., Battu, G., Canevascini, S., and Hajnal, A. (2001). Notch inhibition of RAS signaling through MAP kinase phosphatase LIP-1 during *C. elegans* vulval development. Science *291*, 1055–1058.

Brenner, S. (1974). The genetics of *Caenorhabditis elegans*. Genetics *77*, 71–94.

Caussinus, E., Colombelli, J., and Affolter, M. (2008). Tip-cell migration controls stalk-cell intercalation during *Drosophila* tracheal tube elongation. Curr. Biol. *18*, 1727–1734.

Christensen, S., Kodoyianni, V., Bosenberg, M., Friedman, L., and Kimble, J. (1996). lag-1, a gene required for *lin-12* and *glp-1* signaling in *Caenorhabditis elegans*, is homologous to human CBF1 and *Drosophila* Su(H). Development *122*, 1373–1383.

Diogon, M., Wissler, F., Quintin, S., Nagamatsu, Y., Sookhareea, S., Landmann, F., Hutter, H., Vitale, N., and Labouesse, M. (2007). The RhoGAP RGA-2 and LET-502/ROCK achieve a balance of actomyosin-dependent forces in *C. elegans* epidermis to control morphogenesis. Development *134*, 2469–2479.

Estes, K.A., and Hanna-Rose, W. (2009). The anchor cell initiates dorsal lumen formation during *C. elegans* vulval tubulogenesis. Dev. Biol. *328*, 297–304.

Gally, C., Wissler, F., Zahreddine, H., Quintin, S., Landmann, F., and Labouesse, M. (2009). Myosin II regulation during *C. elegans* embryonic elongation: LET-502/ROCK, MRCK-1 and PAK-1, three kinases with different roles. Development *136*, 3109–3119.

Gov, N.S. (2007). Collective cell migration patterns: follow the leader. Proc. Natl. Acad. Sci. USA *104*, 15970–15971.

Greenwald, I. (2005). LIN-12/Notch signaling in *C. elegans*. WormBook, 1–16.

Herman, T., and Horvitz, H.R. (1999). Three proteins involved in *Caenorhabditis elegans* vulval invagination are similar to components of a glycosylation pathway. Proc. Natl. Acad. Sci. USA *96*, 974–979.

Herman, T., Hartwieg, E., and Horvitz, H.R. (1999). *sqv* mutants of *Caenorhabditis elegans* are defective in vulval epithelial invagination. Proc. Natl. Acad. Sci. USA *96*, 968–973.

Hwang, H.Y., Olson, S.K., Esko, J.D., and Horvitz, H.R. (2003). *Caenorhabditis elegans* early embryogenesis and vulval morphogenesis require chondroitin biosynthesis. Nature *423*, 439–443.

Ihara, S., Hagedorn, E.J., Morrissey, M.A., Chi, Q., Motegi, F., Kramer, J.M., and Sherwood, D.R. (2011). Basement membrane sliding and targeted adhesion remodels tissue boundaries during uterine-vulval attachment in *Caenorhabditis elegans*. Nat. Cell Biol. *13*, 641–651.

Jacobs, D., Beitel, G.J., Clark, S.G., Horvitz, H.R., and Kornfeld, K. (1998). Gain-of-function mutations in the *Caenorhabditis elegans lin-1* ETS gene identify a C-terminal regulatory domain phosphorylated by ERK MAP kinase. Genetics *149*, 1809–1822.

Kamath, R.S., Martinez-Campos, M., Zipperlen, P., Fraser, A.G., and Ahringer, J. (2001). Effectiveness of specific RNA-mediated interference through ingested double-stranded RNA in *Caenorhabditis elegans*. Genome Biol. *2*, RESEARCH0002.

Köppen, M., Simske, J.S., Sims, P.A., Firestein, B.L., Hall, D.H., Radice, A.D., Rongo, C., and Hardin, J.D. (2001). Cooperative regulation of AJM-1 controls junctional integrity in *Caenorhabditis elegans* epithelia. Nat. Cell Biol. *3*, 983–991.

Lackner, M.R., and Kim, S.K. (1998). Genetic analysis of the *Caenorhabditis elegans* MAP kinase gene *mpk-1*. Genetics *150*, 103–117.

Lints, R., and Hall, D.H. (2009). Reproductive system, egglaying apparatus In WormAtlas. http://dx.doi.org/10.3908/wormatlas,1.24.

Lundquist, E.A., Reddien, P.W., Hartwieg, E., Horvitz, H.R., and Bargmann, C.I. (2001). Three *C. elegans* Rac proteins and several alternative Rac regulators control axon guidance, cell migration and apoptotic cell phagocytosis. Development *128*, 4475–4488.

Mello, C.C., Kramer, J.M., Stinchcomb, D., and Ambros, V. (1991). Efficient gene transfer in *C.elegans*: extrachromosomal maintenance and integration of transforming sequences. EMBO J. *10*, 3959–3970.

Miller, D.M., and Shakes, D.C. (1995). Immunofluorescence microscopy. Methods Cell Biol. *48*, 365–394.

Miller, L.M., Gallegos, M.E., Morisseau, B.A., and Kim, S.K. (1993). *lin-31*, a *Caenorhabditis elegans* HNF-3/fork head transcription factor homolog, specifies three alternative cell fates in vulval development. Genes Dev. *7*, 933–947.

Mukhopadhyay, A., Deplancke, B., Walhout, A.J., and Tissenbaum, H.A. (2008). Chromatin immunoprecipitation (ChIP) coupled to detection by quantitative real-time PCR to study transcription factor binding to DNA in *Caenorhabditis elegans*. Nat. Protoc. *3*, 698–709.

Omelchenko, T., Vasiliev, J.M., Gelfand, I.M., Feder, H.H., and Bonder, E.M. (2003). Rho-dependent formation of epithelial "leader" cells during wound healing. Proc. Natl. Acad. Sci. USA *100*, 10788–10793.

Pellegrino, M.W., Farooqui, S., Fröhli, E., Rehrauer, H., Kaeser-Pebernard, S., Müller, F., Gasser, R.B., and Hajnal, A. (2011). LIN-39 and the EGFR/RAS/MAPK pathway regulate *C. elegans* vulval morphogenesis via the VAB-23 zinc finger protein. Development *138*, 4649–4660.

Piekny, A.J., Johnson, J.L., Cham, G.D., and Mains, P.E. (2003). The Caenorhabditis elegans nonmuscle myosin genes *nmy-1* and *nmy-2* function as redundant components of the *let-502*/Rho-binding kinase and *mel-11*/myosin phosphatase pathway during embryonic morphogenesis. Development *130*, 5695–5704.

Pohl, C., and Bao, Z. (2010). Chiral forces organize left-right patterning in *C. elegans* by uncoupling midline and anteroposterior axis. Dev. Cell *19*, 402–412.

Poujade, M., Grasland-Mongrain, E., Hertzog, A., Jouanneau, J., Chavrier, P., Ladoux, B., Buguin, A., and Silberzan, P. (2007). Collective migration of an epithelial monolayer in response to a model wound. Proc. Natl. Acad. Sci. USA *104*, 15988–15993.

Rodríguez-Fraticelli, A.E., Gálvez-Santisteban, M., and Martín-Belmonte, F. (2011). Divide and polarize: recent advances in the molecular mechanism regulating epithelial tubulogenesis. Curr. Opin. Cell Biol. *23*, 638–646.

Sapir, A., Choi, J., Leikina, E., Avinoam, O., Valansi, C., Chernomordik, L.V., Newman, A.P., and Podbilewicz, B. (2007). AFF-1, a FOS-1-regulated fusogen, mediates fusion of the anchor cell in *C. elegans*. Dev. Cell *12*, 683–698.

Schottenfeld, J., Song, Y., and Ghabrial, A.S. (2010). Tube continued: morphogenesis of the *Drosophila* tracheal system. Curr. Opin. Cell Biol. *22*, 633–639.

Sementchenko, V.I., and Watson, D.K. (2000). Ets target genes: past, present and future. Oncogene *19*, 6533–6548.

Sharma-Kishore, R., White, J.G., Southgate, E., and Podbilewicz, B. (1999). Formation of the vulva in *Caenorhabditis elegans*: a paradigm for organogenesis. Development *126*, 691–699.

Sternberg, P.W. (2005). Vulval development. WormBook, 1–28.

Tan, P.B., Lackner, M.R., and Kim, S.K. (1998). MAP kinase signaling specificity mediated by the LIN-1 Ets/LIN-31 WH transcription factor complex during *C. elegans* vulval induction. Cell *93*, 569–580.

Vaughan, R.B., and Trinkaus, J.P. (1966). Movements of epithelial cell sheets in vitro. J. Cell Sci. *1*, 407–413.

Wissmann, A., Ingles, J., McGhee, J.D., and Mains, P.E. (1997). *Caenorhabditis elegans* LET-502 is related to Rho-binding kinases and human myotonic dystrophy kinase and interacts genetically with a homolog of the regulatory subunit of smooth muscle myosin phosphatase to affect cell shape. Genes Dev. *11*, 409–422.

Wissmann, A., Ingles, J., and Mains, P.E. (1999). The *Caenorhabditis elegans mel-11* myosin phosphatase regulatory subunit affects tissue contraction in the somatic gonad and the embryonic epidermis and genetically interacts with the Rac signaling pathway. Dev. Biol. *209*, 111–127.

Xavier Trepat, M.R.W., Angelini, T.E., Millet, E., Weitz, D.A., Butler, J.P., and Fredberg, J.J. (2009). Physical forces during collective cell migration. Nat. Phys. *5*, 426–430.

Zhang, X., and Greenwald, I. (2011). Spatial regulation of *lag-2* transcription during vulval precursor cell fate patterning in *Caenorhabditis elegans*. Genetics *188*, 847–858.

Ziel, J.W., Hagedorn, E.J., Audhya, A., and Sherwood, D.R. (2009). UNC-6 (netrin) orients the invasive membrane of the anchor cell in *C. elegans*. Nat. Cell Biol. *11*, 183–189.

### 3.4.2 The Invading Anchor Cell Induces Lateral Membrane Constriction during Vulval Lumen Morphogenesis in *C. elegans*

My contribution to the manuscript consiste in providing a time-lapse movie with the AH2338 (*qyIs23[$P_{cdh\text{-}3}$>mCherry::PLC$\delta^{PH}$] II;swIs79[ajm-1::gfp, seamcell::gfp, pUnc-119] IV*) strain, taken at the mid/late L3 stage and developing to the L3/L4 stage, showing circumferential actin-rich AC protrusions towards the vulF-vulF apical junctions, which presents Movie S2 in the publication. In addition I performed proofreading of the manuscript and provided scientific input for adaptions to the manuscript.

Article

Developmental Cell

# The Invading Anchor Cell Induces Lateral Membrane Constriction during Vulval Lumen Morphogenesis in *C. elegans*

## Highlights

- Apical cell constrictions initiate lumen formation during vulval morphogenesis
- Anchor cell invasion induces deformation of vulval epithelial cells
- Cell deformation causes the recruitment of the TOCA F-BAR proteins
- TOCA proteins induce lateral constriction of the CDC-42 pathway

## Authors

Qiutan Yang, Daniel Roiz, Louisa Mereu, Michael Daube, Alex Hajnal

## Correspondence

alex.hajnal@imls.uzh.ch

## In Brief

Actomyosin-based forces change cell shapes to sculpt tissues. Using the *C. elegans* vulva as a model for tube morphogenesis, Yang et al. show that anchor cell invasion of the vulval epithelium reorganizes the actomyosin network and induces lateral membrane constriction through recruitment of F-BAR-domain proteins and activation of CDC-42.

Yang et al., 2017, Developmental Cell *42*, 271–285
August 7, 2017 
http://dx.doi.org/10.1016/j.devcel.2017.07.008

CellPress

Developmental Cell
Article

# The Invading Anchor Cell Induces Lateral Membrane Constriction during Vulval Lumen Morphogenesis in *C. elegans*

Qiutan Yang,[1,2] Daniel Roiz,[1,2] Louisa Mereu,[1,2] Michael Daube,[1] and Alex Hajnal[1,3,*]
[1]Institute of Molecular Life Sciences, University of Zurich, Winterthurerstrasse 190, 8057 Zurich, Switzerland
[2]Zurich PhD Program in Molecular Life Sciences, Uni ETH Zürich, 8057 Zurich, Switzerland
[3]Lead Contact
*Correspondence: alex.hajnal@imls.uzh.ch
http://dx.doi.org/10.1016/j.devcel.2017.07.008

## SUMMARY

**During epithelial tube morphogenesis, linear arrays of cells are converted into tubular structures through actomyosin-generated intracellular forces that induce tissue invagination and lumen formation. We have investigated lumen morphogenesis in the *C. elegans* vulva. The first discernible event initiating lumen formation is the apical constriction of the two innermost primary cells (VulF). The VulF cells thereafter constrict their lateral membranes along the apicobasal axis to extend the lumen dorsally. Lateral, but not apical, VulF constriction requires the prior invasion of the anchor cell (AC). The invading AC extends actin-rich protrusions toward VulF, resulting in the formation of a direct AC-VulF interface. The recruitment of the F-BAR-domain protein TOCA-1 to the AC-VulF interface induces the accumulation of force-generating actomyosin, causing a switch from apical to lateral membrane constriction and the dorsal extension of the lumen. Invasive cells may induce shape changes in adjacent cells to penetrate their target tissues.**

## INTRODUCTION

Tubes are the basic building blocks of most epithelial organs (Andrew and Ewald, 2010; Lubarsky and Krasnow, 2003). A key step during the morphogenesis of tubular organs is the invagination of the tissue, which converts a monolayer of epithelial cells into a three-dimensional (3D) structure. The constriction of the apical cell surface is a crucial process that initiates the bending of the invaginating epithelium. Apical constriction has been extensively studied, most notably during gastrulation, vertebrate neurulation, dorsal closure in *Drosophila*, and branching morphogenesis of various tubular organs (Sawyer et al., 2010). In all of these examples, apical constriction is the result of contractile forces generated by the actomyosin network on the apical cortex of the cells. These cell-shape changes can be controlled either by cell-intrinsic factors or by extracellular cues such as diffusible growth factor signals. In particular, during gastrulation cell intrinsic transcription factors that determine the regional cell fates induce apical constriction in the invaginating epithelium, while fibroblast and vascular endothelial growth factors released from neighboring cells induce apical constriction during branching morphogenesis of tubular organs (Helker et al., 2013). In all of these cases, apical constriction is induced through intracellular signaling pathways that control actomyosin contractility, via a CDC-42 or Rho-dependent kinase that phosphorylates and thereby activates the non-muscle myosin light chain regulatory subunit (Heisenberg and Bellaiche, 2013). The subcellular localization and orientation of the actomyosin network plays a pivotal role in determining the directivity and distribution of the intracellular forces between the different cortical domains. Hence, the localized activation of the various actomyosin regulators determines the type of shape changes a cell will undergo.

In this study, we have investigated the cell-shape changes occurring during lumen morphogenesis in the *Caenorhabditis elegans* vulva, the egg-laying organ of the hermaphrodite. The vulva is a tubular organ that passes the fertilized eggs from the uterus to the outside. Thanks to the small number of only 22 cells that form the vulval tube and to the ability to observe the process in real time, vulval development is an excellent model for the study of epithelial morphogenesis at single-cell resolution (Schindler and Sherwood, 2012). Vulval invagination and lumen formation begins in L3 larvae, after the three proximal vulval precursor cells (VPCs), P5.p, P6.p, and P7.p, have each divided twice to generate 12 vulval cells (Figure 1A). At this stage, the gonadal anchor cell (AC), which is located dorsally to the vulval cells, has breached the two basal laminae separating the gonad from the vulva (Sherwood and Sternberg, 2003). Thereafter, the AC invades the vulval epithelium and establishes direct cell-cell contacts with the two innermost primary (1°) VulF cells. The VulF cells then begin to move dorsally and initiate the formation of the vulval lumen (Figure 1A). The remaining vulval cells (VulE through VulA) follow the VulF cells while undergoing their last round of cell divisions. After these cell rearrangements, the vulval tube is formed by a stack of seven toroids that are each generated by the homotypic fusion between vulval cells of the same subfate (Schindler and Sherwood, 2012). Whereas the molecular pathways controlling vulval fate specification and AC invasion are well studied, the events that initiate the formation of the vulval lumen have not yet been characterized. In particular, it is unknown what type of cell-cell interactions and signaling pathways control the cell-shape changes required for wild-type lumen morphogenesis.

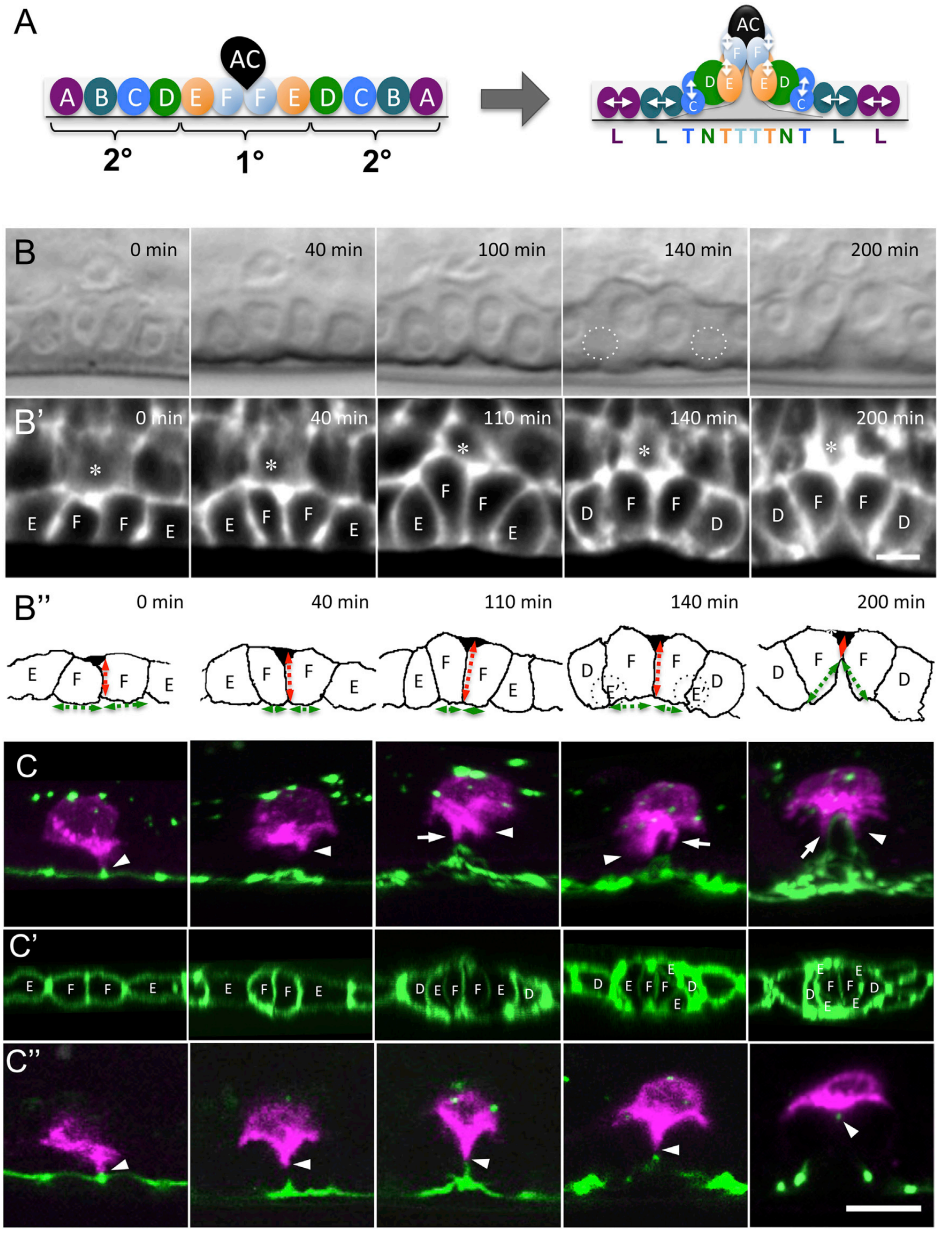


**Figure 1. Sequential Apical and Lateral Constriction of VulF during Lumen Formation**

(A) Schematic showing the cells with the seven vulval subfates, their positions before and during lumen formation, and the directions of the division axes (double-headed arrows) during the last round of cell divisions indicated with double-headed arrows.

(B–B″) Nomarski images (B) and CED-10::GFP expression (B′) during vulval invagination in a wild-type larva. See also Movie S1. For each time point, a mid-sagittal section is shown. The asterisks label the AC and the capital letters the VulF, VulE, and VulD cells. (B″) Outlines of the vulval cells shown in (B′) were generated with CellProfiler using a custom script. The dotted circles at 140 min outline the dividing VulE cells, which are out of focus in the plane shown. The dashed green and red arrows indicate the constriction of the apical and lateral VulF membranes, respectively.

*(legend continued on next page)*

We have used live imaging combined with cell-ablation experiments and cortical tension measurements to dissect the temporal sequence of events occurring during vulval lumen morphogenesis. In contrast to other known models of lumen formation, vulval lumen morphogenesis involves a sequence of apical and lateral membrane constrictions of the VulF cells, which extend the lumen dorsally. The invading AC plays a central role in orchestrating the vulval cell-shape changes. The newly forming AC-VulF interface reorganizes the cortical actomyosin network in the VulF cells and induces the constriction of the VulF cells along their lateral membranes, after apical constriction has been completed. For this purpose, the F-BAR (Bin-Amphiphysin-Rvs) domain protein TOCA-1 (Bai and Grant, 2015) is recruited to the AC-VulF contact sites. TOCA-1 and its paralog TOCA-2 then capture the nonmuscle myosin NMY-2 to reorient the contractile forces in the VulF cells along the dorsoventral axis. In this manner, the temporal sequence of cell-autonomous apical and AC-induced lateral membrane constriction shapes the vulval lumen.

## RESULTS

### Sequential Apical and Lateral Constriction of the VulF Cells during Vulval Lumen Morphogenesis

The formation of the vulval lumen begins after the second round of vulval cell divisions in mid-L3 larvae (Pn.pxx stage). First, the apical membranes of two inner descendants of P6.p (the VulF cells P6.pap and P6.ppa) detach from the cuticle and the cells move dorsally (Figures 1A and 1B). As the vulval lumen gradually expands, the vulval cells undergo their last round of cell divisions to generate 22 cells with seven different subfates (the 1° VulF and VulE cells and the 2° VulD through VulA cells) that form the vulval tube (Sharma-Kishore et al., 1999).

We characterized the cell-shape changes during the early phases of vulval lumen morphogenesis by performing 3D time-lapse microscopy of mid to late L3 larvae. For this purpose, we first observed larvae expressing the CED-10::GFP reporter, which labels the basolateral plasma membranes (Lundquist et al., 2001). Before the emergence of a lumen, the apical VulF membranes began to constrict, resulting in a gradual shortening of the distance between the apical ends of their lateral membranes (40-min time point in Figures 1B–1B″; see Movie S1 and Figure S1A for quantification). The VulE and the 2° cells, on the other hand, did not display signs of apical constriction at this stage. Around the time when the apical constriction of VulF had reached its maximum, the VulE cells underwent their last round of transversal (along the left/right axis) divisions (100-min time point in Figures 1B–1B″), making space for VulD to move toward the vulval midline and establish direct contact with VulF (140-min time point in Figures 1B–1B″ and 1C′). After the VulE divisions, the apical VulF membranes relaxed partially while the lateral membranes between the two VulF cells started to constrict until their apical ends reached the basal apex of the VulF cells, a process we termed lateral constriction (200-min time point in Figures 1B–1B″; see Movie S1 and Figure S1B for quantification). After the lateral constriction had been completed, the VulF cells underwent their last round of divisions. This temporal sequence of apical and lateral VulF membrane constrictions separated by the VulE divisions resulted in the formation of a characteristic pointed vulval lumen that extends to the AC-VulF contact sites (last time point in Figures 1B–1B″).

### The Invading AC Extends Dynamic Protrusions toward the Apical VulF Junctions

Prior to vulval lumen formation, the gonadal AC breaches the two basal laminae that separate the vulval epithelium from the uterus and invades the vulval tissue (Sherwood and Sternberg, 2003). We investigated the morphology of the AC during vulval lumen formation after basal laminae breaching had occurred. For this purpose, we observed lumen formation in animals carrying the $P_{cdh\text{-}3}$>*mCherry*::*PLC*$\delta^{PH}$ reporter, which labels the phosphatidylinositol-4,5-bisphosphate ($PIP_2$) containing actin-rich AC plasma membranes, along with the apical junction (AJ) marker $P_{ajm\text{-}1}$>*ajm-1*::*gfp* (Ziel et al., 2009). As the VulF cells underwent apical constriction, the AC extended circumferential actin-rich protrusions that were directed at the AJs between the two VulF cells (Movie S2, Figures 1C–1C″). After VulE division and during lateral VulF constriction, the AC protrusions gradually retracted dorsally (compare third and fifth panels in Figure 1C″) until the VulF AJs were bent, forming an arch underneath the AC body (fifth panel in Figure 3C; see 3D reconstruction in Movie S3). As a result of these cell-shape changes, a junction between the AC and the VulF cells was formed (arrowhead in the fifth panel of Figure 1C″).

The extension of dynamic AC protrusions toward the VulF AJs suggested an active role of the AC in inducing the vulval cell-shape changes during lumen formation. The AC protrusions may, for example, guide the apical VulF junctions to move dorsally during lateral membrane constriction.

### The AC Induces Lateral VulF Constriction

To test if the AC regulates the shape changes of the vulval cells, we examined the requirement for direct contact formation between VulF and the AC. For this purpose, we observed the *fos-1*(*ar105*) mutant, in which the AC does not breach the basal laminae and the AC protrusions cannot reach the AJs of the VulF cells (Sherwood et al., 2005). *fos-1*(*ar105*) mutants did not exhibit any signs of lateral VulF constriction, while apical constriction was not significantly affected (Figures 2A and 2B; see Figure S1 for quantification). To distinguish whether the absence of basal laminae breaching or the lack of cell-cell contact per se caused the loss of lateral VulF constriction, we ablated the AC at the mid-Pn.pxx stage, after the basal laminae had

(C–C″) 3D reconstructions of the AC labeled with the $P_{cdh3}$>*mCherry*::*PLC*$\delta^{PH}$ reporter in magenta and the apical junctions in the vulval cells labeled with the AJM-1:GFP reporter in green. Each panel shows an individual larva during the distinct phases of lumen formation and corresponding approximately to the time points shown in (B): before apical constriction (0 min in B), during apical constriction (40 min), maximal apical constriction (130 min), VulE division (140 min), and completion of lateral constriction (200 min). (C′) Ventral views of the apical junctions and the rearrangement of the cells after VulE division. (C″) Single z sections showing one of the AC protrusions toward the apical VulF junctions. The arrowheads in (C) and (C″) point to the tips of the front protrusions and the arrows indicate the contralateral protrusions.
See also Movies S2 and S3. Scale bars, 5 μm.

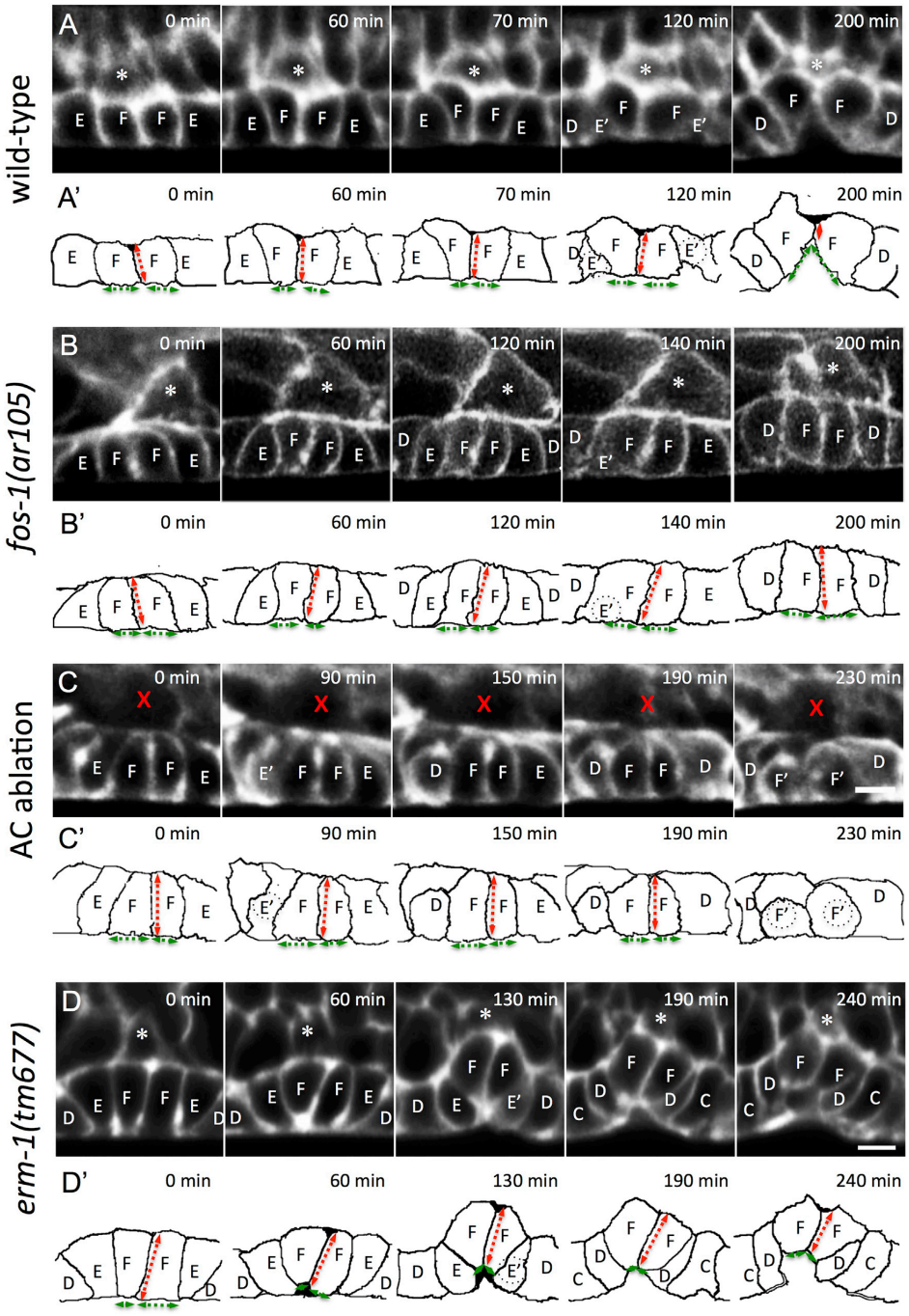


(legend on next page)

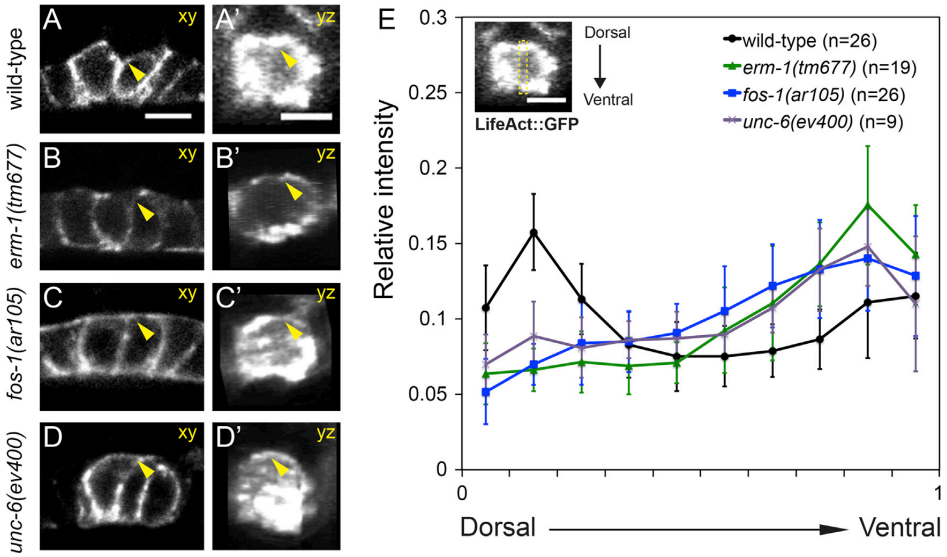


**Figure 3. Localization of the F-Actin during Lumen Formation**

(A and A′) F-actin localization during vulval invagination in a wild-type larva at the Pn.pxx stage detected with the LifeAct::GFP reporter, lateral (xy) view (A) (Farooqui et al., 2012). (A′) 3D reconstruction of F-actin on the lateral VulF membrane. An anterior-posterior (yz) projection of the lateral membranes between the two VulF cells is shown.

(B and B′) Apical mislocalization of F-actin in *erm-1*(*tm677*) mutants.

(C–D′) (C and C′) Disorganized F-actin staining on the lateral VulF membranes in a *fos-1*(*ar105*) and (D and D′) an *unc-6*(*ev400*) mutant larva at the Pn.pxx stage. Note the loss of the ring-shaped F-actin staining in the yz projections in (B′), (C′), and (D′). In each panel, the yellow arrowhead points to the AC-VulF contact sites.

(E) Intensity plots of LifeAct::GFP along the lateral VulF membranes were generated from yz projections as shown in the inset, using a custom script described by Morf et al. (2013) (see also STAR Methods). Error bars indicate the SD and the numbers in parentheses the numbers of animals analyzed.

Scale bars, 5 μm.

been breached but before the onset of lumen formation. Similar to *fos-1*(*ar105*) mutants, AC ablation after basal laminae breaching resulted in the absence of lateral VulF constriction (Figures 2C and S1 for quantification). In both AC-ablated animals and *fos-1*(*ar105*) mutants, we noticed a slight delay in vulval lumen formation. For example, in the AC-ablated animal shown in Figure 2C no lumen was detectable at the 230-min time point, even though both VulF cells had initiated their last round of divisions.

We conclude that AC invasion, which permits the formation of direct AC-VulF contact, is required to induce lateral VulF membrane constriction. Apical VulF constriction, on the other hand, does not depend on direct contact with the AC and hence appears to be an intrinsic property of the 1° VulF cell fate. In the absence of lateral VulF constriction a vulval lumen does form, though at a slower rate, and the lumen is not extended dorsally to reach the AC.

## Accumulation of the Actomyosin Network at the AC-VulF Contact Sites

Contractile forces generated by the actomyosin network induce epithelial cell-shape changes in many developmental processes, including apical constriction during *C. elegans* gastrulation (Sawyer et al., 2010). We thus examined the subcellular localization of the actomyosin network during vulval lumen formation. To visualize actin filaments (F-actin), we used the $P_{dlg\text{-}1}$>*LifeAct::gfp* reporter (Farooqui et al., 2012). During apical and lateral VulF constriction, most of the F-actin signal in the 1° cells was detected on the basolateral cortex and adjacent to the AJs (Figure 3A) (Haag et al., 2014). 3D image reconstructions of the VulF cells during lateral constriction revealed a ring-shaped pattern of F-actin staining on the lateral VulF cortex (Figure 3A′, quantified in 3E).

To observe myosin localization, we performed 3D time-lapse recordings of an endogenous reporter for non-muscle

**Figure 2. Lateral VulF Constriction Requires AC Invasion and Basolateral Actomyosin**

(A and A′) Mid-sagittal sections from 4D time-lapse recordings of the CED-10::GFP reporter in the wild-type. (A′) Outlines of the vulval cells shown in (A).

(B–D′) (B and B′) A *fos-1*(*ar105*) mutant, (C and C′) wild-type after AC ablation at the Pn.pxx stage, and (D and D′) an *erm-1*(*tm677*) mutant exhibiting reduced basolateral actomyosin localization.

The asterisks label the AC and the capital letters the VulF, VulE, and VulD cells. The red cross in (C) indicates the position of the ablated AC corpse. The dashed green and red arrows in the cell outlines indicate the constriction of the apical and lateral VulF membranes, respectively.

For quantification, see Figure S1. Scale bars, 5 μm. See also Movies S4 and S5.

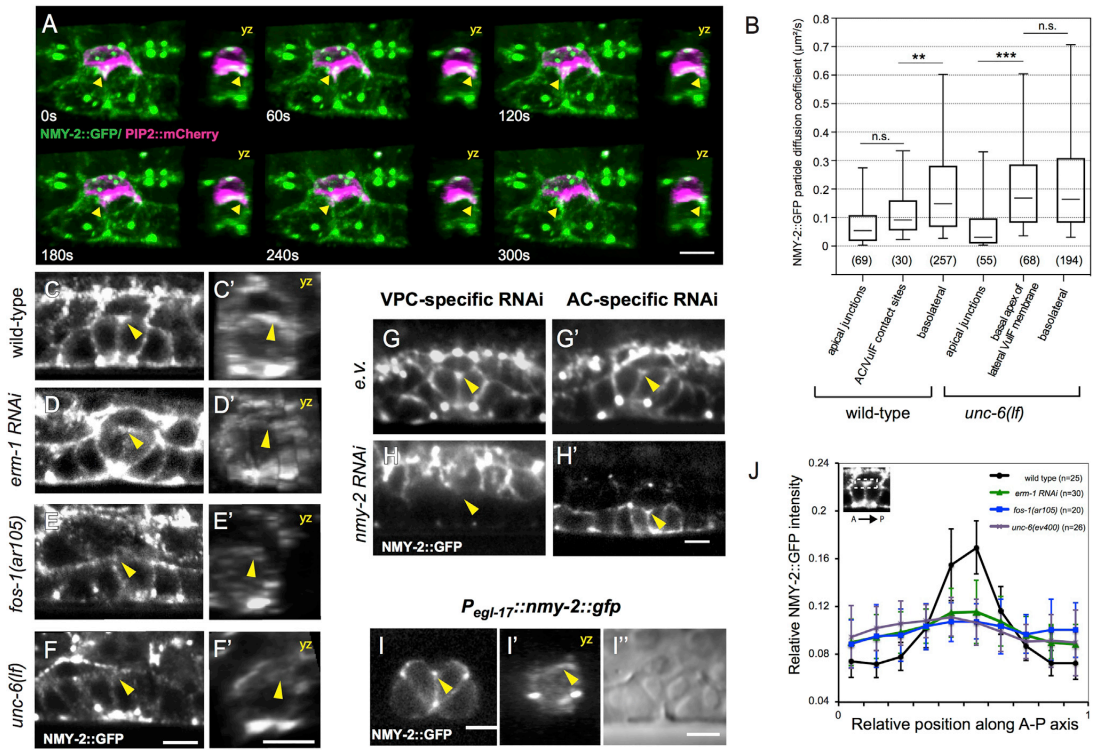


**Figure 4. Recruitment of Dynamic NMY-2 Particles to AC-VulF Contact Sites**

(A) Time-lapse recording of an endogenous NMY-2::GFP reporter in green and the $P_{cdh3}$>*mCherry*::*PLC*$\delta^{PH}$ reporter in magenta during lateral VulF constriction. Two-channel z stacks were recorded every 15 s and 3D reconstructions of selected time points are shown. See Movie S6 for the complete dataset. For each time point, the left panel shows a lateral (xy) and the right panel an anterior-posterior (zy) projection. The arrowheads point to NMY-2::GFP particles approaching the AC contact site.

(B) Box plots showing the normalized diffusion coefficients of NMY-2::GFP particles that were tracked in the different regions of wild-type and *unc-6*(*ev400*) mutants using the μ-track software (Jaqaman et al., 2008) as outlined in Figure S2. The numbers in parentheses indicate the number of particles tracked in a total of 11 wild-type and 9 *unc-6*(*ev400*) recordings. The whiskers indicate the 5% and 95% percentiles. n.s., not significant ($p > 0.05$); **$p < 0.01$; ***$p < 0.001$, two-tailed t test.

(C and C′) Localization of NMY-2::GFP in a wild-type larva at the Pn.pxx stage during vulval invagination. A lateral (xy) view is shown (C). (C′) Anterior-posterior (yz) projection of the lateral membranes between the two VulF cells.

(D–F″) (D–D″) Localization of NMY-2::GFP in an *erm-1* RNAi-treated larva, (E–E″) a *fos-1*(*ar105*) mutant, and (F–F″) an *unc-6*(*ev400*) mutant at the Pn.px stage. Note the loss of NMY-2::GFP accumulation at the AC-VulF contact sites in the xz projections in (D″), (E″), and (F″).

(G–H′) VPC-specific and (G′ and H′) AC-specific RNAi of *nmy-2* in the *nmy-2*::*gfp*; *rde-1*(*lf*); *rrf-3*(*lf*) background. (G) and (G′) show empty vector-treated controls, and (H) and (H′) animals treated with *nmy-2* double-stranded RNA (dsRNA). Note in (H) the loss of NMY-2::GFP accumulation at the AC-VulF contact sites.

(I–I″) 1° lineage-specific expression of NMY-2::GFP using the $P_{egl-17}$::*nmy-2*::*gfp* transgene. (I′) shows a yz projection of the lateral VulF membranes and (I″) a Nomarski image of the same animal. In each panel, the yellow arrowhead points to the AC-VulF contact sites.

(J) Intensity plots of NMY-2::GFP staining along the basal VulF membranes were generated from xy views as shown in the inset, using a custom script described by Morf et al. (2013) (see also STAR Methods). Error bars indicate the SD and the numbers in parentheses the numbers of animals analyzed for each genotype. Scale bars, 5 μm.

myosin II (NMY-2::GFP) along with the $P_{cdh-3}$>*mCherry*::*PLC*$\delta^{PH}$ AC marker (Figure 4A and Movie S6) (Dickinson et al., 2013). Prior to lumen formation, NMY-2::GFP was predominantly localized near the AJs between the vulval cells. However, during lateral constriction the NMY-2::GFP signal became enriched on the basal side of the VulF cells at the AC-VulF contact sites (arrowheads in Figures 4A, 4C, and 4C′, quantified in 4J). Similar to the cells undergoing apical constriction during gastrulation in the embryo (Nance et al., 2005), NMY-2::GFP exhibited a highly dynamic pattern with distinct puncta moving along the VulF membranes (Movie S6). We performed particle tracking on mid-sagittal sections taken at 1-s time intervals to estimate the speed of the of NMY-2::GFP punctae in the VulF cells (Figure S2). This analysis revealed that the movement of NMY-2::GFP puncta, which had reached the AC-VulF contact sites, was

significantly slower compared to puncta on the basolateral VulF membranes at a distance from the AC (Figure 4B).

Taken together, the subcellular distribution of the F-actin network and the dynamic movement of NMY-2 in the VulF cells undergoing lateral constriction suggested that contractile forces are generated not only on the apical cortex but also at the contact sites between the AC and the VulF cells.

### Apical Mislocalization of the Actomyosin Network and Lumen Morphogenesis Defects

To further test the relative contributions of the basolateral and apical actomyosin pools to lumen morphogenesis, we examined *erm-1* mutants (Van Fürden et al., 2004). *erm-1* encodes a member of the Ezrin/Radixin/Moesin (ERM) protein family that is required for basolateral F-actin localization in the vulval cells (Haag et al., 2014). *erm-1*(*tm677*) null mutants exhibited a reduction in basolateral and a concomitant increase in apical F-actin staining in all vulval cells at the Pn.pxx stage (Figure 3B). In particular, no ring-shaped F-actin staining could be observed on the lateral VulF cortex of *erm-1*(*tm677*) mutants (Figures 3B′ and 3E). We next examined whether the apical mislocalization of F-actin in *erm-1*(*lf*) mutants affected NMY-2 distribution. Since the *erm-1* and *nmy-2* genes are located in close proximity on LGI, we used *erm-1* RNAi to observe whether reducing *erm-1* expression altered NMY-2::GFP localization. RNAi knockdown of *erm-1* caused a strong reduction in NMY-2::GFP accumulation at the AC-VulF contact sites in the affected animals (42% affected, n = 71) (Figures 4D, 4D′, and 4J). Moreover, time-lapse microscopy using a CED-10::GFP reporter revealed a characteristic lumen morphogenesis defect in *erm-1*(*tm677*) mutants. Instead of extending the lumen dorsally, the lumen in *erm-1*(*tm677*) mutants had a bulged shape and did not reach the AC-VulF contact sites (Figures 2D and 2D′; Movies S4 and S5). Lateral VulF constriction did not occur in *erm-1*(*tm677*) mutants, while apical VulF constriction was increased when compared with wild-type larvae (Figure S1 for quantification).

These results indicated that the apical mislocalization of the actomyosin network in the VulF cells leads to the loss of lateral VulF constriction and an abnormal lumen morphogenesis. We thus conclude that a balance between apical and basolateral actomyosin-driven membrane constrictions is necessary to shape the vulval lumen.

### Cortical Tension Measurements on the Lateral and Apical VulF Cortex

The results presented so far suggested that a contractile force on the lateral VulF cortex is an important factor in determining the shape of the vulval lumen. To directly test this hypothesis, we measured the cortical tension in the different compartments of the VulF cells during apical and lateral constriction by performing laser nanosurgery experiments with a pulsed two-photon infrared laser (see STAR Methods) (Mayer et al., 2010; Vuong-Brender et al., 2016). During lateral VulF constriction in wild-type animals, we observed a rapid recoil after cutting across the middle section of the lateral VulF cortex (Figure 5A). By contrast, a significantly smaller recoil was observed in *erm-1*(*tm677*) mutants at the same developmental stage, indicating a reduced actomyosin-generated tension on the lateral cortex (Figures 5A and 5B). We also measured the cortical tension generated during apical constriction before the onset of lumen formation (Figures 5C and 5D). This experiment revealed a slight increase in the apical membrane tension in *erm-1*(*tm677*) mutants compared with wild-type larvae at the same stage, which might reflect the increased F-actin concentration on the apical VulF cortex in *erm-1*(*tm677*) mutants.

Finally, we investigated the consequences of cutting across the lateral VulF membranes by observing lumen formation in animals that had undergone laser nanosurgery. As negative control, we examined animals in which the lateral membranes between the distal VulA and VulB cells had been cut (Figure 5E). Lumen formation in animals that recovered from this intervention and repaired the cut site (seen by the reappearance of the CED-10::GFP signal with a small scar remaining on the lateral membrane) was scored around 4 hr later, after the subsequent division of the VulE cells. In the animals cut across the lateral VulF cells, lateral membrane constriction was reduced, and an abnormal lumen was formed in all cases (Figure 5E, quantified in 5F). By contrast, the control animals that were cut across the lateral VulA/B membranes underwent complete lateral VulF constriction and formed a normal lumen (Figures 5E and 5F).

In conclusion, the cortical tension measurements support the notion that the basolateral actomyosin network generates a contractile force to cause lateral VulF constriction during lumen morphogenesis.

### The Invading AC Reorients the Actomyosin Network in the VulF Cells

We next examined the localization of the actomyosin network in mutants defective in AC invasion. In *fos-1*(*ar105*) mutants, the NMY-2::GFP signal at the VulF-AC contact sites was reduced and distributed in irregular patches along the basal VulF and VulE cortex (Figures 4E, 4E′, and 4J). Also, the ring-shaped F-actin staining on the lateral VulF membrane was perturbed (Figures 3C, 3C′, and 3E). To test whether the polarity of the AC is required for the reorganization of the actomyosin network in the VulF cells, we examined *unc-6*(*ev600*) loss-of-function mutants. *unc-6* encodes a Netrin homolog that functions as a guidance signal from the ventral nerve cord neurons by polarizing the invading AC toward the ventral side (Ziel et al., 2009). In the absence of the UNC-6 Netrin guidance signal, no actin-rich protrusions toward the VulF cells are produced and the AC is often misplaced. Similar to *fos-1* mutants, the accumulation of NMY-2::GFP at the AC-VulF contact sites and the ring-shaped F-actin staining were lost in *unc-6*(*ev400*) mutants (Figures 4F, 4F′, 4J, 3D, 3D′, and 3E), indicating that the formation of AC protrusions is necessary to reorganize the actomyosin network in the VulF cells. Furthermore, tracking of the NMY-2::GFP puncta in *unc-6*(*ev600*) mutants indicated that the mobility of NMY-2 puncta at the basal apex of the VulF membranes remains high if no contact is made with the AC (Figures 4B and S2).

Next, we tested whether NMY-2:GFP is recruited to the contact sites in both the AC and VulF cells or if the invading AC induces NMY-2::GFP accumulation exclusively in the VulF cells. For this purpose, we performed tissue-specific *nmy-2* RNAi knockdown using the *qyIs102*[*fos-1*::*rde-1*(+)] (Matus et al., 2010) and *mfIs70*[*lin-31*::*rde-1*(+)] (Barkoulas et al., 2013), transgenes in the *nmy-2*::*gfp*; *rde-1*(*lf*); *rrf-3*(*lf*) background to induce AC-specific and VPC-specific RNAi, respectively. Upon

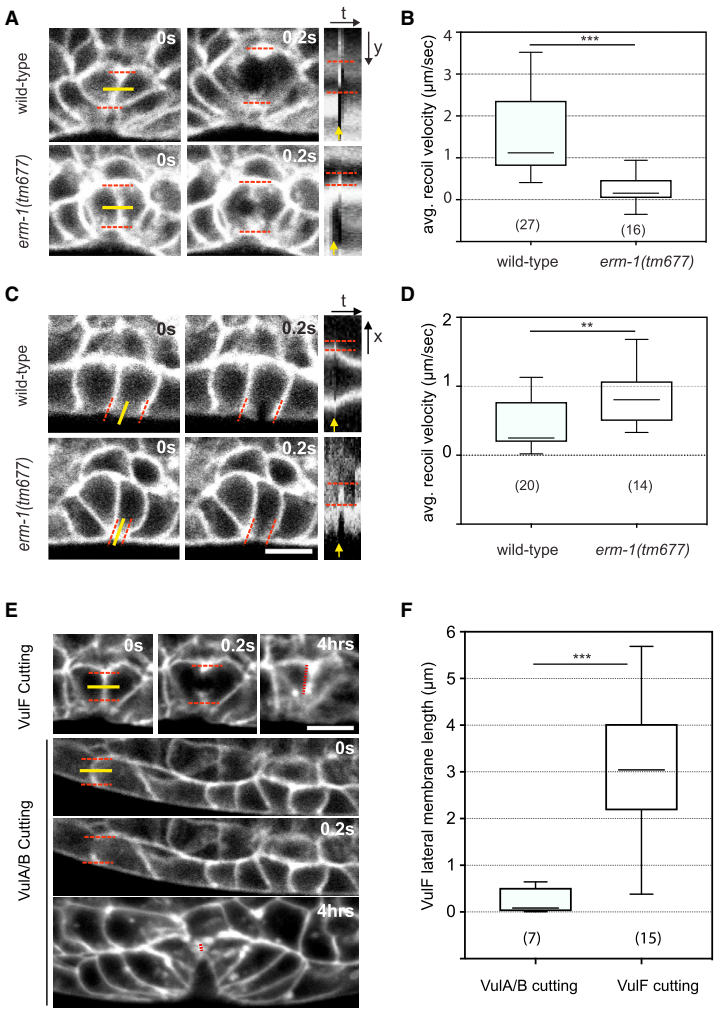


**Figure 5. Cortical Tension Measurements on the Apical and Lateral VulF Membrane**

(A) Membrane recoil on the lateral VulF membrane after laser cutting in a wild-type (top panels) and an *erm-1*(*tm677*) mutant larva (bottom panels) during the lateral constriction phase. The CED-10::GFP reporter was used to visualize the cell membranes. For each example, the animals are shown before (0 s) and in the first frame after the cut (0.2 s). The right panels show kymographs obtained from the recordings.

(B) Box plots showing the average recoil velocities after lateral membrane cutting measured as described in STAR Methods.

(C) Apical VulF membrane recoil after laser cutting in a wild-type (top panels) and an *erm-1*(*tm677*) mutant larva (bottom panels) during the apical constriction phase, as described for (A).

(D) Box plots showing the average recoil velocities after apical membrane cutting.

(E) Lumen formation after cutting the lateral VulF or VulA/B membranes. The animals are shown before (0 s), immediately after (0.2 s), and 4 hr after the cut. The dashed red lines in the +4-hr panels indicate the lengths of the lateral VulF membranes after invagination.

(F) Box plots showing the average length of the lateral VulF membranes measured 4 hr after cutting. In (A), (C), and (E), the dashed red lines indicate the ventral and dorsal extent of the lateral membranes and the solid yellow lines the cutting regions. The yellow arrow in the kymographs indicates the time point of the cutting. In (B), (D), and (F), the whiskers indicate the 5% and 95% percentiles, and the numbers of animals analyzed are indicated by the numbers in parentheses. $^{**}p < 0.01$ and $^{***}p < 0.001$ determined by two-tailed t test. Scale bars, 5 µm.

VPC-specific *nmy-2* RNAi, the accumulation of NMY-2::GFP at the AC-VulF contact sites was strongly reduced in all 22 affected animals (Figures 4G and 4H). By contrast, AC-specific *nmy-2* RNAi did not affect the recruitment of NMY-2::GFP to the AC-VulF interface in 11 out of 13 affected animals (Figures 4G′ and 4H′). However, in two animals NMY-2::GFP accumulation at the AC-VulF contact sites was partially reduced, possibly due to perturbed AC invasion (not shown). Moreover, 1° vulval lineage-specific expression of NMY-2::GFP using the *egl-17* promoter (Burdine et al., 1998) was sufficient to cause NMY-2::GFP recruitment to the AC-VulF contact sites (Figures 4I–4I″).

We conclude that NMY-2 accumulation at the AC-VulF contact sites occurs predominantly in the VulF cells. Thus, the invading AC reorganizes the actomyosin network in the VulF cells, resulting in a switch from apical to lateral VulF membrane constriction.

## Recruitment of the F-BAR-Domain Protein TOCA-1 during Lateral VulF Constriction

We noticed that prior to lateral membrane constriction the invading AC deformed the lateral membranes of the VulF cells at their basal apex, resulting in a basal membrane indentation (see arrowhead in Figure 3A, and Movie S7 for a 3D reconstruction). By contrast, the VulF cells In *fos-1*(*ar105*) mutants, in which the AC does not breach the basal laminae, or in AC-ablated animals were not deformed on their basal side (compare the VulF cell shapes in Figure 2A′ versus 2B′ and 2C′). We thus hypothesized that the membrane deformation of the VulF cells caused by the invading AC constitutes a signal that induces the reorganization of the actomyosin network during lateral membrane constriction. Proteins containing an N-terminal Bar (Bin-Amphiphysin-Rvs) domain bind to curved plasma membranes and activate Rho family small guanosine triphosphatases (GTPases) to remodel the F-actin network at sites where cells experience mechanical membrane deformations (McMahon and Boucrot, 2015). We thus examined *C. elegans* genes known to encode BAR-domain proteins as well as known regulators of actomyosin network for a possible involvement in

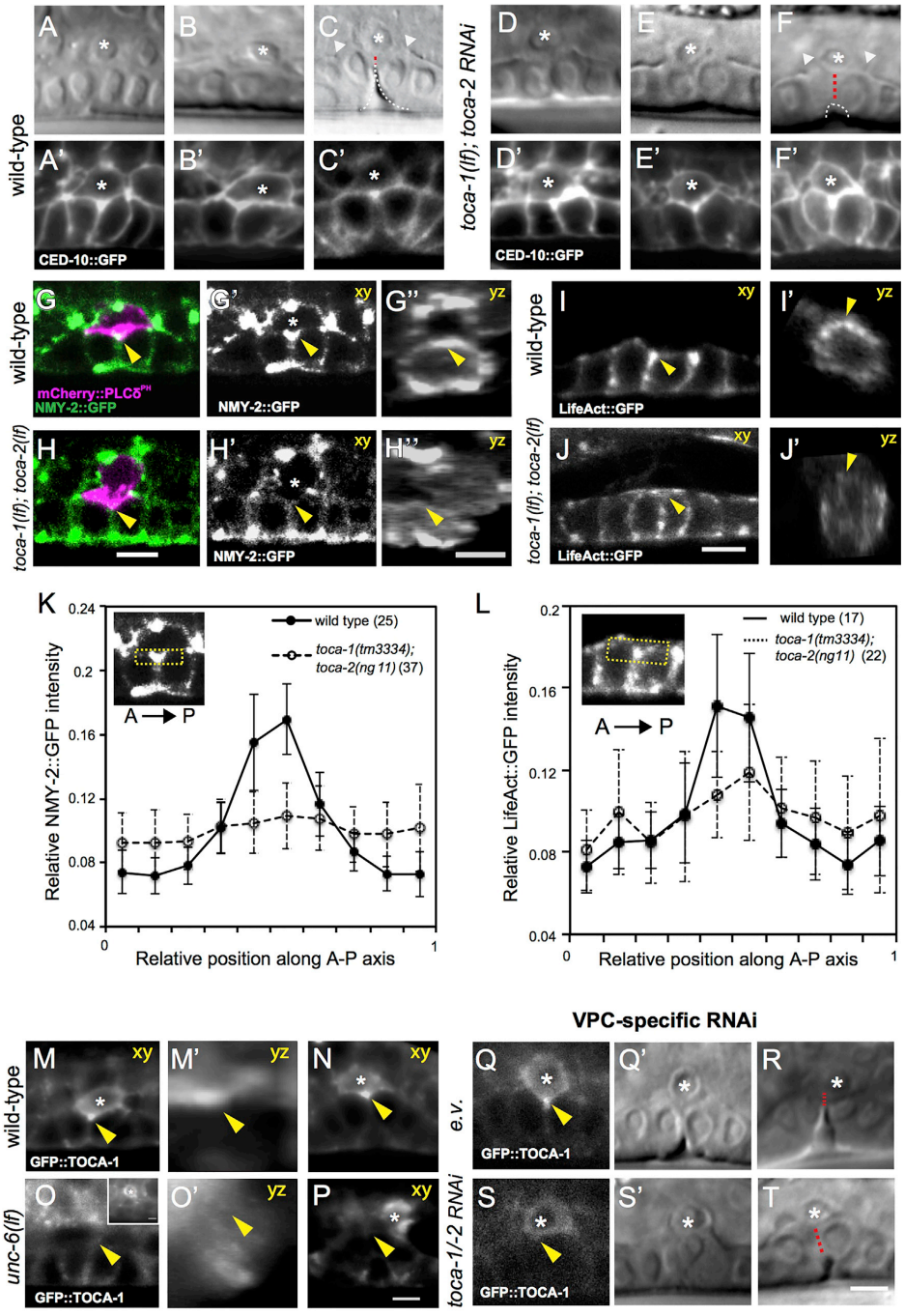


*(legend on next page)*

vulval lumen morphogenesis. To this aim, we performed RNAi knockdown in larvae and used, where available, mutant alleles to score lumen shape and NMY-2::GFP recruitment. The genes examined are listed in Table S1.

Through this targeted screen, we identified *toca-1* (transducer of CDC-42-dependent actin assembly 1) and its paralog *toca-2* as regulators of lumen morphogenesis and NMY-2::GFP localization (Table S1). The *toca* genes encode two highly similar and functionally redundant F-BAR-domain proteins that control actin dynamics and membrane trafficking through a CDC-42/PAR-6/WAVE pathway (Bai and Grant, 2015). In *toca-1*(*tm3334*) single-mutant animals treated with *toca-2* RNAi or in *toca-1*(*tm3334*);*toca-2*(*ng11*) double mutants, the AC was able to breach the basal laminae and establish direct contact with the VulF cells, yet the lumen was abnormally shaped due to a lack of lateral constriction and dorsal lumen extension (Figures 6A–6F′ and S3). Moreover, the recruitment of NMY-2::GFP and F-actin to the AC-VulF contact sites was reduced in *toca-1*(*tm3334*);*toca-2*(*ng11*) double mutants (Figures 6G–6L).

To observe TOCA-1 localization, we generated the endogenous *gfp*::*toca-1*(*zh110*) reporter via CRISPR/Cas9-mediated recombination (Dickinson et al., 2015) (see STAR Methods). GFP::TOCA-1 was expressed in both the AC and the VulF cells, where it was enriched at the AC-VulF contact sites and near the apical VulF junctions, similar to the NMY-2::GFP pattern described above (Figures 6M and 6N). The displacement of the AC in *unc-6*(*ev400*) mutants resulted in the loss of the GFP::TOCA-1 accumulation at the AC-VulF contact sites, indicating that TOCA-1 recruitment requires physical contact between the AC and VulF cells (Figures 6O and 6P). To test whether the VulF membrane deformation induced by the invading AC is required for TOCA-1 recruitment, we observed GFP::TOCA-1 localization in *fos-1*(*ar105*) mutants. The VulF cells were not deformed on their basal side, and GFP::TOCA-1 accumulation at the AC-VulF contacts sites was absent in all *fos-1*(*ar105*) mutants examined (FigureS S4B–B″, n = 21). Moreover, VPC-specific RNAi of *toca-1* and *toca-2* (*toca-1/-2i*) resulted in the loss of TOCA-1::GFP accumulation at the AC-VulF contact sites, while a diffuse signal persisted in the AC. (Figures 6Q–6S′, 68% [n = 28] of the RNAi-treated animals showed a strong downregulation of GFP::TOCA-1 in the vulval cells.) Thus, most if not all of the observed GFP::TOCA-1 accumulation at the AC-VulF contacts sites occurs in the VulF cells. Furthermore, VPC-specific *toca-1/-2* RNAi caused lumen morphogenesis defects in the affected animals, similar to those observed in the *toca-1*(*tm3334*);*toca-2*(*ng11*) double mutants (Figures 6R and 6T, quantified in Figure S3J).

In summary, the invading AC promotes TOCA-1 accumulation in the VulF cells to activate lateral membrane constriction. We propose that the F-BAR-domain proteins TOCA-1 and TOCA-2 are used to sense the mechanical deformation of the VulF cells caused by the invading AC.

## TOCA Proteins Induce Lateral VulF Constriction via the CDC-42/MRCK-1 Pathway

Since TOCA proteins have been shown to control actomyosin dynamics via the CDC-42 small GTPases (Bai and Grant, 2015), we tested the role of the *C. elegans cdc-42* homolog and its downstream effectors during lateral VulF constriction. In particular, the RNAi screen described above (Table S1) identified the MRCK kinase gene *mrck-1* that acts downstream of the CDC-42 GTPase during embryonic elongation to promote actomyosin contraction by phosphorylating the myosin light chain phosphatase MEL-11 (Gally et al., 2009; Nance et al., 2005). To observe NMY-2::GFP recruitment specifically in the VulF cells, we made use of the $P_{egl\text{-}17}$::*nmy-2*::*gfp* reporter described above (Figure 4I). RNAi knockdown of *toca-1/-2*, *cdc-42*, or *mrck-1* each caused a reduced NMY-2::GFP accumulation at the AC-VulF interface (Figures 7A–7E). Moreover, the expression of a dominant-negative mutant of *rho-1* under control of a heat-shock-inducible promoter (Canevascini et al., 2005) resulted in a reduced accumulation of NMY-2::GFP at the AC-VulF contact sites (Figure S5 and Table S1). However, RNAi against the Rho-dependent kinase *let-502* had no effect on NMY-2::GFP localization, even though the later contraction of the vulval toroids was perturbed (Table S1) (Farooqui et al., 2012). Thus, RHO-1 may act in parallel

**Figure 6. The TOCA Proteins Are Required for Actomyosin-Driven Lateral VulF Constriction**

(A–F′) Nomarski images (A–C, D–F) and CED-10::GFP expression (A′–C′, D′–F′) in mid-sagittal sections of wild-type (A–C′) and *toca-1*(*tm3334*); *toca-2* RNAi (D–F′) larvae during vulval lumen formation. (A) and (D) show larvae stages before, (B) and (E) during, and (C) and (F) after lateral VulF constriction. The dashed red lines in (C) and (F) indicate the lengths of the lateral VulF membranes; the white arrowheads point to the gaps in the basal laminae formed by the invading AC, and the asterisks the positions of the AC.

(G–H″) Localization of NMY-2::GFP in green and the $P_{cdh3}$>*mCherry*::*PLC*$\delta^{PH}$ reporter in magenta in wild-type (G–G″) and *toca-1*(*tm3334*);*toca-2*(*ng11*) double-mutant (H–H″) larvae at the Pn.pxx stage during vulval invagination. (G) and (H) are merged images of the mCherry::PLC$\delta^{PH}$ and NMY-2::GFP channels; (G″) and (H″) are yz projections of the lateral VulF membranes in the animals shown in (G′) and (H′).

(I–J′) Localization of the LifeAct::GFP F-actin reporter in wild-type (I) and *toca-1*(*tm3334*);*toca-2*(*ng11*) double-mutant (J) larvae at the Pn.pxx stage. (I′) and (J′) show yz projections of the lateral VulF membranes. In each panel, the yellow arrowhead points to the AC-VulF contact sites.

(K) Intensity plots of NMY-2::GFP along the basal VulF membranes were generated from xy views as shown in the inset and described by Morf et al. (2013) (see also STAR Methods). Error bars indicate the SD and the numbers in parentheses the numbers of animals analyzed for each genotype.

(L) Intensity plots of Lifeact::GFP along the basal VulF membranes as described in (K).

(M–P) Localization of the endogenous GFP::TOCA-1 reporter *zh110* in wild-type (M) and *unc-6*(*ev400*) mutants (O and P) before (M and O) and after (N and P) lumen formation. (M′) and (O′) show yz projections of the lateral VulF membranes. The inset in (O) shows the displaced AC in the *unc-6*(*ev400*) mutant in a different focal plane.

(Q–T) VPC-specific RNAi in the *gfp*::*toca-1*; *rde-1*(*lf*); *rrf-3*(*lf*) background. (Q) and (R) show control animals treated with empty vector and (S) and (T) are *toca-1/-2* RNAi-treated larvae. (Q and Q′) and (S and S′) show animals during constriction, while (R) and (T) are Nomarski images of the stage after constriction has been completed in the wild-type (after VulE division) used for the quantification shown in Figure S3J. Note in (S) the lack of GFP::TOCA-1 accumulation at the AC-VulF contact sites and in (T) the abnormal lumen shape due to a lack of lateral VulF constriction indicated by the dashed red line.

The asterisks mark the AC position and the yellow arrowheads point to the AC-VulF contact sites. Scale bars, 5 μm.

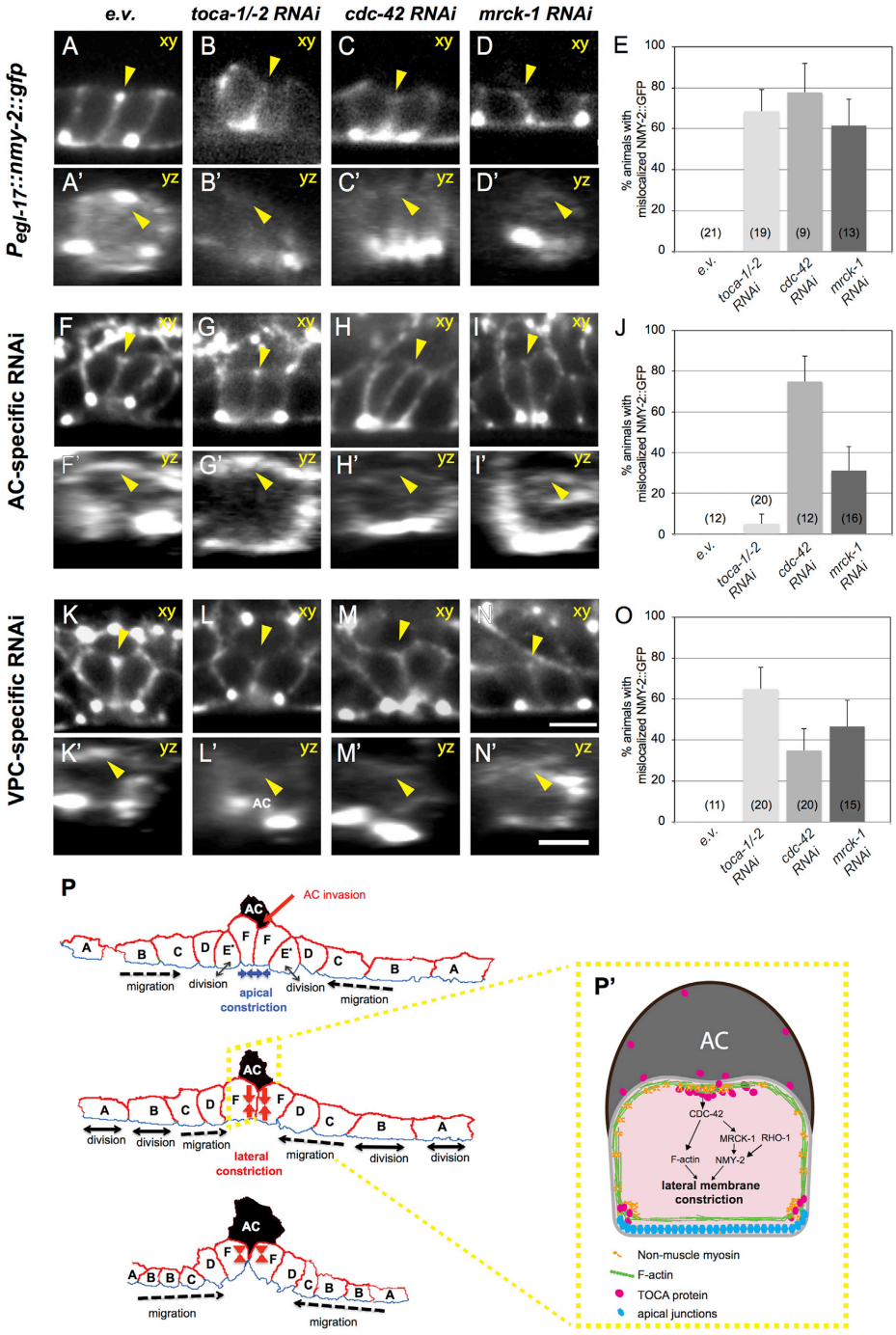


*(legend on next page)*

with CDC-42 to promote lateral VulF constriction through a distinct pathway.

To determine the cellular focus of the TOCA/CDC-42/MRCK-1 pathway, we performed AC- and VPC-specific RNAi in strains carrying the *nmy-2*::*gfp* reporter. VPC- but not AC-specific *toca-1/-2* RNAi caused a similar mislocalization of NMY-2::GFP from the AC-VulF contact sites, as observed in the *toca-1*(*tm3334*);*toca-2*(*ng11*) double mutants (Figures 7G, 7J, 7L, and 7O). By contrast, knockdown of *cdc-42* or *mrck-1* caused reduced NMY-2::GFP recruitment in both the VPC- and AC-specific RNAi strains (Figures 7H–7J and 7M–7O), indicating that the CDC-42/MRCK-1 module is used not only in the VulF cells but also in the AC. Accordingly, CDC-42 was recently shown to promote invadopdia formation in the AC, where it probably acts downstream of the UNC-40 Netrin receptor (Lohmer et al., 2016). Finally, we tested whether TOCA-1 recruitment in the VulF cells depends on CDC-42 signaling by performing AC- and VPC-specific *cdc-42* RNAi in strains carrying the GFP::TOCA-1 reporter. While AC-specific *cdc-42* RNAi resulted in the frequent loss of GFP::TOCA-1 recruitment to the AC-VulF contact sites, VPC-specific *cdc-42* RNAi did not alter GFP::TOCA-1 localization (Figure S6).

Thus, TOCA-1 is recruited to the AC-VulF contact sites independently of CDC-42 activity in the vulval cells, suggesting that TOCA-1 acts upstream of the CDC-42/MRCK-1 pathway to induce actomyosin-driven lateral membrane constriction in the VulF cells.

## DISCUSSION

Vulval morphogenesis in *C. elegans* serves as a powerful model to study how a linear array of epidermal cells forms a 3D tubular organ (Schindler and Sherwood, 2012). Thanks to the relatively small number of 22 cells and recent improvements in 4D live imaging of *C. elegans* larvae (Farooqui et al., 2012), it is possible to observe vulval morphogenesis at high spatial and temporal resolution. In this study, we have characterized the first phase of morphogenesis by observing the events that initiate the formation of the vulval lumen. We show that the invasion of the AC into the vulval epithelium controls the cell-shape changes of the 1° VulF cells during lumen morphogenesis.

### Sequential Apical and Lateral Constrictions Extend the Lumen Dorsally

Apical membrane constriction driven by actomyosin contractions initiates cell invagination in many morphogenetic processes, notably during gastrulation, neurulation, and branching morphogenesis of tubular organs such as the vasculature (Sawyer et al., 2010). Apical constriction leads to cell lengthening and tissue bending, thereby initiating lumen formation. Also during vulval lumen formation, the first discernible cell-shape change is the apical constriction of the two innermost 1° VulF cells (Figure 7P). In contrast to the aforementioned examples, apical VulF constriction is followed by the constriction of the lateral VulF membranes. As a result of these shape changes, the vulval lumen extends dorsally toward the AC and, after the AC has fused with the utse syncytium, the vulval and uterine lumina are connected to each other. To our knowledge, vulval lumen formation is so far the only example whereby not only apical but also lateral constriction of the invaginating cells has been observed. Lateral constriction and apical constriction represent two separate phases during lumen morphogenesis, as apical constriction can occur in the absence of lateral constriction, for example in *erm-1* or *fos-1* mutants. Several experiments show that the lateral VulF constriction does not simply reflect a repositioning or basal sliding of the AJs (Wang et al., 2012) but rather involves an actomyosin-generated force driving the contraction of the lateral cortex. (1) A relatively high tension is detectable on the lateral VulF membranes during lateral VulF constriction. (2) The basolateral actomyosin network is required to create this cortical tension. (3) F-actin is organized in a ring-shaped pattern on the lateral VulF membranes, which is characteristic of contractile membranes. (4) Lateral but not apical VulF constriction requires the formation of direct contact between the VulF cells and the AC in order to recruit the non-muscle myosin NMY-2 to the new contact site.

The transversal division of the VulE cells, which preceded the initiation of lateral VulF constriction in all our recordings, appears to coordinate the temporal sequence of apical and lateral constrictions. It is possible that the division of VulE releases tensions formed through the AJs between the VulF and VulE cells, thus permitting lateral VulF constriction to begin. A similar role for cell divisions in accelerating epithelial invagination has previously been proposed for tracheal placode invagination in the

**Figure 7. A TOCA/CDC-42/MRCK-1 Pathway Regulates NMY-2::GFP Recruitment in the VulF Cells**

(A–D′) $P_{egl-17}$::*nmy-2*::*gfp* larvae at the Pn.pxx stage treated with empty vector as negative control (A and A′), *toca-1/-2* (B and B′), *cdc-42* (C and C′), and *mrck-1* dsRNA (D and D′).

(E) Penetrance of the NMY-2::GFP mislocalization phenotype observed after the different RNAi treatments. The numbers in brackets indicate the numbers of animals scored and the error bars the SD estimated by bootstrapping 1,000 samples.

(F–I′) AC-specific RNAi in *nmy-2*::*gfp* larvae treated with empty vector control (F and F′), *toca-1/-2* (G and G′), *cdc-42* (H and H′), and *mrck-1* dsRNA (I and I′).

(J) Penetrance of the NMY-2::GFP mislocalization phenotype observed after different AC-specific RNAi treatments.

(K–N′) VPC-specific RNAi in *nmy-2*::*gfp* larvae treated with empty vector control (K and K′), *toca-1/-2* (L and L′), *cdc-42* (M and M′), and *mrck-1* dsRNA (N and N′).

(O) Penetrance of the NMY-2::GFP mislocalization phenotype observed after different VPC-specific RNAi treatments. For each RNAi condition, the top panel shows an xy view and the bottom panel a yz projection of the lateral VulF membrane that was generated from the xy view shown above. The yellow arrowheads point to the AC-VulF contact sites.

(P) Model of the cell-shape changes during the different stages of lumen morphogenesis. The cells in the images shown in Figure 1B′ undergoing apical and lateral constriction were traced using the CellProfiler software package using a custom script (Carpenter et al., 2006). The basolateral membranes are shown in red and the apical membranes in blue. The division planes and directions of cell migrations are indicated with solid and dashed arrows, respectively.

(P′) The AC induces lateral VulF constriction by recruiting the TOCA protein complex to the AC-VulF contact sites. TOCA proteins then activate the CDC-42/MRCK-1 pathway in parallel with RHO-1 to induce actomyosin contraction.

Scale bars, 5 μm.

*Drosophila* embryo (Kondo and Hayashi, 2013). In all wild-type larvae observed, the final transversal division of VulF occurred only after the completion of lateral VulF constriction. Therefore, the coordination of vulval cell-shape changes with cell divisions may establish a temporal sequence for the different morphogenetic events during lumen formation.

### AC Invasion Induces Lateral VulF Constriction

The AC plays a unique role that distinguishes vulval lumen formation from other cases of tube morphogenesis. By breaching the basal laminae between the vulval cells and uterus, the AC establishes direct contact with the two VulF cells (Sherwood and Sternberg, 2003). It has previously been reported that the AC is required for the later morphogenesis of the dorsal lumen during vulval tube formation (Estes and Hanna-Rose, 2009). Our study reveals a role of the AC at an early step of vulval morphogenesis, during the initiation of lumen formation, and provides a good rationale for the developmental timing of AC invasion. If the AC has not breached the basal laminae by the mid-L3 stage, vulval lumen formation proceeds, though at a slower speed and without lateral VulF constriction. In the absence of lateral VulF constriction, the vulval lumen does not extend dorsally and cannot be connected to the uterine lumen. The circumferential cell protrusions the AC extends toward the apical VulF junctions during the lateral constriction phase may serve as physical guides that direct the VulF cells dorsally. The loss of lateral constriction in AC-ablated animals and in *fos-1* mutants indicates that the AC not only serves as guidepost but also plays an active role in inducing VulF constriction. This notion is supported by the finding that physical contact between the AC and VulF cells alters the distribution of the actomyosin network in the VulF cells at the onset of lateral constriction. The direct contact formed between the AC and VulF cells induces the recruitment of F-actin, NMY-2, and possibly also other force generators to the basal apex of the lateral membranes between the two VulF cells, thereby reorienting the contractile forces within VulF (Figure 7P′). This mechanism involves the accumulation of the F-BAR-domain protein TOCA-1 at the AC-VulF contact sites, where the basal VulF membranes are bent inward by the ventrally directed AC protrusions. F-BAR-domain proteins typically form crescent-shaped oligomers that can sense membrane curvature and recruit the actin cytoskeleton to the sites of membrane deformation (Fricke et al., 2010; Salzer et al., 2017). Even though TOCA-1 is expressed in both the AC and VulF cells, the tissue-specific RNAi experiments indicate that TOCA-1 recruitment occurs predominantly on the side of the VulF cells, consistent with a role in sensing the deformation of the basal VulF surface. By contrast, the adjacent VulE cells do not undergo lateral constriction because their basal surfaces are not deformed by the AC and the VulE cells do not accumulate TOCA-1 on the apex of their lateral membranes.

Like many other F-BAR-domain proteins, TOCA-1 and its functionally redundant paralog TOCA-2 contain a C-terminal SH3 domain that recruits components of the WAVE complex to regulate F-actin dynamics. During *C. elegans* embryonic morphogenesis and endocytosis in oocytes, TOCA-1 and TOCA-2 activate the CDC-42 pathway and regulate WAVE- and WSP-dependent actin dynamics (Bai and Grant, 2015). We have found that during vulval morphogenesis, the TOCA proteins stabilize the actomyosin network at the contact AC-VulF sites via the CDC-42/MRCK-1 and RHO-1 pathways (Figure 7P′) (Gally et al., 2009). The highly mobile force-generating myosin complexes are trapped once they have reached the VulF-AC contact sites marked by the TOCA complex, where they may further stabilize F-actin bundles in a positive feedback loop. Hence, the loss of TOCA function affects both myosin and F-actin localization in the VulF cells.

There exist striking similarities between AC invasion and the invasion of metastatic tumor cells, at both the molecular and morphological level (Sherwood et al., 2005). In analogy, invasive cells do not only need to change their own shape, but they also induce cell-shape changes in the tissues they invade (Blazejczyk et al., 2015). The conserved F-BAR-domain proteins could play an important role in the target tissues to sense the mechanical cues generated by invading cells (McMahon and Boucrot, 2015). Such a strategy could be used by metastatic tumor cells as they move through the adjacent normal tissue and to penetrate the endothelial cell layer during intravasation (Chiang et al., 2016).

## STAR★METHODS

Detailed methods are provided in the online version of this paper and include the following:

- KEY RESOURCES TABLE
- CONTACT FOR REAGENT AND RESOURCE SHARING
- EXPERIMENTAL MODEL AND SUBJECT DETAILS
  - *C. elegans* Cultures
  - Alleles Used
- METHOD DETAILS
  - Generation of Endogenous gfp::toca-1 Reporter
  - Microscopy and Image Analysis
  - RNA Interference
  - Cell Ablations Experiments
  - Cortical Tension Measurements by Laser Nanosurgery
- QUANTIFICATION AND STATISTICAL ANALYSIS
  - Membrane Length and Intensity Measurements
  - Particle Tracking
  - Statistical Analysis

### SUPPLEMENTAL INFORMATION

Supplemental Information includes six figures, one table, and seven movies and can be found with this article online at http://dx.doi.org/10.1016/j.devcel.2017.07.008.

### AUTHOR CONTRIBUTIONS

Q.Y., D.R., L.M., and M.D. conducted the experiments. Q.Y. and A.H. designed the experiments, analyzed the data, and wrote the manuscript.

### ACKNOWLEDGMENTS

We thank all present and past group members for critical discussion. We are also grateful to T. Vuong and M. Labouesse for help with the cortical tension measurements and to G. Scita for sharing the strains of *toca-1* and *toca-2* mutants, the *C. elegans* Genetics Center, S. Mitani (Japan Knockout Consortium), the Gene Expression Consortium for providing strains, and Andrew Fire for vectors. This research was supported by the Kanton Zürich and by grant

nos. 31003A_146131 and 31003A_166580 from the Swiss National Science Foundation to A.H.

Received: May 31, 2016
Revised: May 15, 2017
Accepted: July 11, 2017
Published: August 7, 2017

## REFERENCES

Andrew, D.J., and Ewald, A.J. (2010). Morphogenesis of epithelial tubes: insights into tube formation, elongation, and elaboration. Dev. Biol. *341*, 34–55.

Bai, Z., and Grant, B.D. (2015). A TOCA/CDC-42/PAR/WAVE functional module required for retrograde endocytic recycling. Proc. Natl. Acad. Sci. USA *112*, E1443–E1452.

Barkoulas, M., van Zon, J.S., Milloz, J., Van Oudenaarden, A., and Félix, M.-A. (2013). Robustness and epistasis in the *C. elegans* vulval signaling network revealed by pathway dosage modulation. Dev. Cell *24*, 64–75.

Blazejczyk, A., Papiernik, D., Porshneva, K., Sadowska, J., and Wietrzyk, J. (2015). Endothelium and cancer metastasis: perspectives for antimetastatic therapy. Pharmacol. Rep. *67*, 711–718.

Brenner, S. (1974). The genetics of *Caenorhabditis elegans*. Genetics *77*, 71–94.

Burdine, R., Branda, C., and Stern, M. (1998). EGL-17(FGF) expression coordinates the attraction of the migrating sex myoblasts with vulval induction in *C. elegans*. Development *125*, 1083–1093.

Canevascini, S., Marti, M., Fröhli, E., and Hajnal, A. (2005). The *Caenorhabditis elegans* homologue of the proto-oncogene ect-2 positively regulates RAS signalling during vulval development. EMBO Rep. *6*, 1169–1175.

Carpenter, A.E., Jones, T.R., Lamprecht, M.R., Clarke, C., Kang, I.H., Friman, O., Guertin, D.A., Chang, J.H., Lindquist, R.A., Moffat, J., et al. (2006). CellProfiler: image analysis software for identifying and quantifying cell phenotypes. Genome Biol. *7*, R100.

Chiang, S.P.H., Cabrera, R.M., and Segall, J.E. (2016). Tumor cell intravasation. A review in the theme: cell and molecular processes in cancer metastasis. Am. J. Physiol. Cell Physiol. *311*, C1–C14.

Dickinson, D.J., Ward, J.D., Reiner, D.J., and Goldstein, B. (2013). Engineering the *Caenorhabditis elegans* genome using Cas9-triggered homologous recombination. Nat. Methods *10*, 1028–1034.

Dickinson, D.J., Pani, A.M., Heppert, J.K., Higgins, C.D., and Goldstein, B. (2015). Streamlined genome engineering with a self-excising drug selection cassette. Genetics *200*, 1035–1049.

Diogon, M., Wissler, F., Quintin, S., Nagamatsu, Y., Sookhareea, S., Landmann, F., Hutter, H., Vitale, N., and Labouesse, M. (2007). The RhoGAP RGA-2 and LET-502/ROCK achieve a balance of actomyosin-dependent forces in *C. elegans* epidermis to control morphogenesis. Development *134*, 2469–2479.

Estes, K.A., and Hanna-Rose, W. (2009). The anchor cell initiates dorsal lumen formation during *C. elegans* vulval tubulogenesis. Dev. Biol. *328*, 297–304.

Farooqui, S., Pellegrino, M.W., Rimann, I., Morf, M.K., Müller, L., Fröhli, E., and Hajnal, A. (2012). Coordinated lumen contraction and expansion during vulval tube morphogenesis in *Caenorhabditis elegans*. Dev. Cell *23*, 494–506.

Fricke, R., Gohl, C., and Bogdan, S. (2010). The F-BAR protein family Actin' on the membrane. Commun. Integr. Biol. *3*, 89–94.

Gally, C., Wissler, F., Zahreddine, H., Quintin, S., Landmann, F., and Labouesse, M. (2009). Myosin II regulation during *C. elegans* embryonic elongation: LET-502/ROCK, MRCK-1 and PAK-1, three kinases with different roles. Development *136*, 3109–3119.

Giuliani, C., Troglio, F., Bai, Z., Patel, F.B., Zucconi, A., Malabarba, M.G., Disanza, A., Stradal, T.B., Cassata, G., Confalonieri, S., et al. (2009). Requirements for F-BAR proteins TOCA-1 and TOCA-2 in actin dynamics and membrane trafficking during *Caenorhabditis elegans* oocyte growth and embryonic epidermal morphogenesis. PLoS Genet. *5*, e1000675.

Haag, A., Gutierrez, P., Bühler, A., Walser, M., Yang, Q., Langouët, M., Kradolfer, D., Fröhli, E., Herrmann, C.J., Hajnal, A., et al. (2014). An *in vivo* EGF receptor localization screen in *C. elegans* identifies the ezrin homolog ERM-1 as a temporal regulator of signaling. PLoS Genet. *10*, e1004341.

Heisenberg, C.-P., and Bellaiche, Y. (2013). Forces in tissue morphogenesis and patterning. Cell *153*, 948–962.

Helker, C.S.M., Schuermann, A., Karpanen, T., Zeuschner, D., Belting, H.G., Affolter, M., Schulte-Merker, S., and Herzog, W. (2013). The zebrafish common cardinal veins develop by a novel mechanism: lumen ensheathment. Development *140*, 2776–2786.

Jaqaman, K., Loerke, D., Mettlen, M., Kuwata, H., Grinstein, S., Schmid, S.L., and Danuser, G. (2008). Robust single-particle tracking in live-cell time-lapse sequences. Nat. Methods *5*, 695–702.

Kamath, R.S., Fraser, A.G., Dong, Y., Poulin, G., Durbin, R., Gotta, M., Kanapin, A., Le Bot, N., Moreno, S., Sohrmann, M., et al. (2003). Systematic functional analysis of the *Caenorhabditis elegans* genome using RNAi. Nature *421*, 231–237.

Kondo, T., and Hayashi, S. (2013). Mitotic cell rounding accelerates epithelial invagination. Nature *494*, 125–129.

Lohmer, L.L., Clay, M.R., Naegeli, K.M., Chi, Q., Ziel, J.W., Hagedorn, E.J., Park, J.E., Jayadev, R., and Sherwood, D.R. (2016). A sensitized screen for genes promoting invadopodia function *in vivo*: CDC-42 and Rab GDI-1 direct distinct aspects of invadopodia formation. PLoS Genet. *12*, e1005786.

Lubarsky, B., and Krasnow, M.A. (2003). Tube morphogenesis: making and shaping biological tubes. Cell *112*, 19–28.

Lundquist, E., Reddien, P., Hartwieg, E., Horvitz, H., and Bargmann, C. (2001). Three *C. elegans* Rac proteins and several alternative Rac regulators control axon guidance, cell migration and apoptotic cell phagocytosis. Development *128*, 4475–4488.

Matus, D.Q., Li, X.-Y., Durbin, S., Agarwal, D., Chi, Q., Weiss, S.J., and Sherwood, D.R. (2010). In vivo identification of regulators of cell invasion across basement membranes. Sci. Signal. *3*, ra35.

Mayer, M., Depken, M., Bois, J.S., Jülicher, F., and Grill, S.W. (2010). Anisotropies in cortical tension reveal the physical basis of polarizing cortical flows. Nature *467*, 617–621.

McMahon, H.T., and Boucrot, E. (2015). Membrane curvature at a glance. J. Cell Sci. *128*, 1065–1070.

Morf, M.K., Rimann, I., Alexander, M., Roy, P., and Hajnal, A. (2013). The *Caenorhabditis elegans* homolog of the Opitz syndrome gene, madd-2/Mid1, regulates anchor cell invasion during vulval development. Dev. Biol. *374*, 108–114.

Nance, J., Lee, J.-Y., and Goldstein, B. (2005). Gastrulation in *C. elegans*. WormBook, 1–13.

Salzer, U., Kostan, J., and Djinović-Carugo, K. (2017). Deciphering the BAR code of membrane modulators. Cell. Mol. Life Sci. *74*, 2413–2438.

Sawyer, J.M., Harrell, J.R., Shemer, G., Sullivan-Brown, J., Roh-Johnson, M., and Goldstein, B. (2010). Apical constriction: a cell shape change that can drive morphogenesis. Dev. Biol. *341*, 5–19.

Schindler, A.J., and Sherwood, D.R. (2012). Morphogenesis of the *Caenorhabditis elegans* vulva. Wiley Interdiscip. Rev. Dev. Biol. *2*, 75–95.

Sharma-Kishore, R., White, J.G., Southgate, E., and Podbilewicz, B. (1999). Formation of the vulva in *Caenorhabditis elegans*: a paradigm for organogenesis. Development *126*, 691–699.

Sherwood, D.R., and Sternberg, P.W. (2003). Anchor cell invasion into the vulval epithelium in *C. elegans*. Dev. Cell *5*, 21–31.

Sherwood, D.R., Butler, J.A., Kramer, J.M., and Sternberg, P.W. (2005). FOS-1 promotes basement-membrane removal during anchor-cell invasion in *C. elegans*. Cell *121*, 951–962.

Van Fürden, D., Johnson, K., Segbert, C., and Bossinger, O. (2004). The *C. elegans* ezrin-radixin-moesin protein ERM-1 is necessary for apical junction remodelling and tubulogenesis in the intestine. Dev. Biol. *272*, 262–276.

Vuong-Brender, T.T.K., Ben Amar, M., Pontabry, J., and Labouesse, M. (2016). The interplay of stiffness and force anisotropies drive embryo elongation. bioRxiv, 095752.

Wang, Y.-C., Khan, Z., Kaschube, M., and Wieschaus, E.F. (2012). Differential positioning of adherens junctions is associated with initiation of epithelial folding. Nature *484*, 390–393.

Ziel, J.W., Hagedorn, E.J., Audhya, A., and Sherwood, D.R. (2009). UNC-6 (netrin) orients the invasive membrane of the anchor cell in *C. elegans*. Nat. Cell Biol. *11*, 183–189.

## STAR★METHODS

### KEY RESOURCES TABLE

| REAGENT or RESOURCE | SOURCE | IDENTIFIER |
|---|---|---|
| Experimental Models: Organisms/Strains | | |
| wild-type *C. elegans* | *Caenorhabditis* Genetics Center | N2 |
| *erm-1*(*tm677*)/*hT2*[*bli-4*(*e937*) *let*(*q782*) *qIs48*]) | Haag et al., 2014 | AH1890 |
| *nmy-2*::*gfp*(*cp13*) | Dickinson et al., 2013 | LP162 |
| *unc-57*(*e406*) | *Caenorhabditis* Genetics Center | CB406 |
| *wve-1*(*ok3308*)/*hT2*[*bli-4*(*e937*) *let*(*q782*) *qIs48*]) | *Caenorhabditis* Genetics Center | VC2706 |
| *rrf-3*(*pk1426*) | *Caenorhabditis* Genetics Center | NL2099 |
| *toca-2*(*ng11*) | Giuliani et al., 2009 | GU662 |
| *abi-1*(*ok640*) | *Caenorhabditis* Genetics Center | RB829 |
| *srgp-1*(*ok300*) | *Caenorhabditis* Genetics Center | VC202 |
| *wsp-1*(*gm324*) | *Caenorhabditis* Genetics Center | NG324 |
| *rde-1*(*ne219*) | *Caenorhabditis* Genetics Center | WM27 |
| *fos-1*(*ar105*)/ *nT1*[*qIs51*,*let*(*m435*)] | *Caenorhabditis* Genetics Center | AH1205 |
| *dyn-1*(*ky51*) | *Caenorhabditis* Genetics Center | CX51 |
| *unc-6*(*ev400*) | *Caenorhabditis* Genetics Center | NM434 |
| *toca-1*(*tm3334*) | Giuliani et al., 2009 | GU1165 |
| *gfp*::*toca-1*(*zh110*) | this study | AH4481 |
| *zhIs396*[$P_{dlg-1}$>*lifeact*::*gfp*::*unc-54 3'utr*, $P_{lin-48}$>*gfp*] | Farooqui et al., 2012 | AH2453 |
| *qyIs50*[$P_{cdh-3}$>*mCherry*::*moeABD*] | Ziel et al., 2009 | NK409 |
| *qyIs23*[$P_{cdh-3}$>*mCherry*::*plc∂PH*] | Ziel et al., 2009 | NK361 |
| *swIs79*[*ajm-1*::*gfp*, $P_{scm-1}$::*gfp*, *unc-119*(+)] | Diogon et al., 2007 | SU140 |
| *qyEx19*[*ced-10*::*gfp*, *unc-119*(+)] | Lundquist et al., 2001 | AH4293 |
| *mfIs70*[*lin-31p*::*rde-1*, *myo-2p*::*gfp*] | Barkoulas et al., 2013 | JU2058 |
| *qyIs102*[$P_{fos-1a}$::*rde-1*;*myo2*::*yfp*; *unc-119*] | Matus et al., 2010 | NK640 |
| *zhEx167*[*hs*::*rho-1*(*dom.neg*), *sur-5*::*gfp*] | Canevascini et al., 2005 | AH995 |
| *zhEx572*[$P_{egl-17}$::*nmy-2*::*gfp*, *myo-2*::*mcherry*] | this study | AH4720 |
| Oligonucleotides | | |
| *toca-1* homology downstream arm forward: AGGATGACGAT GACAAGAGAAATGATAGCTGTAGTTGGGACC | this study | ODR310 |
| *toca-1* homology downstream arm reverse: aacagctatgacc atgttatATAGTGCGGCGCAAAACCCT | this study | ODR311 |
| *toca-1* homology upstream arm forward: CAATTCTTCTCCTTTA CTCATTGTTCGCCGCTTCTTCAAAAG | this study | ODR312 |
| *toca-1* homology upstream arm reverse: acgacggccagtcgccggca CCTGGTAACCGTGAACTATAC | this study | ODR313 |
| *toca-1* sgRNA forward: cctcctattg cgagatgtcttGAATGAACGACAGTTGCAGTTGTTTAAGAGCTATGCTGG | this study | ODR321 |
| *toca-1* sgRNA reverse: CCAGC ATAGCTCTTAAACAACTGCAACTGTCGTTCATTCaagacatctcgcaataggagg | this study | ODR320 |
| Mutagenesis of *toca-1* sgRNA binding site: AATGAACGACAGT TGCAGTTGTTTAAGAGCTATGCTGG | this study | ODR323 |
| Genotyping *toca-1*(*zh110*): CTCTTGGGAGCTACTTTTCG | this study | ODR325 |
| Genotyping *toca-1*(*zh110*): CTGTGATCATGCCAGTATCAG | this study | ODR327 |

(*Continued on next page*)

| *Continued* | | |
|---|---|---|
| REAGENT or RESOURCE | SOURCE | IDENTIFIER |
| Recombinant DNA | | |
| Repair template for *toca-1* CRISPR | this study | pDR19 |
| sgRNA vector for *toca-1* CRISPR | this study | pDR20 |
| Vulva-specific *nmy-2*::*gfp* expression vector | this study | pQY1 |

## CONTACT FOR REAGENT AND RESOURCE SHARING

Further information and requests for resources and reagents should be directed to and will be fulfilled by the Lead Contact, Alex Hajnal (alex.hajnal@imls.uzh.ch).

## EXPERIMENTAL MODEL AND SUBJECT DETAILS

### *C. elegans* Cultures

*C. elegans* strains were maintained at 20°C on standard nematode growth plates as described (Brenner, 1974). The wild-type strain from which all mutant alleles used were derived is *C. elegans* Bristol, variety N2. Newly generated alleles were backcrossed at least three times against the N2 strain before analysis. In all experiments, hermaphrodite larvae were observed at the stages indicated in the figure legends.

### Alleles Used

LGI: *erm-1*(*tm677*), *hT2*[*bli-4*(*e937*) *let*(*q782*) *qIs48*] (*I*;*III*), *nmy-2*::*gfp*(*cp13*) (Dickinson et al., 2013), *unc-57*(*e406*), *wve-1*(*ok3308*), LGII: *rrf-3*(*pk1426*), LGIII: *toca-2*(*ng11*) (Giuliani et al., 2009), *abi-1*(*ok640*), LGIV: *srgp-1*(*ok300*)(*IV*), *wsp-1*(*gm324*)(*IV*), LGV: *rde-1*(*ne219*), *fos-1*(*ar105*), *nT1*[*qIs51*, *let*(*m435*)](*IV*;*V*), LGX: *dyn-1*(*ky51*), *unc-6*(*ev400*) (Ziel et al., 2009), *toca-1*(*tm3334*) (Giuliani et al., 2009), *gfp*::*toca-1*(*zh110*) (this study). Extrachromosomal and integrated arrays: *zhIs396*[$P_{dlg-1}$>*lifeact*::*gfp*::*unc-54 3'utr*, $P_{lin-48}$>*gfp*] (Farooqui et al., 2012), *qyIs50*[$P_{cdh-3}$>*mCherry*::*moeABD*], *qyIs23*[$P_{cdh-3}$>*mCherry*::*plc∂PH*] (Ziel et al., 2009), *swIs79* [*ajm-1*::*gfp*, $P_{scm-1}$::*gfp*, *unc-119*(+)](Diogon et al., 2007), *qyEx19*[*ced-10*::*gfp*, *unc-119*(+)], *mfIs70*[*lin-31p*::*rde-1*, *myo-2p*::*gfp*] (Barkoulas et al., 2013), *qyIs102*[$P_{fos-1a}$::*rde-1*;*myo2*::*yfp*; *unc-119*] (Matus et al., 2010), *zhEx167*[*hs*::*rho-1*(*dom.neg*), *sur-5*::*gfp*] (Canevascini et al., 2005), *zhEx572*[$P_{egl-17}$::*nmy-2*::*gfp*, *myo-2*::*mcherry*] (this study).

## METHOD DETAILS

### Generation of Endogenous gfp::toca-1 Reporter

The endogenous *gfp*::*toca-1*(*zh110*) insertion was generated using the modified CRISPR/CAS9 protocol described by (Dickinson et al., 2015). The oligonucleotides used to generate the sgRNA, the homology arms and for sequencing are listed in the Key Resources Table. The GFP-tag was inserted at the N-terminus. *gfp*::*toca-1*(*zh110*);*toca-2*(*ng11*) double mutants show a wild-type vulval lumen morphology, indicating that the GFP::TOCA-1 fusion protein is functional.

### Microscopy and Image Analysis

Fluorescent images and four-dimensional (4D) recording were obtained using an Olympus BX61 wide-field microscope equipped with a X-light spinning disc confocal system using a 60x Plan Apo lens and a Hamamatsu Orca Flash 4.0 CMOS camera. For the wild-type, the *erm-1* mutant and the AC ablation, we recorded five and for the *fos-1* mutant three larvae each. The graph in Figure S1 shows the mean values ± standard deviations measured in the recordings. For 3D reconstructions, z-stacks with a step size of 0.5 μm were recorded with an Olympus FV1000 or a Zeiss LSM confocal microscope. For 4D recordings of vulval invagination, animals were mounted on 5% agarose pads containing 0.5 mM tetramisole. Images were recorded with an X-light spinning disc system at 10 minute time intervals taking 30 to 40 z-stacks with a step size of 0.3 μm per time point. The layers representing the mid sagittal sections are shown in Figure 3 and Movies S1 and S2. Spinning disc images were processed using the Huygens Deconvolution platform (SVI) to increase the signal to noise ratio and analyzed using Fiji (ImageJ (NIH)) or Imaris (Bit-plane) software.

### RNA Interference

RNA interference (RNAi) was performed using the feeding method as described (Kamath et al., 2003). Briefly, P0 worms were synchronized at the L1 stage, transferred to nematode growth plates containing 3 mM IPTG and 50 ng/ml ampicillin seeded with the desired RNAi bacteria selected from the library described in Kamath et al. (2003) and allowed to grow for 5-7 days at 20°C, after which the surviving F1 progeny was analyzed.

### Cell Ablations Experiments

Worms were mounted on 4% agarose containing 4 mM tetramisole pads for laser ablation. For cell ablations, a Leica DMLB wide-field microscope equipped with a MicroPoint Laser system using a 440nm dye cell containing 5mM coumarin that was coupled to a nitrogen laser (Photonics instruments) set at a pulse rate of 10Hz was used, as described in Farooqui et al. (2012). AC ablations were performed in late L3 larvae at the Pn.pxx stage, in which the AC had breached the basal laminae as scored with Nomarski optics. Ablated worms were rescued from the pads and allowed to recover at 15°C for 2hours before mounting them again for 4D imaging.

### Cortical Tension Measurements by Laser Nanosurgery

L4 larvae were mounted on 4% agarose pads containing 4 mM tetramisole. Cutting of the apical and lateral membranes was performed using a wavelength of 900nm using an Olympus two-photon Fluoview 1000 microscope equipped with a pre-compensated Ti:Sapphire Laser. The input power was set at 2.17± 0.05W, the length of the cutting region (yellow bars in Figure 4) was set at around 2 μm, and the activation time was calculated by the scan speed of 1.25μs/pixel. Animals were imaged at 0.2 sec intervals with a 60x N.A. 1.1 water immersion lens before and after cutting. For each cut, we measured the maximal recoil distance between the edges of the cut membrane as indicated with the dashed red line in Figure 4. Since the maximal recoil velocity exceeded the recording speed, we calculated the average recoil velocity as $v_{average}$= maximal recoil distance/duration of recoil (μm/sec). To quantify lateral VulF constriction after laser cutting, operated larvae were kept on the same agarose pads until the cut had been repaired as detected by the reappearance of the CED-10::GFP signal and the VulE cells had divided, when vulval lumen formation was scored (approximately 4 hours later).

## QUANTIFICATION AND STATISTICAL ANALYSIS

### Membrane Length and Intensity Measurements

Measurements of apical and lateral membrane lengths were conducted on mid-sagittal sections using the measurement tools in Fiji (ImageJ (NIH)) software. The boundaries of the apical VulF membranes were defined by the AJs displaying a stronger CED-10::GFP signal. The length of the lateral VulF membranes was measured from the VulF-AC intersection to the boundary of the apical VulF membrane as shown in Figure S1. Intensity plots of LifeAct::GFP or NMY-2::GFP along the lateral VulF membranes were generated using custom script as described (Morf et al., 2013). For each animal, the intensity in yz-axis projections of the lateral VulF membrane regions (outlined with a yellow dashed box in the example shown in the inset) or in xz-projections (blue dashed boxes) were divided into ten equal segments along the dorso-ventral axis. In each segment, the total intensity was measured and normalized to the summed intensities of all segments.

### Particle Tracking

The NMY-2 punctae in Figure 4 were tracked and analyzed using the μ-track software package (Jaqaman et al., 2008). NMY-2::GFP punctae were automatically selected using a Gaussian mixture model and tracked using the motion analysis module. For each tracked particle, the normalized diffusion coefficient was calculated as a measure of its mobility.

### Statistical Analysis

Data were organized and analyzed using Excel (Microsoft Inc.) spreadsheets and plots were generated in Excel or using the Prism 7 (Graphpad Inc.) software package. All statistical tests such as the calculation of means, standard deviations, 95% CIs and t-tests are described in the figure legends and were performed using the built-in Microsoft Excel functions.

# 4. Discussion

Epidermal growth factor signaling can orchestrate highly complex, intricate and versatile cellular signaling networks, regulating multiple cellular responses. The more we understand about the different induced canonical and non-canonical effectors and their integration and cross-talk with other signaling networks, the more we realize how much we still need to learn about the signaling cascade. In the light of this reflection, it can be of use to confine the number of variables in the quest for novel roles, functions and interactions of EGF signaling. The regulatory players of the EGFR pathway are highly conserved throughout all organisms, but not all organisms harbor equal diversity in the number of encoded ligands and receptors. Analyzing putative functions of EGFR signaling in lower organisms such as *C. elegans* can thus present an advantage in the dissection of the jungle of possible signaling combinations and redundant interactions. *C. elegans* has only one EGF related ligand and one EGFR related receptor we know of. In this thesis, evidence is presented that during vulval induction the sole *C. elegans* EGF ligand LIN-3 is regulated in its secretion through polarization of the signal sending anchor cell and that thereafter, the vulval cells secrete LIN-3 in a reciprocal manner to polarize the AC during vulval morphogenesis. LIN-3 polarity is regulated in part by the general AC polarity, which is largely directed by Netrin receptor UNC-40 localization. In addition, an unknown signaling pathway is involved specifically in the subcellular localization of membrane bound LIN-3, which is independent of $PIP_2$ polarity. We have identified two factors, a seven-pass-transmembrane receptor (SRA-9) and a neuropeptide
(NLP-26), which specifically regulate LIN-3 polarity, but as yet have no clear mechanism for the process. Later during vulva development, LIN-3 expressed from the vulval cells shortly after basal lamina breaching, in turn polarizes subcellular $PIP_2$ localization in the AC in their direction, which is required for dorsal lumen expansion during dorsal vulval lumen morphogenesis.

## 4.1 AC polarity canalizes LIN-3 secretion

### 4.1.1 LIN-3 polarity and subsequent secretion is directed, and biased towards P6.p during wild-type vulval induction

Our data makes it clear that the establishment of the generally accepted LIN-3 EGF gradient during vulval induction is not as simple as hitherto assumed, and that the topic deserves further investigation. Morphogen gradient formation is a complex and essential part of development in multicellular organisms. Yet, how morphogen gradients are formed is still not fully understood. Different mechanisms contribute to their establishment and maintenance, such as diffusion (Duchesne et al., 2012; Makarenkova et al., 2009; Miura et al., 2009), transcytosis (Dierick and Bejsovec, 1998; Kruse et al., 2004) and ligand degradation (Chen and Struhl, 1996; Entchev et al., 2000; Kicheva et al., 2007). In this study, we have investigated how cell polarity instigates directed diffusion (Bozorgui et al., 2015) of the EGF LIN-3 ligand, and thus shapes the morphogen gradient during *C. elegans* vulval induction. Our results have shown that AC polarity is not only required for basal lamina

breaching, but also during vulval induction. Furthermore, polarized LIN-3 EGF secretion is not only directed along a dorso to ventral axis, defined by UNC-6 Netrin signaling, but also by an additional A-P axis that orients the morphogen gradient. NLP-26 and SRA-9 signaling play a major role in this additional axis and provide directional information to the AC, or the ability to sense directional information, of the location of the closest Pn.p cell (Fig. 3.1.4). The AC in turn focuses the bulk of its secreted LIN-3 towards the perceived Pn.p cell, which promotes reinforcement of the 1° vulval cell fate by upregulating LET-23 signaling selectively in this cell. Much of our work is focused on the endogenous *lin-3(zh112)* reporter allele. Therefore, whether its expression-pattern resembles a wild-type situation or could potentially contain artifacts is of great importance for the reliability of our data.

### 4.1.2 Further investigation of the LIN-3 subcellular localization pattern

Mutations conveying a loss of *lin-3* function are lethal. The fact that our endogenous *mNeongreen::lin-3* reporter allele *(zh112)* is viable and does not display any obvious developmental defects shows that vital functions, such as receptor binding by the EGF domain, pre-LIN-3 ligand trafficking, receptor ligand complex endocytosis are not noticeably impaired by the presence of the fluorophore in the fusion protein. An interesting feature that our endogenous *mNeongreen::lin-3* reporter revealed is the subcellular localization pattern observed in the AC. Previously integrated or extracellularly expressed transgenic reporters we had constructed showed LIN-3 expression predominantly at the cell periphery and the plasma membrane (Fig. 3.3.7). The question of interest is now to know, which expression-pattern is most like the wild-type, a question we can never answer with unequivocal conviction, since every reporter we construct induces a deviation from the wild-type state. Also, expression pattern analysis by immunostaining likewise does not doubtlessly represent a wild-type situation, since its effectiveness varies greatly between and within each staining process, and largely depends on the specificity and binding affinity of the primary antibody. Since none these mentioned options are perfect, all we can do is use the tools at hand to conduct well thought-out experiments with the proper controls to draw our conclusions. Since we have no true “wild-type” control, we need to make deductions through comparison amongst the reporters we have. These are, the MoSCI integrant on chromosome I, *zhIs83[frt::lin-3::gfp::frt, unc-119(+)]*, the MoSCI integrant on chromosome II, *zhIs72 [lin-3::gfp, unc-119(+)]*, the endogenous *lin-3(zh112[mNeongreen::LoxP::3xFlag])* on chromosome IV, and the transiently and extrachromosomally expressed *lin-3::citrin* fusion plasmid (pLM2), in which the AC specific *lin-3* enhancer element (mutant allele *e1417*), the EGF domain, but not the transmembrane domain sequences are included (Fig. 3.3.7, A).
Several hypotheses present themselves as to why the reporters display differences that require closer investigation. A main difference between the reporters, is that they do not contain all the known and unknown regulatory elements of the *lin-3* locus, with exception of the endogenous reporter. The *lin-3* locus is vast, encompassing approximately 10 kb. It encodes four splice variants and contains three known transcriptional start sites (Fig. 1.1.3) (Dutt et al., 2004; Hwang, 2004; Saffer et al., 2011). Therefore only the endogenous reporter definitely contains all the regulatory elements and should reflect wild-type regulation and expression levels. It is not clear to what extent additional copies of *lin-3* or increased expression levels impact the overall subcellular localization pattern of the protein. Although our *zhIs83* strain is a MoSCI integrant and thus only has two

additional *lin-3* copies, it shows ectopic vulval induction. This is likely due to regulatory enhancer elements in the vicinity of the insertion site (Fig. 3.3.7, B-D). Thus, LIN-3 is expressed excessively due to upregulation on the translational level. However, the *lin-3*::*gfp* signal is clearly localized to the membrane and polarized nonetheless (Fig. 3.3.7, B-D). The *zhIs72[lin-3::gfp, unc-119(+)]* MoSCI integrand has very weak expression levels, though it is clearly polarized and shows similar *gfp* expression intensity at the membrane and in the cytoplasm, but no clearly distinguishable foci (Matthias Morf Thesis, 2015). Thus, the only reporter with wild-type expression levels is the *zh112* allele. The *zhIs83* reporter is very bright due to the ectopic expression and the *zh112* allele is faint. Why the LIN-3 signal in *zhIs83* strain is thus enriched at the cellular membrane needs to be discussed. A reason could be that wild-type LET-23 receptor and putative LIN-3 processing proteins, such as serine- or metalloproteases could be severely underrepresented compared to the LIN-3 precursor ligand, causing stagnation of ligand processing or internalization, and consequently the increased presence of LIN-3 at the plasma membrane. The excess GFP signal at the plasma membrane in the *zhIs83* strain could mask the putative foci containing sub-cellular expression pattern. What the reporters have in common, is the site of fluorophore integration within the coding sequence. They are all integrated N-terminally of the EGF domain, at the same position (Fig. 3.3.7, A). However, they all express different fluorescent proteins. The *zhIs83* strain has a *gfp* sequence inserted, the *zh112* allele an *mNeongreen* sequence (Hostettler et al., 2017) and the extrachromosomal transgene encodes a *citrin* fluorophore (Zeiser et al., 2011). An unhappy scenario would constitute a situation, in which the mNeongreen fluorophore sequence would promote slight alteration in the 3D structure of LIN-3, or would possess innate attributes promoting the aggregation of the protein and leading to the observed fluorescent foci in the AC. Although such a scenario is not highly probable, we cannot completely reject this possibility. Augmented fluorophore aggregation has been speculated to occur more frequently with mCherry proteins (lab internal experience), but to my knowledge so far no reports of mNeongreen induced protein aggregation exist. Incubation of the *zh112* strain at 15° C produced no obvious alteration in foci occurrence in the AC (personal observation). It is therefore conceivable that the foci represent the wild-type feature, which is further supported by a recent publication, in which a *lin-3::gfp* MoSCI transgene expression in the AC displayed similar intracellular foci (Barkoulas et al., 2016).

Since it is likely that the foci we observe in the *zh112* reporter strain reflect the wild-type situation, further investigation of the nature of the foci would be required. The most likely cause for the foci is explained by intracellular trafficking of newly synthesized LIN-3 localized to the ER, the Golgi or to vesicles on its way to the plasma membrane. To confirm this hypothesis would be relative straight forward and would comprise colocalization experiments with established ER, Golgi or secretory vesicle transgenic markers.

An alternative scenario could represent LIN-3 bound to LET-23 after receptor activation and endocytosed. In this less likely case, we would have expected to see higher mNeongreen::LIN-3 expression intensity in the 1° cell than in the AC. We do see some diffuse signal in the 1° cells, but since it is very weak, we cannot be completely sure of its relevance. With an endogenous *let-23* reporter, fused to a complementing fluorophore sequence such as mCherry (587 nm, emission) or tdTomato (581 nm, emission), we could perform co-localization experiments to see if the signals overlap or not and whether LET-23 is observed in the AC at all during vulval induction. If this would be the case, the source of the ligand could be autocrine signaling by the AC or LIN-3 from the VPCs or the hypodermis (Dutt et al., 2004; Saffer et al., 2011).

### 4.1.3 Implication of P6.p directed LIN-3 secretion by the AC for vulval induction

Our data show that there is a bias in LIN-3 polarity towards the ventrally located VPCs and in particular towards P6.p (Fig. 3.1.1 and 3.1.4.). The implication of this directed LIN-3 polarity is not clear. The observed aberrant phenotypes in vulval induction, 1° fate shift or AC to P6.p alignment in the mutant backgrounds of *nlp-26(zh113)* or *sra-9(zh108)* are, though weakly significant, of very low penetrance (Fig. 3.1.3 and 3.1.4). This brings forth the question of what is really the significance of polarized LIN-3 secretion during vulval induction. Very likely, the answer is that the directed secretion promotes constriction of 1° vulval cell fate adoption to one cell and that there is a feedback mechanism involved, which signals back to the AC to sequester further inductive LIN-3 signaling to the initially upregulated 1° fated P6.p, and thus reinforce and constricts the 1° vulval cell fate induction. The vulval cell fate induction pattern not only depends on LET-60 RAS activation, but is interlinked with Notch signaling (Berset et al., 2001; Shaye and Greenwald, 2002). And recently it has been shown that both pathways play together for LIN-3 induced VPC migration during AC to P6.p alignment (Grimbert et al., 2016; Huelsz-Prince and van Zon, 2017). We suspect that directed LIN-3 secretion has an application in VPC migration towards the AC, which our alignment and 1° cell fate shift results support. To investigate this hypothesis and check for putative parallel interaction of NLP-26 and SRA-9 directed LIN-3 secretion with Notch signaling, we would perform epistasis analysis with *sra-9* and *nlp-26* mutant alleles in combination with a *lin-12* Notch mutant allele or, to prevent the occurrence of two ACs (Greenwald et al., 1983; Kimble and Hirsh, 1979), in a VPC specific *lin-12* knock-out strain. This experiment would confirm or reject putative redundant functions of NLP-26 or SRA-9 with LIN-12 Notch signaling. A second approach in the search for redundant interactions which, when absent could enhance our *sra-9* and *nlp-26* mutant induced synthetic multivulva phenotype in the *gap-1* mutant background, could be taken from the original *gap-1* synMuv finding (Hajnal et al., 1997). Possibly, loss in directed LIN-3 secretion could enhance the *let-23(sy1); gap-1(ga133)* mediated ectopic vulval induction phenotype, by increased expansion of the LIN-3 signaling radius, or it could decrease P6.p specific 1° cell fate induction, or even possibly enhance the low penetrance vulvaless induction observed in the *let-23(sy1); gap-1(ga133)* double mutant (Hajnal et al., 1997). Experiments along these lines would undoubtedly shed more light on the interactions and redundant regulation of LIN-3 gradient formation during vulval induction. In any case, further investigation to the nature of the NLP-26 and SRA-9 induced LIN-3 polarity mechanism will be of great interest.

## 4.2 Epidermal growth factor signaling regulates cell polarity and migration

There have been many previous reports implying that epidermal growth factor signaling can regulate, direct or enhance cell polarity and cell migration during development (Duchek and Rørth, 2001) as well as in cancer cells (Barrandon and Green, 1987; Chen et al., 1994; Mosadegh et al., 2008; Turner et al., 1996; van Rheenen et al., 2007; Wyckoff et al., 2004). Most of these results are founded on cell culture assays, and only few studies show *in-vivo* results or present mechanisms during regular organism development (Duchek and Rørth, 2001; Wyckoff et al., 2000; Wyckoff et al., 2004).
During vulval morphogenesis, we find a regulated cell invasion process, that is required for proper lumen morphogenesis. The evidence presented in this thesis suggests that localized EGF LIN-3 signaling is involved in the regulation of AC polarity and subsequent protrusion formation, enabling normal vulval morphogenesis. Thus, we have an *in-vivo* model, in which we can perform epistatic analysis and look for putative downstream effectors in this process, to advance our knowledge of the relationship in epidermal growth-factor signaling and cancer cell invasion.

### 4.2.1 LIN-3 regulates cell polarity and vulval morphogenesis

One of the main original findings that lead us to investigate *lin-3* in terms of dorsal lumen formation, was that heat-shock induction of LIN-3 lead to abnormal vulval morphogenesis. Later, the putative connection to AC induced dorsal lumen formation was made by evidence of a previous publication (Chang et al., 1999; Estes and Hanna-Rose, 2009). At first, we were not sure, at which point the AC is required for dorsal lumen morphogenesis. Initially, we speculated that the AC is required between the triangle and the X-tree stage to physically expand the dorsal lumen. The AC ablation studies showed us that this is not the case. Rather, the AC is required at an earlier stage during the last round of vulval cell division (Fig. 3.2.2). It is clear that the AC is required for dorsal lumen expansion, however its exact function and the mechanism in the process is not known. Dorsal lumen expansion is likely linked to cell invasion since *unc-6* mutants often show defects in dorsal lumen formation in spite of successful basal lamina breaching (Estes and Hanna-Rose, 2009).
We used dorsal lumen expansion as readout for proper AC invasion during our investigations. However, in my opinion these data do not provide evidence enough to form an explicit conclusion. Dorsal lumen expansion is a process during vulval morphogenesis, which can result in a mutant phenotype resulting from other causes than AC invasion. Independent of the AC, the vulF cells undergo cell shape changes that lead to the dorsal lumen expansion (Yang et al. 2017), and have been shown to be dependent on EGL-26 induced signaling from the vulE cells (Hanna-Rose and Han, 2002). The frequent occurrence of the dorsal lumen phenotype such as under RNAi conditions in highly sensitized genetic backgrounds (Fig. 3.3.3), or as a result of heat shock induction (Fig. 3.3.5), further shows that other factors can cause the phenotype apart from AC invasion. Regarding future experiments on this topic, it would be beneficial to focus on the putative regulation of AC polarity by LIN-3. The dorsal lumen phenotype, however, serves to illustrate a function for hypothetical LIN-3 regulate AC polarity. Likewise, although the *egl-38(n578)* allele concerning results are significant, they only provide an indication towards vulF mediated LIN-3 signaling to the AC, since EGL-38 is a transcription factor that also regulates other factors besides *lin-3*. For the most time, in which the

project was conducted, we were lacking the specific tools to answer our question, whether vulF specific LIN-3 expression really directs AC polarity and subsequent dorsal lumen formation or not. With the relatively recently emerged CRISPR/CAS9 tool, and a *C. elegans* compatible adaption of the system, we were able to, during a completed Master projectunder my supervision, insert two FRT-recombination sites, flanking part of the inscribed EGF domain into the endogenous locus (Master Thesis Silvan Spiri, 2016). Silvan Spiri is continuing the project as a PhD student, and is in the process of engineering the *let-23* locus by insert FRT-recombination sites. With these tools, we will be able to investigate our research question more directly.

The AC-specific *let-23dom-rf* transgene as well as the *mCherry::PLCδ$^{PH}$* reporter interfere with basal lamina breaching (Fig. 3.3.10). It is therefore possible that AC polarity and protrusion formation are regulated by the LET-23 induced PLC and IP3 pathway (Kariya et al., 2004; Vázquez-Manrique et al., 2008; Meisenhelder et al., 1989). The *mCherry::PLCδ$^{PH}$* reporter could inhibit PLC function by blocking its access to $PIP_2$ and impairing its PLC mediated hydrolysis in a dominant-negative like manner. EGF-induced PLC activity has been shown to hydrolyze $PIP_2$ and thus activates and releases the actin depolimerization factor cofilin, promoting actin dissociation and dynamics (van Rheenen et al., 2007), which is important for cytoskeletal rearrangement during cell-protrusion formation. However, the authors could not specify the specific PLC type in their publication because they used PLC inhibitors to show that EGF-mediated cofilin dissociation form $PIP_2$ was significantly impaired when they added the PLC inhibitor. So far, only PLC-γ has been reported to be phosphorylated and induced by EGFR activation (Anderson et al., 1990; Margolis et al., 1990; Van Buskirk and Sternberg, 2007). The *mCherry::PLCδ$^{PH}$* reporter that was utilized as a control in the mentioned basal lamina breaching assay encodes a pleckstrin homology (PH) domain of human PLC-δ, fused to an mCherry fluorophore sequence and is driven by an AC specific promoter (Ziel et al., 2008). All PLC family members bind $PIP_2$ via their PH domain and catalyze its hydrolysis while their differences are given by their regulatory elements. Since the reporter only contains the PH domain of PLC-δ, which specifically promotes association to $PIP_2$, and no other PLC-δ regulatory elements are added (Lemmon et al., 1995), it does not contradict our dominant-negative theory. As mentioned, PLC has been implicated in protrusion formation through its activation of cofilin. The *C. elegans* ADF/cofilin orthologue UNC-60A is expressed in the AC, specifically localizes to invadopodia and is a regulator of AC invasion (Hagedorn et al., 2014). To see if LIN-3 might regulate AC polarity through PLC mediated UNC-60 cofilin activation, I would perform vulF specific *lin-3* depletion and ectopic *lin-3* expression, to see if it alters the expression pattern of the *unc-60* reporter. In addition, I would investigate whether the *unc-60* RNAi mediated basal lamina breaching effect (Hagedorn et al., 2014) is increased by deregulation of LIN-3/LET-23 signaling.

Heat-shock induced ectopic *lin-3* expression caused defects in AC $PIP_2$ polarity (Fig. 3.2.3). This shows that LIN-3 might promote $PIP_2$ recruitment. The Netrin receptor UNC-40 recruits $PIP_2$ and the basal lamina breaching analysis showed that the *egl-38(n578)* mutant allele enhanced the *unc-6(ev400)*, but not the *unc-40* invasion defect (Fig. 3.2.6 and 3.2.S1). This indicates that LIN-3 directed $PIP_2$ polarity might be integrated at the level of UNC-40. An integrator of the LIN-3 signaling could be through the integrin heterodimer INA-1/PAT-3. The integrins can recruit the UNC-40 receptor, and can recruit F-actin independently of UNC-40 and $PIP_2$. Integrin mutants or ectopic integrin expression promote defects in F-actin polarity in the AC, but do not so much affect $PIP_2$ polarity (Hagedorn et al., 2009; Wang et al., 2014b). *unc-40* mutants have defects in $PIP_2$ polarity, but relatively wild-type actin polarity (Wang et al., 2014b), because in absence of UNC-40 F-actin is

still anchored at the invasive membrane by integrins (Hagedorn et al., 2009).
There exist several reports showing that EGF induced cell migration or cell ruffling are dependent of integrin signaling in mammalian cells (Azimifar et al., 2012; Boscher and Nabi, 2013). EGF Stimulation of epidermoid carcinoma cells in an EGF directed chemotaxis assay induced relocalization of α6β4 integrins from hemidesmosomes to lamellipodia and promoted cell migration. The authors further showed that EGFR co-localized with α6β4 integrins and promotes their phosphorylation through Protein Kinase C (PKC) activation (Rabinovitz et al., 1999). In *C. elegans* it has been shown that integrins indirectly negatively regulate LET-23 EGFR signaling via talin recruitment (Walser et al., 2017), but there are no reports showing vise-versa regulation.
Thus, previous findings support the possibility that LIN-3 might direct AC polarity and protrusion formation or migration during vulval morphogenesis by directing integrin localization. Loss of integrin function does not essentially interfere with $PIP_2$ polarity, however depolarization of integrin likewise depolarizes $PIP_2$ (Hagedorn et al., 2009). The $PIP_2$ depolarization is dependent on UNC-40 and integrins can recruit UNC-40. Therefore, we propose that localized LIN-3 signaling from the vulF cells could recruit the integrin hetero-dimer INA-1/PAT-3 to the AC membrane facing the vulF cells, which further promotes UNC-40 and $PIP_2$ accumulation at the site. For the mechanism, by which LIN-3 would instigate AC mediated dorsal lumen morphogenesis, we see two likely possibilities. In the first, LIN-3 signaling might direct circumferential AC protrusions around the vulF cells, a process required for lateral vulF constriction and subsequent dorsal lumen extension (Yang et al., 2017). Second, the LIN-3 signal might serve as an orientation signal for the AC to form its protrusions around the vulF-vulF lateral membrane, rather than the vulF-vulE lateral membrane. The second hypothesis is backed up by the results regarding *let-23dom-rf* and *lin-3i* induced AC mispositioning (Fig. 3.2.4 and 3.3.2). In this case, even in the absence of the vulF specific LIN-3 signal, the AC would form protrusion in-between or around vulF-vulF lateral membrane most of the time, because it would be situated in the right position by default and only be mispositioned under unusual conditions. This would explain the low penetrance of both the AC mispositioning and the dorsal lumen expansion phenotypes for both strains.

### 4.2.2 The conundrum of reciprocal LIN-3 signaling

A main difficulty for our hypothesis is that the AC expresses LIN-3 from the early/mid L2 stage on, up to the time it fuses with the utse syncytium (Personal observation). On the other hand, we only see very diffuse and very weak LIN-3 expression in the 1° vulval cells at the mid-late L3 larval stage, which is significantly overshadowed by the stronger expression in the AC. Thus, how could the AC sense a signal it is already producing at a higher concentration?
LIN-3 is synthesized as a transmembrane protein. Thus, it requires ectodomain shedding by a specific protease for secretion. The only LIN-3 processing protease so far identified is the serine protease ROM-1, and it has only been shown to function in the vulval tissue, not in the AC (Dutt et al., 2004). It is not known, which metallo- or serineprotease processes LIN-3 in the AC, but unless the AC forms cytonemes, there must be a protease that regulates LIN-3 secretion from the AC (Thomas et al., 1990). Even though there is very likely such a protease, its temporal and spatial expression and functionality are unknown. It is possible that the LIN-3 signal observed in the AC at the late L3 stage, is no longer processed and thus remains membrane-bound. In this case, paracrine

or even juxtacrine LIN-3 signaling could be perceived by the AC and distinguished from its own LIN-3 ligand. ROM-1 expression was observed in the VPCs during vulval cell fate induction, but is absent from the vulval cells at the mid-late L4 stage (Dutt et al., 2004). The vulva specific LIN-3 signal could therefore be juxtacrine. Membrane-anchored EGF was shown to recruit its downstream effectors EGFR RAS ERK and actin, which formed a signaling complexes at the site of the anchored ligand, and could also be recruited when EGF was expressed in a soluble form (Singhai et al., 2014). Thus, we have different potential hypothesis that fit our data. However, further evidence is required to confirm or reject them.

## 4.3 Outlook

### 4.3.1 Future experiments regarding putative LIN-3 directed AC polarity

In retrospect and in context of current literature and the well-established CRISPR/Cas9 system, I see the effective and critical experiments that could be performed more clearly. At the onset of my investigation, our view was not so clear since it was not definite what the cause of the studied dorsal lumen phenotype could be, and at which developmental stage our investigative focus should be directed. But, I believe this project will be further pursued and my gained insights can serve as guidelines for following investigations.
I would propose that all following experiments should be performed with the newly generated endogenous FLP/FRT *lin-3* and prospective *let-23* knock-out strains, and that the main focus should be placed on AC polarity, AC positioning and basal lamina breaching as phenotypic readouts.
This said, one should nonetheless initially verify whether the dorsal lumen morphogenesis defect is reproduced with the novel tools. The rest of the future experiments would be focused on different elements of AC polarity and its regulators. If the ACs $PIP_2$ polarity defect can be confirmed, I would determine at what level AC polarity is regulated, and check for redundancy with known pathways, such as Netrin and integrin signaling. Thus, I would analyze relevant translational reporters, such as for *unc-40*, *pat-3*/*ina-1, unc-60, plc-3* and F-actin localization. Recently, the *C. elegans* cofilin homolog, UNC-60 has been shown to regulate invadopodia formation during AC invasion. Translational reporter expression of LET-60 has been found to be polarized in the AC (Hagedorn et al., 2014). Mammalian PLC-$\gamma$, the *C. elegans* PLC-3 homolog, has been shown to act directly downstream of ErbB (Anderson et al., 1990; Chattopadhyay et al., 1999) and LET-23 (Kariya et al., 2004) signaling. Moreover, PLC signaling has been implicated in $PIP_2$ hydrolysis dependent cofilin release (van Rheenen et al., 2007). Thus, I would investigate how aberrant LIN-3 expression affects PLC-3 and UNC-60 expression patterns in the AC.
To add a functional readout, I would investigate basal lamina breaching efficiency upon LIN-3 LET-23 deregulation, in combination with mutations in the mentioned genes (*unc-40, unc-6, unc-60, plc-3, pat-3* and *pat-3*/*ina-1*).

### 4.3.2 Future experiments regarding regulation of polarized LIN-3 secretion from the AC

To strengthen our data, I would endeavor to determine a clear functionality of polarized LIN-3 secretion during vulval induction. I would look for redundant interactions and analyze vulval induction and the occurrence of 1° cell fate shift as a readout in different genetic backgrounds, such as *lin-12(lf)* and *let-23(sy1);gap-1(ga133)*.
Regarding the location of action of our candidate proteins, NLP-26 and SRA-9, further data would be of great advantage. Our CRISPR/Cas9 generated *nlp-26(zh113)* mutant allele has an inserted *gfp* sequence in the endogenous locus before the signal sequence. The expression seems to be detectable in the VPCs, however the signal is very weak. We therefore cannot undoubtedly conclude that it is expressed in the VPCs (Fig. 3.1.4). Possibly, two copies simply do not provide enough fluorescence for undisputable detection when the fusion-protein is distributed in the cytoplasm. To avoid

these putative effects, we are constructing a new endogenous reporter with an added nuclear localization signal (NLS) to reduce diffusion and enhance its concentration in the smaller compartment of the nucleus.
For SRA-9, we had generated a new deletion allele (*zh108*), but have no endogenous reporter yet. We would therefore endeavor to construct such a reporter, and include an NLS signal.

# 5. Materials and Methods

## 5.1 Animal methods

### 5.1.1 Alleles

Unless specified otherwise, *C. elegans* strains were maintained at 20 °C on NGM (NematodeGrowth Medium) plates applying standard methods (Brenner, 1974).
The *C. elegans* Bristol variant N2, was used as wild-type (WT) reference and strains used for the experiments and generated crosses were derivatives of N2.
The following alleles and transgenes were used:
LG I: *zhIs83[frt::lin-3::gfp::frt, unc-119(+)]; unc-40(e271)* (Stavoe and Colón-Ramos, 2012)
LG II: *qyIs23[$P_{cdh-3}$>PLC∂$^{PH}$::mCherry, unc-119(+)]* (Ziel et al., 2008), *rrf-3(pk1426)* (Simmer et al., 2002), *let-23(sa62) /mnC1* (Katz et al., 1996), *let-23(sy1)* (Katz et al., 1996), ttTi5605 (Frøkjær-Jensen et al., 2008), *sra-9(zh108)*
LG III: *unc-32(e189) mpk-1(ga117)/qc1* (Lackner and Kim, 1998), *unc-119(ed3)* , *madd-2(tr103)* (Alexander et al., 2010)
LG IV: *egl-38(n578)* (Zhang et al., 2005), *let-60(n1046)* (Han and Sternberg, 1990), *qyIs10[lam-1::gfp; unc-119(+)]*(Hagedorn et al., 2009), *lin-3(n1059)/nT1* (Liu et al., 1999), *zhIs061[$P_{cdh-3}$>let-23(dom-rf)::gfp; $P_{myo-2}$>mCherry], zhIs038[let-23::gfp, unc-119(+)]* (Haag et al., 2014), *lin-3(e1417)* (Hwang, 2004), *lin-3(zh112[mNeongreen::LoxP::3xFlag])*
LG V: *rde-1(ne219)* (Tabara et al., 1999), *swIs79[ajm-1::gfp, seamcell::gfp, unc-119(+)]* (Mohler et al., 2002), *syIs51[$P_{cdh-3}$>cfp, unc-119(+)]* (Inoue et al., 2002), *srh-247(tm6072*)(Gift from Dr. S. Mitani/ NBRP), *fos-1(ar105)/nT1[sqIs51, let-XX(m435)], nlp-26(zh113[gfp::LoxP::3xFlag])*
LG X: *unc-6(ev400)* (Hedgecock et al., 1990), *syIs11[$P_{hs}$>lin-3EGF]* (Katz et al., 1995), *gap-1(ga133)* (Hajnal et al., 1997), *bar-1(ga80)* (Eisenmann et al., 1998), *qyIs66[[$P_{cdh-3}$>unc-40::gfp, $P_{myo-2}$>yfp]* (Ziel et al., 2008)

Extra chromosomal arrays and integrated transgenes:
*zhEx418[$P_{lin-31}$>rde-1; $P_{myo-2}$>mCherry], zhEx518[$P_{lin-31}$>lin-3hairpin; $P_{myo-2}$>mcherry], zhEx544[$P_{vab-23}$>lin-3::gfp; Psur-5>gfp], zhEx584[$P_{hs}$>cas-9; sglin3sp; $P_{myo-2}$>mcherry*], qyIs103 [fos-1a > rde-1] (Hagedorn et al., 2009), *gaIs47[$P_{lin-31}$>mpk-1(gf), $P_{lin-31}$>dmek(gf)]* (Gift from Stuart K. Kim, Stanford University School of Medicine)

### 5.1.2 Strains

*AH4490 gap-1(ga133) X*

*AH4491 gap-1(ga133) X; sra-9(zh108) II*

*AH4501 sra-9(zh108)*

*AH4536 nlp-26(zh113[gfp::LoxP::3xFlag]) V*

*AH4548 lin-3(zh112[mNeongreen::LoxP::3xFlag]) IV*

*AH4555 nlp-26(zh113[gfp::LoxP::3xFlag]) V*

*AH4628 lin-3(zh112[mNeongreen::LoxP::3xFlag]) IV; nlp-26(zh113[GFP::LoxP::3xFlag]) V; qyIs23[$P_{cdh-3}$::PLC∂$^{PH}$::mCherry, unc-119(+)] II*

*AH4681 qyIs23[$P_{cdh-3}$>mCherry::PH; unc-119(+)] II; sra-9(zh108) II; lin-3(zh112[mNeongreen::LoxP::3xFlag]) IV*

*AH4710 gap-1(ga133) X*

*AH4713 nlp-26::gfp V*

*AH4714 nlp-26::gfp V; gap-1*

*AH4714 nlp-26::gfp V; gap-1*

*AH4769 unc-6(ev400) X; qyIs23[$P_{cdh-3}$::PLC∂$^{PH}$::mCherry, unc-119(+)] II; lin-3(zh112[mNeongreen::LoxP::3xFlag]) IV*

*AH2331 qyIs23 II;egl-38(n578) IV*

*AH2338 qyIs23[$P_{cdh-3}$::PLC∂$^{PH}$::mCherry; unc-119(+)] II;swIs79[ajm-1::GFP, seamcell::GFP, pUnc-119] IV*

*AH2340 qyIs23[$P_{cdh-3}$::PLC∂$^{PH}$::mCherry; unc-119(+)] II; let-60(n1046) IV*

*AH2362 qyIs23[$P_{cdh-3}$::PLC∂$^{PH}$::mCherry; unc-119(+)] II;syIs11[$P_{hs}$::lin-3soluble]*

*AH2363 qyIs23[$P_{cdh-3}$::PLC∂$^{PH}$::mCherry;unc-119(+)] II;egl-38(n578)IV; swIs79[ajm-1::GFP, seamcell::GFP, pUnc-119] IV*

*AH3163 zhIs83[frt::lin-3::gfp::frt, unc-119(+)] I*

*AH3172 rrf-3(pk1426)II; qyIs10[lam-1::gfp; unc-119(+)] IV; rde-1(ne219)V; unc-6(ev400)X; zhEx418[$P_{lin-31}$::rde-1; $P_{myo-2}$::mCherry]*

*AH3259 unc-6(ev400) X; syIs51[$P_{cdh-3}$::cfp, unc-119] V*

*AH3402 lin-3(n1059)/nT1 IV; zhIs83[frt::lin-3::gfp::frt, unc-119(+)] I*

*AH4374 egl-38(n578)IV;qyIs23[$P_{cdh-3}$::PLC∂$^{PH}$::mCherry; unc-119(+)] II;ajm-1::gfp;zhEx544.1[$P_{vab-23}$::lin-3;sur-5::gfp]*

*AH4470 egl-38(n578)IV;qyIs23[$P_{cdh-3}$::PLC∂$^{PH}$::mCherry; unc-119(+)] II;ajm-1::gfp;zhEx544.2[$P_{vab-23}$::lin-3;sur-5::gfp]*

*AH4508 zhEX584zhEx[$P_{hs}$::cas-9;SG lin3sp; $P_{myo-2}$::mCherry]*

*AH4509 zhEx[$P_{hs}$::cas-9;SG lin3sp; $P_{myo-2}$::mCherry]*

*AH2840 zhIs061[$P_{cdh-3}$::let-23(dom-rf)::gfp;$P_{myo-2}$::mCherry] IV*

*AH3164 zhIs061[$P_{cdh-3}$::let-23(dom-rf)::gfp;$P_{myo-2}$::mCherry] IV ; unc-6(ev400) X*

*AH2804 rrf-3(pk1426)II; swIs79[ajm-1::GFP, seamcell::GFP, pUnc-119] IV; rde-1(ne219)V; zhEx418[$P_{lin-31}$::rde-1; $P_{myo-2}$::mCherry]*

*AH3164 zhIs061[$P_{cdh-3}$::let-23(dom-rf)::gfp;myo-2::mcherry] IV ; unc-6(ev400) X*

*AH2805 swIs79[ajm-1::GFP, seamcell::GFP, pUnc-119] V; qyIs23[$P_{cdh-3}$>mCherry::PH; unc-119(+)]; zhEx518.1[$P_{lin-31}$::lin-3hairpin; $P_{myo-2}$::mCherry]*

*AH2806* *swIs79[ajm-1::GFP, seamcell::GFP, pUnc-119] V; qyIs23[$P_{cdh-3}$>mCherry::PH; unc-119(+)]; zhEx518.2[$P_{lin-31}$::lin-3hairpin; $P_{myo-2}$::mch]*

*AH3099* *egl-38(n578) IV; unc-6(ev400) X*

*AH4542* *lin-3(zh114[FRT::lin-3::LoxP::FRT]) IV*

*AH2417* *rrf-3(pk1426)II; unc-119(ed4)III; zhIs038[let-23::gfp, unc-119(+)] IV; rde-1(ne219)V; zhEx418[lin-31::rde-1genomic; myo2-mcherry]*

JU2058 *rrf-3(pk1426) II; mfIs70[lin-31p::rde-1, myo-2p::GFP] IV; rde-1(ne219) V*

*NK640* *rrf-3(pk1426)II; unc-119(ed4)III; rde-1(ne219)V; qyIs102[fos-1ap::rde-1;myo2::yfp; unc-119]*

### 5.1.3 RNAi

RNA interference (RNAi) was performed using the feeding method as described (Kamath et al., 2003). P0 worms were synchronized at the L1 stage, transferred to NGM plates containing 3 mM IPTG and 50 ng/ml ampicillin seeded with the indicated RNAi bacteria and allowed to grow for 5-7 days at 20°C, after which the F1 progeny was analyzed.
The used clones (*lin-3, egl-38, pas-6, empty*) were taken from the Ahringer library (Kamath and Ahringer, 2003) the *let-23* clone was constructed from genomic DNA (pLM16).

### 5.1.4 Heat shock treatment

The worms grown on 60mm diameter NGM plates and sealed with parafilm. The sealed plates were submerged in a 33° C warm water bath and incubated for 30min. Then they were recovered, unsealed and left to recover at 20°C.

### 5.1.5 Worm bleaching and staging

Two to four NGM plates, confluent with not starved adult worms were transferred with $H_2O$ to a 15 ml falcon tube. The falcon tube was centrifuged for 1 minute at 1'100 rpm and the supernatant was discarded, leaving 1 ml solution and worms remaining. After adding 200 µl of 10-15% sodium hypochloride and 100 µm 5M NaOH, the worms were vortexed until no floating bodies were detected. The bleach was attenuated to 14 ml with $H_2O$ and washed four times with $H_2O$. The eggs were left to hatch overnight on a shaker at RT and plated on NGM plates grown with OP50 *E. coli*.

### 5.1.6 Mito Tracker staining

The basement membrane was stained by MitoTracker Red CMXRos, from Thermo Fisher, according to the manufacturers protocol. The worms were incubated in a solution of 10 µM MitoTracker Red in M9 buffer (Brenner, 1974) at RT for 2 hr, under exclusion of light sources. The worms were then allowed to recover for 30 min on NGM agar plates.

### 5.1.7 Microinjection

Microinjection for the generation of extrachromosomal lines was performed as described in (Mello et al., 1991) using purified plasmid or PCR DNA at a concentration of 50 ng/µl or 30 ng/µl respectively. The transformation markers pCFJ90 ($P_{myo-2}$>*mCherry*) and pTG96 ($P_{sur-5}$>*gfp*) were used at a concentration of 2.5 ng/µl (Frøkjær-Jensen et al., 2008) or 30 ng/µl respectively, and pBluescript-KS plasmid was used to achieve a final DNA concentration of 150 ng/µl in a total volume of 15µl.
For CRISPR/Cas9 or Mosci injections the injection mix was prepared as described in Arribere et al 2014, Dickinson et al., 2015 and Frokajer et al 2008 respectively (Dickinson et al., 2015; Frøkjær-Jensen et al., 2008).
Injections were done on a Leica DM-IRB Injection microscope.

## 5.2 DNA methods

### 5.2.1 PCR

PCR products used for genotyping of strains or RNAi clones, by fragment length analysis or by sequencing analysis, were performed according to the Taq-PCR protocol of ©2008 Invitrogen Corporation or using a PCR Protocol for LongAmp® Taq DNA Polymerase (M0323). For all PCR reactions performed, the annealing temperature was set at 58° or according to empirically tested optimum. All Fusion-PCR reactions were performed with the Phusion high-fidelity DNA polymerase according to the protocol of Finnzymes (Espoo, Finland). The DNA fragments generated by the PCR reactions were visualized using agarose gel electrophoresis and ethidium bromide staining.
The annealing temperatures were estimated with the Finnzyme Tm calculator (https://www.finnzymes.fi/tm_determination.html).

### 5.2.2 Oligonucleotides for genotyping

| Genotyping of | 5' Primer | 3' Primer | Size | Sequencing |
|---|---|---|---|---|
| *egl-38(n578)* | OLM30 (attgaagacactgacgggac) | OLM31 (aacaggatctgtcagaccagg) | 420 bp | OLM30 |
| *gap-1(ga133)* | OPG182 (CTGTTATCCCCTATTTTAGTGG) | OPG183 (CTCTTGCTGGATCCACTTCAC) | 206 bp (mut) / 491 bp (wt) | |
| *lin-3 W1* | OLM69 (cgattcctgaacgacttctagtcg) | OLM68 (ggtacagagccactattttcagc) | 187 bp | OLM69 |
| *lin-3(n1059) W2* | OLM63 (ctgtcatcacaacgcgacatgccacg) | OLM62 (gaacgaggagttgcgccgtgc) | 250 bp | OLM63 |
| *mNeon::lin-3(zh112)* | OLM138 (GACACTACAACCACATGTGTTCG) | OLM134 (ACGAGTGCCTTCCCAACCCTGTGG) | 3.6 kb (mut) / 2.6 kb (wt) | |
| *gfp::nlp-26(zh113)* | OSS35 (GATGACAAATCGCATCACCGGAAGC) | OSS38 (CTGTGTTCTGATTATCGGCAGTTTC) | 1.8 kb (mut) / 850 bp (wt) | |
| *rde-1(ne219)* | OLM6 (cctggacattcgatcatctgaag) | OLM7 (cgtttcacgatccaaacagattcg) | 865 bp | OLM6 |
| *sra-9(zh108)* | OMMO219(AGCATATGAAGAATATGTGG) | OMMO267(TCTCAGGAGAACCATATTAG) | 5 kb (mut) / 2 kb (wt) | |
| *srh-247(TM6072)* | OLM188 (CGTGCCAGGAACATATTCTACCCC)<br>in deletion: | OLM189 (GACCAACTATTTCGCgtTATTAAG)<br>OLM190 (CATTTTTCGAAATCCCCGTGTGC) | 779 bp (mut) / 1015 bp (wt) | OLM191 |
| EG8078 (oxTi185) Chr I | OLM59 (catggagatggtacagatgc) | OLM60 (CCAATGGCTCCTGAAAAAGA) | 1.6 kb | |
| *rrf-3(pk1426)* | OJE70 (GTTCTCCGAGTTCGCATCAAG)<br>OJE69 (GTCACGCCATCGCGCTCAAATG) | OJE68 (CAACGTATTCATCGCGAAGAGTC) | 501 bp (mut) / 327 bp (wt) | |
| oxTi185 + lin-3::gfp (pLM1) | OTS190 (gaatgacgagagagtatgcaaagg) | OLM59 (catggagatggtacagatgc) | 1.8 kb | |

### 5.2.3 RNAi clone construction

pLM16 was transformed into the HT115(DE3) RNAi strain, an RNase III-deficient *E. coli* strain with IPTG-inducible T7 polymerase activity.

### 5.2.4 Miniprep by Alkalyne Lysis

Miniprep Plasmid DNA extraction was performed by a Alkalyne Lysis. Overnight liquid cultures were transferred into 1.5 ml Eppendorf tubes and centrifuged at 4000 rpm for 1 min, the supernatant was removed and the pellet further processed. 200 µl of Midiprep solution I was added to pellet and mixture was vortexed until the bacterial pellet was completely re-suspended. 200 µl of Miniprep solution II was added and tubes were shaken and inverted. 200 µl of Miniprep solution III was added and tubes were again shaken and inverted. Tubes were then centrifuged at 14000 rpm for 10 min. The supernatant was transferred to a new Eppendorf tube and 800 µl of 100 % cool (-20 C°) EtOH was added. The tubes were shaken and inverted and centrifuged at 4 °C, at 14000 rpm for 15 min. The supernatant was removed, 1 ml of 70 % EtOH was added and mixture was centrifuge again for 5 min at 14000 rpm. The supernatant was removed and the pellet was left to dry at room temperature, until all the remaining liquid residues evaporated. The dried pellet was re-suspended in 50 µl of ddH2O and the yield measured with nanodrop.

Miniprep Soltution I:
EDTA; 10 mM; pH 8
Tris-HCL; 50 mM; pH7.5
RNAse A; 100 µg/ml
In ddH2O

Miniprep Soltution II:
SDS; 1%
NaOH; 0.2 M
In ddH2O

Miniprep Soltution III:
KoAC; 2.55 M; pH4.8
In ddH2O

### 5.2.5 Midiprep

MidiPreps were performed using the "QIAfilter Plasmid Midi Kit" (Qiagen) according to the manufacturer's protocol, and adapted as follows: After step 13, the pellet was resolved in 400 µl of TE, transferred to a 1.5 ml Eppendorf tube, and the DNA was precipitated with 40 µl of 3M NaAc and 800 µl of 100% ice-cold EtOH. After incubation at -80° C for 10 minutes, the sample was centrifuged for 10 minutes at 14'000 rpm at 4° C. The supernatant was discarded and the pellet was resuspended in 100 µl of TE.

### 5.2.6 Cloned Plasmids

pMMO10 *gfp::lin-3* for mosci insertion
*lin-3* was amplified in two part from genomic DNA with primer pairs
OMMO118 (tttcctaggCATCGTTGACTGACTCATG),
OJE131 (AGTCGACCTGCAGGCATGCAAGCTgagacacgattctgaaac),
OJE132 (GGCATGGATGAACTATACAAAccttcgtggtttcgtcaa),
OMMO119 (tttcctaggCGACATCAAGGTTCACGG), using Phusion polymerase (NEB).
GFP was amplified with primers C (AGCTTGCATGCCTGCAGGTCG) (Hobert, 2002) , OMMO77 (TTTGTATAGTTCATCCATGCC) from pPD95.75 (gift from Andrew Fire). These three fragments were fused using fusion PCR and subcloned into pGEM-Teasy (Promega). The lin-3 fragment was then cloned into pCFJ151 (Frøkjær-Jensen et al., 2008) with AvrII.
Plasmid constructed by Matthias Morf.

pLM1 *FRT::gfp::lin-3::FRT* template for Mosci insertion
The insertion template was generated by PCR from pMMO10 with
OLM54 (AAAcctaggGAAGTTCCTATTCTCTAGAAAGTATAGGAACTTcCATCGTTGACTGACTCATGCCAC)
OLM55
(AAAcctaggGAAGTTCCTATACTTTCTAGAGAATAGGAACTTCcgacatcaaggttcacggagaga)
and cloned into the AvrII locus of the pCFJ151 plasmid (Frøkjær-Jensen et al., 2008).

pLM2 *lin-3::citrin*
Repair plasmid for *citrin* insertion via CRISPR into the *lin-3* locus by Co-CRISPR (Arribere et al., 2014). Three PCR products were amplified for the three way Fusion-pcr, the PCR templates amplified
0.8 kb from pMMO10 with OLM72 (AGAAGTTCCTATTCTCTAGAAAGTATAGGAACTTcACACCGCCAAAATGTTGTATGC) and OLM95 (AGAGAATAGGAACTTCTGGCGGGTACTTGAATATTTACG) and
0.85 kb of *citrin* from pJA255 (Addgene plasmid # 21508) with OLM97 (GGAGGGTACCGGTAGAAAAAATGAGTAAAGGAGAAGAAC) and OLM98 (CTTGACGAAACCACGAAGGTTTGTATAGTTCGTCCATGC) as well as
1.47 kb with OLM76 (CATGGACGAACTATACAAACCTTCGTGGTTTCGTC) and OLM77 (CTTTCTAGAGAATAGGAACTTCAGGCGTTGTAGAAATCG). The fusion PCR was cloned into the pGEM-T vector (Promega).

pLM3 *Pvab-23>lin-3::gfp*
The 3.4 kb of the *vab-23* promoter was amplifies with OLM50 (gcattttccgcattttggCGATGCGCGTCGAATCTATA ) and OLM51 (AGGTTAAGCCGTAATGGGCACC) from the pZK930 plasmid (Pellegrino et al., 2011) and fused to 7.7kb of *lin-3::gfp* amplified with OLM52 (ggcgacatcaaggttcacggag) and OMMO96 (ccaaaatgcggaaaatgctac) from pMMO10 and cloned in to the pGEM-T vector (Promega)

pLM4 *lin-3::FRT::lin-3*
Repair plasmid for FRT insertion via CRISPR into the *lin-3* locus by Co-CRISPR (Arribere et al., 2014). The PCRs amplified 1 kb of genomic *lin-3* with OLM70 (TACctaggCGGATCGTCGGCTTGTCGGTG) and OLM71 (AGAGAATAGGAACTTCTGGCGGGTACTTGAATATTTACG) and 0.8 kb of genomic

*lin-3* with OLM72 (AGAAGTTCCTATTCTCTAGAAAGTATAGGAACTTcACACCGCCAAAATGTTGTATGC), OLM73 (CTTCTCCTTTACTCATGAGACACGATTCTGAAAC), introducing a FRT site into the fusion product. The fusion PCR was cloned into the pGEM-T vector (Promega).

pLM8 SGN2 CCTTCTTGTTGGCCTTGTAT
Single guide N2 ATACAAGGCCAACAAGAAGG to insert a *gfp* into *nlp-26* locus with pLM6 as Donor template. The plasmid was cloned through NEB's Q5 Site-Directed Mutagenesis Kit into pDD162 (Addgene plasmid # 47549) with OSS7 (CCTTCTTGTTGGCCTTGTATGTTTTAGAGCTAGAAATAG-CAAG)

pLM9 SGN3 TACAAGGCCAACAAGAAGGA
Single guide N3 ATACAAGGCCAACAAGAAGG to insert *gfp* into *nlp-26* locus with pLM6 as Donor template. The plasmid was cloned through NEB's Q5 Site-Directed Mutagenesis Kit into pDD162 (Addgene plasmid # 47549) with OSS8 (TACAAGGCCAACAAGAAGGAGTTTTAGAGCTAGAAATAG-CAAG)

pLM10 SGN4 TCTTGTTGGCCTTGTATCCG
Single guide N4 sequence ATACAAGGCCAACAAGAAGG was cloned through NEB's Q5 Site-Directed Mutagenesis Kit into pDD162 (Addgene plasmid # 47549) with OSS9 (TCTTGTTGGCCTTGTATCCG-GTTTTAGAGCTAGAAATAGCAAG), to insert a GFP into the *nlp-26* locus with pLM6 as Donor template.

pLM12 SG3A gttcttgacgaaaccacgaa
Single guide SG3A sequence gttcttgacgaaaccacgaa was cloned through NEB's Q5 Site-Directed Mutagenesis Kit into pDD162 (Addgene plasmid # 47549) with OLM177 (gttcttgacgaaaccacgaaGTTT-TAGAGCTAGAAATAGCAAG), to insert a *mNeongreen* into the *lin-3* locus with pLM5 as Donor template.

pLM13 SG3B cagaatcgtgtctcccttcg
Single guide SG3A sequence cagaatcgtgtctcccttcg was cloned through NEB's Q5 Site-Directed Mutagenesis Kit into pDD162 (Addgene plasmid # 47549) with OSS1 (cagaatcgtgtctcccttcgGTTT-TAGAGCTAGAAATAGCAAG), to insert a *mNeongreen* into the *lin-3* locus with pLM5 as Donor template.

pLM15 SG2A targeting *lin-3* sequence ATTTCAGAATCTTGACTGGA
The plasmid was cloned through site directed mutagenesis with the Phusion PCR (invitrogen) protocol with *PU6::unc-119_sgRNA* plasmid(Addgene plasmid # 46169) with OLM82 (GCAAATCTA-AATGTTTATTTCAGAATCTTGACTGGAGTTTTAGAGCTAGAAATAGCAAGTTA) and OLM83 (CTAGCTC-TAAAACTCCAGTCAAGATTCTGAAATAAACATTTAGATTTGCAATTCAATTATATAG)

pLM16 *let-23* genomic DNA in L4440
The RNAi clone plasmid was generated by amplifying 2kb of genomic *let-23* DNA OLM36 (TTT-TAGATCTgctatggaggatgtaagcag), and OIN129 (catttctcggattctttccg). The PCR product as well as the insertion vector L4440 were digested with EcoRI and BglII and the PCR was ligated into the L4440

(a gift from Andrew Fire (Addgene plasmid # 1654)).

pLM17 *let-23::gfp* A to G for zhIS061
A gateway Plasmid encoding the cytoplasmic C-terminal domain of *let-23* fused to *gfp* in pJE08 (Haag et al., 2014) was used as template to introduced a point mutation by site directed mutagenesis with the OLM13 primer, which introduced an A to G single nucleotide polymorphism and a subsequent tyrosine to cysteine transformation at position Y1063 in LET-23, representing a conserved tyrosine in of the EGFR kinase domain (Bae et al., 2012). The transgene zhIS061 only encodes a dominant-reduction of function protein, because a mistake in the design of for the cloning of the plasmid was made, and only discovered 5 years later. Originally, a Threonine to Isoleucine inducing SNP should have been introduced at location T1064, which would have resulted in a sy16 allele and a conformational change, leading to a complete loss of Kinase function (Aroian and Sternberg, 1991; Aroian et al., 1994)

pLM18 SG3A gttcttgacgaaaccacgaa
SG3A targeting *lin-3.* The plasmid was cloned through site directed mutagenesis with the Phusion PCR (invitrogen) protocol with *PU6::unc-119_sgRNA* plasmid (Addgene plasmid # 46169) with OLM113 (GCAAATCTAAATGTTTgttcttgacgaaaccacgaaGTTTTAGAGCTAGAAATAGCAAGTTA) and OLM114 (CTAGCTCTAAAACttcgtggtttcgtcaagaacAAACATTTAGATTTGCAATTCAATTATATAG)

pLM19 SG3B cagaatcgtgtctcccttcg
SG3B targeting *lin-3.* The plasmid was cloned through site directed mutagenesis with the Phusion PCR (invitrogen) protocol with *PU6::unc-119_sgRNA* plasmid(Addgene plasmid # 46169) with OLM115 (GCAAATCTAAATGTTTcagaatcgtgtctcccttcgGTTTTAGAGCTAGAAATAGCAAGTTA) and OLM116 (CTAGCTCTAAAACcgaagggagacacgattctgAAACATTTAGATTTGCAATTCAATTATATAG)

## 5.3 Generated alleles and strains

*hIs83* *frt::lin-3::gfp::frt, unc-119(+)*
The *zhIs83[frt::lin-3::gfp::frt, unc-119(+)]*AH3402 strain was generated according to the Mos1 transposon mediated Single Copy Integration (MosSCI) protocol (Zeiser et al., 2011). The insertion plasmid (pLM1) was injected at a concentration of 50 ng/µl together with co-injectionmarkers according to the Zeisler (Zeiser et al., 2011) protocol into the EG8078 strain (CGC) and integrated at the oxTi185 insertion site on Chromosome I (http://www.wormbuilder.org).

*zhIs061* *$P_{cdh-3}$>let-23(dom-redfunc)::gfp;myo-2::mcherry*
The series of fusion PCR for zhIs061 was generated from four parts:
1. OLM16 (ATAGAAAAGTTGTAGAGCATGATGTCCTTACC) and OEF239 (CCGATAGAGGGAGGGTATCGCATggacggtcggtccgttttgtataggg) from genomic DNA
2. OLM27 (ATGCGATACCCTCCCTCTATCGGTTC) and OLM19 (gaacaacattgcgaccagctg) from *let-23* cDNA
3. OLM25 (cctgcaaaacatgtagttcagctggtcgc) and OLM29 (agctgggtgtgaatgcataccc) from genomic *let-23* DNA
4. OJE54 (TGTACAAAGTGGCATTCACTTGAATGGATG) and OJE55 (ATAATAAAGTTGCCAGCGACGATATCCATTAGTGC) from plasmid DNA pLM17
The integrated *zhIs061*[*$P_{cdh-3}$>let-23(dom-rf)::gfp;myo-2::mcherry*] transgene was first generated as an extrachromosomal array (*zhEX522*), by injecting the fusion PCR at 25 ng/µl with pCFJ90 ($P_{myo-2}$*>mcherry*) at 3 ng/µl, and filled up with bluescript to a final concentration of 130 ng/µl, which was later integrated by X-ray irradiation as a multicopy insertion.

*zhEx418* *$P_{lin-31}$::rde-1; $P_{myo-2}$>mcherry*
The extrachromosomal array was generated by fusion of two PCR fragments. Fusion templates were 2.3kb of the *lin-31* promoter, amplified from PB253 (Tan et al., 1998) with OPG309(ACGAGG AGCGGTGGTGTGGCCAGC) and OMMO86(GCACAGGGAGAAAGAGCATG) and 3.9 kb of the *rde-1* gene amplified from genomic DNA with OLM1 (atgtcctcgaattttcccgaattggaaaaagg) and OLM2 (ggcaattgtttcagcatgaaacaagc), making a fusion product of 6.2 kb. The purified fusion PCR was injected at 20 ng/µl , (P*myo-2>mcherry*) 8 ng/µl and filled up with bluescript DNA to a total of 150 ng/µl. The extrachromosomal array was later spontaneously integrated.

*zhEx517* *$P_{egl-38}$>gfp; Pmyo-2>mcherry*
The array was generated by injecting 15 ng/µl of the fusion PCR of 5 kb of the *egl-38* promoter from genomic DNA with OLM32 (ccggagcatagcaactccgag) and OLM37 (CTTCTCCTTTACTCATtcaacgaaaggacctttcacg) with 1.7 kb of *gfp* with OMMO76 (ATGAGTAAAGGAGAAGAAC) and D (AAGGGCCCGTACGGCCGACTAGTAGG) together with ($P_{myo-2}$*>mcherry*) 6 ng/µl and filled up with bluescript to a concentration of 140 ng/µl.

*zhEx518* *$P_{lin-31}$>lin-3hairpin; Pmyo-2>mcherry*
The array was generated by injecting the *lin-3::hairpin* pLM12,13 and 15 at each 25 ng/µl and the plasmid *Phs>cas-9* pMB67 (Addgene plasmid # 47947) at 50 ng/µl as well as pCFJ90 ($P_{myo-2}$*>mCherry*) at 2.5 ng/µl.

*zhEx544* $P_{vab-23}$*>lin-3::gfp; sur-5::gfp*
The array was generated by injecting 20 ng/µl of the plasmid pLM3, 50 ng/µl of pTG96 (P*sur-5>gfp*) and filled up with bluescript to a concentration of 170 ng/µl.

zhEx584 $P_{hs}$*>cas-9; sglin3sp(pLM12;pLM13;pLM15); Pmyo-2>mcherry*
The array was generated by injecting the lin-3 specific single guides pLM15, pLM18 and pLM19 at each 25 ng/µl and the plasmid *Phs>cas-9* pMB67 (Addgene plasmid # 47947) at 50 ng/µl as well as pCFJ90 (P*myo-2>mcherry*) at 2.5 ng/µl.

**CRISPR/CAS9 generated alleles**
*zh112* *mNeongreen::lin-3*
To insert the *mNeongreen::3xFlag* sequence in the 5` prime region of the *lin-3* locus, the CRISPR/Cas9 system (Jinek et al., 2012) according to the Dickinson protocol (Dickinson et al., 2015) was applied. The repair template plasmid pLM5 was injected at a concentration of 8 ng/µl, the two single guides with integrated CAS9 plasmids pLM12 and pLM13 at a concentration of 40 ng/µl together with the recommended Co-injectionmarkers pGH8 (Addgene 19359) at 10 ng/µl, pCFJ104 (Addgene 19328) at 5 ng/µl and pCFJ90 (19327) at 2.5 ng/µl. Further Selection was done according to the Dickinson protocol.

*zh113* *gfp::nlp-26*
To insert the *gfp::3xFlag* sequence in the 5` prime region of the *nlp-26* locus, the CRISPR/Cas9 system (Jinek et al., 2012) according to the Dickinson protocol (Dickinson et al., 2015) was applied. The repair template plasmid pLM7 was injected at a concentration of 10 ng/µl, the three single guides with integrated CAS9 plasmids pLM8, pLM9 and pLM10 at a concentration of 50 ng/µl together with the recommended Co-injectionmarkers pGH8 (Addgene 19359) at 10 ng/µl, pCFJ104 (Addgene 19328) at 5 ng/µl and pCFJ90 (19327) at 2.5 ng/µl. Further Selection was done according to the Dickinson protocol.

*zh108* *sra-9* deletion
The *sra-9(zh108)* deletion allele was generated according to the Arribere et al. 2014 (Arribere et al., 2014) protocol.
ACCAATTGAATTGCTGGATGTTTTAGAGCTAGAAATAGC

## 5.4 Microscopy and image analysing tools and techniques

### 5.4.1 Microscopy and image analysis

Most images were acquired using an Olympus BX61 wide-field microscope equipped with a Cr.E.S.T. X-light spinning disc confocal system, a Lumencor SPECTRA X light engine and a Hamamatsu Orca CCD camera, controlled by the Visitron VisiView 2.1.1 software.
Other images were made using a Leica DMRA wide-field microscope with a Hamamatsu ORCA-ER camera controlled by Openlab 5.0.2.
Images were processed using Huygens Deconvolution (SVI) for z-stacks where indicated, Fiji (ImageJ (NIH)) and Adobe Photoshop.

For time-lapse imaging, worms were mounted on 4% agarose containing with an approximately 1.25 mM tetramisole suspension, covered by a coverslip and sealed with Halocarbon oil 700 (Sigma). Z-stacks were recorded on an Olympus BX61 wide-field microscope equipped with a X-light spinning disc confocal system unit and using a60x Plan Apo lens and a Hamatsu Orca CCD camera. The time-laps intervals were between 18-25 minutes and the Z spacing was 0.4 µm. In most attempts, the animals failed to develope at all, or died. To minimize this effect, the laser intensity power, for excitation in the mCherry (575nm) and GFP (475nm) channels, was set at 15 percent during spinning-disc light microscope imaging.

### 5.4.2 Cell ablations

The AC was ablated between the late L3 up to the early L4 larval stages, as specified in results. The VPC ablations of P3.p to P7.p were performed at the late L2 larval stage. The worms were mounted on 3-4% agarose pads and ablated using a Leica DMR wide-field microscope equipped with Micro-Point Laser system (Photonic Instruments) as described in (Farooqui et al., 2012).

### 5.4.3 AC polarity analysis

General AC polarity quantification, referring to the *qyIs23*[$P_{cdh\text{-}3}$*>PLC∂$^{PH}$::mCherry; unc-119(+)*] reporter expression pattern was done by using a custom written, semi-automated scripts in ImageJ and R applied to deconvolved wide-field z-stacks with a Z-spacing of 0.13 µm (Morf et al., 2013). (Image deconvolution was performed with the Huygens software provided by; the Center for Microscopy and Image Analysis, University of Zurich). For AC polarity analysis in the *zhEx518*[$P_{lin\text{-}31}$*>lin-3i;* $P_{cdh\text{-}3}$*>PLC∂$^{PH}$::mCherry*] strain, the AC was scored as depolarized upon phenotypic characteristics of the $PIP_2$ expression pattern.

### 5.4.4 AC positioning scoring

The AC was scored as mispositioned when at least half of the AC nucleus was centered over one of the vulE cells at the P6.pxx cell stage.

### 5.4.5 Basal lamina breaching scoring

The basal lamina breaching by the AC was scored in Nomarski optics at the indicated larval and Pn.p cell-divisional stage. The scoring was determined form the P6.pxx stage on, after the 1° fated vulF cells start apical constriction and invagination. This allowed a reliable scoring in the *unc-6* mutant background. For the tissue specific RNAi the basal lamina breaching was scored with the *qyIs10[lam-1::gfp]* marker according to Hagedorn et al. 2009 (Hagedorn et al., 2009).

### 5.4.6 Statistical analysis

Statistical analyses for the general AC quantification were performed by bootstrapping using a custom written script for R (Morf et al., 2013). Chi-Square, Fisher's exact test or t-tests were performed in excel or R.

## 5.5 Immunocytochemistry

### 5.5.1 Antibody staining utilizing Freez-cracking

Permeabillization by Freeze cracking
The freeze-cracking procedure was adapted from protocols described in (Shakes et al., 2012).
The staged L2/L3 larvae were washed 5x in M9 buffer and 10 µl was mounted on 3x Poly-L-Lysin (0.1%, SIGMA) coated slides. The slides were frozen on a liquid Nitrogen cooled metal block and cracking was performed after 10 minutes.

Light Fixation
The slides were immediately immersed in -30°C cooled absolute Methanol for 2 minutes, following -30°C cooled absolute Acetone for 4 minutes. They were allowed to air-dry at RT for 5 minutes and then rehydrated for 15 minutes in 1x PBS buffer.

Antibody-staining
The staining was performed directly on the fixed slides with hydrophobic boundaries encircling the worms with a PAP-pen. Volume per slide ranged between 50ul-200ul.
Blocking was done for 30 minutes at RT with a 5% ABA buffer (1x PBS, 0.05% Triton, 5% BSA).
The 1° Antibody MH27 was added at a dilution of (1:30) and FLAG antibody at a dilution of (1:100), in a 3% ABA buffer (1x PBS, 0.05% Triton, 3% BSA) and left over night at 4°C. All 2° Antibody were applied with a 1:200 dilution and left to incubated for 2 hours at RT.
Washing was performed with 0.05% PBS-T (0.05% Triton) buffer at RT 3x for 30 minutes (1°) and 3x 15 minutes (2°) respectively.

Hoechst staining
The Nuclei were visualized using Hoechst staining in a 1:1000 dilution from a Hoechst® dye stock of 10 mg/ml (ThermoFisher). Worms were incubated in dye for 5 minutes. And washed 3x in PBS-T buffer for 15 minutes.
Finally slides were mounted with 20-40 µl Mowiol (Aldrich, 4–88) mounting medium per slide and covered with a coverslip and let dry for one hour or kept at 4° for later analysis.

Antibodies
1° antibodies that were used: Monoclonal mouse ANTI-FLAG M2 (F3165, Sigma-Aldrich) and monoclonal mouse anti AJM-1 (MH27) (Francis and Waterston, 1991) serum.
2° Antibody: Tetramethyl Rhodamine lsothiocyanate (TRITC)-conjugated affinity pure Donkey Anti-Mouse lgG (H+L) (715-025-150, Jackson ImmunoReserJrch Laboratories, Inc.)

# 6. References


**Abdus-Saboor, I., Mancuso, V. P., Murray, J. I., Palozola, K., Norris, C., Hall, D. H., Howell, K., Huang, K. and Sundaram, M. V.** (2011). Notch and Ras promote sequential steps of excretory tube development in C. elegans. *Development* **138**, 3545–3555.

**Adrain, C., Strisovsky, K., Zettl, M., Hu, L., Lemberg, M. K. and Freeman, M.** (2011). Mammalian EGF receptor activation by the rhomboid protease RHBDL2. *EMBO Rep*. 12, 421–427.

**Alexander, M., Selman, G., Seetharaman, A., Chan, K. K. M., D'Souza, S. A., Byrne, A. B. and Roy, P. J.** (2010). MADD-2, a homolog of the Opitz syndrome protein MID1, regulates guidance to the midline through UNC-40 in Caenorhabditis elegans. *Developmental Cell* **18**, 961–972.

**Anderson, D., Koch, C. A., Grey, L., Ellis, C., Moran, M. F. and Pawson, T.** (1990). Binding of SH2 domains of phospholipase C gamma 1, GAP, and Src to activated growth factor receptors. *Science* **250**, 979–982.

**Aroian, R. V. and Sternberg, P. W.** (1991). Multiple functions of let-23, a Caenorhabditis elegans receptor tyrosine kinase gene required for vulval induction. *Genetics* **128**, 251–267.

**Aroian, R. V., Lesa, G. M. and Sternberg, P. W.** (1994). Mutations in the Caenorhabditis elegans let-23 EGFR-like gene define elements important for cell-type specificity and function. *EMBO J.* **13**, 360–366.

**Arribere, J. A., Bell, R. T., Fu, B. X. H., Artiles, K. L., Hartman, P. S. and Fire, A. Z.** (2014). Efficient marker-free recovery of custom genetic modifications with CRISPR/Cas9 in Caenorhabditis elegans. *Genetics* **198**, 837–846.

**Azimifar, S. B., Böttcher, R. T., Zanivan, S., Grashoff, C., Krüger, M., Legate, K. R., Mann, M. and Fässler, R.** (2012). Induction of membrane circular dorsal ruffles requires co-signalling of integrin-ILK-complex and EGF receptor. *J. Cell. Sci.* **125**, 435–448.

**Bae, Y.-K., Sung, J. Y., Kim, Y.-N., Kim, S., Hong, K. M., Kim, H. T., Choi, M. S., Kwon, J. Y. and Shim, J.** (2012). An in vivo C. elegans model system for screening EGFR-inhibiting anti-cancer drugs. *PLoS ONE* **7**, e42441.

**Barkoulas, M., Vargas Velazquez, A. M., Peluffo, A. E. and Félix, M.-A.** (2016). Evolution of New cis-Regulatory Motifs Required for Cell-Specific Gene Expression in Caenorhabditis. *PLoS Genet* **12**, e1006278.

**Barrandon, Y. and Green, H.** (1987). Cell migration is essential for sustained growth of keratinocyte colonies: the roles of transforming growth factor-alpha and epidermal growth factor. *Cell* **50**, 1131–1137.

**Berset, T., Hoier, E. F., Battu, G., Canevascini, S. and Hajnal, A.** (2001). Notch inhibition of RAS signaling through MAP kinase phosphatase LIP-1 during C. elegans vulval development. *Science* **291**, 1055–1058.

**Bilder, D.** (2004). Epithelial polarity and proliferation control: links from the Drosophila neoplastic tumor suppressors. *Genes & Development* **18**, 1909–1925.

**Bjorge, J. D., Chan, T. O., Antczak, M., Kung, H. J. and Fujita, D. J.** (1990). Activated type I phosphatidylinositol kinase is associated with the epidermal growth factor (EGF) receptor following EGF stimulation. *Proc. Natl. Acad. Sci. U.S.A.* **87**, 3816–3820.

**Boscher, C. and Nabi, I. R.** (2013). Galectin-3- and phospho-caveolin-1-dependent outside-in integrin signaling mediates the EGF motogenic response in mammary cancer cells. *Mol. Biol. Cell* **24**, 2134–2145.

**Bozorgui, B., Teimouri, H. and Kolomeisky, A. B.** (2015). Theoretical analysis of degradation mechanisms in the formation of morphogen gradients. *J Chem Phys* **143**, 025102.

**Braendle, C. and Félix, M.-A.** (2008). Plasticity and errors of a robust developmental system in different environments. *Developmental Cell* **15**, 714–724.

**Brenner, S.** (1974). The genetics of Caenorhabditis elegans. *Genetics* **77**, 71–94.

**Brown, C. L., Coffey, R. J. and Dempsey, P. J.** (2001). The proamphiregulin cytoplasmic domain is required for basolateral sorting, but is not essential for constitutive or stimulus-induced processing in polarized Madin-Darby canine kidney cells. *J. Biol. Chem.* **276**, 29538–29549.

**Chamberlin, H. M. and Sternberg, P. W.** (1994). The lin-3/let-23 pathway mediates inductive signalling during male spicule development in Caenorhabditis elegans. *Development* **120**, 2713–2721.

**Chan, S. S., Zheng, H., Su, M. W., Wilk, R., Killeen, M. T., Hedgecock, E. M. and Culotti, J. G.** (1996). UNC-40, a C. elegans homolog of DCC (Deleted in Colorectal Cancer), is required in motile cells responding to UNC-6 netrin cues. *Cell* **87**, 187–195.

**Chang, C., Newman, A. P. and Sternberg, P. W.** (1999). Reciprocal EGF signaling back to the uterus from the induced C. elegans vulva coordinates morphogenesis of epithelia. *Current Biology* **9**, 237–246.

**Chang, H., Riese, D. J., Gilbert, W., Stern, D. F. and McMahan, U. J.** (1997). Ligands for ErbB-family receptors encoded by a neuregulin-like gene. *Nature* **387**, 509–512.

**Chattopadhyay, A., Vecchi, M., Ji, Q. S., Mernaugh, R. and Carpenter, G.** (1999). The role of individual SH2 domains in mediating association of phospholipase C-gamma1 with the activated EGF receptor. *J. Biol. Chem.* **274**, 26091–26097.

**Chen, P., Xie, H., Sekar, M. C., Gupta, K. and Wells, A.** (1994). Epidermal growth factor receptor-mediated cell motility: phospholipase C activity is required, but mitogen-activated protein kinase activity is not sufficient for induced cell movement. *J Cell Biol* **127**, 847–857.

**Chen, S.-J., Luan, J., Zhang, H.-S., Ruan, C.-P., Xu, X.-Y., Li, Q.-Q. and Wang, N.-H.** (2012). EGFR-mediated G1/S transition contributes to the multidrug resistance in breast cancer cells. *Mol. Biol. Rep.* **39**, 5465–5471.

**Chen, X., Kojima, S.-I., Borisy, G. G. and Green, K. J.** (2003). p120 catenin associates with kinesin and facilitates the transport of cadherin-catenin complexes to intercellular junctions. *J Cell Biol* **163**, 547–557.

**Chen, Y. and Struhl, G.** (1996). Dual roles for patched in sequestering and transducing Hedgehog. *Cell* **87**, 553–563.

**Clandinin, T. R., DeModena, J. A. and Sternberg, P. W.** (1998). Inositol trisphosphate mediates a RAS-independent response to LET-23 receptor tyrosine kinase activation in C. elegans. *Cell* **92**, 523–533.

**Cluzel, C., Saltel, F., Lussi, J., Paulhe, F., Imhof, B. A. and Wehrle-Haller, B.** (2005). The mechanisms and dynamics of (alpha)v(beta)3 integrin clustering in living cells. *J Cell Biol* **171**, 383–392.

**Corvera, S., D'Arrigo, A. and Stenmark, H.** (1999). Phosphoinositides in membrane traffic. *Curr. Opin. Cell Biol.* **11**, 460–465.

**Cowley, G. P., Smith, J. A. and Gusterson, B. A.** (1986). Increased EGF receptors on human squamous carcinoma cell lines. *Br. J. Cancer* **53**, 223–229.

**Dahlhoff, M., Schäfer, M., Wolf, E. and Schneider, M. R.** (2013). Genetic deletion of the EGFR ligand epigen does not affect mouse embryonic development and tissue homeostasis. *Exp. Cell Res.* 319, 529–535.

**David, M., Wong, L., Flavell, R., Thompson, S. A., Wells, A., Larner, A. C. and Johnson, G. R.** (1996). STAT activation by epidermal growth factor (EGF) and amphiregulin. Requirement for the EGF receptor kinase but not for tyrosine phosphorylation sites or JAK1. *J. Biol. Chem.* **271**, 9185–9188.

**Davis, M. A., Ireton, R. C. and Reynolds, A. B.** (2003). A core function for p120-catenin in cadherin turnover. *J Cell Biol* **163**, 525–534.

**Davis, M. W., Birnie, A. J., Chan, A. C., Page, A. P. and Jorgensen, E. M.** (2004). A conserved metalloprotease mediates ecdysis in Caenorhabditis elegans. *Development* **131**, 6001–6008.

**Dawson, J. P., Berger, M. B., Lin, C.-C., Schlessinger, J., Lemmon, M. A. and Ferguson, K. M.** (2005). Epider-

mal growth factor receptor dimerization and activation require ligand-induced conformational changes in the dimer interface. *Mol. Cell. Biol.* **25**, 7734–7742.

**Dempsey, P. J. and Coffey, R. J.** (1994). Basolateral targeting and efficient consumption of transforming growth factor-alpha when expressed in Madin-Darby canine kidney cells. *J. Biol. Chem.* **269**, 16878–16889.

**Dempsey, P. J., Meise, K. S., Yoshitake, Y., Nishikawa, K. and Coffey, R. J.** (1997). Apical enrichment of human EGF precursor in Madin-Darby canine kidney cells involves preferential basolateral ectodomain cleavage sensitive to a metalloprotease inhibitor. *J Cell Biol* **138**, 747–758.

**Di Fiore, P. P., Pierce, J. H., Fleming, T. P., Hazan, R., Ullrich, A., King, C. R., Schlessinger, J. and Aaronson, S. A.** (1987). Overexpression of the human EGF receptor confers an EGF-dependent transformed phenotype to NIH 3T3 cells. *Cell* **51**, 1063–1070.

**Dickinson, D. J., Pani, A. M., Heppert, J. K., Higgins, C. D. and Goldstein, B.** (2015). Streamlined Genome Engineering with a Self-Excising Drug Selection Cassette. *Genetics* **200**, 1035–1049.

**Dierick, H. A. and Bejsovec, A.** (1998). Functional analysis of Wingless reveals a link between intercellular ligand transport and dorsal-cell-specific signaling. *Development* **125**, 4729–4738.

**Dolgin, E. S., Félix, M.-A. and Cutter, A. D.** (2008). Hakuna Nematoda: genetic and phenotypic diversity in African isolates of Caenorhabditis elegans and C. briggsae. *Heredity (Edinb)* **100**, 304–315.

**Duchek, P. and Rørth, P.** (2001). Guidance of cell migration by EGF receptor signaling during Drosophila oogenesis. *Science* **291**, 131–133.

**Duchesne, L., Octeau, V., Bearon, R. N., Beckett, A., Prior, I. A., Lounis, B. and Fernig, D. G.** (2012). Transport of fibroblast growth factor 2 in the pericellular matrix is controlled by the spatial distribution of its binding sites in heparan sulfate. *PLoS Biol* **10**, e1001361.

**Dutt, A., Canevascini, S., Froehli-Hoier, E. and Hajnal, A.** (2004). EGF Signal Propagation during C. elegans Vulval Development Mediated by ROM-1 Rhomboid. *PLoS Biol* **2**, e334–16.

**Ebnet, K., Suzuki, A., Horikoshi, Y., Hirose, T., Meyer Zu Brickwedde, M. K., Ohno, S. and Vestweber, D.** (2001). The cell polarity protein ASIP/PAR-3 directly associates with junctional adhesion molecule (JAM). *EMBO J.* **20**, 3738–3748.

**Edgley, M. L., Baillie, D. L., Riddle, D. L. and Rose, A. M.** (2006). Genetic balancers. *WormBook* 1–32.

**Eisenmann, D. M., Maloof, J. N., Simske, J. S., Kenyon, C. and Kim, S. K.** (1998). The beta-catenin homolog BAR-1 and LET-60 Ras coordinately regulate the Hox gene lin-39 during Caenorhabditis elegans vulval development. *Development* **125**, 3667–3680.

**Entchev, E. V., Schwabedissen, A. and González-Gaitán, M.** (2000). Gradient formation of the TGF-beta homolog Dpp. *Cell* **103**, 981–991.

**Estes, K. A. and Hanna-Rose, W.** (2009). The anchor cell initiates dorsal lumen formation during C. elegans vulval tubulogenesis. *Developmental Biology* **328**, 297–304.

**Falls, D. L.** (2003). Neuregulins: functions, forms, and signaling strategies. *Exp. Cell Res.* **284**, 14–30.

**Farooqui, S., Pellegrino, M. W., Rimann, I., Morf, M. K., Mereu, L., Fröhli, E. and Hajnal, A.** (2012). Coordinated Lumen Contraction and Expansion during Vulval Tube Morphogenesis in Caenorhabditis elegans. *Developmental Cell* **23**, 494–506.

**Ferguson, E. L. and Horvitz, H. R.** (1985). Identification and characterization of 22 genes that affect the vulval cell lineages of the nematode Caenorhabditis elegans. *Genetics* **110**, 17–72.

**Fernandes, J. S. and Sternberg, P. W.** (2007). The tailless Ortholog nhr-67 Regulates Patterning of Gene Expression and Morphogenesis in the C. elegans Vulva. *PLoS Genet* **3**, e69–14.

**Fire, A., Xu, S., Montgomery, M. K., Kostas, S. A., Driver, S. E. and Mello, C. C.** (1998). Potent and specific genetic interference by double-stranded RNA in Caenorhabditis elegans. *Nature* **391**, 806–811.

**Francis, R. and Waterston, R. H.** (1991). Muscle cell attachment in Caenorhabditis elegans. *J Cell Biol* **114**, 465–479.

**Freed, D. M., Alvarado, D. and Lemmon, M. A.** (2015). Ligand regulation of a constitutively dimeric EGF receptor. *Nat Comms* **6**, 7380–7.

**Frøkjær-Jensen, C., Davis, M. W., Hopkins, C. E., Newman, B. J., Thummel, J. M., Olesen, S.-P., Grunnet, M. and Jorgensen, E. M.** (2008). Single-copy insertion of transgenes in Caenorhabditis elegans. *Nat. Genet.* **40**, 1375–1383.

**Funamoto, S., Meili, R., Lee, S., Parry, L. and Firtel, R. A.** (2002). Spatial and temporal regulation of 3-phosphoinositides by PI 3-kinase and PTEN mediates chemotaxis. *Cell* **109**, 611–623.

**Gao, L., Wang, F.-Q., Li, H.-M., Yang, J.-G., Ren, J.-G., He, K.-F., Liu, B., Zhang, W. and Zhao, Y.-F.** (2016). CCL2/EGF positive feedback loop between cancer cells and macrophages promotes cell migration and invasion in head and neck squamous cell carcinoma. *Oncotarget* **7**, 87037–87051.

**Garrard, S. M., Capaldo, C. T., Gao, L., Rosen, M. K., Macara, I. G. and Tomchick, D. R.** (2003). Structure of Cdc42 in a complex with the GTPase-binding domain of the cell polarity protein, Par6. *EMBO J.* **22**, 1125–1133.

**Garrington, T. P. and Johnson, G. L.** (1999). Organization and regulation of mitogen-activated protein kinase signaling pathways. *Curr. Opin. Cell Biol.* **11**, 211–218.

**Gassama-Diagne, A., Yu, W., Beest, ter, M., Martin-Belmonte, F., Kierbel, A., Engel, J. and Mostov, K.** (2006). Phosphatidylinositol-3,4,5-trisphosphate regulates the formation of the basolateral plasma membrane in epithelial cells. *Nat Cell Biol* **8**, 963–970.

**Goldstein, B. and Hird, S. N.** (1996). Specification of the anteroposterior axis in Caenorhabditis elegans. *Development* **122**, 1467–1474.

**González-Mariscal, L., Betanzos, A., Nava, P. and Jaramillo, B. E.** (2003). Tight junction proteins. *Prog. Biophys. Mol. Biol.* **81**, 1–44.

**Graus-Porta, D., Beerli, R. R., Daly, J. M. and Hynes, N. E.** (1997). ErbB-2, the preferred heterodimerization partner of all ErbB receptors, is a mediator of lateral signaling. *EMBO J.* **16**, 1647–1655.

**Green, J. L., Inoue, T. and Sternberg, P. W.** (2008). Opposing Wnt pathways orient cell polarity during organogenesis. *Cell* **134**, 646–656.

**Greenwald, I. S., Sternberg, P. W. and Horvitz, H. R.** (1983). The lin-12 locus specifies cell fates in Caenorhabditis elegans. *Cell* **34**, 435–444.

**Grimbert, S., Tietze, K., Barkoulas, M., Sternberg, P. W., Félix, M.-A. and Braendle, C.** (2016). Anchor cell signaling and vulval precursor cell positioning establish a reproducible spatial context during C. elegans vulval induction. *Developmental Biology* 1–13.

**Guo, G., Gong, K., Wohlfeld, B., Hatanpaa, K. J., Zhao, D. and Habib, A. A.** (2015). Ligand-Independent EGFR Signaling. *Cancer Res.* **75**, 3436–3441.

**Haag, A., Gutierrez, P., Bühler, A., Walser, M., Yang, Q., Langouët, M., Kradolfer, D., Fröhli, E., Herrmann, C. J., Hajnal, A., et al.** (2014). An in vivo EGF receptor localization screen in C. elegans Identifies the Ezrin homolog ERM-1 as a temporal regulator of signaling. *PLoS Genet* **10**, e1004341.

**Hagedorn, E. J., Kelley, L. C., Naegeli, K. M., Wang, Z., Chi, Q. and Sherwood, D. R.** (2014). ADF/cofilin promotes invadopodial membrane recycling during cell invasion in vivo. *J Cell Biol* **204**, 1209–1218.

**Hagedorn, E. J., Yashiro, H., Ziel, J. W., Ihara, S., Wang, Z. and Sherwood, D. R.** (2009). Integrin Acts Upstream of Netrin Signaling to Regulate Formation of the Anchor Cell•s Invasive Membrane in C. elegans. *Developmental Cell* **17**, 187–198.

**Hagedorn, E. J., Ziel, J. W., Morrissey, M. A., Linden, L. M., Wang, Z., Chi, Q., Johnson, S. A. and Sherwood, D. R.** (2013). The netrin receptor DCC focuses invadopodia-driven basement membrane transmigration in vivo. *J Cell Biol* **201**, 903–913.

**Hajnal, A.** (2014). *Sequential apical and lateral cell constrictions induce vulval lumen morphogenesis in*.

**Hajnal, A., Whitfield, C. W. and Kim, S. K.** (1997). Inhibition of Caenorhabditis elegans vulval induction by gap-1 and by let-23 receptor tyrosine kinase. *Genes & Development* **11**, 2715–2728.

**Han, M. and Sternberg, P. W.** (1990). let-60, a gene that specifies cell fates during C. elegans vulval induction, encodes a ras protein. *Cell* **63**, 921–931.

**Hanna-Rose, W. and Han, M.** (2002). The Caenorhabditis elegans EGL-26 protein mediates vulval cell morphogenesis. *Developmental Biology* **241**, 247–258.

**Harris, R. C., Chung, E. and Coffey, R. J.** (2003). EGF receptor ligands. *Exp. Cell Res.* **284**, 2–13.

**Hartsock, A. and Nelson, W. J.** (2008). Adherens and tight junctions: structure, function and connections to the actin cytoskeleton. *Biochim. Biophys. Acta* **1778**, 660–669.

**Hedgecock, E. M., Culotti, J. G. and Hall, D. H.** (1990). The unc-5, unc-6, and unc-40 genes guide circumferential migrations of pioneer axons and mesodermal cells on the epidermis in C. elegans. *Neuron* **4**, 61–85.

**Hill, A. J., Mansfield, R., Lopez, J. M. N. G., Raizen, D. M. and Van Buskirk, C.** (2014). Cellular Stress Induces a Protective Sleep-like State in C. elegans. *Current Biology* **24**, 2399–2405.

**Hill, R. J. and Sternberg, P. W.** (1992). The gene lin-3 encodes an inductive signal for vulval development in C. elegans. *Nature* **358**, 470–476.

**Hinkle, C. L., Sunnarborg, S. W., Loiselle, D., Parker, C. E., Stevenson, M., Russell, W. E. and Lee, D. C.** (2004). Selective roles for tumor necrosis factor alpha-converting enzyme/ADAM17 in the shedding of the epidermal growth factor receptor ligand family: the juxtamembrane stalk determines cleavage efficiency. *J. Biol. Chem.* **279**, 24179–24188.

**Hobert, O.** (2002). PCR fusion-based approach to create reporter gene constructs for expression analysis in transgenic C. elegans. *BioTechniques* **32**, 728–730.

**Holbro, T., Beerli, R. R., Maurer, F., Koziczak, M., Barbas, C. F. and Hynes, N. E.** (2003). The ErbB2/ErbB3 heterodimer functions as an oncogenic unit: ErbB2 requires ErbB3 to drive breast tumor cell proliferation. *Proc. Natl. Acad. Sci. U.S.A.* **100**, 8933–8938.

**Hollander, den, A. I., Brink, ten, J. B., de Kok, Y. J., van Soest, S., van den Born, L. I., van Driel, M. A., van de Pol, D. J., Payne, A. M., Bhattacharya, S. S., Kellner, U., et al.** (1999). Mutations in a human homologue of Drosophila crumbs cause retinitis pigmentosa (RP12). *Nat. Genet.* **23**, 217–221.

**Hollander, den, A. I., Heckenlively, J. R., van den Born, L. I., de Kok, Y. J., van der Velde-Visser, S. D., Kellner, U., Jurklies, B., van Schooneveld, M. J., Blankenagel, A., Rohrschneider, K., et al.** (2001). Leber congenital amaurosis and retinitis pigmentosa with Coats-like exudative vasculopathy are associated with mutations in the crumbs homologue 1 (CRB1) gene. *Am. J. Hum. Genet.* **69**, 198–203.

**Horvath, P. and Barrangou, R.** (2010). CRISPR/Cas, the immune system of bacteria and archaea. *Science* **327**, 167–170.

**Hoskins, R., Hajnal, A. F., Harp, S. A. and Kim, S. K.** (1996). The C. elegans vulval induction gene lin-2 encodes a member of the MAGUK family of cell junction proteins. *Development* 122, 97–111.

**Hostettler, L., Grundy, L., Käser-Pébernard, S., Wicky, C., Schafer, W. R. and Glauser, D. A.** (2017). The Bright Fluorescent Protein mNeonGreen Facilitates Protein Expression Analysis In Vivo. *G3* **7**, 607–615.

**Huelsz-Prince, G. and van Zon, J. S.** (2017). Canalization of C. elegans Vulval induction against Anatomical Variability. *Cell Systems* **4**, 219–230.e6.

**Hwang, B. J.** (2004). A cell-specific enhancer that specifies lin-3 expression in the C. elegans anchor cell for vulval development. *Development* **131**, 143–151.

**Hwang, B. J., Meruelo, A. D. and Sternberg, P. W.** (2007). C. elegans EVI1 proto-oncogene, EGL-43, is necessary for Notch-mediated cell fate specification and regulates cell invasion. *Development* **134**, 669–679.

**Inoue, T., Sherwood, D. R., Aspöck, G., Butler, J. A., Gupta, B. P., Kirouac, M., Wang, M., Lee, P.-Y., Kramer, J. M., Hope, I., et al.** (2002). Gene expression markers for Caenorhabditis elegans vulval cells. *Mechanisms of Development* **119 Suppl 1**, S203–9.

**Iwamoto, R., Handa, K. and Mekada, E.** (1999). Contact-dependent growth inhibition and apoptosis of epidermal growth factor (EGF) receptor-expressing cells by the membrane-anchored form of heparin-binding EGF-like growth factor. *J. Biol. Chem.* **274**, 25906–25912.

**Janmey, P. A. and Lindberg, U.** (2004). Cytoskeletal regulation: rich in lipids. *Nat. Rev. Mol. Cell Biol.* **5**, 658–666.

**Jiang, H.-S. and Wu, Y.-C.** (2014). LIN-3/EGF promotes the programmed cell death of specific cells in Caenorhabditis elegans by transcriptional activation of the pro-apoptotic gene egl-1. *PLoS Genet* **10**, e1004513.

**Jiang, L. I. and Sternberg, P. W.** (1998). Interactions of EGF, Wnt and HOM-C genes specify the P12 neuroectoblast fate in C. elegans. *Development* **125**, 2337–2347.

**Jinek, M., Chylinski, K., Fonfara, I., Hauer, M., Doudna, J. A. and Charpentier, E.** (2012). A programmable dual-RNA-guided DNA endonuclease in adaptive bacterial immunity. *Science* **337**, 816–821.

**Johansson, A., Driessens, M. and Aspenström, P.** (2000). The mammalian homologue of the Caenorhabditis elegans polarity protein PAR-6 is a binding partner for the Rho GTPases Cdc42 and Rac1. *J. Cell. Sci.* **113 ( Pt 18)**, 3267–3275.

**Jones, J. T., Akita, R. W. and Sliwkowski, M. X.** (1999). Binding specificities and affinities of egf domains for ErbB receptors. *FEBS Lett.* **447**, 227–231.

**Kaech, S. M., Whitfield, C. W. and Kim, S. K.** (1998). The LIN-2/LIN-7/LIN-10 complex mediates basolateral membrane localization of the C. elegans EGF receptor LET-23 in vulval epithelial cells. *Cell* **94**, 761–771.

**Kamath, R. S. and Ahringer, J.** (2003). Genome-wide RNAi screening in Caenorhabditis elegans. *Methods* **30**, 313–321.

**Kariya, K.-I., Bui, Y. K., Gao, X., Sternberg, P. W. and Kataoka, T.** (2004). Phospholipase Cepsilon regulates ovulation in Caenorhabditis elegans. *Developmental Biology* **274**, 201–210.

**Katz, W. S., Hill, R. J., Clandinin, T. R. and Sternberg, P. W.** (1995). Different levels of the C. elegans growth factor LIN-3 promote distinct vulval precursor fates. *Cell* **82**, 297–307.

**Katz, W. S., Lesa, G. M., Yannoukakos, D., Clandinin, T. R., Schlessinger, J. and Sternberg, P. W.** (1996). A point mutation in the extracellular domain activates LET-23, the Caenorhabditis elegans epidermal growth factor receptor homolog. *Mol. Cell. Biol.* **16**, 529–537.

**Kemphues, K. J., Priess, J. R., Morton, D. G. and Cheng, N. S.** (1988). Identification of genes required for cytoplasmic localization in early C. elegans embryos. *Cell* **52**, 311–320.

**Kicheva, A., Pantazis, P., Bollenbach, T., Kalaidzidis, Y., Bittig, T., Jülicher, F. and González-Gaitán, M.** (2007). Kinetics of morphogen gradient formation. *Science* **315**, 521–525.

**Kimble, J. and Hirsh, D.** (1979). The postembryonic cell lineages of the hermaphrodite and male gonads in Caenorhabditis elegans. *Developmental Biology* **70**, 396–417.

**Kruse, K., Pantazis, P., Bollenbach, T., Jülicher, F. and González-Gaitán, M.** (2004). Dpp gradient formation by dynamin-dependent endocytosis: receptor trafficking and the diffusion model. *Development* **131**, 4843–4856.

**Lackner, M. R. and Kim, S. K.** (1998). Genetic analysis of the Caenorhabditis elegans MAP kinase gene mpk-1. *Genetics* **150**, 103–117.

**Leaman, D. W., Pisharody, S., Flickinger, T. W., Commane, M. A., Schlessinger, J., Kerr, I. M., Levy, D. E. and Stark, G. R.** (1996). Roles of JAKs in activation of STATs and stimulation of c-fos gene expression by epidermal growth factor. *Mol. Cell. Biol.* **16**, 369–375.

**Lemmon, M. A., Ferguson, K. M., O'Brien, R., Sigler, P. B. and Schlessinger, J.** (1995). Specific and high-affinity binding of inositol phosphates to an isolated pleckstrin homology domain. *Proc. Natl. Acad. Sci. U.S.A.* **92**, 10472–10476.

**Li, C., Franklin, J. L., Graves-Deal, R., Jerome, W. G., Cao, Z. and Coffey, R. J.** (2004). Myristoylated Naked2 escorts transforming growth factor alpha to the basolateral plasma membrane of polarized epithelial cells. *Proc. Natl. Acad. Sci. U.S.A.* **101**, 5571–5576.

**Li, C., Hao, M., Cao, Z., Ding, W., Graves-Deal, R., Hu, J., Piston, D. W. and Coffey, R. J.** (2007). Naked2 acts as a cargo recognition and targeting protein to ensure proper delivery and fusion of TGF-alpha containing exocytic vesicles at the lower lateral membrane of polarized MDCK cells. *Mol. Biol. Cell* **18**, 3081–3093.

**Liu, J., Tzou, P., Hill, R. J. and Sternberg, P. W.** (1999). Structural requirements for the tissue-specific and tissue-general functions of the Caenorhabditis elegans epidermal growth factor LIN-3. *Genetics* **153**, 1257–1269.

**Liu, P., Cheng, H., Roberts, T. M. and Zhao, J. J.** (2009). Targeting the phosphoinositide 3-kinase pathway in cancer. *Nat Rev Drug Discov* **8**, 627–644.

**Lohmer, L. L., Clay, M. R., Naegeli, K. M., Chi, Q., Ziel, J. W., Hagedorn, E. J., Park, J. E., Jayadev, R. and Sherwood, D. R.** (2016). A Sensitized Screen for Genes Promoting Invadopodia Function In Vivo: CDC-42 and Rab GDI-1 Direct Distinct Aspects of Invadopodia Formation. *PLoS Genet* **12**, e1005786–29.

**Luetteke, N. C., Qiu, T. H., Peiffer, R. L., Oliver, P., Smithies, O. and Lee, D. C.** (1993). TGF alpha deficiency results in hair follicle and eye abnormalities in targeted and waved-1 mice. *Cell* **73**, 263–278.

**Luetteke, N. C., Qiu, T. H., Fenton, S. E., Troyer, K. L., Riedel, R. F., Chang, A. and Lee, D. C.** (1999). Targeted inactivation of the EGF and amphiregulin genes reveals distinct roles for EGF receptor ligands in mouse mammary gland development. *Development* 126, 2739–2750.

**Macdonald-Obermann, J. L. and Pike, L. J.** (2014). Different epidermal growth factor (EGF) receptor ligands show distinct kinetics and biased or partial agonism for homodimer and heterodimer formation. *J. Biol. Chem.* **289**, 26178–26188.

**Maehama, T. and Dixon, J. E.** (1998). The tumor suppressor, PTEN/MMAC1, dephosphorylates the lipid second messenger, phosphatidylinositol 3,4,5-trisphosphate. *J. Biol. Chem.* **273**, 13375–13378.

**Makarenkova, H. P., Hoffman, M. P., Beenken, A., Eliseenkova, A. V., Meech, R., Tsau, C., Patel, V. N., Lang, R. A. and Mohammadi, M.** (2009). Differential interactions of FGFs with heparan sulfate control gradient formation and branching morphogenesis. *Sci Signal* **2**, ra55–ra55.

**Mao, Y. S. and Yin, H. L.** (2007). Regulation of the actin cytoskeleton by phosphatidylinositol 4-phosphate 5 kinases. *Pflugers Arch.* **455**, 5–18.

**Margolis, B., Li, N., Koch, A., Mohammadi, M., Hurwitz, D. R., Zilberstein, A., Ullrich, A., Pawson, T. and Schlessinger, J.** (1990). The tyrosine phosphorylated carboxyterminus of the EGF receptor is a binding site for GAP and PLC-gamma. *EMBO J.* **9**, 4375–4380.

**Martel, V., Racaud-Sultan, C., Dupe, S., Marie, C., Paulhe, F., Galmiche, A., Block, M. R. and Albiges-Rizo, C.** (2001). Conformation, localization, and integrin binding of talin depend on its interaction with phosphoinositides. *J. Biol. Chem.* **276**, 21217–21227.

**Martin-Belmonte, F., Gassama, A., Datta, A., Yu, W., Rescher, U., Gerke, V. and Mostov, K.** (2007). PTEN-mediated apical segregation of phosphoinositides controls epithelial morphogenesis through Cdc42. *Cell* **128**, 383–397.

**Massagué, J. and Pandiella, A.** (1993). Membrane-anchored growth factors. *Annu. Rev. Biochem.* **62**, 515–541.

**Meisenhelder, J., Suh, P. G., Rhee, S. G. and Hunter, T.** (1989). Phospholipase C-gamma is a substrate for the PDGF and EGF receptor protein-tyrosine kinases in vivo and in vitro. *Cell* **57**, 1109–1122.

**Mello, C. C., Kramer, J. M., Stinchcomb, D. and Ambros, V.** (1991). Efficient gene transfer in C.elegans: extrachromosomal maintenance and integration of transforming sequences. *EMBO J.* **10**, 3959–3970.

**Metzstein, M. M., Stanfield, G. M. and Horvitz, H. R.** (1998). Genetics of programmed cell death in C. elegans: past, present and future. *Trends Genet.* **14**, 410–416.

**Miura, T., Hartmann, D., Kinboshi, M., Komada, M., Ishibashi, M. and Shiota, K.** (2009). The cyst-branch difference in developing chick lung results from a different morphogen diffusion coefficient. *Mechanisms of Development* **126**, 160–172.

**Moghal, N. and Sternberg, P. W.** (2003). Extracellular domain determinants of LET-23 (EGF) receptor tyrosine kinase activity in Caenorhabditis elegans. *Oncogene* **22**, 5471–5480.

**Mohler, W. A., Shemer, G., del Campo, J. J., Valansi, C., Opoku-Serebuoh, E., Scranton, V., Assaf, N., White, J. G. and Podbilewicz, B.** (2002). The type I membrane protein EFF-1 is essential for developmental cell fusion. *Developmental Cell* **2**, 355–362.

**Morf, M. K., Rimann, I., Alexander, M., Roy, P. and Hajnal, A.** (2013). The Caenorhabditis elegans homolog of the Opitz syndrome gene, madd-2/Mid1, regulates anchor cell invasion during vulval development. *Developmental Biology* **374**, 108–114.

**Mosadegh, B., Saadi, W., Wang, S.-J. and Jeon, N. L.** (2008). Epidermal growth factor promotes breast cancer cell chemotaxis in CXCL12 gradients. *Biotechnol. Bioeng.* **100**, 1205–1213.

**Newman, A. P., White, J. G. and Sternberg, P. W.** (1996). Morphogenesis of the C. elegans hermaphrodite uterus. *Development* **122**, 3617–3626.

**Pellegrino, M. W., Farooqui, S., Frohli, E., Rehrauer, H., Kaeser-Pebernard, S., Muller, F., Gasser, R. B. and Hajnal, A.** (2011). LIN-39 and the EGFR/RAS/MAPK pathway regulate C. elegans vulval morphogenesis via the VAB-23 zinc finger protein. *Development* **138**, 4649–4660.

**Qadota, H., Inoue, M., Hikita, T., K ppen, M., Hardin, J. D., Amano, M., Moerman, D. G. and Kaibuchi, K.** (2007). Establishment of a tissue-specific RNAi system in C. elegans. *Gene* 400, 166–173.

**Quiros, M. and Nusrat, A.** (2014). RhoGTPases, actomyosin signaling and regulation of the epithelial Apical Junctional Complex. *Semin. Cell Dev. Biol.* **36**, 194–203.

**Rabinovitz, I., Toker, A. and Mercurio, A. M.** (1999). Protein kinase C-dependent mobilization of the alpha6beta4 integrin from hemidesmosomes and its association with actin-rich cell protrusions drive the chemotactic migration of carcinoma cells. *J Cell Biol* **146**, 1147–1160.

**Raizen, D. M., Zimmerman, J. E., Maycock, M. H., Ta, U. D., You, Y.-J., Sundaram, M. V. and Pack, A. I.** (2008). Lethargus is a Caenorhabditis elegans sleep-like state. *Nature* **451**, 569–572.

**Reinhart, B. J., Slack, F. J., Basson, M., Pasquinelli, A. E., Bettinger, J. C., Rougvie, A. E., Horvitz, H. R. and Ruvkun, G.** (2000). The 21-nucleotide let-7 RNA regulates developmental timing in Caenorhabditis elegans. *Nature* **403**, 901–906.

**Ririe, T. O., Fernandes, J. S. and Sternberg, P. W.** (2008). The Caenorhabditis elegans vulva: a post-embryonic gene regulatory network controlling organogenesis. *Proc. Natl. Acad. Sci. U.S.A.* **105**, 20095–20099.

**Rodriguez-Viciana, P., Warne, P. H., Dhand, R., Vanhaesebroeck, B., Gout, I., Fry, M. J., Waterfield, M. D. and Downward, J.** (1994). Phosphatidylinositol-3-OH kinase as a direct target of Ras. *Nature* **370**, 527–532.

**Roepstorff, K., Grandal, M. V., Henriksen, L., Knudsen, S. L. J., Lerdrup, M., Grøvdal, L., Willumsen, B. M. and van Deurs, B.** (2009). Differential effects of EGFR ligands on endocytic sorting of the receptor. *Traffic* **10**, 1115–1127.

**Roh, M. H. and Margolis, B.** (2003). Composition and function of PDZ protein complexes during cell polarization. *Am. J. Physiol. Renal Physiol.* **285**, F377–87.

**Roh, M. H., Makarova, O., Liu, C.-J., Shin, K., Lee, S., Laurinec, S., Goyal, M., Wiggins, R. and Margolis, B.** (2002). The Maguk protein, Pals1, functions as an adapter, linking mammalian homologues of Crumbs and Discs Lost. *J Cell Biol* **157**, 161–172.

**Saarikangas, J., Zhao, H. and Lappalainen, P.** (2010). Regulation of the actin cytoskeleton-plasma membrane interplay by phosphoinositides. *Physiol. Rev.* **90**, 259–289.

**Saffer, A. M., Kim, D. H., van Oudenaarden, A. and Horvitz, H. R.** (2011). The Caenorhabditis elegans Synthetic Multivulva Genes Prevent Ras Pathway Activation by Tightly Repressing Global Ectopic Expression of lin-3 EGF. *PLoS Genet* **7**, e1002418–11.

**Sahin, U., Weskamp, G., Kelly, K., Zhou, H.-M., Higashiyama, S., Peschon, J., Hartmann, D., Saftig, P. and Blobel, C. P.** (2004). Distinct roles for ADAM10 and ADAM17 in ectodomain shedding of six EGFR ligands. *J Cell Biol* **164**, 769–779.

**Sandgren, E. P., Luetteke, N. C., Palmiter, R. D., Brinster, R. L. and Lee, D. C.** (1990). Overexpression of TGF alpha in transgenic mice: induction of epithelial hyperplasia, pancreatic metaplasia, and carcinoma of the breast. *Cell* **61**, 1121–1135.

**Sasaki, T., Irie-Sasaki, J., Jones, R. G., Oliveira-dos-Santos, A. J., Stanford, W. L., Bolon, B., Wakeham, A., Itie, A., Bouchard, D., Kozieradzki, I., et al.** (2000). Function of PI3Kgamma in thymocyte development, T cell activation, and neutrophil migration. *Science* **287**, 1040–1046.

**Scheid, M. P. and Woodgett, J. R.** (2001). PKB/AKT: functional insights from genetic models. *Nat. Rev. Mol. Cell Biol.* **2**, 760–768.

**Schlessinger, J.** (2000). Cell signaling by receptor tyrosine kinases. *Cell* **103**, 211–225.

**Shakes, D. C., Miller, D. M. and Nonet, M. L.** (2012). Immunofluorescence microscopy. *Methods Cell Biol.* **107**, 35–66.

**Sharma-Kishore, R., White, J. G., Southgate, E. and Podbilewicz, B.** (1999). Formation of the vulva in Caenorhabditis elegans: a paradigm for organogenesis. *Development* **126**, 691–699.

**Shaye, D. D. and Greenwald, I.** (2002). Endocytosis-mediated downregulation of LIN-12/Notch upon Ras activation in Caenorhabditis elegans. *Nature* **420**, 686–690.

**Shaye, D. D. and Greenwald, I.** (2011). OrthoList: a compendium of C. elegans genes with human orthologs. *PLoS ONE* **6**, e20085

**Sherwood, D. R., Butler, J. A., Kramer, J. M. and Sternberg, P. W.** (2005). FOS-1 promotes basement-membrane removal during anchor-cell invasion in C. elegans. *Cell* **121**, 951–962.

**Shin, K., Straight, S. and Margolis, B.** (2005). PATJ regulates tight junction formation and polarity in mammalian epithelial cells. *J Cell Biol* **168**, 705–711.

**Simmer, F., Tijsterman, M., Parrish, S., Koushika, S. P., Nonet, M. L., Fire, A., Ahringer, J. and Plasterk, R. H. A.** (2002). Loss of the putative RNA-directed RNA polymerase RRF-3 makes C. elegans hypersensitive to RNAi. *Current Biology* **12**, 1317–1319.

**Singh, A. B. and Harris, R. C.** (2005). Autocrine, paracrine and juxtacrine signaling by EGFR ligands. *Cell. Signal.* **17**, 1183–1193.

**Singh, A. B., Sugimoto, K. and Harris, R. C.** (2007). Juxtacrine activation of epidermal growth factor (EGF) receptor by membrane-anchored heparin-binding EGF-like growth factor protects epithelial cells from anoikis while maintaining an epithelial phenotype. *J. Biol. Chem.* **282**, 32890–32901.

**Singh, B., Bogatcheva, G., Washington, M. K. and Coffey, R. J.** (2013). Transformation of polarized epithelial cells by apical mistrafficking of epiregulin. *Proc. Natl. Acad. Sci. U.S.A.* **110**, 8960–8965.

**Singhai, A., Wakefield, D. L., Bryant, K. L., Hammes, S. R., Holowka, D. and Baird, B.** (2014). Spatially defined EGF receptor activation reveals an F-actin-dependent phospho-Erk signaling complex. *Biophys. J.* **107**, 2639–2651.

**Slamon, D. J., Clark, G. M., Wong, S. G., Levin, W. J., Ullrich, A. and McGuire, W. L.** (1987). Human breast cancer: correlation of relapse and survival with amplification of the HER-2/neu oncogene. *Science* **235**, 177–182.

**Snutch, T. P. and Baillie, D. L.** (1983). Alterations in the pattern of gene expression following heat shock in the nematode Caenorhabditis elegans. *Can. J. Biochem. Cell Biol.* **61**, 480–487.

**Stavoe, A. K. H. and Colón-Ramos, D. A.** (2012). Netrin instructs synaptic vesicle clustering through Rac GTPase, MIG-10, and the actin cytoskeleton. *J Cell Biol* **197**, 75–88.

**Sternberg, P. W.** (1988). Lateral inhibition during vulval induction in Caenorhabditis elegans. *Nature* **335**, 551–554.

**Sternberg, P. W.** (2004). Developmental biology. A pattern of precision. *Science* **303**, 637–638.

**Sternberg, P. W. and Horvitz, H. R.** (1986). Pattern formation during vulval development in C. elegans. *Cell* **44**, 761–772.

**Stinchcomb, D. T., Shaw, J. E., Carr, S. H. and Hirsh, D.** (1985). Extrachromosomal DNA transformation of Caenorhabditis elegans. *Mol. Cell. Biol.* **5**, 3484–3496.

**Straight, S. W., Shin, K., Fogg, V. C., Fan, S., Liu, C.-J., Roh, M. and Margolis, B.** (2004). Loss of PALS1 expression leads to tight junction and polarity defects. *Mol. Biol. Cell* **15**, 1981–1990.

**Sulston, J. E. and White, J. G.** (1980). Regulation and cell autonomy during postembryonic development of Caenorhabditis elegans. *Developmental Biology* **78**, 577–597.

**Suzuki, M., Raab, G., Moses, M. A., Fernandez, C. A. and Klagsbrun, M.** (1997). Matrix metalloproteinase-3 releases active heparin-binding EGF-like growth factor by cleavage at a specific juxtamembrane site. *J. Biol. Chem.* **272**, 31730–31737.

**Tabara, H., Sarkissian, M., Kelly, W. G., Fleenor, J., Grishok, A., Timmons, L., Fire, A. and Mello, C. C.** (1999). The rde-1 gene, RNA interference, and transposon silencing in C. elegans. *Cell* **99**, 123–132.

**Takeichi, M.** (1988). The cadherins: cell-cell adhesion molecules controlling animal morphogenesis. *Development* **102**, 639–655.

**Takemura, T., Kondo, S., Homma, T., Sakai, M. and Harris, R. C.** (1997). The membrane-bound form of heparin-binding epidermal growth factor-like growth factor promotes survival of cultured renal epithelial cells. *J. Biol. Chem.* **272**, 31036–31042.

**Tan, P. B., Lackner, M. R. and Kim, S. K.** (1998). MAP kinase signaling specificity mediated by the LIN-1 Ets/LIN-31 WH transcription factor complex during C. elegans vulval induction. *Cell* **93**, 569–580.

**Thomas, C. G., Wang, W., Jovelin, R., Ghosh, R., Lomasko, T., Trinh, Q., Kruglyak, L., Stein, L. D. and Cutter, A. D.** (2015). Full-genome evolutionary histories of selfing, splitting, and selection in Caenorhabditis. *Genome Res.* **25**, 667–678.

**Thomas, J. H., Stern, M. J. and Horvitz, H. R.** (1990). Cell interactions coordinate the development of the C. elegans egg-laying system. *Cell* **62**, 1041–1052.

**Tice, D. A., Biscardi, J. S., Nickles, A. L. and Parsons, S. J.** (1999). Mechanism of biological synergy between cellular Src and epidermal growth factor receptor. *Proc. Natl. Acad. Sci. U.S.A.* **96**, 1415–1420.

**Turner, T., Chen, P., Goodly, L. J. and Wells, A.** (1996). EGF receptor signaling enhances in vivo invasiveness of DU-145 human prostate carcinoma cells. *Clin. Exp. Metastasis* **14**, 409–418.

**Tzahar, E., Moyer, J. D., Waterman, H., Barbacci, E. G., Bao, J., Levkowitz, G., Shelly, M., Strano, S., Pinkas-Kramarski, R., Pierce, J. H., et al.** (1998). Pathogenic poxviruses reveal viral strategies to exploit the ErbB signaling network. *EMBO J.* **17**, 5948–5963.

**Van Buskirk, C. and Sternberg, P. W.** (2007). Epidermal growth factor signaling induces behavioral quiescence in Caenorhabditis elegans. *Nat. Neurosci.* **10**, 1300–1307.

**van Rheenen, J., Song, X., van Roosmalen, W., Cammer, M., Chen, X., Desmarais, V., Yip, S.-C., Backer, J. M., Eddy, R. J. and Condeelis, J. S.** (2007). EGF-induced PIP2 hydrolysis releases and activates cofilin locally in carcinoma cells. *J Cell Biol* **179**, 1247–1259.

**Van Zoelen, E. J., Stortelers, C., Lenferink, A. E. and Van de Poll, M. L.** (2000). The EGF domain: requirements for binding to receptors of the ErbB family. *Vitam. Horm.* **59**, 99–131.

**Vázquez-Manrique, R. P., Nagy, A. I., Legg, J. C., Bales, O. A. M., Ly, S. and Baylis, H. A.** (2008). Phospholipase C-epsilon regulates epidermal morphogenesis in Caenorhabditis elegans. *PLoS Genet* **4**, e1000043.

**Voutev, R. and Hubbard, E. J. A.** (2008). A "FLP-Out" system for controlled gene expression in Caenorhabditis elegans. *Genetics* **180**, 103–119.

**Walser, M., Umbricht, C. A., Fröhli, E., Nanni, P. and Hajnal, A.** (2017). β-Integrin de-phosphorylation by the Density-Enhanced Phosphatase DEP-1 attenuates EGFR signaling in C. elegans. *PLoS Genet* 13, e1006592.

**Wang, M. and Sternberg, P. W.** (2000). Patterning of the C. elegans 1 degrees vulval lineage by RAS and Wnt pathways. *Development* **127**, 5047–5058.

**Wang, Q., Chen, X.-W. and Margolis, B.** (2007). PALS1 regulates E-cadherin trafficking in mammalian epithelial cells. *Mol. Biol. Cell* **18**, 874–885.

**Wang, Q., Hurd, T. W. and Margolis, B.** (2004). Tight junction protein Par6 interacts with an evolutionarily conserved region in the amino terminus of PALS1/stardust. *J. Biol. Chem.* **279**, 30715–30721.

**Wang, Y., Du, D., Fang, L., Yang, G., Zhang, C., Zeng, R., Ullrich, A., Lottspeich, F. and Chen, Z.** (2006). Tyrosine phosphorylated Par3 regulates epithelial tight junction assembly promoted by EGFR signaling. *EMBO J.* **25**, 5058–5070.

**Wang, Z. and Sherwood, D. R.** (2011). Dissection of genetic pathways in C. elegans. *Methods Cell Biol.* **106**, 113–157.

**Wang, Z., Chi, Q. and Sherwood, D. R.** (2014a). MIG-10 (lamellipodin) has netrin-independent functions and is a FOS-1A transcriptional target during anchor cell invasion in C. elegans. *Development* **141**, 1342–1353.

**Wang, Z., Linden, L. M., Naegeli, K. M., Ziel, J. W., Chi, Q., Hagedorn, E. J., Savage, N. S. and Sherwood, D. R.** (2014b). UNC-6 (netrin) stabilizes oscillatory clustering of the UNC-40 (DCC) receptor to orient polarity. *J Cell Biol* **206**, 619–633.

**Ward, C. W., Hoyne, P. A. and Flegg, R. H.** (1995). Insulin and epidermal growth factor receptors contain the cysteine repeat motif found in the tumor necrosis factor receptor. *Proteins* **22**, 141–153.

**Wasserman, J. D., Urban, S. and Freeman, M.** (2000). A family of rhomboid-like genes: Drosophila rhomboid-1 and roughoid/rhomboid-3 cooperate to activate EGF receptor signaling. *Genes & Development* **14**, 1651–1663.

**Wee, P. and Wang, Z.** (2017). Epidermal Growth Factor Receptor Cell Proliferation Signaling Pathways. *Cancers (Basel)* **9**, 52.

**Whitfield, C. W., Bénard, C., Barnes, T., Hekimi, S. and Kim, S. K.** (1999). Basolateral localization of the Caenorhabditis elegans epidermal growth factor receptor in epithelial cells by the PDZ protein LIN-10. *Mol. Biol. Cell* **10**, 2087–2100.

**Wodarz, A., Hinz, U., Engelbert, M. and Knust, E.** (1995). Expression of crumbs confers apical character on plasma membrane domains of ectodermal epithelia of Drosophila. *Cell* **82**, 67–76.

**Wong, A. J., Bigner, S. H., Bigner, D. D., Kinzler, K. W., Hamilton, S. R. and Vogelstein, B.** (1987). Increased expression of the epidermal growth factor receptor gene in malignant gliomas is invariably associated with gene amplification. *Proc. Natl. Acad. Sci. U.S.A.* **84**, 6899–6903.

**Wong, S. T., Winchell, L. F., McCune, B. K., Earp, H. S., Teixidó, J., Massagué, J., Herman, B. and Lee, D. C.** (1989). The TGF-alpha precursor expressed on the cell surface binds to the EGF receptor on adjacent cells, leading to signal transduction. *Cell* **56**, 495–506.

**Wyckoff, J., Wang, W., Lin, E. Y., Wang, Y., Pixley, F., Stanley, E. R., Graf, T., Pollard, J. W., Segall, J. and Condeelis, J.** (2004). A paracrine loop between tumor cells and macrophages is required for tumor cell migration in mammary tumors. *Cancer Res.* **64**, 7022–7029.

**Xiao, K., Allison, D. F., Buckley, K. M., Kottke, M. D., Vincent, P. A., Faundez, V. and Kowalczyk, A. P.** (2003). Cellular levels of p120 catenin function as a set point for cadherin expression levels in microvascular endothelial cells. *J Cell Biol* **163**, 535–545.

**Yamanaka, T., Horikoshi, Y., Sugiyama, Y., Ishiyama, C., Suzuki, A., Hirose, T., Iwamatsu, A., Shinohara, A. and Ohno, S.** (2003). Mammalian Lgl forms a protein complex with PAR-6 and aPKC independently of PAR-3 to regulate epithelial cell polarity. *Current Biology* **13**, 734–743.

**Yang, Q., Roiz, D., Mereu, L., Daube, M. and Hajnal, A.** (2017). The Invading Anchor Cell Induces Lateral Membrane Constriction during Vulval Lumen Morphogenesis in C. elegans. *Developmental Cell* **42**, 271–285.e3.

**Yap, A. S., Crampton, M. S. and Hardin, J.** (2007). Making and breaking contacts: the cellular biology of cadherin regulation. *Curr. Opin. Cell Biol.* **19**, 508–514.

**Yochem, J., Gu, T. and Han, M**. (1998). A new marker for mosaic analysis in Caenorhabditis elegans indicates a fusion between hyp6 and hyp7, two major components of the hypodermis. *Genetics* 149, 1323–1334.

**Yochem, J., Weston, K. and Greenwald, I.** (1988). The Caenorhabditis elegans lin-12 gene encodes a transmembrane protein with overall similarity to Drosophila Notch. *Nature* **335**, 547–550.

**Yonezawa, N., Nishida, E., Iida, K., Yahara, I. and Sakai, H.** (1990). Inhibition of the interactions of cofilin, destrin, and deoxyribonuclease I with actin by phosphoinositides. *J. Biol. Chem.* **265**, 8382–8386.

**Yun, C.-H., Mengwasser, K. E., Toms, A. V., Woo, M. S., Greulich, H., Wong, K.-K., Meyerson, M. and Eck, M. J.** (2008). The T790M mutation in EGFR kinase causes drug resistance by increasing the affinity for ATP. *Proc. Natl. Acad. Sci. U.S.A.* **105**, 2070–2075.

**Zand, T. P., Reiner, D. J. and Der, C. J.** (2011). Ras Effector Switching Promotes Divergent Cell Fates in C. elegans Vulval Patterning. *Developmental Cell* **20**, 84–96.

**Zeiser, E., Frøkjær-Jensen, C., Jorgensen, E. and Ahringer, J.** (2011). MosSCI and Gateway Compatible Plasmid Toolkit for Constitutive and Inducible Expression of Transgenes in the C. elegans Germline. *PLoS ONE* **6**, e20082–6.

**Zhang, G., Sleiman, S. F., Tseng, R.-J., Rajakumar, V., Wang, X. and Chamberlin, H. M.** (2005). Alteration of the DNA binding domain disrupts distinct functions of the C. elegans Pax protein EGL-38. *Mechanisms of Development* **122**, 887–899.

**Ziel, J. W., Hagedorn, E. J., Audhya, A. and Sherwood, D. R.** (2008). UNC-6 (netrin) orients the invasive membrane of the anchor cell in C. elegans. *Nat Cell Biol* **11**, 183–189.

# 7. Appendix

## 7.1 Abbreviations

| | |
|---|---|
| 1° | Primary |
| 2° | Secondary |
| 3° | Tertiary |
| AC | Anchor cell |
| A-P | Anterior - Posterior |
| AR | amphiregulin |
| BTC | betacellulin |
| *C. elegans* | Caenorhabditis elegans |
| CRISPR | Clustered Regularly Interspaced Short Palindromic Repeats |
| Cas | CRISPR associated |
| DNA | Desoxyribonucleic acid |
| dNTP | Desoxyribonukleosidtriphosphate |
| D-V | Dorso - Ventral |
| ECM | Extra cellular matrix |
| E. coli | Escherichia coli |
| EGF | Epidermal growth factor |
| HB-EGF | EGF-like growth factor |
| EPG | epigen |
| EPR | epiregulin |
| EGL | Egg laying defective |
| EGFR | Epidermal growth factor receptor |
| ER | Endoplasmatic reticulum |
| ERK | Extracellular-signal Regulated Kinase |
| F1 | first filial generation |
| F2 | second filial generation |
| FLP | Flippase |
| FRT | FLP recognition targets |
| gf | gain of function |
| GFP | Green fluorescent protein |
| GFR | Growth factor receptor |
| IPTG | Isopropyl-β-D-thiogalactopyranosid |
| lf | Loss of function |
| LIN | Lineage defective |
| LET | Lethal |
| MAPK | Mitogen-activated protein kinase |
| MDCK | Madin-Darby canine kidney |
| µl | Microliter |

| | |
|---|---|
| µm | Micrometer |
| MosSCI | Mos1-mediated single copy insertion |
| MosTic | Mos1 excision-induced transgene-instructed gene conversion |
| Muv | Multivulva |
| NGM | Nematode Growth Media |
| N2 | C. elegans wild-type strain |
| P0 | parental generation |
| PCR | Polymerase chain reaction |
| PDZ | postsynaptic density/discs large/zonula occludens |
| PIP2 | phosphatidylinositol 4,5-bisphosphate |
| PLC | Phospholipase C |
| Pvl | Produring vulva |
| RAS | Rat sarcoma |
| rf | Reduction of function |
| RNAi | RNA interference |
| RT | Room temperature |
| RTK | Receptor Tyrosine Kinase |
| SynMuv | Synthetic Multivulva |
| shRNA | short hairpin RNA |
| TF | Transcription Factor |
| TGF-α | Transforming growth factor alpha |
| TM | Transmembrane |
| UNC | Uncoordinated |
| UTR | Untranslated region |
| utse | uterine seam-cell |
| uv | uterine ventral (cell) |
| VPCs | Vulval Precursor Cells |
| Vul | Vulvaless |
| WT | wild-type |
| zhEx | Zurich Extrachromosomal array |
| zhIs | Zurich Integrated array |

## 7.2 Curriculum vitae

Personal Information
Family name: MEREU
First name: Louisa
Date of birth: 04.09.1985
Home town: Walenstadt SG (CH)
Nationality: Swiss
Matriculation No.: 05-730-403

Education

2012 – 2017 **PhD Dr. sc. nat.**
Doctoral thesis: "Cell Polarity Shapes the Epidermal Growth Factor Morphogen Gradient During Vulval Induction and Reciprocal Epidermal Growth Factor Signaling Orients Cell Polarity to Promote Vulval Morphogenesis". Carried out under the supervision of Prof. Dr. Alex Hajnal, Institute of Molecular Life Sciences, University of Zurich, Switzerland.

2011 – 2012 **Master of Science in Genetics**
Master Thesis: "LIN-3 EGF regulates dorsal lumen formation in the *C. elegans* vulva". Carried out under the Supervision of Prof. Dr. Alex Hajnal,
at the Institute of Molecular Life Sciences, of the University of Zurich, Switzerland.

2005 – 2010 **Bachelor of Science in Biology**
University of Zurich, Switzerland.

2001 – 2005 **Matura Typus M**
Kantonsschule Stadelhofen, Zürich

## 7.3 Publications

**Farooqui, S., Pellegrino, M. W., Rimann, I., Morf, M. K., Mereu, L., Fröhli, E. and Hajnal, A.** (2012). Coordinated Lumen Contraction and Expansion during Vulval Tube Morphogenesis in *Caenorhabditis elegans*. *Developmental Cell* **23**, 494–506.

**Yang, Q., Roiz, D., Mereu, L., Daube, M. and Hajnal, A.** (2017). 'The Invading Anchor Cell Induces Lateral Membrane Constriction during Vulval Lumen Morphogenesis in *C. elegans. Developmental Cell* **42**, 271–285.e3.

## 7.4 Poster Presentations and Teaching experience

"The role of LIN-3 EGF during morphogenesis of the dorsal lumen in the vulva"
Louisa Mueller, Matthias Morf and Alex Hajnal
18th International *C. elegans* Meeting, Madison, Wisconsin, USA, 2012

"The role of LIN-3 EGF during morphogenesis of the dorsal lumen in the vulva"
Louisa Mueller, Matthias Morf and Alex Hajnal
19th International *C. elegans* Meeting, Los Angeles, USA, 2013

"The Epidermal Growth Factor acts as guidance cue during anchor cell invasion in *C. elegans*"
Louisa Mueller, Matthias Morf and Alex Hajnal
FEBS EMBO 2014 Conference, Paris, France, 2014

"The Epidermal Growth Factor acts as guidance cue during anchor cell invasion in *C. elegans*"
Louisa Mueller, Matthias Morf and Alex Hajnal
The 6th EMBO meeting, Birmingham, United Kingdom, 2015

"Synthetic whole genome RNAi screen identifies novel regulators of directional EGF secretion from the anchor cell"
Louisa Mereu, Matthias K. Morf, Silvan Spiri, Juan M. Escobar-Restrepo, Peter Gutierrez, Michael Daube, Alex Hajnal
The 7th EMBO meeting, Mannheim, Germany, 2016

**Teaching experiences**

2012 – date Assistant in various courses from M.Sc. in biology and Medical faculty.
Bio260: "Molecular Biology Course for Biology and Medicine"
Bio 323: "Modern genetics and genomics"
Bio 321: "Microscopy in Cell and Developmental Biology"
Medical course: "Zellwachstum und Zelltod in *C. elegans*"

2015 - 2016 Supervision of a M.Sc. project;
"Engineering the Canenorhabditis elegans lin-3 egf locus using the CRISPR/Cas9 system with a self-excising drug selection cassette mechanism"
Silvan Spiri, Institute of Molecular Life Sciences,
University of Zurich, Switzerland.

## 7.5 Acknowledgements

Foremost, I would like to thank Prof. Dr. Alex Hajnal for his supervision of this study and for his support, interest and confidence in my work. He is an excellent boss, and encouraged me to choose a topic, bases of my interest, and gave me the freedom to follow the work in the direction of my choice, but still providing guidelines and valuable insight from his vast knowledge and experience to drive my work in a successful direction. I will always cherish his unfailing optimism and positive reassurance.

Next, I want to thank Dr. Matthias Morf, my supervisor during my Master project, which laid the foundation for part of my PhD project. I learned a great deal from Matthias and appreciated all his valuable input during the course of my studies. He is a really great scientist, and I am grateful to have received the chance to follow up on his excellent work, in the "A whole genome RNAi screen identifies novel regulators of LIN-3 polarity" project.

Then I want to thank all the members of my thesis committee, Prof. Dr. Markus Affolter, Prof. Dr. Esther Stoeckli and Prof. Dr. Stefan Luschnig for their discussions and helpful suggestions during my PhD studies, providing external and objective insight into my project that helped to guide the direction my project was taking at the time.

I also sincerely thank all the present and former members of the Hajnal lab. It was always a pleasant, fun and welcoming environment to work in, and I cherish all the interactions we had on the scientific as well as the social level. From the former members, I especially want to thank Erika Fröhli for the help she provided when I had troubles in cloning or injection, and I also dearly cherished her on a personal level. I also want to thank Juan Escobar, Daniel Roiz, Jonas Hartmann, Charlotte Lambert, Tobias Schmid, Stefanie Nusser, Christoph Umbricht, Sarfarazhussain Farooqui, Fabienne Largey, Annina Schneider, Itay Naktimon and Quitan Yang for their lively discussions, inputs and the warm, fun atmosphere in our group at all time. In the Hajnlal Lab you can ask anyone for help and advice and it is given freely.

Of the present lab members, I thank Dr. Evelyn Lattmann, Andrea Haag, Sabrina Maxeiner, Dr. Tinri Aegerter-Wilmser, Dr. Michael Walser, Aleksandra Fergin, Ting Deng, Svenia Heinze, Adrian Henggeler, Elisa Pircher, Steve Grein and Michael Daube for providing a pleasant atmosphere and a ready ear to discuss successes and troubles and other fun topics. It is a great pleasure to work with you all. I also especially thank Michael Daube for his support and profound helpfulness. You can always come to him with a problem, and he will do his best and take time to help. Another special thanks goes to Silvan Spiri on account of his great work on the master project, following up on the "LIN-3 dorsal lumen project". It was really a pleasure to work with you. Someone who we might say works behind the scenes, but whose work is essential in our undisturbed pursuance of science, is Irene Hofmann. Dear Irene, thanks for all your work and especially the effort and fight you undertook to enforce and establish the 80% PhD position, for myself and all others who followed.

And last, but not least I want to thank my family for their support during this challenging time. My Father, my husband and his parents supported me by providing the means and taking care of my children, and thus enabled me to pursue my PhD studies. I am grateful to have been able to complete my PhD thesis with the addition of two wonderful children at the close.